Convolutional Models
for
Landmine Identification
with
Ground Penetrating Radar

Convolutional Models
for
Landmine Identification
with
Ground Penetrating Radar

Proefschrift

ter verkrijging van de graad van doctor
aan de Technische Universiteit Delft,
op gezag van de Rector Magnificus prof. dr. ir. J. T. Fokkema,
voorzitter van het College voor Promoties,
in het openbaar te verdedigen op 21 januari 2005 om 10.30 uur

door

Friedrich ROTH

Geofysicus (Master of Science)
geboren te München, Duitsland

Dit proefschrift is goedgekeurd door de promotoren:

Prof. ir. P. van Genderen
Prof. dr. ir. M. H. G. Verhaegen

Samenstelling promotiecommissie:

Rector Magnificus	voorzitter
Prof. ir. P. van Genderen	Technische Universiteit Delft, promotor
Prof. dr. ir. M. H. G. Verhaegen	Technische Universiteit Delft, promotor
Prof. dr. ir. P. M. van den Berg	Technische Universiteit Delft
Prof. dr. G. R. Olhoeft	Colorado School of Mines, USA
Prof. dr. M. Sato	Tohoku University, Japan
Prof. dr. sci. O. G. Yarovyi	Karazin Kharkiv National University, Oekraïne
Prof. dr. ir. L. P. Ligthart	Technische Universiteit Delft, reservelid

Published and distributed by DUP Science

DUP Science is an imprint of
Delft University Press
P.O. Box 98
2600 MG Delft
The Netherlands
Telephone: +31 15 27 85 678
Telefax: +31 15 27 85 706
E-mail: info@library.tudelft.nl

ISBN 90-407-2568-3

Keywords: ground penetrating radar, landmine identification, deconvolution

Printed in The Netherlands

The research described in this thesis was funded by the Technology Foundation STW, applied science division of the Dutch Organization for Scientific Research NWO.

TABLE OF CONTENTS

CHAPTER 1 INTRODUCTION 1

CHAPTER 1

INTRODUCTION

1.1 The Global Landmine Problem[1]

First improvised landmine forms appeared in European warfare in the early 18th century. Often going by the French term *fougasse*, these improvised landmines were shallowly buried bombs covered with scrap metal or gravel to serve as shrapnel. Similar forms of landmines were also used in the 19th century in the American Civil War. Modern mechanically fused antitank (AT) landmines were first introduced by Imperial Germany during World War I in response to Britain's invention of the tank. These mines were large devices, which were easily detected, removed and redeployed by the enemy. To address this problem, smaller antipersonnel (AP) landmines were developed for deployment around AT mines, thereby preventing their removal. By the end of World War I, all major participants had started manufacturing and using landmines. During World War II, landmines became an integral weapon on the battlefield. Not only had their design by then been refined, military forces also started to use AP landmines as a weapon in their own right. Originally developed as a tactical, defensive weapon intended to slow down enemy troops and protect military bases and infrastructure, the introduction of landmines that are deployable by air in the 1960s led to the use of landmines for military offensives, e.g. during the Vietnam War. Furthermore, landmines were increasingly used against civilian populations, terrorizing communities and rendering agricultural land unusable. Landmines have since then been widely used during internal and independence conflicts in all regions of the world. Especially in less developed countries, landmines became the weapon of choice for government troops, paramilitaries and guerilla forces since they are cheap, readily available and effective.

Today more than 80 countries are affected to some degree by landmines and/or unexploded ordnance (see figure 1.1). Countries that are most severely landmine contaminated are Afghanistan, Angola, Burundi, Bosnia & Herzegovina, Cambodia, Chechnya, Colombia, Iraq, Nepal and Sri Lanka. The total number of landmines that remain deployed in post-conflict areas is estimated at around 60 million, causing more than 15,000 new casualties every year.

The negative impact of landmines on communities in (post)-conflict areas is severe and diverse. Beyond living with the constant danger of getting injured or killed and associated psychological trauma, landmine contamination has a strong adverse economical effect. It costs between $ 300 and $ 1000 to remove a landmine and $ 100 to $ 3000 to provide an artificial limb. Agricultural fields, farming land, road networks and water resources usually remain unusable or inaccessible, greatly impeding recovery from the conflict. In addition, landmines hinder the work of help organizations, e.g. the delivery of help supplies, as well as the work of international peacekeeping troops.

Reducing the impact of landmines requires a variety of related activities, which are generally summarized under the term *Mine Action*. Naturally, a key task of Mine Action is *demining*[2]. Other important activities are mine awareness training and social work to help landmine

---

[1] This information has been compiled from the websites of the following organizations: The Canadian Landmine Foundation (www.canadianlandmine.org), The International Campaign to Ban Landmines (www.icbl.org), UN Mine Action Service (www.mineaction.org).

[2] *Demining* includes activities which lead to the removal of landmine hazards, including technical survey, mapping, clearance, marking, post-clearance documentation and handover of cleared land.

victims and their families. Complementary to these activities, the international community seeks a long-term solution to the landmine problem by imposing a ban on landmines. A first step to restrict the use of landmines was achieved in 1981 through the UN Convention on Certain Conventional Weapons, Protocol II, which was amended 1996 and signed by 67 countries as of January 2002. In 1999, a complete ban on AP landmines including their use, development, stockpile and transfer entered into force as the Ottawa Treaty on the Antipersonnel Mine Ban Convention, signed by 143 countries as of September 2004.

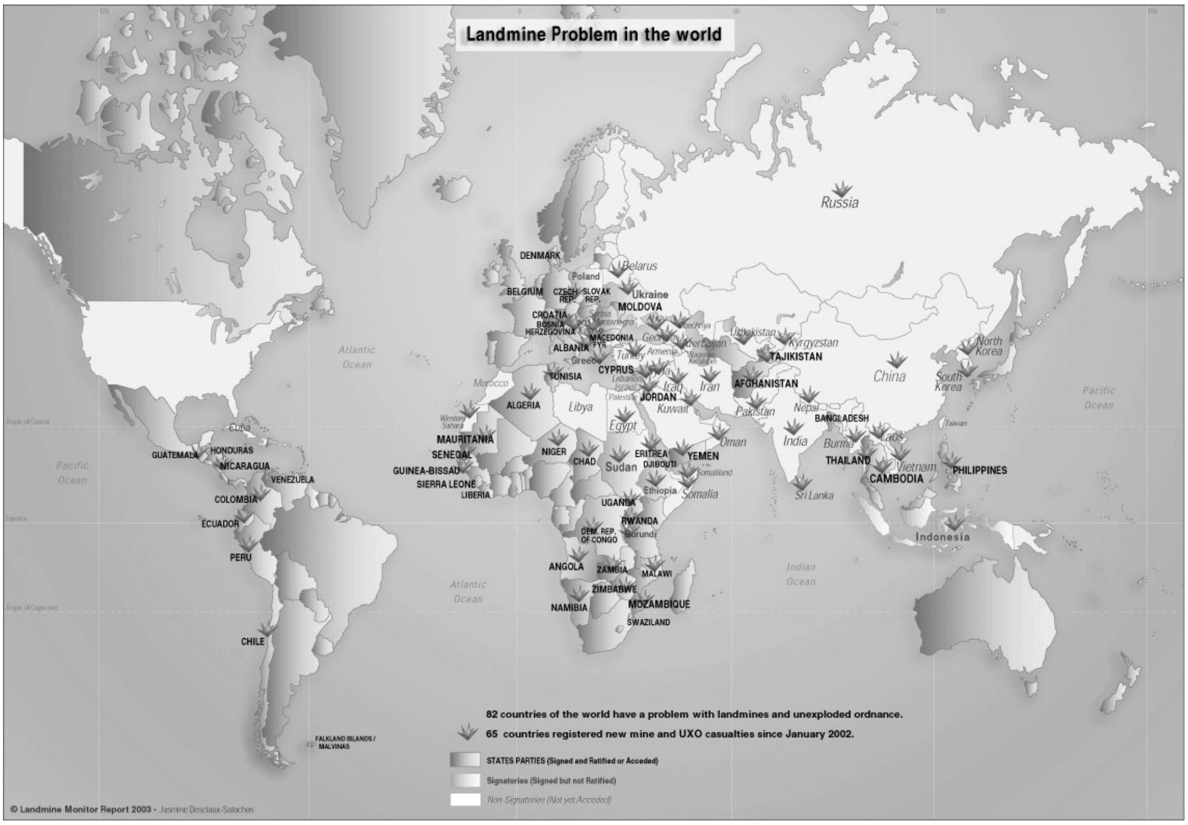

Figure 1.1: Map of mine affected countries. (source: Landmine Monitor Report 2003).

1.2 Current Demining Techniques[3]

Demining is an important part of Mine Action. Today most humanitarian mine clearance is carried out using a combination of manual demining and dog detection, with mechanical demining gaining more and more share. For quality control, demining organizations tend to employ a combination of these techniques before an area is declared free of mines.

Manual demining

In manual demining (figure 1.2a), the deminer uses an electromagnetic induction metal detector and a prodding stick to investigate every square centimeter of ground in front of him. The metal detector gives an audible alert when metal is present in the ground. The deminer

---

[3] The information has been compiled from the websites of the following organizations: MgM People Against Landmines (www.mgm.org), Geneva International Centre for Humanitarian Demining (www.gichd.org).

then uses the prodding stick to probe the ground and feel for the side of the suspected mine. Manual demining can be applied almost everywhere and is usually reliable. However, it has the disadvantage of being a very dangerous, slow and hence expensive procedure. A severe limitation of the metal detector is its inability to distinguish between landmines and harmless pieces of metal, e.g. junk or metal shrapnel from former bomb explosions. As a result, metal detectors give rise to a high number of false alarms, each of which need to be carefully examined as if it was a landmine, thereby slowing down the clearing process tremendously. Furthermore, some landmines contain very little metal, so-called low-metal content landmines, or no metal at all, making their detection extremely difficult or impossible, respectively.

Dog detection

Dogs have the skill to scent explosive molecules that leak out of landmines and migrate slowly to the surface of the ground, and can be trained to locate landmines. The search is conducted with the dog on a long leash (figure 1.2b). If the dog detects the scent of explosives, it lies down with its nose pointing to the origin of the “signal”. The spot is marked and later investigated by manual demining. Apart from detecting individual landmines, dogs are also used for the important task of determining which areas are not mined, an activity referred to as area reduction. Dog detection has the advantage of being faster than manual demining and, since it is based on explosive detection, false alarms are much less likely. The main limitations are that dogs can only concentrate for a few hours and that it is not well understood under which conditions a dog will miss a landmine. In addition, in tropical climates dogs are prone to illness.

Mechanical demining

Until the late 1980s, mechanical demining machines were primarily used by the military in situations where speed of clearance was a priority over reliability. Since then demining machines have been developed specifically for the purpose of humanitarian demining and new improved systems are continuously emerging on the commercial market (figure 1.2c). The main applications of demining machines are for area reduction and ground preparation for manual demining. The latter includes vegetation removal, breaking-up hard soil, as well as metal contamination reduction through the use of magnets. In addition, machines are starting to be used for mine clearance and, as the understanding of their performance grows, clearance machines are gaining more and more acceptance by the demining community. The main disadvantages of mechanical demining are that sometimes machines are unreliable, require repair and, due to their size, cannot access all areas.

Manual demining with the metal detector, dog detection and mechanical demining will most likely continue to be the preferred techniques for mine clearance in the time to come. However, these techniques have their limitations and there is great interest to develop new landmine detection sensors for both military and humanitarian needs, which can provide fast and reliable clearance with a low false alarm rate. The challenge to technology and science in developing landmine detection sensors is immense. Not only do more than 350 different types of landmines exist, but also they are buried at different depths, in different soils, in different terrains affected by varying weather conditions. Clearly, no one sensor will work well under all these conditions. Hence, future landmine detection systems are likely to use combinations of different types of sensors to increase the detection and reduce the false alarm rate (MacDonald *et al,* 2003). A sensor that has demonstrated great potential for use in such a multi-sensor system is *Ground Penetrating Radar* (GPR).

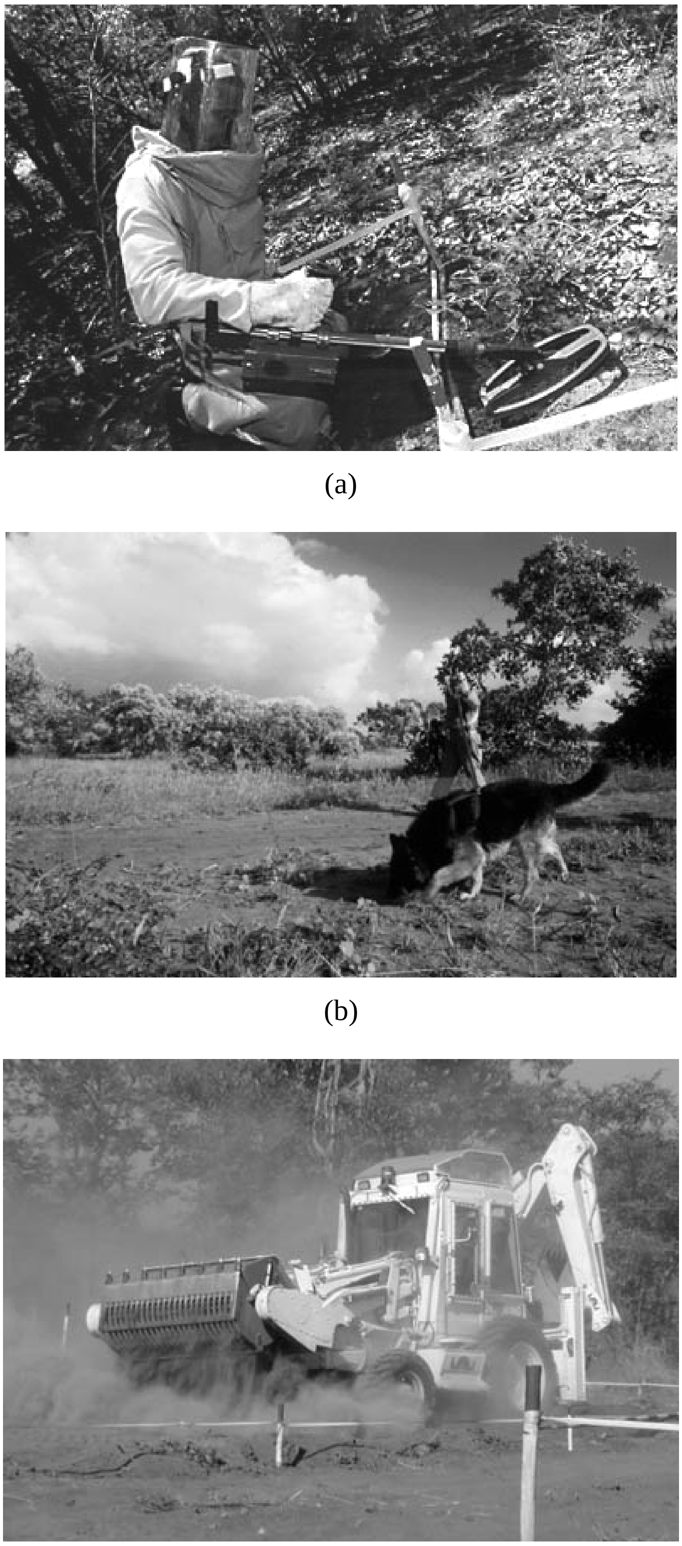

(a)

(b)

(c)

Figure 1.2: Current demining techniques:
(a) Manual demining with the metal detector.
(b) Dog detection.
(c) Mechanical demining. The MgM ROTAR sieves the soil for landmines.

1.3 Ground Penetrating Radar (GPR) for Landmine Detection and Identification

Ground Penetrating Radar is a non-invasive sensing technique, which uses electromagnetic waves to locate and characterize objects or interfaces beneath the surface of the ground or manmade structures. First successful uses of GPR go back to as early as the 1930s, mainly as a technique for ice depth probing (Stern, 1930). With the introduction of commercial systems in the 1970s, the range of applications of GPR technology has been ever expanding. Application examples include the location of buried utilities, the inspection of highways and airport runways, the detection of underground tunnels and subsurface voids and archeological surveys.

The main components of a typical GPR system are illustrated in figure 1.3. The transmitter generates an electric signal, which is radiated by the transmitting antenna. Reflections of the radiated wave from above and below the ground are measured by the receiving antenna, digitized by the receiver, and stored on a computer for further processing and interpretation.

Based on the type of signals used to probe the subsurface, a distinction is made between pulsed (time-domain) GPR systems and stepped frequency (frequency-domain) GPR systems. Most GPR antenna systems are bistatic consisting of one transmitting and one receiving antenna. During the data acquisition, which is generally done along straight scanning lines, the two antennas are kept at a constant distance (offset) and orientation from each other. Variations to this simple bistatic antenna configuration exist in the form of array systems, which use multiple transmitting and receiving antennas for either fast data acquisition and/or multi-offset measurements, and polarimetric systems, which measure both the co- and cross-polar components of the reflected wavefield for two-orthogonal transmitting polarizations.

Fueled by the successful application in a wide a range of subsurface investigation problems, since the mid-1990s there are has been an increased interest to develop GPR technology for a challenging new application: Landmine detection.[4] The potential benefits of a *demining GPR*[5] can be summarized as follows:

- Reduction of the false alarm rate by target identification[6] based on measured target responses.
- Ability to detect both plastic and metal cased landmines.
- Ability to detect both surface-laid and buried landmines.
- Ability to determine the depth and the horizontal position of an object.
- Possibility to scan the ground with the antennas elevated at a safe distance from the ground surface.
- Possibility for combination with other sensor technology.

---

[4] Actually, some research on landmine detection with GPR started as early as the late 1970s, e.g. Chan *et al* (1979).

[5] The term *demining GPR* is used throughout this thesis to describe a GPR system that supports demining operations.

[6] In this thesis, *identification* is understood as “the process of estimating whether a detected object is a landmine” and not “the process of determining the landmine type, e.g. PMA-3”. This usage is in agreement with the IEEE standard definition of *identification*: “The knowledge that a particular radar return signal is from a specific target.” (source: The IEEE Standard Dictionary of Electrical and Electronic Terms, 6th Edition)

An existing and promising sensor combination, in which GPR is utilized, is with the metal detector, e.g. the Minetect system from ERA Technology (UK) or the AN/PSS-14 (formerly HSTAMIDS) system from CyTerra Corporation (USA). In this combination the target identification capability of GPR is used to reduce the number of false alarms of the metal detector and to detect completely non-metal mines. This combination constitutes an improvement to the well-established stand-alone metal detector and hence leads to easier acceptance by the demining community. When used in the combination with the metal detector, the GPR acts mostly as a support sensor, which means that it is used to confirm a detection of the primary sensor, in this case the metal detector. Most likely in the near future this will be the main role of GPR in landmine detection, stressing the importance of the development of reliable GPR target identification methods.

As reflected by current research trends, a demining GPR can be used as what I call a probing sensor, an imaging sensor or a combination of both.

- When used as a probing sensor, the GPR data is analyzed on the basis of individual *A-scans*[7]. The objective is to detect and/or identify an object that is buried at the position where the analyzed A-scan was measured.
- When used as an imaging sensor, the objective is to create a focused 2D or 3D image of the subsurface from multiple A-scans measured over a grid. The image is then used to detect, locate and characterize buried objects that lie below the measurement area. The imaging sensor approach also includes inversion-based techniques that aim to reconstruct the spatial distribution of the constitutive parameters (dielectric permittivity, magnetic permeability and conductivity) in the subsurface.

In either approach, it is important to have accurate information on the radiation characteristics of the GPR antennas. Furthermore, imaging requires knowledge of the wave velocity distribution in the ground and accurate antenna positioning. As a consequence, the use of a demining GPR as an imaging sensor is more restrictive than when being used in the localized probing mode. In this thesis, the attention is focused on GPR as a probing sensor.

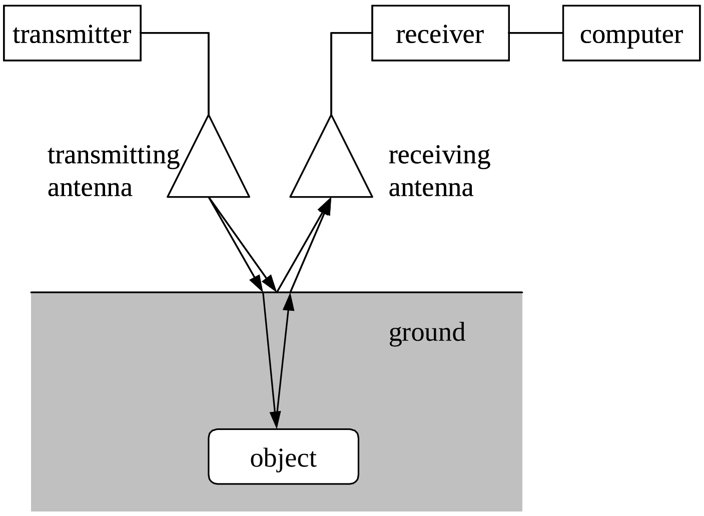

Figure 1.3: Illustration of a typical GPR system.

---

[7] The term *A-scan* refers to a time sampled GPR return measured at one antenna position.

1.4 The GPR Response of a Landmine and its Use for Target Identification

Early-time versus late-time target response

Target identification in the probing mode is based on the concept of a target response, also commonly referred to as target signature. The target response contains two components, namely the early-time (forced) and late-time (natural) response of the target (Kostylev, 1994). The early-time response has a finite duration and is formed while the incident wave passes through and along the outside of the target. The late-time response refers to the target's natural modes, which build up after the target has been illuminated by the incident wave. Landmine and unexploded ordnance (UXO) identification based on complex natural resonances (CNR) computed from the late-time response has been the topic of extensive research throughout the years (Chen and Peters, 1997; Baum, 1998). The motivation to work with CNR stems from the fact that the resonances are target orientation independent and lead to a small number of characterizing parameters. However, the resonances of a buried target are generally highly damped compared to those in air and thus may be extremely difficult, if not impossible, to measure. This is especially true for plastic cased landmines (Huynen, 2003). Hence, the research described in this thesis is entirely based on the early-time target response, which is much stronger than the late-time response.

The early-time response of a landmine depends on its size, shape and internal structure. Consequently, the early-time response carries valuable target information and can be used for landmine identification. However, it is well known that the early-time response depends not only on the electromagnetic properties of the landmine, but also on those of the soil in which the landmine is buried. In addition, the early-time response is dependent on the orientation of the landmine with respect to the incident and scattering directions. For these reasons, simple target identification techniques based on template matching or feature based classification become unreliable or might even fail completely. Clearly, in order to design a reliable identification algorithm or specify the conditions under which an identification algorithm will fail, it is important to understand the factors that determine the early-time response of a landmine.

Up to now the understanding of the early-time response of landmines is mostly limited to knowledge obtained from numerical simulations (Geng and Carin, 1999; Sullivan *et al*, 1999; Roth *et al*, 2001; Strifors *et al*, 2002; Johnson and Burkholder, 2004) and experience from actual GPR measurements (Carin *et al*, 1999; Zanzi *et al*, 2002; Kovalenko and Yarovoy, 2003; JRC Landmine Signature Database). Although this knowledge is very useful to evaluate or predict sensor performance and landmine responses under varying burial conditions, it does not lend itself naturally to establish a direct link between measured GPR responses and target characteristics, e.g. target size and depth of burial. A different strategy with which this link is easily made is convolutional GPR modeling introduced below.

Since this thesis is solely concerned with the *early-time target response*, in the remainder of the text the prefix *early-time* will be omitted for convenience.

Convolutional models & the target impulse response

To identify landmines from GPR data, it is necessary to have practical models relating the measured target response to the main response determining factors and associated data processing algorithms, which ideally allow for real-time target identification. These requirements suggest representing the measured target response through a convolutional model, which describes the sequence of radiation, propagation, target scattering and receiving, and using deconvolution to estimate the target impulse response, which embodies information on target characteristics (e.g. outer dimensions, contrast, internal structure).

The concept of convolution and deconvolution in GPR applications is not new (Daniels *et al*, 1988). However, up to now research in this area has focused on impulse response characterization of the antennas (Scheers *et al*, 2000) and the development of GPR specific deconvolution algorithms (Turner, 1994; Scheers *et al*, 2001; Savelyev *et al*, 2003), leaving the target impulse response and its relation to target characteristics mostly unexplored. Furthermore, all these works impose a convolutional representation of the GPR data by definition rather than deriving it from physical principles.

The first of a few notable contributions towards a better understanding of the impulse response of a buried target was made by Chan *et al* (1981) who used the well-established Physical Optics (PO) approach in radar target impulse response modeling (Kennaugh and Moffatt, 1960) to derive a simple analytical expression for the impulse response of a metal target buried in a lossy ground. Twenty years later, Nag and Peters (2001) extended the work of Chan *et al* for application to buried homogeneous dielectric targets that are rotationally symmetric. For both types of targets (metal and dielectric), PO predicts a simple relationship between the target impulse response and the cross-section profile of the “illuminated” part of the target. This profile is commonly known as the target profile function. Based on their findings, Chan *et al* postulated the possibility to image a buried target based on a few A-scans or, if the target is rotationally symmetric, one single A-scan. Nag and Peters applied this idea to image a buried PMA-3 landmine with limited success. One of the limitations they faced was that the operating band of their GPR system did not include frequencies below 1.2 GHz, which are necessary to reconstruct the target profile function. In addition, the validity of PO for scattering from a plastic cased landmine is fundamentally limited by its inability to describe scattering from the bottom of the landmine and from internal mine structure. Hence, it is questionable whether PO provides a good approximation to the target impulse response of a buried plastic cased landmine. It should also be noted that, as in the work of Chan *et al*, the derivations of Nag and Peters neglect the radar hardware and assume the target in an unbounded host medium with the same properties as the ground, i.e. the ground surface is not accounted for.

Summarizing, these shortcomings establish a need for further scientific developments in the area of convolutional GPR modeling, especially the derivation of impulse response models for plastic cased landmines. Other important factors that need to be modeled are the presence of the ground surface and the radar hardware. Complementary to this, a deconvolution based target characterization procedure should be developed, which estimates important target characteristics that ultimately allow identifying whether a detected target is likely to be a mine or no mine. Target characteristics that are useful in this respect are the outer dimensions of the target, its material properties (e.g. its dielectric permittivity), a description of its internal structure (e.g. the presence of an air gap), and its depth of burial.

1.5 Scope of the Research

This thesis provides a comprehensive treatise of new developments in the area of convolutional GPR modeling and deconvolution with application to AP landmine identification, which are the outcome my PhD research. The treatise addresses all major aspects of the problem:

- The derivation of frequency- and time-domain convolutional models[8] describing electromagnetic scattering from a buried *minelike target*[9]. Novelties include simple analytic expressions for the target transfer function/impulse response, a previously unpublished far-field backscattering representation of the half-space electric Green's tensor, and a host medium transformation law, which relates the response of a minelike target buried in a lossless ground to its response in a lossy ground.
- The introduction of point source/receiver models for the GPR antennas and the receiver chain, thereby extending the time-domain convolutional scattering model to account for the radar hardware. The so-obtained convolutional GPR model is the first of its kind, which gives analytic expressions for all components of the GPR chain (hardware, propagation to and from the target, the target impulse response). The model is formulated for both buried and surface-laid minelike targets.
- The development of preprocessing algorithms that extract the response of the target to be identified from the measured GPR data. Novelties include a weighted moving average background subtraction (WMA-BS) technique, which accurately recovers the amplitude and shape of the target response along the entire diffraction hyperbola, and a transformation of the measured scattering matrix, termed target frame transformation with which a target orientation independent target response is obtained.
- The development of a deconvolution based target characterization procedure. Novelties include a deconvolution algorithm, termed subset selection deconvolution, which significantly reduces the ill-posedness and ill-conditioning of the radar signal deconvolution problem. As a further novelty, the estimated impulse responses can be inverted for target characteristics, e.g. its outer dimensions and its depth of burial.

Together these new developments form a framework of theoretical models and data processing algorithms, which opens the possibility to identify plastic and metal cased AP landmines from GPR data within a very short computation time. This possibility has been verified with success based on 3D finite-difference time-domain (FDTD) and experimental GPR data.

---

[8] A *convolutional model* describes a linear time-invariant process as the convolution of a number of time functions. The terms *frequency-domain convolutional model* and *time-domain convolutional model* are used in this thesis to distinguish between the frequency-domain and time-domain representations of a convolutional model, respectively. Note that convolution in the time-domain is equivalent to multiplication in the frequency-domain.

[9] The term *minelike target* describes a target whose size, shape and electromagnetic properties resemble those of a landmine.

1.6 Thesis Outline

Following this introduction, **chapter 2** presents a detailed analysis of scattering from homogeneous minelike target. The analysis consists of two parts, first the development of the relevant electromagnetic scattering theory, and second, application of this theory for target characterization based on deconvolution processing. Starting from source-type integral representations of the scattered field, I derive frequency- and time-domain convolutional models describing plane wave backscattering from a homogeneous minelike target including expressions for its target transfer function/impulse response. To account for the different scattering behavior of plastic and metal cased landmines, two types of minelike targets are considered, the dielectric minelike target and the metal minelike target. Essential steps in the derivation are the linearization of the scattering problem through either the Born or the PO scattering approximation, depending on whether a dielectric or a metal target is considered, and application of a new far-field backscattering representation of the half-space Green's tensor. The derivation of the convolutional models is followed by a review of common deconvolution algorithms, i.e. Wiener filtering and ridge regression, and some of their shortcomings for use in target characterization are pointed out. These shortcomings lead to the development of the new subset selection deconvolution algorithm that uses the derived target impulse response expressions as a priori information on the specific form of the impulse response to be recovered. The estimated impulse responses can be inverted for either target size or material properties using the derived time-domain convolutional scattering model, and a target characterization procedure based on this idea is proposed. The proposed target characterization procedure and the validity of the underlying scattering models are then tested using simulated data examples obtained by 3D FDTD modeling. At the end of the chapter, attention is drawn to the influence of losses in the ground on the target response. Here I use similarity analysis in the Laplace domain to derive a host medium transformation law, which relates the time-domain response of a homogeneous dielectric minelike target buried in a lossless ground to its time-domain response in a lossy ground. The working of the transformation law is illustrated using a 3D FDTD data example.

In **chapter 3**, I further take up dielectric minelike target and generalize the scattering theory of chapter 2 to account for internal mine structure, specifically a thin air gap or a small piece of metal. The generalization follows directly from a Born-type linearization of the volume integral representation of the scattered field in which the contrast of the inclusion has been defined by means of the Rayleigh scattering approximation. As a result of the generalization, the target impulse response of the dielectric minelike target is simply augmented by an additional term describing the effect of the inclusion, thus making it straightforward to extend the target characterization procedure for homogeneous minelike targets, proposed in chapter 2, to targets with internal structure. Again, the validity of scattering models and the performance of the now extended target characterization procedure are demonstrated using 3D FDTD data examples.

For application of the derived scattering models and the target characterization procedure to GPR data, the radar hardware needs to be considered and data preprocessing algorithms need to be developed. Both these issues are addressed in **chapter 4**. After presenting a polarimetric video impulse GPR system developed by IRCTR[10], models for its transmitting antenna and receiver chain are introduced, which enter as additional terms in the time-domain convolutional scattering model of chapters 2 and 3. In this way, a convolutional model for the

---

[10] International Research Centre for Telecommunications-Transmission and Radar, Delft University of Technology.

GPR response of buried minelike target is obtained. In addition, a convolutional model for the GPR response of a surface-laid minelike target is presented, which follows from similar considerations. Following the derivation of the convolutional GPR models, a simple, yet accurate calibration procedure is introduced, which estimates important hardware characteristics, namely the effective radiated waveform and the direct wave signal, both of which are required for subsequent data (pre)processing. The data preprocessing is primarily concerned with the extraction of target responses that are suitable for target identification. To this end, two new algorithms are introduced, the WMA-BS technique, which removes the direct wave signal and the ground reflection signal from each measured A-scan, and the target frame transformation, a polarimetric preprocessing step required for the identification of targets with a preferential scattering axis, e.g. an elongated bombshell. The workings of both preprocessing algorithms are illustrated using data acquired with the IRCTR video impulse GPR. Finally, a slightly modified version of the subset selection based target characterization procedure of chapters 2 and 3 is presented which operates on the preprocessed A-scan at the apex of the target response hyperbola and, as before, provides information on either target size or target material properties.

To validate the full data processing chain consisting of the radar calibration, preprocessing and target characterization, I acquired data with the IRCTR video impulse GPR at a controlled indoor environment over a variety of dielectric and metal minelike targets, both surface-laid and buried. The data acquisition and the results from the data processing are detailed in **chapter 5**.

Finally, in **chapter 6**, I give an overview of the most important results that were achieved and formulate some conclusions that can be drawn from this research. Here I also point out some of the limitations of the presented material with regard to application in real minefields and solutions to these limitations are suggested in the form of recommendations for future research.

CHAPTER 2

SCATTERING FROM A HOMOGENEOUS MINELIKE TARGET

This chapter presents a detailed treatment of plane wave scattering from a buried AP landmine, which for simplicity is approximated here as either a homogeneous dielectric or metal minelike target. The objectives of the treatment are twofold. The first objective is to represent the scattering through a convolutional model and derive target transfer function/impulse response approximations, which describe the scattering behavior of the target and are simple closed-form expressions in terms of target size, shape and electromagnetic contrast. The second (and complementary) objective is the development of a deconvolution based target characterization procedure, which uses knowledge of the incident and the scattered field to estimate target characteristics, e.g. its outer dimensions.

The unifying element of all scattering models presented in this chapter is that they are derived from source-type integral representations of the scattered field (Chew, 1990, ch. 8) and assume a linear relationship between the scattering currents and the incident field. The scattering from a dielectric minelike target is formulated using the volume integral representation in combination with the Born approximation, an approach which can easily be extended to account for internal mine structure as will be described in more detail in chapter 3. The scattering from a metal minelike target is formulated using the surface integral representation in combination with the Physical Optics (PO) approximation. Apart from this difference, great care is taken to treat the scattering from dielectric and metal minelike targets in a uniform manner, thereby yielding target transfer functions/impulse response models of the same form.

The development of the deconvolution based target characterization procedure is to a great part driven by the necessity to reduce the ill-posedness[1] and the ill-conditioning[2] inherent to the deconvolution of band-limited signals. A number of deconvolution algorithms designed to improve the conditioning exist among which Wiener filtering and ridge regression, but, as will be demonstrated, these algorithms are unable to provide the amplitude information and the temporal resolution required for target characterization. To overcome these problems, a new deconvolution algorithm is devised, termed subset selection deconvolution, which uses the derived target impulse response models for minelike targets as a priori information on the specific form of the impulse response to be estimated. The target characterization procedure, which builds on the subset selection deconvolution algorithm, inverts the impulse response obtained by deconvolution for target characteristics.

The chapter is organized as follows. In section 2.1, frequency- and time-domain convolutional models for plane wave backscattering from a buried minelike target are derived, including expressions for the target transfer function/impulse response. Essential steps in the derivation are the linearization of the scattering problem through either the Born or the PO scattering approximation, as described above, and application of a new far-field backscattering representation of the half-space Green’s tensor, which is derived in section 2.1.3. In section 2.2, a review of common deconvolution algorithms is given, which illustrates their unsuitability for target characterization based on simple synthetic data examples. Following this review, the subset selection deconvolution algorithm is developed and integrated into a target characterization procedure, which uses the derived convolutional scattering models to

---

[1] A problem is ill-posed if it has no exact or unique solution.

[2] A problem is ill-conditioned if its solution varies widely in response to small errors in the measurements.

estimate a target's outer dimensions or, in the case of a dielectric minelike target, its permittivity. In section 2.3, the performance of the proposed target characterization procedure and the validity of the underlying scattering models are demonstrated using 3D finite-difference time-domain (FDTD) data examples. Section 2.4 takes a little side step and derives a host medium transformation law, which relates the time-domain response of a dielectric minelike target buried in a lossless ground to its time-domain response in a lossy ground. The working of the transformation law is illustrated using a 3D FDTD data example. In section 2.5, the main contributions of the material presented in this chapter are highlighted and discussed.

2.1 Convolutional Models for Backscattering from a Buried Minelike Target

In this section, source-type integral representations of the scattered field are used to derive frequency- and time-domain convolutional models for backscattering from a buried minelike target illuminated by a downward propagating (locally) uniform plane wave. As shown in figure 2.1, the ground is modeled as a half-space with admittivity $\hat{y}_1 = \boldsymbol{i}\omega\varepsilon_1 + \sigma_1$ and impedivity $\hat{z}_1 = \hat{z}_0 = \boldsymbol{i}\omega\mu_0$, where $\boldsymbol{i}$ is $\sqrt{-1}$, ω denotes angular frequency, ε_1 is the ground dielectric permittivity, σ_1 is the ground conductivity, and μ_0 is the vacuum magnetic permeability. To account for the different scattering behavior of plastic and metal cased landmines, two target types will be distinguished: the dielectric minelike target and the metal minelike target.

- The dielectric minelike target, treated in subsection 2.1.1, is characterized by the permittivity ε_t and constitutes an admittivity contrast $\Delta\hat{y} = \hat{y}_t - \hat{y}_1$, where $\hat{y}_t = \boldsymbol{i}\omega\varepsilon_t$. Its permeability is assumed to be equal to that of the ground, i.e. μ_0.
- The metal minelike target, treated in subsection 2.1.2, is assumed to be a perfect electrical conductor (PEC).

The target is located on the *z*-axis at a depth *d* and we are interested in the backscattered field at a height *h* above the ground. Note that the *z*-axis is pointing downward.

2.1.1 The dielectric minelike target

Frequency-domain formulation

The field $\mathbf{E}^s$ scattered by the dielectric minelike target may be represented through the volume integral

$$\mathbf{E}^s(\boldsymbol{x}) = \iiint\limits_{\substack{\text{target}\\\text{volume}}} \tilde{\mathbf{G}}(\boldsymbol{x}, \boldsymbol{x}')\mathbf{J}^s(\boldsymbol{x}')\,dV' \tag{2.1}$$

in which $\mathbf{J}^s$ is the volume scattering current within the target and $\tilde{\mathbf{G}}$ is the half-space electric Green's tensor.

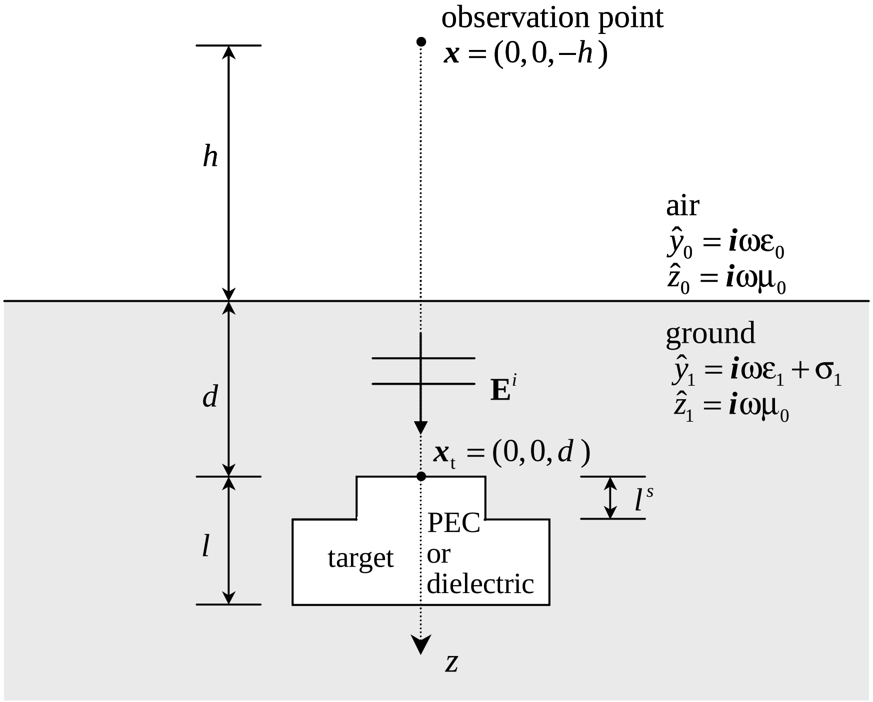

Figure 2.1: Backscattering from a buried minelike target illuminated by a downward propagating plane wave. In the figure, l denotes the target height whereas l^s is the distance from the onset of the target to its shadow boundary.

Plastic cased landmines are often composed of materials with permittivities close to that of the ground (Dasgupta *et al*, 1999). We therefore consider the target to be a weak scatterer, allowing the assumption of a linear relationship between the scattering current $\mathbf{J}^s$ and the plane wave incident field $\mathbf{E}^i$:

$$\mathbf{J}^s(\boldsymbol{x}) = \chi\mathbf{E}^i(\boldsymbol{x}) = \chi\mathbf{E}^i(\boldsymbol{x}_t)e^{-ik_1(z-d)} \quad , \tag{2.2}$$

where $k_1 = (-\hat{z}_1\hat{y}_1)^{1/2}$ is the wavenumber in the ground, $\boldsymbol{x}_t = (0,0,d)$ refers to the target location, and χ denotes a generalized contrast whose functional form depends on the specific weak scattering approximation considered, viz. the Born approximation with which

$$\chi = \Delta\hat{y} \tag{2.3}$$

or the modified Born approximation (Van der Kruk, 2001, p. 87-90) with which

$$\chi = \Delta\hat{y}\frac{3\hat{y}}{\Delta\hat{y} + 3\hat{y}} \quad . \tag{2.4}$$

The Born approximation assumes that the electric field within the target is equal to the incident field $\mathbf{E}^i$. At radar frequencies, this assumption is considered to be valid as long as the magnitude of the complex phase difference between the wave propagating through the target and the incident field is much less than unity. As shown by Habashy *et al* (1993), this is equivalent to requiring

$$\left|k_1 D(\Delta\hat{y}/\hat{y}_1)\right| \ll 1 \quad , \tag{2.5}$$

where D is the characteristic size of the target, in our case its height l (see figure 2.1). The modified Born approximation is derived from the assumption that the target can be considered as being made up of non-interacting point scatterers. Note that as the magnitude of the admittivity contrast $\Delta\hat{y}$ decreases, the generalized contrast χ given by the modified Born approximation reduces to that of the Born approximation. Since both approximations are closely related, let us proceed for simplicity by considering the Born approximation only.

Next, we would like to find a suitable representation of the Green's tensor $\tilde{\mathbf{G}}$. Assuming a horizontal polarization for the incident field in eq. (2.2), only the first and the second column of the Green's tensor are relevant. The general formulae for the tensor elements of these two columns are given in subsection 2.1.3. They involve Hankel transforms

$$\int_0^\infty f(\lambda) J_n(\lambda\rho) d\lambda \tag{2.6}$$

in which f are singular complex kernel functions, J_n (n = 0,1,2) are Bessel functions of the first kind and order n, ρ is the horizontal distance between the observation point $\boldsymbol{x}$ and the source point $\boldsymbol{x}'$, and the integration variable λ is the horizontal wavenumber. In their general form, the Green's tensor elements can only be evaluated numerically (Xiong and Tripp, 1997). However, as shown in section 2.1.4, the complexity of the Green's tensor reduces significantly for backscattering from a small target ($\rho \approx 0$) and far-field observation ($k_0 h \gg 1$), leading to the approximation

$$\tilde{\mathbf{G}}(\boldsymbol{x}, \boldsymbol{x}') \approx -\hat{z}_0 T_{g\to a}\,\zeta(h,d)\frac{e^{-i(k_0 h + k_1 z')}}{4\pi(h+d)}\begin{bmatrix}1 & 0\\ 0 & 1\\ 0 & 0\end{bmatrix}, \tag{2.7}$$

where $k_0 = \omega(\mu_0\varepsilon_0)^{1/2}$ is the wavenumber in air, $T_{g\to a}$ is the normal incidence ground-to-air Fresnel transmission coefficient given by

$$T_{g\to a} = \frac{2k_1}{k_0 + k_1} \tag{2.8}$$

and ζ is a coefficient accounting for the refraction related spreading at the ground surface and is defined as

$$\zeta(h,d) = \frac{h+d}{h\dfrac{k_1}{k_0} + d}\ . \tag{2.9}$$

Substituting the scattering current given by eq. (2.2) and the backscattering Green's tensor for far-field observation given by eq. (2.7) into eq. (2.1) and integrating over x and y, the backscattered field at a height h above the ground can be written as

$$\mathbf{E}^s(\boldsymbol{x}) = \frac{T_{g\to a}\,\zeta(h,d)\,e^{-i(k_0 h + k_1 d)}}{2\sqrt{\pi}(h+d)}\mathrm{H}_\mathrm{t}(\omega)\mathbf{E}^i(\boldsymbol{x}_\mathrm{t}) \tag{2.10}$$

with

$$\mathrm{H_t}(\omega) = -\frac{\hat{z}_0}{2\sqrt{\pi}} \Delta\hat{y} \int_{z'=d}^{d+l} e^{-i2k_1(z'-d)} S_{xy}(z') dz' \ , \tag{2.11}$$

where the function $S_{xy}(z)$ describes the vertical profile of the horizontal cross-section of the target and *l*, as before, refers to the target height.

Equation (2.10) represents a convolutional model in the frequency-domain relating the scattered field $\mathbf{E}^s$ at the observation point to the incident field $\mathbf{E}^i$ at the target location. The first term on the right-hand side simply describes the phase shift, the propagation loss, the spreading loss and the ground-to-air transmission associated with the one-way propagation from the target to the observation point. The quantity $\mathrm{H_t}(\omega)$ is the target transfer function. Note from eq. (2.11) that the target transfer function is independent of the target depth *d* and the height *h* of the observation point.

For ease of evaluation, let us use integration by parts to rewrite eq. (2.11) in the equivalent form

$$\mathrm{H_t}(\omega) = \frac{i\hat{z}_0}{4\sqrt{\pi}k_1} \Delta\hat{y} \int_{z'=d^-}^{(d+l)^+} e^{-i2k_1(z'-d)} \partial_{z'} S_{xy}(z') dz' \tag{2.12}$$

from which it is possible to “read off” the transfer function of targets whose shape is characterized by sharp jumps in cross-section because then $\partial_{z'} S_{xy}(z')$ simply becomes a series of delta functions.

Time-domain formulation

The frequency-domain convolutional scattering model given by eqs. (2.10)-(2.12) is valid for any type of soil as long as it is non-magnetic. Analytical transformation of the model into the time-domain, however, requires that the velocity v_1 and the attenuation α_1 in the ground, which are related to the wavenumber by

$$k_1 = \frac{\omega}{v_1} - i\alpha_1 \ , \tag{2.13}$$

are frequency independent.

Therefore, transformation into the time-domain is generally only possible when the ground is lossless. Both polarization losses and conduction losses[3] will generally cause v_1 and α_1 to be functions of frequency. It is important to note that both types of losses also result in the transmission coefficient $T_{g\rightarrow a}$ and the refraction related spreading term ζ to be complex and frequency dependent. Accordingly, in the time-domain they become functions of time and their effect on the scattered field is no longer a simple multiplication but a convolution operation.

---

[3] Conduction losses are associated with charge transport phenomena, whereas polarization losses refer to the energy dissipation associated with polarization processes. In soils, conduction losses can predominantly be attributed to ionic conduction in water and polarization losses to the orientational polarization of water molecules. The overall strength of these losses is therefore directly related to water content. Dry soils are generally characterized by very low losses. Due to polarization losses, the soil permittivity becomes complex and frequency dependent. Conduction losses are described by a non-zero conductivity.

To analytically transform the convolutional model into the time-domain, let us therefore consider a simplified lossy ground model, which is commonly assumed in GPR problems and for which the velocity v_1 and the attenuation α_1 remain frequency independent. The underlying assumptions are as follows:

1) The polarization losses are negligible.
2) The conduction loss term $\sigma_1/(\varepsilon_0\omega)$ is smaller than one.

With these assumptions, v_1 and α_1 are simply

$$v_1 = \frac{c}{\sqrt{\varepsilon_{r,1}}} \tag{2.14}$$

and

$$\alpha_1 = \frac{\mu_0}{2}\sigma_1 v_1 \ , \tag{2.15}$$

where $c = (\mu_0\varepsilon_0)^{-1/2}$ is the wave velocity in air and $\varepsilon_{r,1}$ is the relative permittivity of the ground. Then, using eq. (2.13) in eq. (2.10), we find the time-domain convolutional scattering model

$$\mathbf{e}^s(\boldsymbol{x},t) = \frac{T_{g\to a}\,\zeta(h,d)\,e^{-\alpha_1 d}}{2\sqrt{\pi}\,(h+d)}\,\delta\!\left(t-\frac{h}{c}-\frac{d}{v_1}\right)\otimes \mathrm{h}_{\mathrm{t}}(t)\otimes \mathbf{e}^i(\boldsymbol{x}_{\mathrm{t}},t) \ , \tag{2.16}$$

where $\delta(t)$ is the delta function, $\mathrm{h}_{\mathrm{t}}(t)$ is the target impulse response, and $\otimes$ denotes convolution.[4]

It is important to point out that this result is not entirely correct, since we have neglected the time-dependence of the transmission coefficient $T_{g\to a}$ and the refraction related spreading term ζ, which does not necessarily vanish even for the simplified lossy ground model, and we assume their expressions for a lossless ground, i.e.

$$T_{g\to a} = \frac{2\sqrt{\varepsilon_{r,1}}}{1+\sqrt{\varepsilon_{r,1}}} \tag{2.17}$$

$$\zeta(h,d) = \frac{h+d}{h\sqrt{\varepsilon_{r,1}}+d} \ , \tag{2.18}$$

to be adequate approximations for their lossy counterparts. This approach is in line with that followed by other researchers, e.g. Scheers (2001, p. 5-12).

To find the target impulse response, we make the substitution $z' = v_1 t/2 + d$ in (2.11), which, considering the transformation pair $(i\omega) \leftrightarrow \partial_t$, implies that

$$\mathrm{h}_{\mathrm{t}}(t) = -\frac{v_1}{4\sqrt{\pi}c^2}\left(\Delta\varepsilon_r\partial_t^2 + \frac{\Delta\sigma}{\varepsilon_0}\partial_t\right)\left(S_{xy}\!\left(\frac{v_1 t}{2}+d\right)e^{-\alpha_1 v_1 t}\right). \tag{2.19}$$

---

[4] Throughout this thesis, upper and lower case letters are used to distinguish between frequency- and time-domain representations of the same quantity/function.

Here $\Delta\varepsilon_r$ and $\Delta\sigma$ denote the contrasts in relative permittivity and conductivity between the target and the ground. In the case of no losses, the target impulse response reduces to

$$\mathrm{h}_{\mathrm{t}}(t) = -\frac{v_1}{4\sqrt{\pi}c^2}\Delta\varepsilon_r \partial_t^2 S_{xy}\left(\frac{v_1 t}{2} + d\right) . \tag{2.20}$$

Equation (2.19) states that, under the Born approximation, the time function of the impulse response resulting from the relative permittivity contrast $\Delta\varepsilon_r$ is determined by the 2nd derivative of the target's cross-section profile along the vertical. On the other hand, the part of the target impulse response associated with the conductivity contrast $\Delta\sigma$ is determined by the 1st derivative of the target's cross-section profile along the vertical. This difference is a direct result of the difference in how $\Delta\varepsilon_r$ and $\Delta\sigma$ enter the admittivity contrast $\Delta\hat{y} = \varepsilon_0(\boldsymbol{i}\omega\Delta\varepsilon_r + \Delta\sigma/\varepsilon_0)$.

In summary, losses in the ground generally lead to frequency dependent scattering, propagation and transmission behavior which is difficult, if not impossible, to describe analytically in the time-domain. Due to this limitation, **in the remainder of this thesis, I will mainly consider time-domain scattering for the case of a lossless ground**. An exception forms section 2.4, where I will develop a theoretical framework based on similarity analysis for transforming the time-domain response of a dielectric minelike target buried in a lossless ground to its time-domain response in a lossy ground. For the reader who is interested in more detailed information about electromagnetic properties of lossy soils, I recommend the treatises by Olhoeft (1998), Powers (1995) and Keller (1987).

Target transfer function/impulse response of a circular dielectric disk

In view of landmine identification, an important special case is that of a circular disk with constant cross-section S_{xy}, which is a representative shape for a large class of landmines, e.g. *PMA-3* and *Type 72* (see figure 2.2). From eq. (2.12), the disk's transfer function is simply

$$\mathrm{H}_{\mathrm{t}}(\omega) = \frac{\boldsymbol{i}\hat{z}_0}{4\sqrt{\pi}k_1}\Delta\hat{y}\, S_{xy}\left(1 - e^{-i2k_1 l}\right) , \tag{2.21}$$

which, for a lossless ground, corresponds to the target impulse response

$$\mathrm{h}_{\mathrm{t}}(t) = -\frac{v_1}{4\sqrt{\pi}c^2}\Delta\varepsilon_r S_{xy}\left(\dot{\delta}(t) - \dot{\delta}(t - 2l/v_1)\right) . \tag{2.22}$$

Here $\dot{\delta}(t)$ denotes the 1st time derivative of the delta function, i.e. a differentiation operator. Looking at eq. (2.22), we see that **the disk differentiates the waveform of the incident field**. The first differentiation operator at $t = 0$ relates to backscattering from the top of the target whereas the second at $t = 2l/v_1$ relates to backscattering from the bottom of the target.


(a) (b)

Figure 2.2: Examples of circular disk-shaped AP landmines: (a) *PMA-3*, (b) *Type 72*.
(source: Website of the Canadian Forces National Defence Mine/countermine Information Centre, http://ndmic-cidnm.forces.gc.ca)

Demining GPR systems generally use ultra-wide bandwidths extending beyond the frequency range in which the phase criterion of eq. (2.5) underlying the Born approximation is satisfied. To extend the applicability of eq. (2.22) to demining GPR systems, two phenomenological modifications are therefore introduced. First, the velocity of the wave propagating through the target is allowed to be different to that in the ground by introducing the effective target velocity v_{t}^{eff}. And second, an attenuation factor $\Gamma \leq 1$ is introduced, which accounts for the weakening of the backscattering from the bottom of the target. With these modifications, eq. (2.22) becomes

$$\mathrm{h}_{\mathrm{t}}(t) = -\frac{v_{\mathrm{t}}^{eff}}{4\sqrt{\pi}c^2}\Delta\varepsilon_r S_{xy}\left(\dot{\delta}(t) - \Gamma\dot{\delta}\left(t - 2l/v_{\mathrm{t}}^{eff}\right)\right). \tag{2.23}$$

Simply speaking, the value of Γ is just an indicator of the extent to which the Born approximation is valid, with good validity being expressed by values close to one. Interestingly, the FDTD simulation and experimental results presented in this chapter and chapter 5, respectively, indicate that Γ is related to the target's aspect ratio, defined as the ratio of its radius over its height. Specifically, the results suggest that the Born approximation becomes less valid as the aspect ratio decreases. This may be explained by the contribution of the edge-diffracted wave to the field inside the target during the time it takes for the incident wave to pass through the target. Clearly, this contribution may not be neglected as the target aspect ratio decreases, making the Born assumption break down.

2.1.2 The metal minelike target

Frequency-domain formulation

The field $\mathbf{E}^s$ scattered by the metal minelike target may be represented through the surface integral

$$\mathbf{E}^s(\boldsymbol{x}) = \iint\limits_{\substack{\text{target}\\\text{surface}}} \tilde{\mathbf{G}}(\boldsymbol{x},\boldsymbol{x}')\mathbf{J}^s(\boldsymbol{x}')dS', \tag{2.24}$$

in which $\mathbf{J}^s$ is the surface scattering current and, as in eq. (2.1), $\tilde{\mathbf{G}}$ is the half-space electric Green’s tensor.

We make use of the fact that the casings of many landmines have flat or smooth surfaces. Neglecting the creeping wave, we can then use Physical Optics (PO) to approximate the surface scattering current $\mathbf{J}^s$ as

$$\mathbf{J}^s(\boldsymbol{x}) = \begin{cases} 2\boldsymbol{n}\times\mathbf{H}^i(\boldsymbol{x}) & \text{illuminated side of the target} \\ 0 & \text{shadow side of the target} \end{cases} \tag{2.25}$$

(Damarla *et al*, 2000), where $\boldsymbol{n}$ denotes the unit vector normal to the surface of the target and $\mathbf{H}^i$ is the incident magnetic field. The incident magnetic field is related to the incident electric field through one of Maxwell’s equations, viz.

$$\mathbf{H}^i(\boldsymbol{x}) = -\frac{\nabla\times\mathbf{E}^i(\boldsymbol{x})}{\hat{z}_1} = \frac{\boldsymbol{i}k_1}{\hat{z}_1}\boldsymbol{u}_z\times\mathbf{E}^i(\boldsymbol{x}_\mathrm{t})e^{-\boldsymbol{i}k_1(z-d)} \ , \tag{2.26}$$

so that on the illuminated side of the target

$$\mathbf{J}^s(\boldsymbol{x}) = 2\frac{\boldsymbol{i}k_1}{\hat{z}_1}\begin{bmatrix} -\boldsymbol{n}\cdot\boldsymbol{u}_z & 0 \\ 0 & -\boldsymbol{n}\cdot\boldsymbol{u}_z \\ \boldsymbol{n}\cdot\boldsymbol{u}_x & \boldsymbol{n}\cdot\boldsymbol{u}_y \end{bmatrix}\mathbf{E}^i(\boldsymbol{x}_\mathrm{t})e^{-\boldsymbol{i}k_1(z-d)} \ . \tag{2.27}$$

Here $\boldsymbol{u}_x$, $\boldsymbol{u}_y$ and $\boldsymbol{u}_z$ refer to the unit vectors in the *x*, *y*, and *z* directions, respectively.

Substituting the approximations (2.27) and (2.7) for the surface scattering current $\mathbf{J}^s$ and the half-space Green’s tensor $\tilde{\mathbf{G}}$ into eq. (2.24) and following the surface integration procedure set forth by Kennaugh and Moffatt (1965), it is found that the convolutional scattering model for the dielectric minelike target given by eq. (2.10) also holds for the metal minelike target, only that now the target transfer function $\mathrm{H}_\mathrm{t}(\omega)$ is

$$\mathrm{H}_\mathrm{t}(\omega) = -\frac{\boldsymbol{i}k_1}{\sqrt{\pi}}\int_{z'=d^-}^{(d+l^s)^+} e^{-i2k_1(z'-d)}\partial_{z'}S_{xy}(z')dz' \ . \tag{2.28}$$

Note that the transfer function integral in eq. (2.28) is identical to that in eq. (2.12) for the dielectric minelike target, except for the upper integration limit now being determined by l^s, which is the distance from the onset of the target to its shadow boundary (see figure 2.1).

It is important to point out that in obtaining this result we were able to neglect the contribution of the *z*-component of the surface scattering current $\mathbf{J}^s$ to the scattered field as a result of the far-field assumption. As such, PO effectively does not account for any depolarization phenomena and therefore is more suited for describing the backscattering behavior of rotationally symmetric metal minelike targets.

Time-domain formulation

By analogy to finding the time-domain counterpart of eq. (2.12), the target transfer function given by eq. (2.28) can be transformed to yield the target impulse response

$$\mathrm{h}_{\mathrm{t}}(t) = -\frac{1}{\sqrt{\pi} v_1} \partial_t^2 S_{xy}\left(\min\left(v_1 t/2 + d, l^s + d\right)\right) , \tag{2.29}$$

where, as before, the ground is assumed lossless.

Target transfer function/impulse response of a circular metal disk

Let us again consider the special case of a circular disk with constant cross-section S_{xy}. From (2.28), its transfer function is

$$\mathrm{H}_{\mathrm{t}}(\omega) = -\frac{ik_1}{\sqrt{\pi}} S_{xy} . \tag{2.30}$$

Given a lossless ground, its target impulse response immediately follows as

$$\mathrm{h}_{\mathrm{t}}(t) = -\frac{1}{\sqrt{\pi} v_1} S_{xy} \dot{\delta}(t) . \tag{2.31}$$

We see that **specular scattering from a circular metal disk differentiates the waveform of the incident field**, just as is the case for a circular dielectric disk.

2.1.3 Exact and approximate representations of the half-space electric Green's tensor

Since the far-field backscattering approximation of the half-space electric Green's tensor given by eq. (2.7) is fundamental to the convolutional scattering models presented in the previous sections, it is important that its derivation be specified and that the differences with previously published half-space Green's tensor approximations are pointed out.

Let us write

$$\tilde{\mathbf{G}}(\boldsymbol{x}, \boldsymbol{x}') = \begin{bmatrix} \mathrm{G}_{xx} & \mathrm{G}_{xy} \\ \mathrm{G}_{yx} & \mathrm{G}_{yy} \\ \mathrm{G}_{zx} & \mathrm{G}_{zy} \end{bmatrix} \tag{2.32}$$

for the first two columns of the half-space electric Green's tensor, where, e.g., G_{yx} is the y-component of the electric field due to a buried x-directed point electric dipole of unit strength. The tensor elements may be derived from the electric vector potential (also commonly referred to as Hertz vector) obtained from solving the two-media boundary value problem, as described for example by Baños (1966) or Raiche (1974). The resulting general formulae for the tensor elements are

$$\mathrm{G}_{xx} = -\frac{\hat{z}_0}{2\pi}\left(\int_0^\infty \frac{e^{-u_0 h - u_1 z'}}{u_0 + u_1} J_0(\lambda\rho)\lambda d\lambda - \frac{1}{2}\int_0^\infty \frac{e^{-u_0 h - u_1 z'}}{k_1^2 u_0 + k_0^2 u_1}\left(J_0(\lambda\rho) - \cos(2\phi) J_2(\lambda\rho)\right)\lambda^3 d\lambda\right) \tag{2.33a}$$

$$\mathrm{G}_{yx} = -\frac{\hat{z}_0}{4\pi}\sin(2\phi)\int_0^\infty \frac{e^{-u_0 h - u_1 z'}}{k_1^2 u_0 + k_0^2 u_1} J_2(\lambda\rho)\lambda^3 d\lambda \tag{2.33b}$$

$$\mathrm{G}_{zx} = \frac{\hat{z}_0}{2\pi}\cos(\phi)\int_0^\infty u_1 \frac{e^{-u_0 h - u_1 z'}}{k_1^2 u_0 + k_0^2 u_1} J_1(\lambda\rho)\lambda^2 d\lambda \tag{2.33c}$$

$$\mathrm{G}_{xy} = \mathrm{G}_{yx} \tag{2.33d}$$

$$\mathrm{G}_{yy} = -\frac{\hat{z}_0}{2\pi}\left(\int_0^\infty \frac{e^{-u_0 h - u_1 z'}}{u_0 + u_1} J_0(\lambda\rho)\lambda d\lambda - \frac{1}{2}\int_0^\infty \frac{e^{-u_0 h - u_1 z'}}{k_1^2 u_0 + k_0^2 u_1}\left(J_0(\lambda\rho) + \cos(2\phi) J_2(\lambda\rho)\right)\lambda^3 d\lambda\right) \tag{2.33e}$$

$$\mathrm{G}_{zy} = \frac{\hat{z}_0}{2\pi}\sin(\phi)\int_0^\infty u_1 \frac{e^{-u_0 h - u_1 z'}}{k_1^2 u_0 + k_0^2 u_1} J_1(\lambda\rho)\lambda^2 d\lambda \tag{2.33f}$$

The integration variable $\lambda = (k_x^2 + k_y^2)^{1/2}$ is the horizontal wavenumber, and $u_0 = (\lambda^2 - k_0^2)^{1/2}$ and $u_1 = (\lambda^2 - k_1^2)^{1/2}$ are the corresponding vertical propagation constants in air and in the ground, respectively. The functions J_n (n = 0,1,2) are Bessel functions of the first kind and order n. Furthermore, polar coordinates (ρ,ϕ) with respect to the source point $\boldsymbol{x}'$ have been introduced, which satisfy $x - x' = \rho\cos(\phi)$ and $y - y' = \rho\sin(\phi)$.

Next, we take advantage of the fact that we consider backscattering, i.e. $x = y = 0$, and that antipersonnel landmines are small, i.e. $x' \approx 0$ and $y' \approx 0$ for all points of the target, by letting the radius ρ go to zero. As a result, the tensor elements given by eqs. (2.33a)- (2.33f) reduce to

$$\mathrm{G}_{xx} = \mathrm{G}_{yy} = -\frac{\hat{z}_0}{2\pi}\left(\int_0^\infty \frac{e^{-u_0 h - u_1 z'}}{u_0 + u_1}\lambda d\lambda - \frac{1}{2}\int_0^\infty \frac{e^{-u_0 h - u_1 z'}}{k_1^2 u_0 + k_0^2 u_1}\lambda^3 d\lambda\right) \tag{2.34a}$$

$$\mathrm{G}_{yx} = \mathrm{G}_{zx} = \mathrm{G}_{xy} = \mathrm{G}_{zy} = 0. \tag{2.34b}$$

It should be noted that eqs. (2.34a) and (2.34b) are exact and valid for all frequencies and field regions (near-, intermediate-, and far-field). Accordingly, for small targets, a cross-polar component in the backscattered field can only originate from a cross-polar component in the scattering current. Expanding on this thought a bit further, within the range of validity of eq. (2.2) the cross-polar backscattered field vanishes completely even for non-rotationally symmetric dielectric targets. This should be kept in mind when using polarimetric information to distinguish between plastic cased landmines and other buried objects.

To find an approximate far-field expression for G_{xx} and G_{yy}, let us use the fundamental integrals

$$U(z', h, \rho) = 2\int_0^\infty \frac{e^{-u_0 h - u_1 z'}}{u_0 + u_1} J_0(\lambda\rho)\lambda d\lambda \tag{2.35}$$

and

$$V(z', h, \rho) = 2\int_0^\infty \frac{e^{-u_0 h - u_1 z'}}{k_1^2 u_0 + k_0^2 u_1} J_0(\lambda\rho)\lambda d\lambda \tag{2.36}$$

introduced by Baños to rewrite eq. (2.34a) as

$$\mathrm{G}_{xx} = \mathrm{G}_{yy} = -\frac{\hat{z}_0}{4\pi}\left(U(z', h, 0) - \frac{1}{2}\left(k_1^2 + \partial_{z'}^2\right)V(z', h, 0)\right). \tag{2.37}$$

On the basis of Baños' series expansions of the fundamental integrals for points near the z-axis, i.e. Baños' eqs. (5.33) and (5.38), U and V can be represented in terms of reciprocal powers of $\boldsymbol{i}k_0h$ to obtain

$$U\left(z',h,0\right)=\frac{2e^{-\boldsymbol{i}\left(k_0h+k_1z'\right)}}{\left(1+n\right)h}n\left(1-\frac{E_1^U}{\boldsymbol{i}k_0h}+\frac{nE_2^U}{\left(\boldsymbol{i}k_0h\right)^2}\mp\ldots\right) \tag{2.38}$$

with expansion coefficients

$$E_1^U=-1+n+n^2\alpha \tag{2.39a}$$

$$E_2^U=-2+n\left(1-3\alpha\right)+n^2\left(1+2\alpha\right)+n^3\left(\alpha+\alpha^2\right) \tag{2.39b}$$

and

$$V\left(z',h,0\right)=\frac{2e^{-\boldsymbol{i}\left(k_0h+k_1z'\right)}}{\left(1+n\right)h}\frac{1}{k_1^2}\left(1-\frac{nE_1^V}{\boldsymbol{i}k_0h}+\frac{nE_2^V}{\left(\boldsymbol{i}k_0h\right)^2}\mp\ldots\right) \tag{2.40}$$

with expansion coefficients

$$E_1^V=-1+n\left(1+\alpha\right) \tag{2.41a}$$

$$E_2^V=-2+n\left(4-\alpha\right)-n^2\left(5+2\alpha\right)+n^3\left(3+3\alpha+\alpha^2\right)\ , \tag{2.41b}$$

where $n=k_0/k_1$ is the complex index of refraction and $\alpha=\boldsymbol{i}k_1z'$. Note that since this thesis assumes a $e^{\boldsymbol{i}\omega t}$ time dependence in the frequency domain in contrast to Baños who assumes a $e^{-\boldsymbol{i}\omega t}$ time dependence, Baños' expansions and those given here are complex conjugates of each other. Neglecting terms containing non-canceling negative powers of k_0h in accordance with the far-field assumption $k_0h\gg1$, eq. (2.38) can be approximated as

$$U\left(z',h,0\right)\approx\frac{2e^{-\boldsymbol{i}\left(k_0h+k_1z'\right)}}{\left(1+n\right)h}n\left(1-n\frac{z'}{h}+\left(n\frac{z'}{h}\right)^2\mp\ldots\right), \tag{2.42}$$

which for $z'/h<\left|n\right|^{-1}$ suggests

$$U\left(z',h,0\right)\approx\frac{2e^{-\boldsymbol{i}\left(k_0h+k_1z'\right)}}{\left(1+n\right)h}n\left(1+n\frac{z'}{h}\right)^{-1}\ . \tag{2.43}$$

In the same manner, from eq. (2.40) it can be shown that in the far-field

$$\left(k_1^2+\partial_{z'}^2\right)V\left(z',h,0\right)\approx0\ . \tag{2.44}$$

Substituting eqs. (2.43) and (2.44) into eq. (2.37), we find that the first two columns of the Green's tensor for the case of backscattering from a small target and far-field observation can be approximated as

$$\tilde{\mathbf{G}}\left(\boldsymbol{x},\boldsymbol{x}'\right)\approx-\hat{z}_0T_{g\to a}\zeta\left(h,z'\right)\frac{e^{-\boldsymbol{i}\left(k_0h+k_1z'\right)}}{4\pi\left(h+z'\right)}\begin{bmatrix}1&0\\0&1\\0&0\end{bmatrix}, \tag{2.45}$$

where, as before, $T_{g\to a}=2/(1+n)$ is the normal incidence ground-to-air Fresnel transmission coefficient and ζ is the refraction spreading term defined by eq. (2.9).

Further simplification is achieved by assuming that $(z'-d)/(h+d)\ll 1$, which is reasonable for antipersonnel landmines whose height $l=(z'-d)_{\max}$ is usually not greater than a few centimeters, e.g. 5 cm. Then, from Taylor series expansions, $1/(h+z')\approx 1/(h+d)$ and $\zeta(h,z')\approx\zeta(h,d)$ with which eq. (2.45) becomes the Green's tensor approximation underlying the convolutional scattering models presented in sections 2.1.1 and 2.1.2, i.e. eq. (2.7).

As a final remark, it is important to point out the differences with the approximate field expressions initially given by Baños and later refined by King and Shen (1979). Their approximations are derived from the same series expansions of *U* and *V* that are used here. However, contrary to the approach followed above, they simplify based on the assumption $|n|\ll 1$, which Baños motivates by his interest in describing the low-frequency case, where, for earth materials, conduction currents dominate over displacement currents. At radar frequencies, however, $|n|\ll 1$ is usually not satisfied, e.g. $n\approx 0.5$ for a lossless ground with a relative permittivity of 4. As a consequence, the applicability of King and Shen's far-field approximation given by

$$\mathrm{G}_{xx}\approx-\hat{z}_0T_{g\to a}\frac{e^{-i(k_0h+k_1z')}}{4\pi h}n \tag{2.46}$$

is more limited than for the far-field approximation given by eq. (2.45). It is interesting to note that, in contrast to King and Shen's approximation, eq. (2.45) agrees with the widely used far-field approximation of the free-space Green's tensor, as can be observed immediately by simply setting $k_1=k_0$. From eq. (2.45), King and Shen's far-field approximation is found to be valid high above the ground ($h\to\infty$), in which case $\zeta(h,z')\approx n$ and $1/(h+z')\approx 1/h$.

2.1.4 Special case: A minelike target in an unbounded host medium (air)

This section gives a brief discussion of scattering from a minelike target embedded in an unbounded host medium (full-space) such as air. Although this scattering problem might seem far-fetched from any realistic landmine scattering scenario, it has practical use for the derivation of an approximate convolutional model for the GPR response of a surface-laid minelike target. Furthermore, if the relation between the half-space and the full-space problem is well understood, results and insight which have been obtained for the full-space problem, e.g. through simulations, can be easily transferred to the half-space problem.

Scattering from a minelike target in an unbounded host medium may be treated as a special case of scattering from a buried minelike target, in which the properties of the "air" are equal to those of the ground. Hence, setting $k_0=k_1$ in eq. (2.10) and introducing the distance $r_\mathrm{t}=h+d$, which is the radial distance between the target and the observation point, directly yields a far-field backscattering convolutional model for the full-space problem:

$$\mathbf{E}^s(\boldsymbol{x})=\frac{e^{-ik_1r_\mathrm{t}}}{2\sqrt{\pi}r_\mathrm{t}}\mathrm{H}_\mathrm{t}(\omega)\mathbf{E}^i(\boldsymbol{x}_\mathrm{t})\ . \tag{2.47}$$

An important result is that the target transfer function $\mathrm{H}_\mathrm{t}(\omega)$ remains unchanged and is given by either eq. (2.12) or eq. (2.28), depending on whether a dielectric or a metal minelike target is considered. Alternatively, eq. (2.47) can be derived using the same procedure as outlined in sections 2.1.1 and 2.1.2, but, instead of using the half-space Green's tensor, we now make use of the full-space Green's tensor

$$\tilde{\mathbf{G}}(\boldsymbol{x},\boldsymbol{x}') = -\hat{z}_0 \frac{e^{-\boldsymbol{i}k_1 r}}{4\pi r} \begin{bmatrix} b_1 \frac{(x-x')^2}{r^2} + b_2 & b_1 \frac{(x-x')(y-y')}{r^2} & b_1 \frac{(x-x')(z-z')}{r^2} \\ b_1 \frac{(x-x')(y-y')}{r^2} & b_1 \frac{(y-y')^2}{r^2} + b_2 & b_1 \frac{(y-y')(z-z')}{r^2} \\ b_1 \frac{(x-x')(z-z')}{r^2} & b_1 \frac{(y-y')(z-z')}{r^2} & b_1 \frac{(z-z')^2}{r^2} + b_2 \end{bmatrix}, \tag{2.48a}$$

where

$$r = \|\boldsymbol{x}-\boldsymbol{x}'\| \tag{2.48b}$$

$$b_1 = -1 + \frac{3\boldsymbol{i}}{(k_1 r)} + \frac{3}{(k_1 r)^2} \tag{2.48c}$$

$$b_2 = 1 - \frac{\boldsymbol{i}}{(k_1 r)} - \frac{1}{(k_1 r)^2} \tag{2.48d}$$

(Ward and Hohmann, 1987, p. 181), which for the case of far-field backscattering from a small target simplifies to

$$\tilde{\mathbf{G}}(\boldsymbol{x},\boldsymbol{x}') \approx -\hat{z}_0 \frac{e^{-\boldsymbol{i}k_1 r}}{4\pi r_{\mathrm{t}}} \begin{bmatrix} 1 & 0 & 0 \\ 0 & 1 & 0 \\ 0 & 0 & 0 \end{bmatrix}. \tag{2.49}$$

The details of this derivation can be found in Roth *et al* (2002).

If the host medium is air, eq. (2.47) can be transformed into the time-domain to yield

$$\mathbf{e}^s(\boldsymbol{x},t) = \frac{1}{2\sqrt{\pi} r_{\mathrm{t}}} \delta\left(t - \frac{r_{\mathrm{t}}}{c}\right) \otimes \mathrm{h}_{\mathrm{t}}(t) \otimes \mathbf{e}^i(\boldsymbol{x}_{\mathrm{t}},t) \ . \tag{2.50}$$

This result will be used in chapter 4 to derive a convolutional model for the GPR response of a surface-laid minelike target. Clearly, this is a rather crude way of dealing with the problem of scattering from a surface-laid minelike target, and a more elegant derivation would involve the half-space Green's tensor for the case that both the source and the observation point are located in the air.

2.2 Deconvolution and Target Characterization

2.2.1 Formulation of the deconvolution problem

To begin with, we might ask ourselves the question, what we would like deconvolution to do for us. In seismic deconvolution, which has been studied extensively over the decades

(Yilmaz, 1987), the main objective is to improve the temporal resolution of the data by compressing the source wavelet, thereby resolving closely spaced layering. Accordingly, whether the output of the deconvolution describes the true impulse response of the earth is usually not considered as important as that the data look "better" in some sense, the latter usually being the criteria for judging the performance of a seismic deconvolution algorithm. Clearly, for buried target characterization improving the temporal resolution is not the only objective. Rather, we wish to use deconvolution to accurately estimate the target impulse response $\mathrm{h}_\mathrm{t}(t)$, which carries information on target size and contrast, and is independent of target depth and the height at which the scattered field is observed. In practice, however, it is impossible to directly estimate $\mathrm{h}_\mathrm{t}(t)$, as can be seen from the convolutional scattering model given by eq. (2.16): The best we can do is to estimate a scaled and shifted version of the target impulse response, which hereinafter will be denoted as $\mathrm{h}(t)$. Although this might seem undesirable at first, it has the advantage that the time shift can be used to determine the depth of burial, which is useful information for AP landmine identification since these types of mines are usually buried no deeper than 10 cm. Furthermore, the target depth information can be used to undo the spherical and refraction induced spreading effects, which ultimately allows us to recover the target impulse response $\mathrm{h}_\mathrm{t}(t)$ and to determine target properties.

Whenever deconvolution is applied, a convolutional model needs to be invoked. The following discussion on deconvolution algorithms is based on a generic convolutional model, which simply assumes a linear time-invariant process creating an output signal $\mathrm{y}(t)$ in response to an input signal $\mathrm{x}(t)$. Mathematically, the input-output relationship of the process is expressed as

$$\mathrm{y}(t) = \mathrm{h}(t) \otimes \mathrm{x}(t) \ , \tag{2.51}$$

where $\mathrm{h}(t)$ is the impulse response of the process.

An example of such a process is backscattering from a buried minelike target. Comparing the convolutional scattering model given by eq. (2.16) to eq. (2.51), the input signal $\mathrm{x}(t)$ can be identified with the incident field $\mathrm{e}^i(\boldsymbol{x}_\mathrm{t}, t)$ and the output signal $\mathrm{y}(t)$ with the scattered field $\mathrm{e}^s(\boldsymbol{x}, t)$. Other examples are the convolutional GPR signal models for surface-laid and buried targets, which will be introduced in chapter 4. In this case, the input signal $\mathrm{x}(t)$ is the effective radiated waveform and the output signal $\mathrm{y}(t)$ is the measured target response signal.

Based on the generic convolutional model of eq. (2.51), the general formulation of the deconvolution problem then is to estimate the unknown impulse response $\mathrm{h}(t)$ from an input-output pair ($\mathrm{x}(t), \mathrm{y}(t)$). Alternatively, the deconvolution of the input signal $\mathrm{x}(t)$ from the output signal $\mathrm{y}(t)$ may be viewed as a filtering operation, which when applied to $\mathrm{y}(t)$ yields the unknown impulse response $\mathrm{h}(t)$.

In section 2.2.2, a review of some of the most commonly used frequency- and time-domain deconvolution algorithms is given. Using simple synthetic data examples, it will be shown that for ultra-wideband (UWB) radar signals these methods fail to accurately estimate the impulse response $\mathrm{h}(t)$, hence making them unsuitable for buried target characterization. This shortcoming led to the development of a new deconvolution method, termed subset selection deconvolution, which uses a priori information on the specific form of the impulse response $\mathrm{h}(t)$ to be estimated and is presented in section 2.2.3. Following the general description of subset selection deconvolution, section 2.2.4 describes how subset selection deconvolution can be used to characterize buried disk-shaped minelike targets.

2.2.2 Review of common deconvolution algorithms

Inverse and Wiener filtering in the frequency-domain

Suppose that a filter operator $\mathrm{f}(t)$ exists which compresses the input signal $\mathrm{x}(t)$ into a spike, i.e.

$$\mathrm{x}(t)\otimes \mathrm{f}(t)=\delta(t)\ . \tag{2.52}$$

The filter $\mathrm{f}(t)$ is called **inverse filter** and when applied to the output signal $\mathrm{y}(t)$ given by eq. (2.51), the impulse response $\mathrm{h}(t)$ is obtained. Inverse filtering is most conveniently carried out in the frequency-domain according to

$$\mathrm{H}(\omega)=\mathrm{Y}(\omega)\mathrm{F}(\omega)\ , \tag{2.53}$$

where $\mathrm{F}(\omega)$ is simply the inverse of the complex spectrum of the input signal $\mathrm{x}(t)$:

$$\mathrm{F}(\omega)=\frac{1}{\mathrm{X}(\omega)}=\frac{1}{|\mathrm{X}(\omega)|}e^{-i\phi_{\mathrm{x}}(\omega)}\ . \tag{2.54}$$

Here, $|\mathrm{X}(\omega)|$ and $\phi_{\mathrm{x}}(\omega)$ represent the amplitude and phase spectra of $\mathrm{x}(t)$. In practice, radar signals are always band limited. Hence to avoid dividing by values close to zero in eq. (2.54), a small positive constant ε is usually added to the amplitude spectrum before division. Equation (2.54) then takes the form

$$\mathrm{F}(\omega)=\frac{1}{|\mathrm{X}(\omega)|+\varepsilon}e^{-i\phi_{\mathrm{x}}(\omega)}\ . \tag{2.55}$$

Adding a small positive constant ε to the amplitude spectrum is commonly referred to as prewhitening (Yilmaz, 1987, p. 103).

So far noise-free output signals have been assumed. In practice, however, we will always deal with noisy signals, e.g. as a result of external electromagnetic interference (EMI) or receiver noise. Even when synthetic data examples are considered, some noise is introduced in the form of round-off errors that are caused by the limited machine precision. It is therefore important to understand how the inverse filter performs given noisy output signals. Usually there is added noise, and hence the noisy output signal $\hat{\mathrm{y}}(t)$ can be written as

$$\hat{\mathrm{y}}(t)=\mathrm{y}(t)+\mathrm{n}(t)=\mathrm{h}(t)\otimes \mathrm{x}(t)+\mathrm{n}(t)\ , \tag{2.56}$$

where $\mathrm{n}(t)$ denotes the noise. In the frequency-domain, eq. (2.56) is

$$\hat{\mathrm{Y}}(\omega)=\mathrm{H}(\omega)\mathrm{X}(\omega)+\mathrm{N}(\omega)\ . \tag{2.57}$$

Looking at eq. (2.55), we see that the amplitude spectrum of the (approximate) inverse filter applies a large gain to those frequencies of the output signal where the input signal has low energy. Hence, when applied to a noisy output signal the effect of the filter on the noise is to blow up the noise at frequencies where the input signal is weak. To overcome this problem, the **Wiener filter** has been developed, which is an optimal filter in the sense that it minimizes the least squares error between the desired filter output $\mathrm{H}(\omega)$ and the actual filter output $\hat{\mathrm{H}}(\omega)=\hat{\mathrm{Y}}(\omega)\mathrm{F}(\omega)$, viz.

$$\frac{1}{2\pi}\int_{-\infty}^{\infty}\left|\hat{\mathrm{H}}(\omega)-\mathrm{H}(\omega)\right|^2 d\omega = \min . \tag{2.58}$$

(Note that this is equivalent to requiring that the total energy of the error between the desired and the actual filter output is minimized.) If the output signal $\mathrm{Y}(\omega)$ and the noise $\mathrm{N}(\omega)$ are uncorrelated, it is straightforward to show that the filter $\mathrm{F}(\omega)$ satisfying eq. (2.58) is

$$\mathrm{F}(\omega)=\left(\frac{1}{1+\left|\mathrm{N}(\omega)\right|^2/\left|\mathrm{Y}(\omega)\right|^2}\right)\frac{1}{\left|\mathrm{X}(\omega)\right|}e^{-i\phi_{\mathrm{X}}(\omega)} \tag{2.59}$$

(Press *et al*, 1992, p. 547-549). Since $\left|\mathrm{X}(\omega)\right|^2=\mathrm{X}(\omega)\mathrm{X}^*(\omega)$, the Wiener filter may also be written as

$$\mathrm{F}(\omega)=\frac{\mathrm{X}^*(\omega)}{\left|\mathrm{X}(\omega)\right|^2+\left|\mathrm{N}(\omega)\right|^2/\left|\mathrm{H}(\omega)\right|^2} , \tag{2.60}$$

which is how it usually appears in the literature. Here, the asterisk is used to denote the "complex conjugate". Notice that the term $\left|\mathrm{N}(\omega)\right|^2/\left|\mathrm{Y}(\omega)\right|^2$ in eq. (2.59) can be interpreted as the reciprocal of the signal-to-noise ratio. Accordingly, the Wiener filter will approach the inverse filter given by eq. (2.55) at frequencies where the noise is negligible and approach zero at frequencies where the noise dominates. This is how the Wiener filter avoids blowing up the noise.

Implementation of the Wiener filter as in eq. (2.59) requires knowledge of the signal und noise power spectral densities $\left|\mathrm{Y}(\omega)\right|^2$ and $\left|\mathrm{N}(\omega)\right|^2$. This is the main drawback of the Wiener filter, since there is no way to do this from the noisy output signal $\hat{\mathrm{y}}(t)$ alone without some assumption or additional information. The most commonly applied solution to this problem is to simply assume that the unknown impulse response $\mathrm{h}(t)$ and the noise $\mathrm{n}(t)$ both represent white processes. Under this assumption, the reciprocal of the signal-to-noise ratio $\left|\mathrm{N}(\omega)\right|^2/\left|\mathrm{Y}(\omega)\right|^2$ may be replaced by the ratio $\lambda/\left|\mathrm{X}(\omega)\right|^2$, where λ is a properly chosen regularization parameter. Thus, the Wiener filter becomes

$$\mathrm{F}(\omega)=\left(\frac{1}{1+\lambda/\left|\mathrm{X}(\omega)\right|^2}\right)\frac{1}{\left|\mathrm{X}(\omega)\right|}e^{-i\phi_{\mathrm{X}}(\omega)} \tag{2.61}$$

or equivalently, when written in the form of eq. (2.60),

$$\mathrm{F}(\omega)=\frac{\mathrm{X}^*(\omega)}{\left|\mathrm{X}(\omega)\right|^2+\lambda} . \tag{2.62}$$

To illustrate the working of the Wiener filter, let us consider the synthetic data example of figure 2.3. The input signal $\mathrm{x}(t)$ (figure 2.3a) is the effective radiated waveform of an actual demining GPR, the IRCTR video impulse radar, which will be described in more detail in chapter 4. It covers a bandwidth of 0.6-2.7 GHz (-10 dB level) and has been sampled using a time interval of $\Delta t = 6.8$ ps. The impulse response $\mathrm{h}(t)$ (figure 2.3b) has two spikes and is zero otherwise. The first spike occurs at time sample $i=50$ and has an amplitude of $\mathrm{h}(t_i)=1$; the second spike occurs at time sample $j=125$ and has an amplitude of $\mathrm{h}(t_j)=-0.5$. The temporal distance t_j-t_i between the two spikes has been chosen such that it is small compared to the duration of the main pulse of the input signal. The output signal $\mathrm{y}(t)$ (figure 2.3c) has been obtained by convolving $\mathrm{x}(t)$ with $\mathrm{h}(t)$.

Figure 2.4 summarizes the results of applying the Wiener filter to the output signal $\mathrm{y}(t)$ for increasing values of the regularization parameter ($1 \le \lambda \le 10^{10}$). The left column displays the estimated impulse response $\hat{\mathrm{h}}(t)$ obtained from inverse Fourier transforming the Wiener filter output $\hat{\mathrm{H}}(\omega)$, whereas the right column displays the data fit between the predicted and the actual output signal. The quality of the data fit is quantified using the relative error defined as

$$\text{rel. error} = \frac{\left\| \hat{\mathrm{h}}(t) \otimes \hat{\mathrm{x}}(t) - \hat{\mathrm{y}}(t) \right\|}{\left\| \hat{\mathrm{y}}(t) \right\|} , \tag{2.63}$$

where $\hat{\mathrm{x}}(t)$ and $\hat{\mathrm{y}}(t)$ are the input and output signals that are used in the estimation of $\hat{\mathrm{h}}(t)$, and $\| \; \|$ denotes the ℓ_2 norm. **The relative error will be used throughout this thesis to quantify the deconvolution data fit.** In the example of figure 2.4, $\hat{\mathrm{x}}(t)$ and $\hat{\mathrm{y}}(t)$ are the true input and output signals, i.e. $\hat{\mathrm{x}}(t) = \mathrm{x}(t)$ and $\hat{\mathrm{y}}(t) = \mathrm{y}(t)$.

Here a few observations:

- The regularization parameter λ needs to be at least 10^6 in order for the two-spike structure of the impulse response to become clearly visible. Hence, even in this (in theory) noise-free synthetic data example the regularization is not just necessary to avoid division by zero, but also to counteract the computer round-off errors (see above).
- A good data fit does not necessarily mean that the estimated impulse response $\hat{\mathrm{h}}(t)$ resembles the true impulse response $\mathrm{h}(t)$ of figure 2.3b.
- The Wiener Filter has the tendency to smear out the impulse response, resulting in underestimation of amplitudes and reduced temporal resolution. Note that the smearing becomes stronger with increasing λ. This smearing is caused by the term in parentheses in eq. (2.61), which is close to unity at frequencies where the power spectral density $\left|\mathrm{X}(\omega)\right|^2$ of the input signal is strong and close to zero at frequencies where it is weak, i.e. the term acts as a bandpass filter. As a consequence, the Wiener Filter always produces a bandpass filtered version of the true impulse response. As λ increases, the frequency band, which the Wiener filter passes, becomes narrower.

Probably the optimal solution in terms of similarity between the estimated and the true impulse response and in terms of data fit is the one obtained for $\lambda = 10^6$. However, different data noise levels require different choices of λ. To illustrate this non-uniqueness of the optimal value for λ, the Wiener filtering was repeated, but with the output signal of figure 2.3c contaminated by *white Gaussian noise*[5]. The Wiener filter results for an output signal-to-

---

[5] *White Gaussian noise* is characterized by a flat frequency spectrum and a Gaussian amplitude distribution in the time-domain. To avoid misunderstandings, it is important to point out that this type of random noise is used in this section only as a convenient tool to analyze the noise sensitivity of deconvolution algorithms. It is not suggested here that white Gaussian noise is fully representative for the noise typically present in GPR data. In fact, a major source of noise in GPR data is clutter, i.e. unwanted reflections, which in a physical sense may be viewed as deterministic rather than random. As such, the noise sensitivity results presented in this section should be understood as indicative rather than quantitative. More information on clutter and a way to minimize it are presented in section 4.3.

noise ratio of 20dB are presented in figure 2.5. The results demonstrate that in this case choosing $\lambda = 10^6$ is insufficient and suggest choosing $\lambda = 10^8$ instead.

In conclusion, even in the noise-free case, Wiener filtering is incapable of recovering the true impulse response, but only a bandpass filtered version thereof. Probably the biggest difficulty in dealing with the Wiener filter is choosing a regularization parameter λ, which works for different operating scenarios in terms of noise level, output signal shape and output signal strength. Working with a varying regularization parameter has the disadvantage of making it difficult to compare estimated impulse responses, which after all is what we would like to do for target characterization/identification.

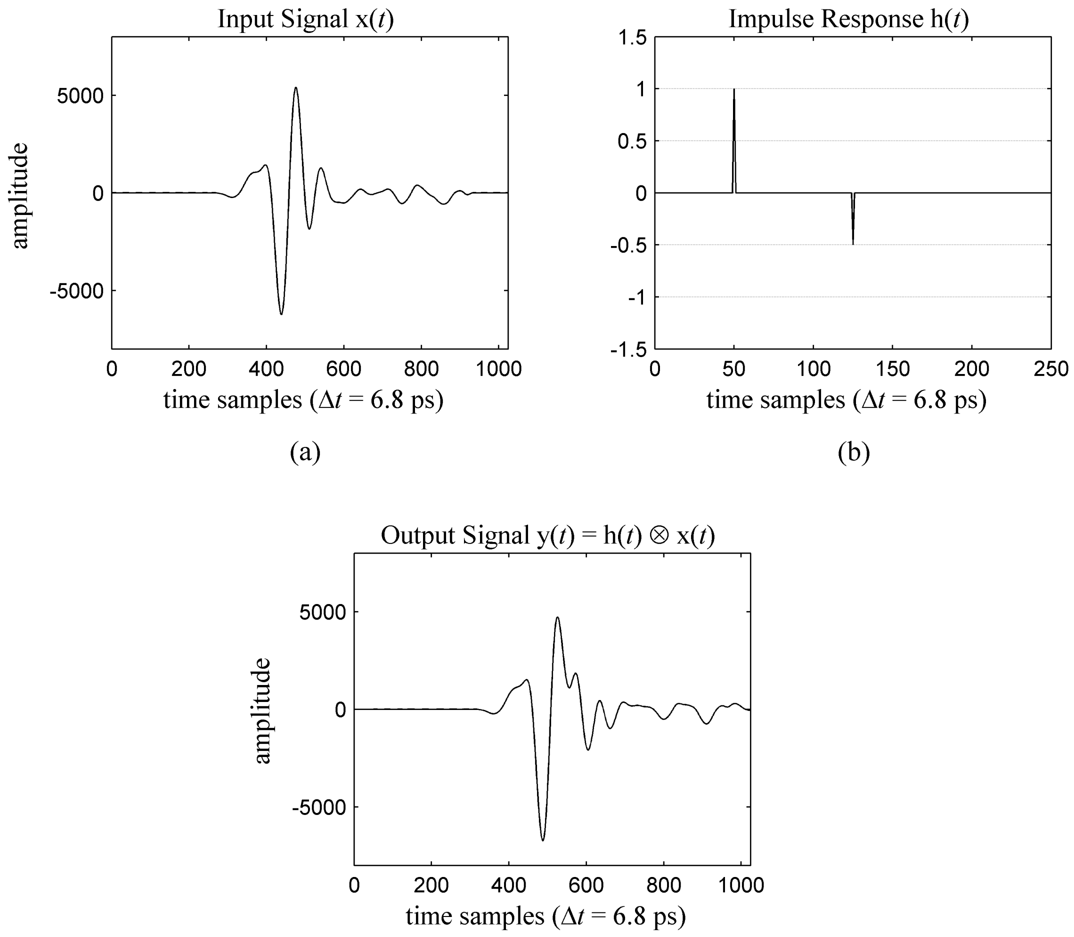

(a) (b)

(c)

Figure 2.3: Synthetic data example used for the deconvolution analysis:
(a) input signal $x(t)$
(b) two-spike impulse response $h(t)$
(c) output signal $y(t)$ obtained from convolving $x(t)$ with $h(t)$.

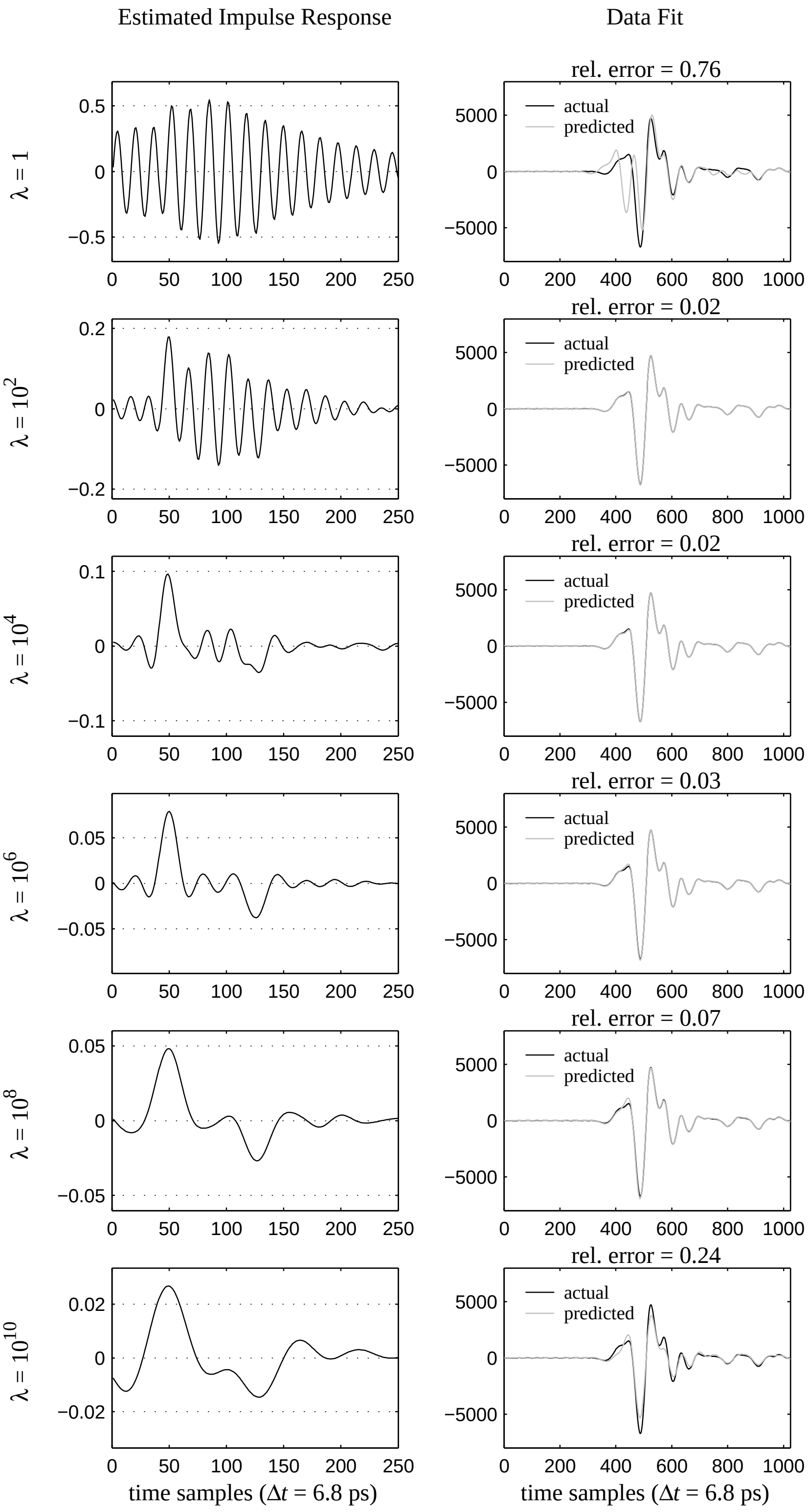

Figure 2.4: Wiener filter deconvolution of the input signal of figure 2.3a from the output signal of figure 2.3c. The left column shows the estimated impulse response for increasing λ and the right column shows the associated data fits between the predicted and the actual output signal.

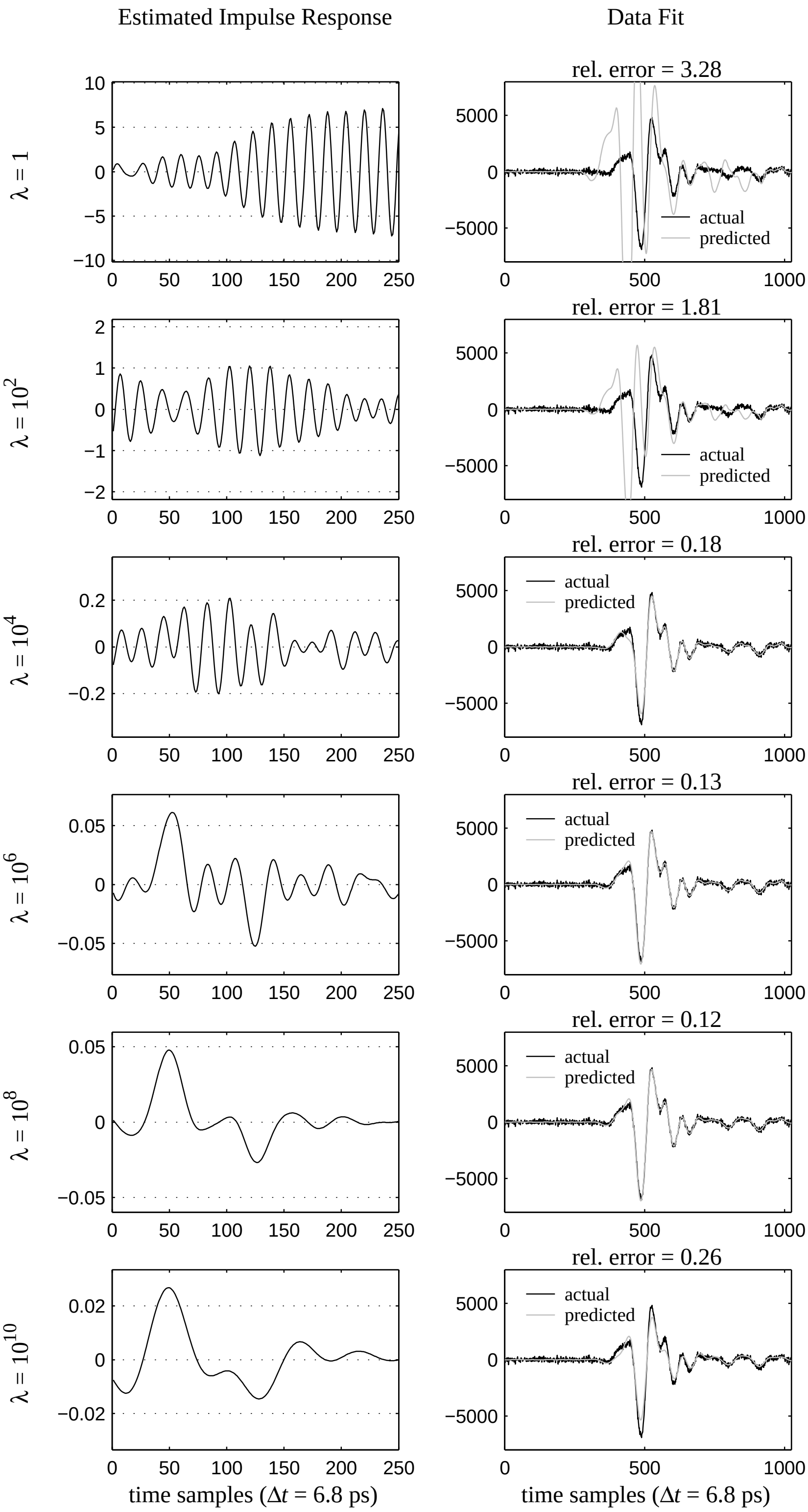

Figure 2.5: Wiener filter deconvolution as in figure 2.4, but with white Gaussian noise added to the output signal (output SNR: 20 dB).

Least squares deconvolution in the time-domain

In practice, we always deal with sampled signals. The convolutional model of eq. (2.51) can therefore be expressed in matrix form as

$$\mathbf{y} = \mathbf{X}\mathbf{h}\,, \tag{2.64}$$

where $\mathbf{y} = \left[\mathrm{y}(t_1)\cdots\mathrm{y}(t_M)\right]^T$ and $\mathbf{h} = \left[\mathrm{h}(t_1)\cdots\mathrm{h}(t_N)\right]^T$ are vector representations of the output signal and the unknown impulse response, respectively, and **X** is the convolution matrix defined as

$$\mathbf{X} = \left[\mathbf{x}_1 \quad \mathbf{x}_2 \quad \cdots \quad \mathbf{x}_N\right] = \begin{bmatrix} \mathrm{x}(t_1) & 0 & \cdots & 0 \\ \mathrm{x}(t_2) & \mathrm{x}(t_1) & \ddots & \vdots \\ \vdots & \mathrm{x}(t_2) & \ddots & 0 \\ \vdots & \vdots & \ddots & \mathrm{x}(t_1) \\ \mathrm{x}(t_{M-2}) & \vdots & \ddots & \mathrm{x}(t_2) \\ \mathrm{x}(t_{M-1}) & \mathrm{x}(t_{M-2}) & \ddots & \vdots \\ \mathrm{x}(t_M) & \mathrm{x}(t_{M-1}) & \cdots & \mathrm{x}(t_{M-N+1}) \end{bmatrix} \quad (N \le M)\,, \tag{2.65}$$

i.e. its column vectors $\mathbf{x}_i$ $(i = 1,\ldots,N)$ are simply shifted (delayed) and truncated versions of $\mathbf{x} = \left[\mathrm{x}(t_1)\cdots\mathrm{x}(t_M)\right]^T$, which is the vector representation of the input signal. Here, the superscript T is used to denote the "transpose".

Equation (2.64) describes an overdetermined linear system of equations, whose solution is the unknown impulse response. Accordingly, the time-domain deconvolution problem can be stated as follows: Find a vector **h** such that $\mathbf{X}\mathbf{h} = \mathbf{y}$ or nearly so. This problem may be formulated as a least squares problem, which tries to minimize the error between the predicted and the true output signal, i.e.

$$\min_{\mathbf{h}} \left\|\mathbf{X}\mathbf{h} - \mathbf{y}\right\|^2 . \tag{2.66}$$

Differentiating eq. (2.66) with respect to **h** and setting the result equal to zero, the least squares solution $\mathbf{h}_{LS}$ is found to satisfy the so-called normal equations

$$\mathbf{X}^T\mathbf{X}\mathbf{h}_{LS} = \mathbf{X}^T\mathrm{y} . \tag{2.67}$$

Note from eq. (2.65) that the convolution matrix **X** has full column rank by definition, i.e. its column vectors are linearly independent. Thus $\mathbf{X}^T\mathbf{X}$ is invertible and the least squares solution is simply

$$\mathbf{h}_{LS} = \left(\mathbf{X}^T\mathbf{X}\right)^{-1}\mathbf{X}^T\mathrm{y} . \tag{2.68}$$

Before presenting some least squares deconvolution examples, it is worth examining some analytical properties of the least squares problem that are specific to time-domain deconvolution of ultra-wideband radar signals.

- **Zero residual** – The linearity and time invariance of the underlying process, e.g. backscattering from a buried minelike target, guarantees that **y** lies in the column space of the convolution matrix **X**. Therefore, in principle, time-domain deconvolution is a so-called zero residual least squares problem (Golub and Van

Loan, 1983, p.139), meaning that the residual of the least squares solution defined as

$$\mathbf{r} = \mathbf{X}\mathbf{h}_{LS} - \mathbf{y} \tag{2.69}$$

is zero. In practice, a non-zero residual of the least squares solution can therefore always be attributed to inaccurate knowledge of the input and output signals, e.g. as a result of noise or clutter.

- **Ill-posedness and ill-conditioning** – From the definition of the convolution matrix **X**, we see that neighboring columns only differ by very small time shifts, thereby making each column nearly dependent on its neighboring columns. This near rank deficiency of **X** causes ambiguity in the least squares solution because the norm of the residual does not have a well-defined minimum. Hence, the deconvolution problem is ill-posed. Moreover, due to the near rank deficiency of **X**, even small errors in the output signal **y** induce large errors in the estimate of the unknown impulse response vector **h**. In other words, the deconvolution problem is not just ill-posed but also ill-conditioned. The best way to illustrate this is through the singular value decomposition of **X**, i.e.

$$\mathbf{X} = \sum_{i=1}^{R} \sigma_i \mathbf{u}_i \mathbf{v}_i^T = \mathbf{U}_R \mathbf{\Sigma}_R \mathbf{V}_R^T \ , \tag{2.70a}$$

where

$$\mathbf{U}_R = \begin{bmatrix} \mathbf{u}_1 & \cdots & \mathbf{u}_R \end{bmatrix} \in \mathbb{R}^{M\times R} \tag{2.70b}$$

$$\mathbf{V}_R = \begin{bmatrix} \mathbf{v}_1 & \cdots & \mathbf{v}_R \end{bmatrix} \in \mathbb{R}^{N\times R} \tag{2.70c}$$

$$\mathbf{\Sigma}_R = \begin{bmatrix} \sigma_1 & & 0 \\ & \ddots & \\ 0 & & \sigma_R \end{bmatrix} \quad (\sigma_1 \geq \sigma_2 \geq \cdots \geq \sigma_R > 0) \tag{2.70d}$$

$$R = \operatorname{rank}(\mathbf{X}) \tag{2.70e}$$

(Golub and Van Loan, 1983, p. 16-20), with which the least squares solution of eq. (2.68) may be written as

$$\mathbf{h}_{LS} = \mathbf{V}_R \mathbf{\Sigma}_R^{-1} \mathbf{U}_R^T \mathbf{y} = \sum_{i=1}^{R} \frac{\mathbf{u}_i^T \mathbf{y}}{\sigma_i} \mathbf{v}_i \ . \tag{2.71}$$

Here, the σ_i are the non-zero singular values of **X** and the vectors $\mathbf{u}_i$ and $\mathbf{v}_i$ are the corresponding left and right singular vectors, respectively. Note that, since **X** has full column rank, $R = N$. The expansion of the least squares solution given by eq. (2.71) immediately shows that small errors in the output signal **y** can cause large changes in $\mathbf{h}_{LS}$ if the smallest singular value σ_R is close to zero, which is the case when **X** is nearly rank deficient. A measure for this error sensitivity is provided by the condition number of **X**, defined as the ratio

$$\kappa(\mathbf{X}) = \frac{\sigma_1}{\sigma_R} \ . \tag{2.72}$$

> As an example, the convolution matrix corresponding to the input signal of figure 2.3a has a condition number of $\kappa(\mathbf{X}) \approx 2.9 * 10^7$ (assuming 250 columns), which is extremely large and hence indicates that the deconvolution problem is very ill-conditioned.

Let us now return to the synthetic data example of figure 2.3. In the absence of noise, least squares deconvolution is able to exactly recover the true impulse response, as shown in figure 2.6. However, adding as little as –70 dB of white Gaussian noise to the output signal of figure 2.3c results in an impulse response estimate that is completely wrong, as shown in figure 2.7. This immediately rules out application of simple least squares deconvolution to demining GPR systems whose dynamic range with respect to the receiver noise level is typically of the order of 70 dB (see section 4.1.1). Two observations are worth pointing out. First, note that, although the estimated impulse response is completely wrong, the data fit is essentially perfect. And second, the impulse response estimate has extremely large coefficients. A simple trick to get a better result is to add white Gaussian noise to the input signal, thereby improving the conditioning of the convolution matrix. In essence, this is identical to prewhitening for a stable inverse filter (see eq. (2.55)). An example of the improvement to the solution is given in figure 2.8, showing the deconvolution result obtained when –40 dB of white Gaussian noise is added to the input signal of figure 2.3a. The condition number of the perturbed convolution matrix now is only 1489 (compare this to $2.9 * 10^7$ for the noise-free input signal), leading to a much more stable solution. The two-spike structure of the impulse response is now visible, however, as was the case with the Wiener filter, the estimate is smeared, leading to an underestimation of the amplitudes of the spikes as well as a limited temporal resolution.

From these examples, it is clear that simple least squares deconvolution in the time-domain will only work properly in the absence of noise and hence is of no practical use for ultra-wideband radar signals.

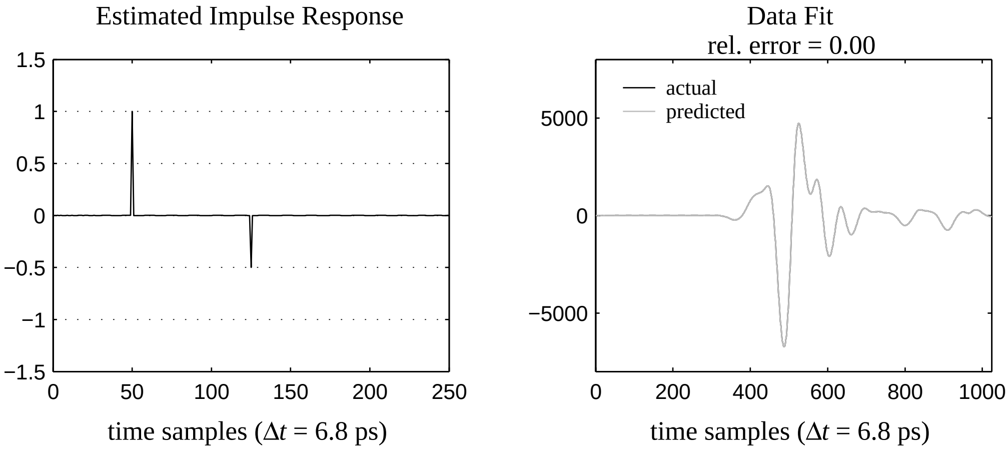

Figure 2.6: Least squares deconvolution of the input signal of figure 2.3a from the output signal of figure 2.3c. Shown are the estimated impulse response and the associated data fit between the predicted and the actual output signal. Note that the actual output signal is not visible due to the essentially perfect data fit.

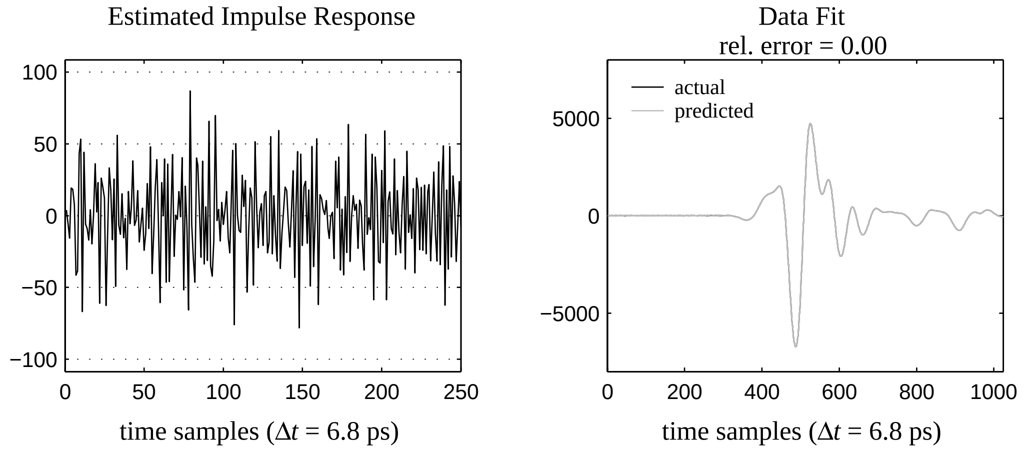

Figure 2.7: Least squares deconvolution as in figure 2.6, but with white Gaussian noise added to the output signal (output SNR: 70 dB).

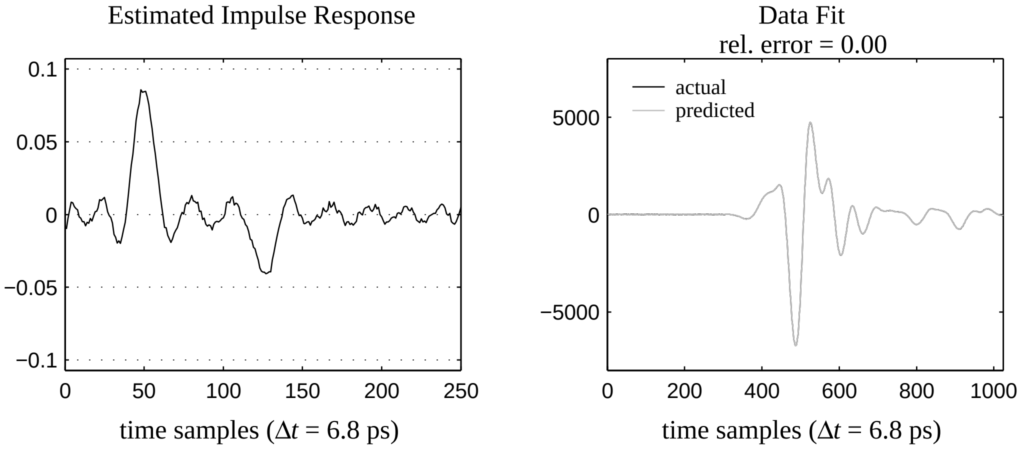

Figure 2.8: Least squares deconvolution as in figure 2.6, but with white Gaussian noise added to the output signal (output SNR: 70 dB) and to the input signal (input SNR: 40 dB).

Regularized least squares deconvolution in the time-domain (ridge regression)

In the previous section, we saw that simple time-domain least squares deconvolution is very sensitive to additive noise and has the tendency to produce impulse response estimates with extremely large coefficients (see figure 2.7). Therefore, it makes sense to regularize the least squares problem by penalizing impulse responses whose total power is “out of bounds”. This can be achieved by solving the following minimization problem:

$$\min_{\mathbf{h}} \left(\left\| \mathbf{Xh} - \mathbf{y} \right\|^2 + \lambda \left\| \mathbf{h} \right\|^2 \right) , \tag{2.73}$$

where λ is a properly chosen regularization parameter. Increasing λ pulls the solution away from minimizing the squared norm of the residual $\left\| \mathbf{Xh} - \mathbf{y} \right\|^2$ in favor of minimizing the total power $\left\| \mathbf{h} \right\|^2$ of the impulse response. This type of regularization is commonly referred to as **ridge regression**. The normal equations for the regularized deconvolution problem may be found by rewriting eq. (2.73) as a regular least squares minimization problem

$$\min_{\mathbf{h}} \left\| \begin{bmatrix} \mathbf{X} \\ \sqrt{\lambda}\mathbf{I} \end{bmatrix} \mathbf{h} - \begin{bmatrix} \mathbf{y} \\ \mathbf{0} \end{bmatrix} \right\|^2 , \tag{2.74}$$

implying that

$$\begin{bmatrix} \mathbf{X} \\ \sqrt{\lambda}\mathbf{I} \end{bmatrix}^T \begin{bmatrix} \mathbf{X} \\ \sqrt{\lambda}\mathbf{I} \end{bmatrix} \mathbf{h}_{RR} = \begin{bmatrix} \mathbf{X} \\ \sqrt{\lambda}\mathbf{I} \end{bmatrix}^T \begin{bmatrix} \mathbf{y} \\ \mathbf{0} \end{bmatrix} \tag{2.75}$$

or equivalently

$$\left[\mathbf{X}^T\mathbf{X} + \lambda\mathbf{I}\right]\mathbf{h}_{RR} = \mathbf{X}^T\mathrm{y} \ . \tag{2.76}$$

Here, $\mathbf{h}_{RR}$ is the ridge estimate of the unknown impulse response and **I** denotes a $N \times N$ identity matrix. The solution of the normal equations is

$$\mathbf{h}_{RR} = \left[\mathbf{X}^T\mathbf{X} + \lambda\mathbf{I}\right]^{-1} \mathbf{X}^T\mathrm{y} \ . \tag{2.77}$$

Looking at these equations, we see that, not only does ridge regression penalize impulse responses with large total power, it also counteracts the ill-conditioning of the deconvolution problem. Augmenting **X** by the regularization term $\sqrt{\lambda}\mathbf{I}$ improves the condition number of the convolution matrix, therefore resulting in normal equations that are less ill-conditioned. Consequently, the ridge estimate $\mathbf{h}_{RR}$ is less sensitive to errors in the input and output signals. The disadvantage of ridge regression is that the regularization term also introduces an error in the impulse response estimate. Therefore, the choice of the regularization parameter λ is a trade-off between the error in the impulse response estimate resulting from errors in the input and output signals and that introduced by the regularization term itself. Procedures for determining an optimal regularization parameter exist (Astanin and Kostylev, 1997; Savelyev *et al*, 2003), however all of them require knowledge of the size of the errors in the input and output signals, which are not known a priori and may differ from one operating scenario to the next. Hence, the choice of the regularization parameter is non-unique, just as it is for the Wiener filter.

Figure 2.9 shows the results of applying ridge regression deconvolution to the synthetic data example of figure 2.3 for the case that the output signal is contaminated by white Gaussian noise with a signal-to-noise ratio of 70 dB. The deconvolution was carried out for increasing values of the regularization parameter ($0 \le \lambda \le 10^{10}$). Note that for $\lambda = 0$ ridge regression becomes simple least squares, the results for which have already been presented in figure 2.7. The results show that ridge regression acts very much like the Wiener filter. It smears out the impulse response, thereby loosing amplitude information and temporal resolution. The smearing becomes stronger with increasing λ. The optimal value for λ is by no means indicated by the data fit between the predicted and the actual (noisy) output signal. In fact, all values of λ yield a near-to-perfect data fit, with the exception of $\lambda = 10^{10}$. The choice of the optimal value for λ is further complicated by its dependence on the noise level, as indicated by figure 2.10, showing the ridge regression deconvolution results for the case that the output signal-to-noise ratio is 20 dB. In this case, in order for the two-spike structure of the impulse response to become clearly visible, λ needs to be at least 10^8 in contrast to 10^2 for the output signal-to-noise ratio of 70dB (see figure 2.9). Hence, as for the Wiener filter, no one value of λ will work well for all operating scenarios.

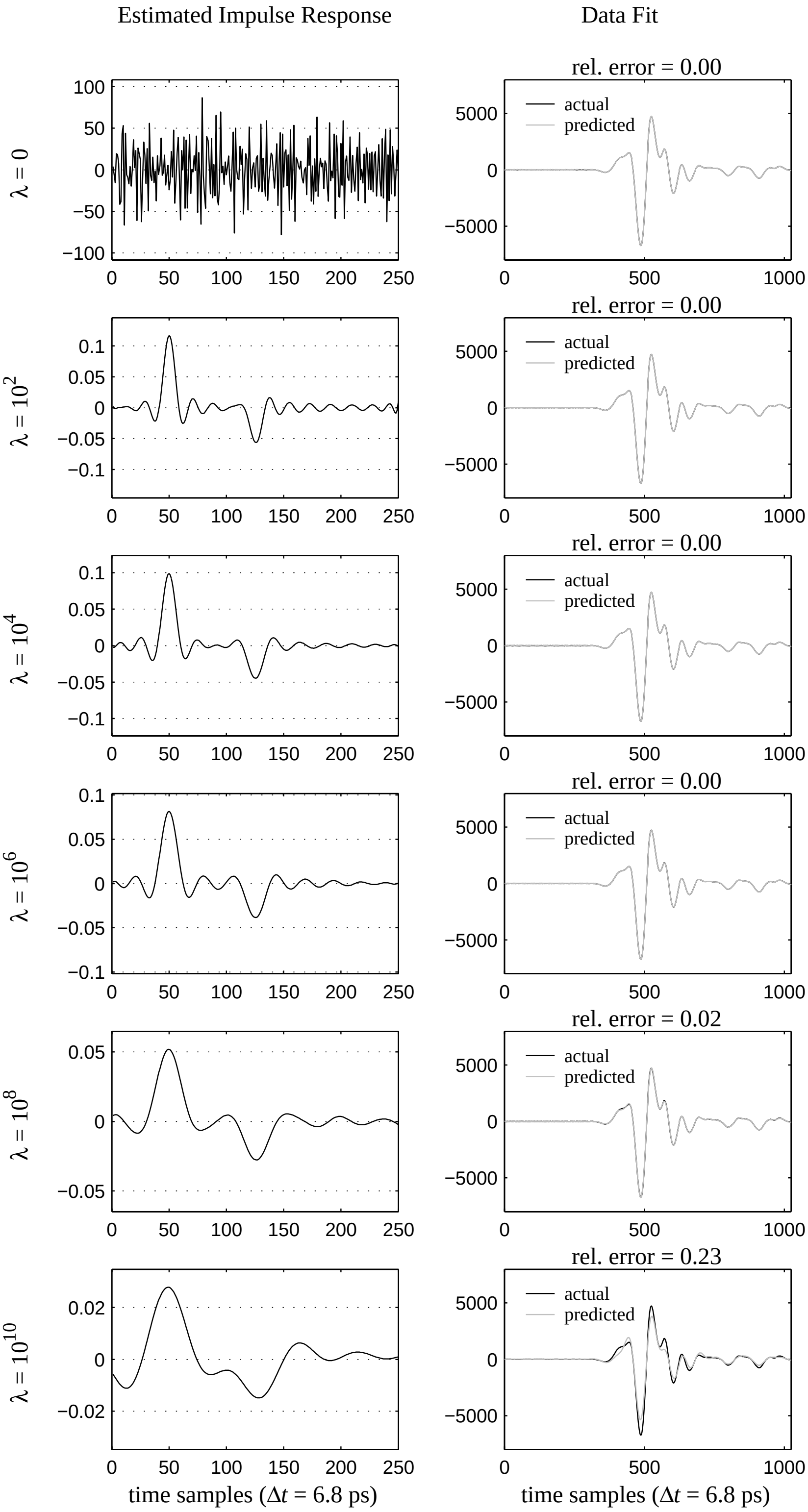

Figure 2.9: Ridge regression deconvolution of the input signal of figure 2.3a from the output signal of figure 2.3c to which white Gaussian noise has been added (output SNR: 70 dB). The left column shows the estimated impulse response for increasing λ and the right column shows the associated data fits between the predicted and the actual (noisy) output signal.

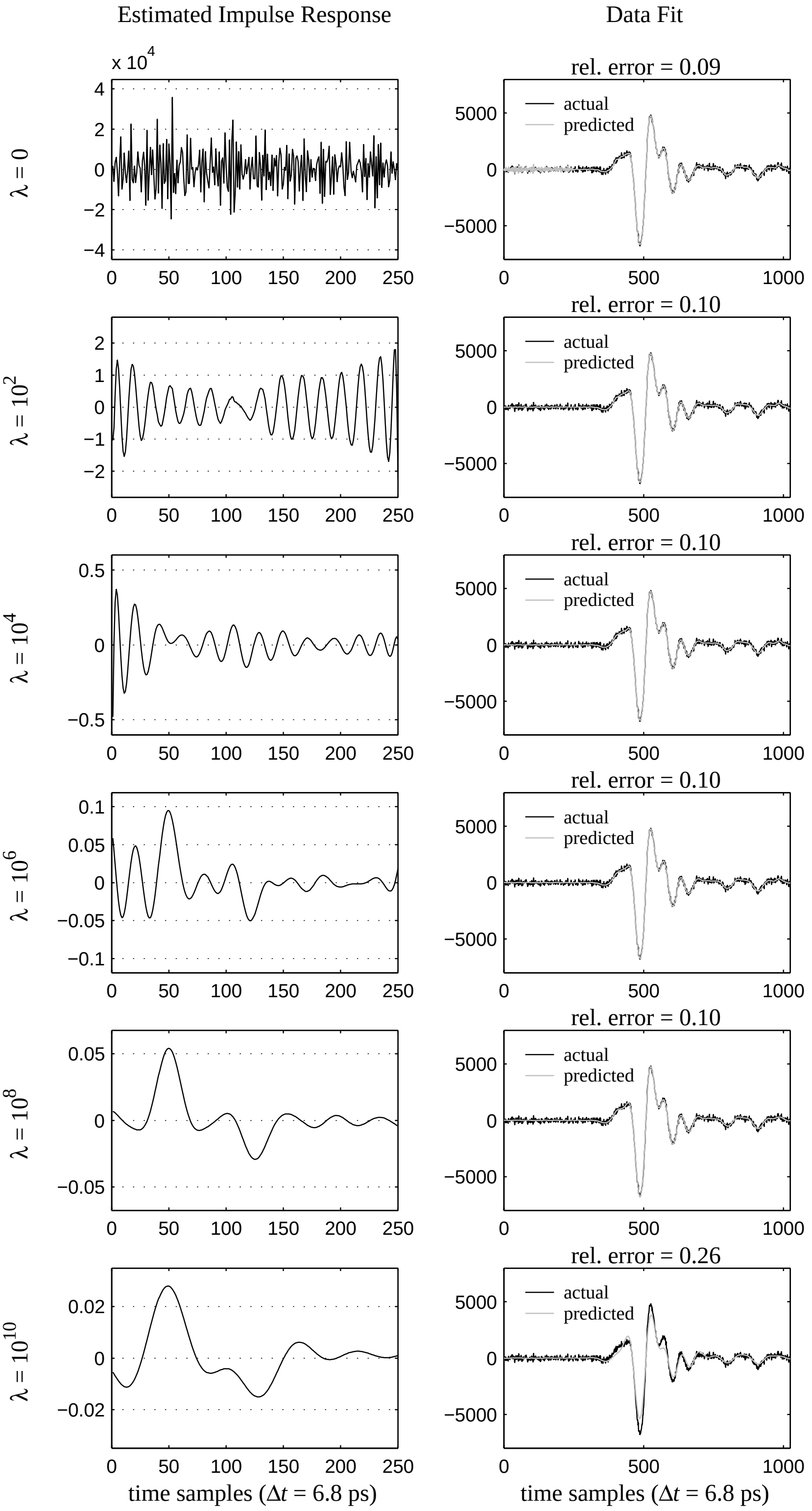

Figure 2.10: Ridge regression deconvolution as in figure 2.9, but with an output SNR of 20 dB.

2.2.3 Subset selection deconvolution

The review of deconvolution algorithms in the previous section showed that Wiener filtering and ridge regression have the general tendency to produce smeared out versions of the true impulse response. Therefore, any impulse response amplitude information, which may be related to target size or contrast, is lost. Their use for target characterization is further hampered by their reliance on a regularization parameter, whose optimal choice is non-obvious. Different regularization parameters lead to different impulse response estimates and hence the question “which is the better answer?”. Clearly, for the purpose of target characterization, we ideally seek a deconvolution method, which is insensitive to errors in the input and output signals, gives an accurate estimate of the magntitude of the impulse response and provides good resolution in time. In the following, a deconvolution algorithm satisfying these criteria is presented.

The ill-posedness of the least squares deconvolution in the time-domain may be viewed as a problem of redundancy. The redundancy expresses itself through the fact that it suffices to use only a few columns of the convolution matrix **X** to obtain very close predictions of the output signal vector **y**. Hence, rather than using all N columns of **X,** the least squares problem may be constrained by seeking an impulse response with at most $n \ll N$ non-zero coefficients. The positions of the non-zero coefficients determine which columns of **X** are used for the approximation of **y**. The process of selecting the columns is usually referred to as *subset selection* (Golub and Van Loan, 1983, p. 415).

Meaningful[6] application of subset selection to deconvolution requires that the following two criteria be satisfied:

- The true impulse response **h** is sparse or at least adequately represented so.
- Some a priori knowledge on the form of the impulse response **h** exists, such as the number of non-zero coefficients and how they are arranged.

For GPR signal deconvolution, the first criterion is equivalent to requiring that the output signal is primarily a result of scattering from sharp layer boundaries or interfaces, e.g. the top and the bottom surface of a target. The second criterion requires that we have some idea of the type of target we wish to characterize, e.g. a landmine, or of the number of layers in the ground. More specifically, for the characterization of minelike targets, the impulse response models derived in section 2.1 can be used to specify an appropriate number of non-zero impulse response coefficients, as will be explained in more detail in the following section.

Of primary importance for the work described in this thesis is the estimation of impulse responses with one or two non-zero coefficients. In these two cases, subset selection can be achieved by permutation, i.e. solving a reduced least squares problem for all possible positions of the non-zero impulse response coefficients and then selecting the solution which gives the smallest residual overall. Thus, subset selection deconvolution may be formulated as

$$\min_{i}\left(\min_{\mathrm{h}(t_i)}\left\|\mathbf{x}_i \mathrm{h}(t_i)-\mathbf{y}\right\|^2\right) \qquad (1 \le i \le N) \tag{2.78}$$

or

---

[6] Meaningful in the sense that the estimated impulse response is not just a mathematical curiosity.

$$\min_{i,j}\left(\min_{\begin{bmatrix}\mathrm{h}(t_i)\\ \mathrm{h}(t_j)\end{bmatrix}}\left\|\begin{bmatrix}\mathbf{x}_i & \mathbf{x}_j\end{bmatrix}\begin{bmatrix}\mathrm{h}(t_i)\\ \mathrm{h}(t_j)\end{bmatrix}-\mathbf{y}\right\|^2\right) \qquad (1 \le i < j \le N)\ , \tag{2.79}$$

depending on whether one or two non-zero impulse response coefficients are considered.

Clearly, computation time will generally prohibit the use of simple permutation for subset selection deconvolution involving more than two non-zero impulse response coefficients if the processing is to be done in real-time. Other subset selection strategies then become necessary. One possible strategy is to start off with an impulse response consisting of one or two non-zero coefficients and then iteratively select the position for the next non-zero coefficient, while keeping the previous selected positions fixed. Note that this approach will usually produce a sub-optimal selection. Alternatively, it is possible to use templates, which describe predefined arrangements of impulse response coefficients. Detailed information on the use of iterative methods and templates for subset selection deconvolution of GPR signals can be found in the work of Van der Lijn (2002).

To illustrate the advantages of subset selection deconvolution, let us again consider the synthetic data example of figure 2.3. The result of applying subset selection deconvolution in the absence of noise is shown in figure 2.11, whereas the result for the case that the output signal is contaminated by white Gaussian noise with a signal-to-noise ratio of 20 dB is shown in figure 2.12. Remarkably, even in the noisy case subset selection is able to exactly recover the true impulse response. As such, subset selection clearly outperforms Wiener filtering and ridge regression. The two latter algorithms required the use of a large regularization parameter to be able to deal with an output signal-to-noise ratio of 20 dB, causing strong smearing of the impulse response, as illustrated in figures 2.5 and 2.10. The robustness of the subset selection algorithm to noise is further demonstrated by figure 2.13, showing the size of the residual of the reduced least squares solution for each position index pair (i, j) searched by the algorithm. The size of the residual has a well-defined minimum at $(i, j) = (50,125)$, which are the true positions of the two spikes in the impulse response.

Thus, subset selection provides a robust tool for the estimation of sparse impulse responses. Both amplitude and temporal information of the impulse response can be recovered very accurately. Therefore, subset selection deconvolution is well suited for target characterization, as shall be explained further in the following section.

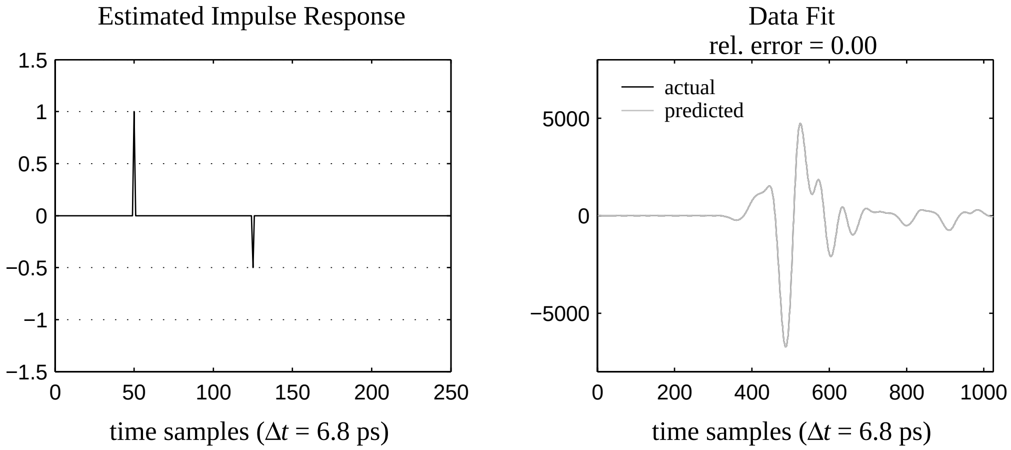

Figure 2.11: Subset selection deconvolution of the input signal of figure 2.3a from the output signal of figure 2.3c. Shown are the estimated impulse response and the corresponding data fit between the predicted and the actual output signal. Note that the actual output signal is not visible due to the essentially perfect data fit.

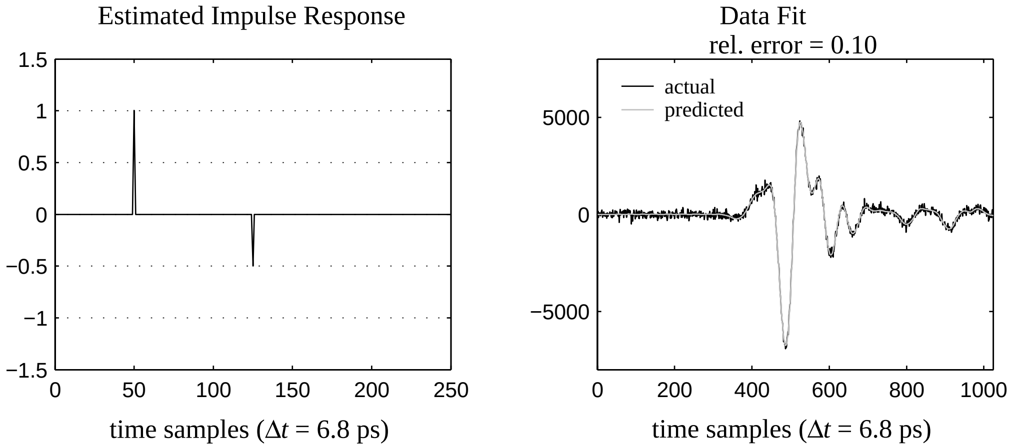

Figure 2.12: Subset selection deconvolution as in figure 2.11, but with white Gaussian noise added to the output signal (output SNR: 20 dB).

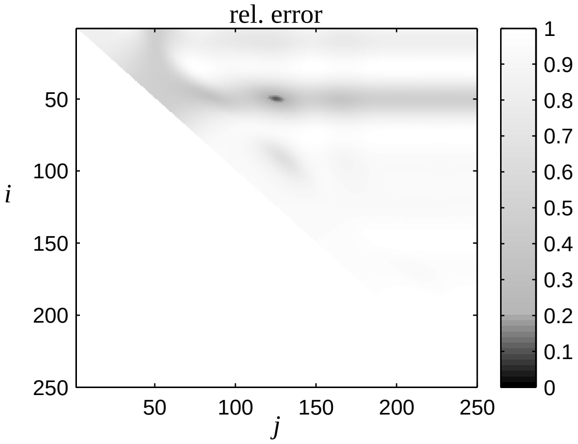

Figure 2.13: Relative error function for the subset selection deconvolution example shown in figure 2.12.

2.2.4 Target characterization

This section describes how subset selection deconvolution can be used to characterize circular disk-shaped minelike targets. Because the impulse response of these types of targets consists of just one (metal disk) or two (dielectric disk) differentiation operators, they naturally lend themselves to characterization by subset selection deconvolution. The following characterization procedure pertains to the configuration shown in figure 2.1, i.e. plane wave backscattering for which the convolutional model of eq. (2.16) has been derived, and assumes knowledge of the incident and the scattered fields. In chapter 4, the characterization procedure will be generalized for application to measured GPR responses of both surface-laid and buried minelike targets.

The primary processing step of the characterization procedure is the deconvolution of the incident field $\mathrm{e}^i(\boldsymbol{x}_\mathrm{t},t)$ from the backscattered field $\mathrm{e}^s(\boldsymbol{x},t)$. The underlying convolutional model is

$$\mathrm{e}^s(\boldsymbol{x},t)=\mathrm{h}(t)\otimes\mathrm{e}^i(\boldsymbol{x}_\mathrm{t},t)\ , \tag{2.80}$$

which is simply eq. (2.51) with the input signal $\mathrm{x}(t)$ replaced by $\mathrm{e}^i(\boldsymbol{x}_\mathrm{t},t)$ and the output signal $\mathrm{y}(t)$ replaced by $\mathrm{e}^s(\boldsymbol{x},t)$.

Subset selection deconvolution requires a sparse parameterization of the impulse response $\mathrm{h}(t)$ to be estimated. Appropriate parameterizations directly follow from substitution of the target impulse response models given by eqs. (2.23) and (2.31) into the convolutional scattering model of eq. (2.16). Doing so for the circular dielectric disk yields the parameterization

$$\mathrm{h}(t)=\mathrm{h}_1\dot{\delta}(t-\tau_1)+\mathrm{h}_2\dot{\delta}(t-\tau_2)\ , \tag{2.81}$$

where

$$\mathrm{h}_1=-\frac{T_{g\to a}\zeta(h,d)}{8\pi(h+d)}\frac{v_\mathrm{t}^{eff}}{c^2}\Delta\varepsilon_r S_{xy}\ , \tag{2.82a}$$

$$\tau_1 = \frac{h}{c} + \frac{d}{v_1} \ , \tag{2.82b}$$

$$\mathrm{h}_2 = -\Gamma \mathrm{h}_1 \ , \tag{2.82c}$$

$$\tau_2 = \tau_1 + \frac{2l}{v_\mathrm{t}^{eff}} \ . \tag{2.82d}$$

Likewise, the parameterization for the buried circular metal disk is found to be

$$\mathrm{h}(t) = \mathrm{h}_1 \dot{\delta}(t - \tau_1) \tag{2.83}$$

where

$$\mathrm{h}_1 = -\frac{T_{g\to a}\zeta(h,d)}{2\pi(h+d)} \frac{1}{v_1} S_{xy} \ , \tag{2.84a}$$

$$\tau_1 = \frac{h}{c} + \frac{d}{v_1} \ . \tag{2.84b}$$

These parameterizations suggest using the time derivative of the incident field to create the convolution matrix **X**, because then the subset selection deconvolution equations (2.76) and (2.77) can be used directly to estimate of the impulse response parameters h_1 & τ_1 and h_2 & τ_2 (if applicable). Equivalently, as shown by Van der Lijn *et al* (2003), it is possible to introduce discrete representations for the differentiation operators[7], leading to subset selection deconvolution equations of the same form as (2.78) and (2.79). In this thesis, mainly the first approach has been used. Another practical thing to do when dealing with dielectric disks is to constrain the subset selection by discarding solutions for which $\mathrm{h}_1\mathrm{h}_2 > 0$, i.e. for which the two differentiation operators in eq. (2.81) have the same polarity, since this would contradict eq. (2.82c) (remember that Γ is positive by definition). Furthermore, note from eq. (2.84a) that the impulse response coefficient h_1 obtained for a circular metal disk will always be negative.

Once the impulse response parameters have been estimated by subset selection deconvolution, they can be related to target characteristics by means of eqs. (2.82) and (2.84). Note from eq. (2.82a) that, for a dielectric disk, target size and target contrast are inherently unresolved, i.e. an increase in target cross-section S_{xy} cannot be distinguished from an increase in target contrast $\Delta\varepsilon_r$. The same ambiguity exists between the target height *l* and the effective target velocity v_t^{eff} both of which determine the impulse response length $\tau_2 - \tau_1$, as can be seen from eq. (2.82d). Consequently, it is only possible to infer possible combinations of target characteristics. This means that in practice two types of inversions are possible. These are inversion for target size and inversion for material properties:

- Inversion for target size refers to the estimation of the cross-section S_{xy} (or radius for that matter) and the target height *l* from the impulse response coefficient h_1 and the impulse response length $\tau_2 - \tau_1$ by specifying a target relative permittivity $\varepsilon_{r,\mathrm{t}}$ and an effective target velocity v_t^{eff} that are generic for the type of target to be characterized.

---

[7] A discrete differentiation operator can be represented as a pair of neighboring spikes of opposite polarity and equal magnitude $1/\Delta t$ with Δt being the time sampling interval.

- Inversion for material properties refers to the estimation of the target relative permittivity $\varepsilon_{r,\mathrm{t}}$ and the effective target velocity v_{t}^{eff} from the impulse response coefficient h_1 and the impulse response length $\tau_2 - \tau_1$ by assuming a cross-section S_{xy} and a target height *l*.

In contrast, for a metal disk, it only makes sense to invert the impulse response for target size, in this case estimating its cross-section S_{xy} from the impulse response coefficient h_1.

An indication of the nature of the target, i.e. whether it is made of dielectric material or metal, is given by the generally strong target response magnitude that can be expected from a metal target and the fact that in most soils the contrast $\Delta\varepsilon_r$ of the main constituents of a plastic cased landmine (plastic, explosive, air) is negative. Hence, the polarity of the target response of a plastic cased landmine is generally reversed to that of a metal cased landmine, which is also reflected by the impulse response coefficient h_1 being positive. The sign of h_1 obtained by subset selection deconvolution can therefore be used as an indicator whether the appropriate impulse response parameterization was selected out of the two possible ones, i.e. eq. (2.81) or eq. (2.83).

2.3 3D Finite-Difference Time-Domain (FDTD) Simulation Results and Verification

In the previous section, a target characterization procedure was presented, which combines subset selection deconvolution with the time-domain convolutional scattering model and the target impulse response models derived in section 2.1 to estimate the size or the material properties of a buried circular disk-shaped minelike target. To check the accuracy of the target characterization procedure as well as the validity of the underlying the scattering models, the responses of 6 buried circular disks were simulated using a 3D FDTD modeling program (Mur, 2001).

The FDTD program uses a total field formulation and allows for excitation by a plane wave incident field originating from outside the computational domain through the use of Mur's total field absorbing boundary conditions (ABCs) (Mur, 1998). Scattered fields are obtained by simply repeating a simulation for the case that there is no target (with everything else unchanged) and then subtracting the so-obtained incident field data from the previously modeled total field data. Since the original implementation of the total field ABCs assumed a target in air, they were modified here for a half-space background medium, i.e. air and ground. This generalization was readily achieved by reevaluating the incident field terms in the ABCs, as suggested in Mur (1998). With this modification, it was then possible to do the simulations for exactly the same configuration as the one for which the convolutional scattering models and target impulse response models were derived, i.e. plane wave backscattering as shown in figure 2.1. For the plane wave incident field, a linear polarization in the *x*-direction and a waveform equal to a Ricker wavelet (2nd derivative of a Gaussian pulse) with a peak amplitude frequency of 1.5 GHz was selected. Accordingly, the simulated target responses shown and analyzed in this section refer to the *x*-component of the scattered field. To ensure good simulation accuracy, a very small cell size of 2.5 mm was used in all three coordinate directions together with the corresponding Courant time step.

Of the simulated disks, five were dielectric and one was metal. The dielectric disks included three with a relative permittivity of 2.8 (similar to the explosive TNT) (Bruschini *et al*, 1998), one with a relative permittivity of 2.1 (Teflon) (Von Hippel, 1954, p. 332), and one with a relative permittivity of 1.0 (air). The metal disk was modeled as a perfect electrical conductor (PEC). The disks - hereinafter referred to as *TNT Disk 1* through *3*, *Teflon Disk 1*, *Air Disk 1*, and *Metal Disk 1* - were given a radius between 3 and 7.5 cm and a height of either 4 or 6 cm, which are typical for AP landmines. The disks were considered at depths between 2.5 and 10 cm in a lossless ground with a relative permittivity of 2.5 (*Teflon Disk 1* and *Air Disk 1*) and 4.0 (*TNT Disk 1* through *3* and *Metal Disk 1*). The ground relative permittivity of 2.5 is representative for the sand at the experimental facility where the GPR data presented in chapter 5 were acquired. The reason for this choice was to determine the effective target velocities of *Teflon Disk 1* and *Air Disk 1* for later use in the analysis of the experimental data.[8] The ground relative permittivity of 4.0 chosen for the other four disks is representative for dry sandy and dry loamy soils (Daniels, 1996, p.33). A list of all simulated disks, their properties and the conditions under which they were simulated is given in table 2.1.

A requisite for the target characterization procedure to work is that the spreading term

$$\frac{\zeta(h,d)}{2\sqrt{\pi}(h+d)}=\frac{1}{2\sqrt{\pi}\left(h\sqrt{\varepsilon_{r,1}}+d\right)} \tag{2.85}$$

in the convolutional scattering model of eq. (2.16) accurately describes the dependency of the target response magnitude on observation height and target depth. To analyze the accuracy of the spreading term, the peak-to-peak amplitude of the simulated target response of *TNT Disk 1* and eq. (2.85) were plotted against each other as a function of observation height and target depth, the result of which is shown in figure 2.14. To make a comparison possible, the peak-to-peak amplitude and the spreading term were both normalized with respect to $h=50$ cm and $d=2.5$ cm. Looking at figure 2.14a, we observe that eq. (2.85) well predicts the increase in target response magnitude that results from a decrease in observation height down to $h=10$ cm. When going even closer to the ground, the predicted increase in target response magnitude starts to deviate from the simulated increase because then the far-field observation assumption is violated. The decrease in target response magnitude resulting from an increase in target depth is well predicted for all target depths, as can be seen from figure 2.14b. It is interesting to note that, in the depth range that is typical for antipersonnel landmines, the target response magnitude is only slightly affected by target depth. In contrast, the magnitude can be increased multifold by measuring the scattered field closer to the ground.

Performing subset selection deconvolution as outlined in section 2.2.4 on the simulated target responses gave the impulse response parameters listed in table 2.2. Figure 2.15 gives three examples of the generally good data fit between the responses predicted by the impulse response estimates and the simulated responses, the first of *TNT Disk 1*, the second of *Metal Disk 1*, and the last of *Teflon Disk 1*. The good data fit demonstrates that the axial response of a buried circular disk-shaped minelike target is well modeled by an impulse response as in eqs. (2.81) and (2.83), respectively, consisting of one or two differentiation operators. Note that the specular response of *Metal Disk 1* is followed by a multiple reflection between the target and the ground surface and the creeping wave, both of which in this particular case arrive at about the same time. Additional simulations of buried metal disks showed that for smaller target depths (e.g. $d=2.5$ cm) and disk sizes ($\text{radius} < 5$ cm) the first multiple and the creeping wave generally overlap with the specular response, making waveform based identification of metal targets a non-trivial task.

---

[8] In fact, later on it was learned that the sand at the experimental facility has a slightly different relative permittivity, namely 2.6.

Figure 2.16 illustrates the relationship between the impulse response parameters of the TNT disks obtained by deconvolution and their size. We see that there is indeed a linear relationship between the coefficient h_1 and the cross-section S_{xy}, and between the impulse response length $\tau_2 - \tau_1$ and the disk height *l*, as predicted by eq. (2.82). Fitting a straight line to the data points in figure 2.16b gives the effective target velocity $v_t^{eff} \approx 16.6$ cm/ns, which is higher than the wave velocity in the ground, $v_1 \approx 15.0$ cm/ns, but lower than the intrinsic target velocity, $v_t \approx 17.9$ cm/ns.

The linear relationships between h_1 and the cross-section S_{xy} and between $\tau_2 - \tau_1$ and the disk height *l* (dielectric disk only) form the basis for inverting the estimated impulse response parameters for target size. Doing the inversion for the TNT disks and *Metal Disk 1* yielded the disk radii and heights listed in table 2.3. The inversions were carried out using eqs. (2.82) and (2.84) and assumed knowledge of the observation height *h* and the target depth *d*. The size inversion for the TNT disks additionally required the specification of their relative permittivity $\varepsilon_{r,t} = 2.8$ and their effective target velocity $v_t^{eff} = 16.6$ cm/ns.[9] The good agreement between the estimated and the true disk dimensions (shown in parentheses) demonstrates that the convolutional scattering model of eq. (2.16) together with the target impulse response models of eqs. (2.23) and (2.31) accurately describes the scattering from a buried circular disk. Furthermore, the inversion results demonstrate that it is possible to estimate disk radius and height with millimeter accuracy.

Table 2.4 lists the results of inverting the impulse response parameters obtained for the dielectric disks for material properties, i.e. target relative permittivity $\varepsilon_{r,t}$ and effective target velocity v_t^{eff}. The inversions were carried out using eq. (2.82) in which the true disk dimensions had been substituted, i.e. they are assumed known. We see that the relative permittivities of all disks were recovered with an error of less than 11 % with respect to the permittivity contrast, the only exception being *Air Disk 1* when buried 2.5 cm deep, in which case the inversion error was 19 %. Most likely this error can be attributed to the estimated effective target velocity v_t^{eff} being too low, since the inversion for *Air Disk 1* when buried 10 cm deep, which involved a higher v_t^{eff}, worked fine. This hints to one of the problems of the inversion for material properties. Not only do we need to know the disk dimensions (as well as the observation height *h* and the target depth *d* for that matter), also the estimation of v_t^{eff} needs to be sufficiently good for an accurate recovery of the disk permittivity. This problem is mostly relevant when the impulse response length $\tau_2 - \tau_1$ is short since then the estimation of v_t^{eff} becomes more sensitive to errors.[10] This is further aggravated by the fact that subset selection deconvolution has a harder time estimating very short impulse responses than it has estimating longer ones. Still, the inversion results demonstrate that in theory the relative permittivity of a buried dielectric disk can be estimated very accurately. Furthermore, they demonstrate that the convolutional scattering model of eq. (2.16) together with the target impulse response model of eq. (2.23) accurately describes the scattering from a buried dielectric disk, just as the results of the inversion for target size did.

Some interesting observations can be made from looking at the values of the attenuation factor Γ in table 2.2. As may be expected, Γ is closest to one for *Teflon Disk 1* and closest to zero for *Air Disk 1,* which demonstrates that Γ truly is a measure of the extent to which the Born approximation is valid. Furthermore, *TNT Disk 3* has a smaller Γ than *TNT Disk 1*

---

[9] Unfortunately, no estimate of v_t^{eff} other than that from fitting the data points in figure 2.16b was available, limiting the significance of the estimated disk heights.

[10] This follows immediately from the derivative of v_t^{eff} with respect to $\tau_2 - \tau_1$: $\partial_{\tau_2 - \tau_1} v_t^{eff} = -2l/(\tau_2 - \tau_1)^2$.

although both have the same height *l*. This suggests that the validity of the Born approximation deteriorates as the target aspect ratio decreases. This phenomenon shall be looked at further in chapter 5 when analyzing experimental GPR data. Interestingly, even though the Born approximation was not satisfied for any of the simulations (this would require $\Gamma = 1$), the non-validity did not negatively affect the inversion for target size and the inversion for material properties.

In this context, the inversion for target size and the inversion for material properties were also carried out under the modified Born approximation which simply requires the substitution

$$\Delta\varepsilon_r \to \Delta\varepsilon_r \frac{3\varepsilon_r}{\Delta\varepsilon_r + 3\varepsilon_r} \tag{2.86}$$

in eq. (2.82a). No significant changes or improvements in the inversion results were observed. In general, the estimated radii and the estimated relative permittivity contrasts were slightly lower than those estimated under the "standard" Born approximation. Therefore, the "standard" Born approximation will continue to be the "workhorse" in this thesis.

As a final remark, it should be mentioned that, when dealing with measured GPR signals, the reliance of the target characterization procedure on knowledge of the observation height as well as target depth presents no limitation as these can be estimated from the arrival time of the ground reflection and that of the target response. In fact, as the experimental results of chapter 5 will show, observation height and target depth can be estimated with millimeter accuracy, which is sufficiently accurate for use in the inversions.

Table 2.1: Description of the circular disks and the conditions under which they were simulated.

Target Name	**Target Material Type**	**Target Dimensions**			**Ground Rel. Permittivity**	**Target Depths**
		radius [cm]	height *l* [cm]	aspect ratio*	$\varepsilon_{r,1}$	*d* [cm]
TNT Disk 1	dielectric, $\varepsilon_{r,t} = 2.8$	5.0	4.0	1.25	4.0	2.5, 5.0, 7.5 & 10.0
TNT Disk 2	dielectric, $\varepsilon_{r,t} = 2.8$	7.5	6.0	1.25	4.0	2.5 & 10.0
TNT Disk 3	dielectric, $\varepsilon_{r,t} = 2.8$	3.0	4.0	0.75	4.0	2.5 & 10.0
Teflon Disk 1	dielectric, $\varepsilon_{r,t} = 2.1$	5.0	4.0	1.25	2.5	2.5 & 10.0
Air Disk 1	dielectric, $\varepsilon_{r,t} = 1.0$	5.0	4.0	1.25	2.5	2.5 & 10.0
Metal Disk 1	PEC	5.0	4.0	1.25	4.0	2.5 & 10.0

* Ratio of the radius over the height.

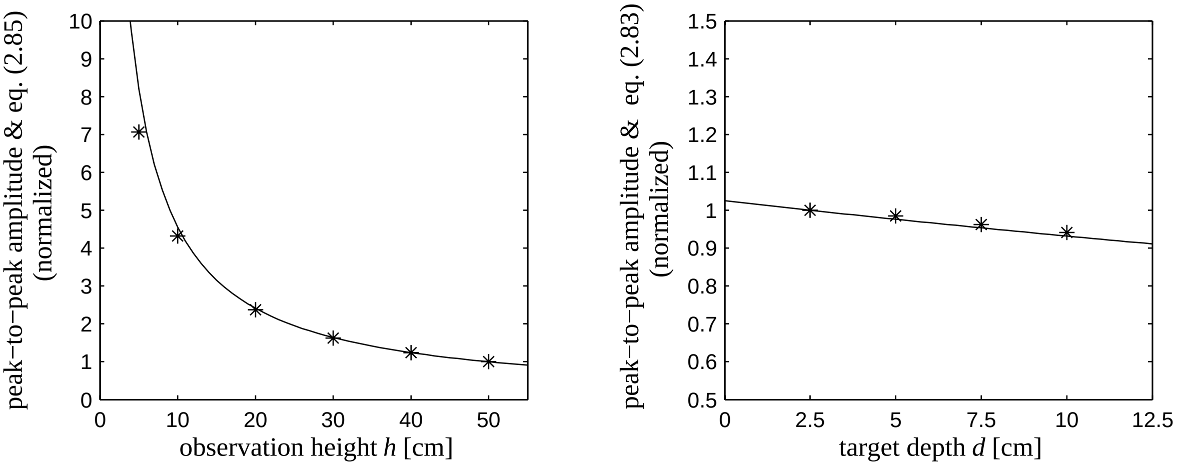

(a) (b)

Figure 2.14: Peak-to-peak amplitude of the simulated response of *TNT Disk 1* [stars] versus the spreading term of eq. (2.85) [line] displayed as a function of (a) observation height given $d = 2.5$ cm and (b) target depth given $h = 50$ cm .

Table 2.2: Subset selection deconvolution results.

Target Name	**Target Depth** d [cm]	**Obs. Height** h [cm]	**Impulse Response Parameters**							**Rel. Error**
			h_1 $[*10^{-4}]$	τ_1		h_2 $[*10^{-4}]$	$\tau_2 - \tau_1$		Γ	
				samples	[ns]		samples	[ns]		
TNT Disk 1	2.5	30.0	15.5	123	1.184	-11.2	50	0.482	0.73	0.07
	10.0	30.0	14.0	175	1.685	-10.0	50	0.482	0.72	0.05
TNT Disk 2	2.5	30.0	34.4	123	1.184	-22.3	73	0.703	0.65	0.08
	10.0	30.0	31.3	175	1.685	-20.7	73	0.703	0.66	0.06
TNT Disk 3	2.5	30.0	5.5	122	1.175	-3.2	53	0.510	0.58	0.12
	10.0	30.0	5.0	174	1.676	-2.9	53	0.510	0.58	0.10
Teflon Disk 1	2.5	30.0	6.9	119	1.146	-5.8	43	0.414	0.83	0.06
	10.0	30.0	6.1	160	1.541	-5.0	43	0.414	0.83	0.04
Air Disk 1	2.5	30.0	39.4	119	1.146	-12.4	32	0.308	0.31	0.05
	10.0	30.0	32.5	160	1.541	-12.7	29	0.279	0.39	0.05
Metal Disk 1	2.5	30.0	-197.6	126	1.213	n/a	n/a	n/a	n/a	0.17
	10.0	30.0	-159.8	177	1.704	n/a	n/a	n/a	n/a	0.08

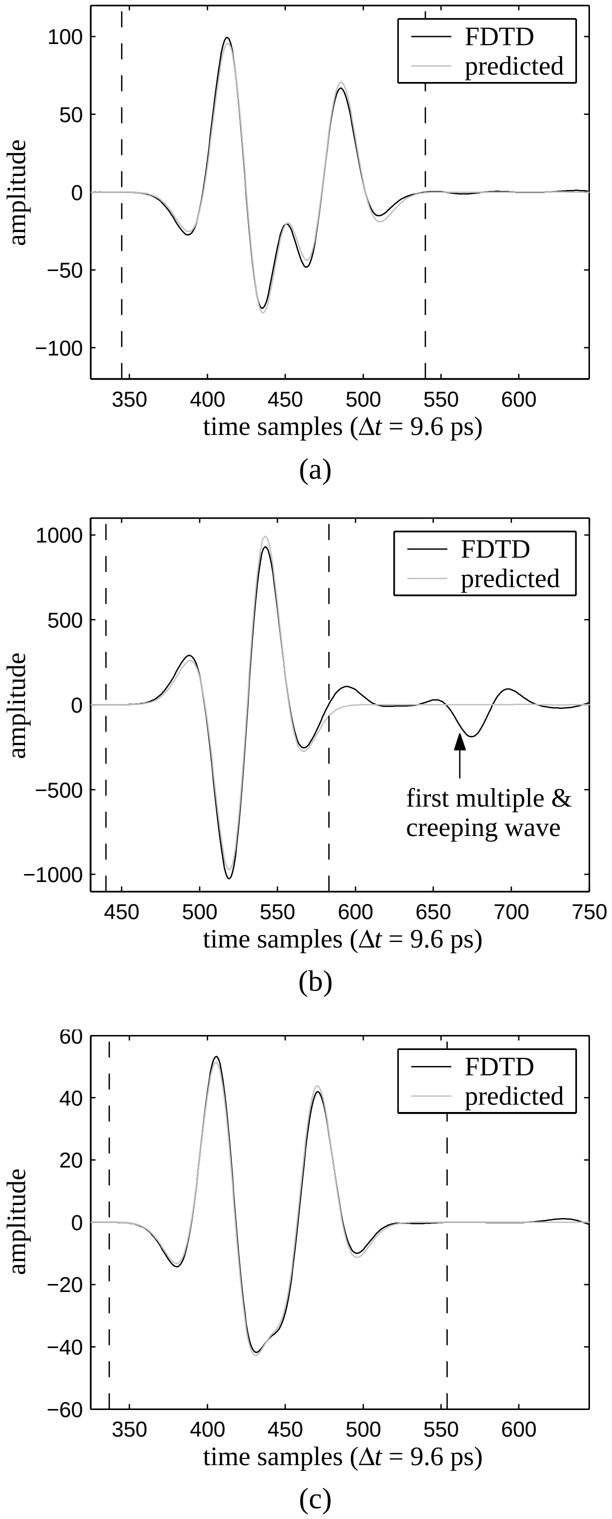

Figure 2.15: Examples of the data fit between the predicted (deconvolution) and the simulated response:
(a) *TNT Disk 1* (d = 2.5 cm & h = 30 cm)
(b) *Metal Disk 1* (d = 10 cm & h = 30 cm)
(c) *Teflon Disk 1* (d = 2.5 cm & h = 30 cm).
The dashed lines define the part of the response, which was fit by the deconvolution algorithm.

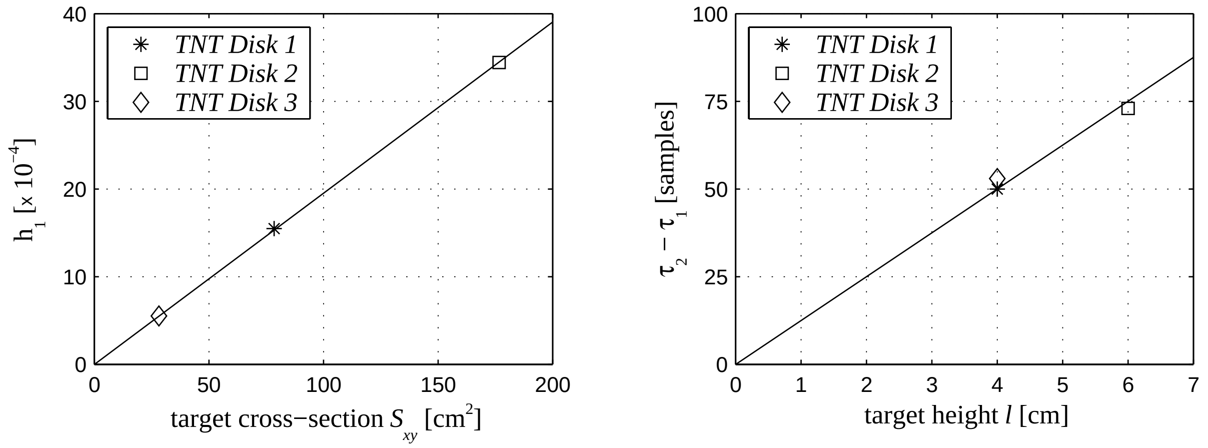

(a) (b)

Figure 2.16: Deconvolution results for the TNT disks (d = 2.5 cm & h = 30 cm):
(a) h_1 vs. S_{xy}
(b) $\tau_2 - \tau_1$ vs. l.
The straight lines represent least squares fits to the data points.

Table 2.3: Results of the inversion for target size.

Target Name	**Target Depth** d [cm]	**Observation Height** h [cm]	**Inversion for Target Size***	
			target radius [cm]	target height l [cm]
TNT Disk 1	2.5	30.0	5.1 (5.0)	4.0 (4.0)
	10.0	30.0	5.2 (5.0)	4.0 (4.0)
TNT Disk 2	2.5	30.0	7.6 (7.5)	5.8 (6.0)
	10.0	30.0	7.7 (7.5)	5.8 (6.0)
TNT Disk 3	2.5	30.0	3.1 (3.0)	4.2 (4.0)
	10.0	30.0	3.1 (3.0)	4.2 (4.0)
Metal Disk 1	2.5	30.0	5.3 (5.0)	n/a (4.0)
	10.0	30.0	5.0 (5.0)	n/a (4.0)

The values included in parentheses are the true values.

* For the TNT disks the inversion was based on $\Delta\varepsilon_r = 2.8 - 4 = -1.2$ and $v_t^{eff} = 16.6$ cm/ns.

Table 2.4: Results of the inversion for material properties.

Target Name	**Target Depth** d [cm]	**Observation Height** h [cm]	**Inversion for Material Properties** * $\varepsilon_{r,t}$	 v_{t}^{eff} [cm/ns]
TNT Disk 1	2.5	30.0	2.74 (2.8)	16.6
	10.0	30.0	2.72 (2.8)	16.6
TNT Disk 2	2.5	30.0	2.79 (2.8)	17.1
	10.0	30.0	2.77 (2.8)	17.1
TNT Disk 3	2.5	30.0	2.69 (2.8)	15.7
	10.0	30.0	2.67 (2.8)	15.7
Teflon Disk 1	2.5	30.0	2.08 (2.1)	19.3
	10.0	30.0	2.08 (2.1)	19.3
Air Disk 1	2.5	30.0	0.72 (1.0)	26.0
	10.0	30.0	0.97 (1.0)	28.6

The values included in parentheses are the true values.

[*] Based on the true disk dimensions.

2.4 Host Medium Transformation of the Response of a Dielectric Minelike Target

The motivation for the work described in this section has been the following question: Is it possible to predict the target response of a buried plastic cased landmine given its response in another soil? The usefulness of such a prediction would be tremendous. Suppose the response of a buried landmine for a specific soil type is known from laboratory measurements. We could then use this knowledge to identify the same type of landmine in a minefield where the soil properties are different to those in the laboratory, e.g. because the soil type is different or due to weather related changes in soil water content.

The following analysis is primarily concerned with how the response of a landmine changes when the soil becomes lossy. A similar problem, though for the late-time response, has been addressed by Baum (1998), who derived an expression relating the free space natural frequencies of a perfectly conducting target to those in a simple lossy medium characterized by a static conductivity and a relative dielectric permittivity. Baum's transformation is an example of a well-studied procedure for EM field transformation based on similarity analysis in the Laplace domain. Similarity analysis has been used to derive transformations for tensorial Green's functions (De Hoop, 1996), (Verweij, 2001), and primary (incident) fields (Gershenson, 1997). In section 2.4.1, it shall be demonstrated that a transformation law for the field scattered by a buried dielectric minelike target can be derived in an analogous manner by relating the scattering currents using the Born approximation. The derived transformation law is then illustrated in section 2.4.2 for a circular dielectric disk whose response has been simulated by FDTD for both a lossless and a lossy host medium.

2.4.1 Theory

Formulation of the scattering problem

The transformation law is derived for plane wave scattering from the homogeneous dielectric target, introduced in section 2.1, fully embedded in the l^{th} layer of an n-layered host medium, as shown in figure 2.17. The dielectric permittivities of the layers are ε_i $(i=1,\ldots,n)$. For simplicity, the magnetic permeability of all layers is assumed to be that of vacuum, i.e. μ_0. A global loss model is introduced by considering layer conductivities that are related to the layer permittivities by $\sigma_i(\gamma)=\gamma\varepsilon_i$, where the parameter γ is an arbitrary positive constant with units of reciprocal time. Setting γ equal zero defines a corresponding lossless host medium.

In the Laplace domain, the volume integral representation of the scattered field $\mathbf{E}^s$ is of the same form as in the frequency domain, i.e. it is of the same form as eq. (2.1). Thus, for any observation point $\boldsymbol{x}$ we have

$$\mathbf{E}^s(\boldsymbol{x},s;\gamma)=\iiint_{\substack{\text{target}\\\text{volume}}}\tilde{\mathbf{G}}(\boldsymbol{x},\boldsymbol{x}',s;\gamma)\mathbf{J}^s(\boldsymbol{x}',s;\gamma)\,dV' , \tag{2.87}$$

where, for clarity, the dependencies on the Laplace transform parameter s and the loss scaling factor γ have been indicated explicitly. Note that here $\tilde{\mathbf{G}}$ is no longer the half-space electric Green's tensor but the electric Green's tensor for the n-layered host medium. The objective of the transformation law is to express $\mathbf{E}^s(\boldsymbol{x},s;\gamma)$ in terms of $\mathbf{E}^s(\boldsymbol{x},s;0)$.

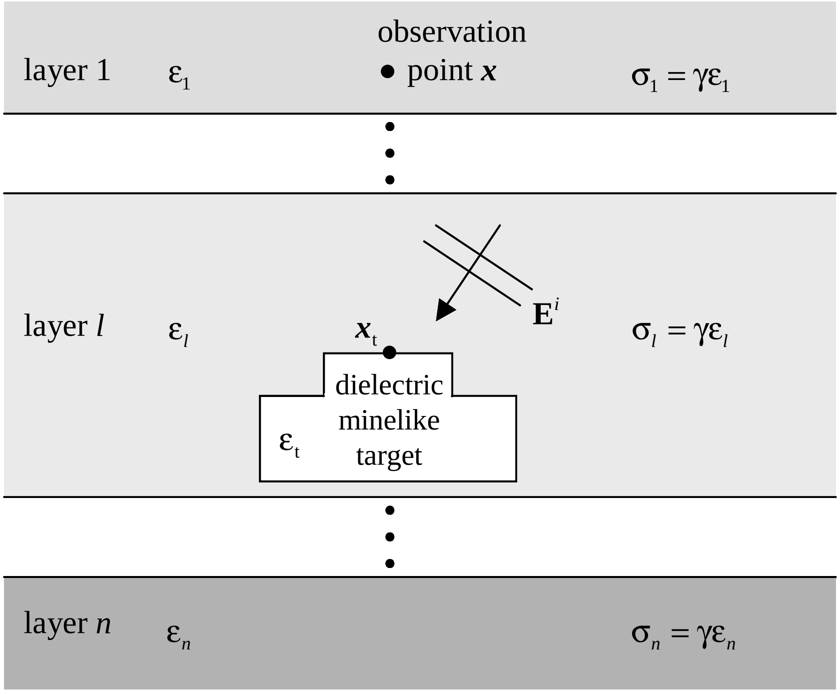

Figure 2.17: A homogeneous dielectric minelike target embedded in a layered host medium is illuminated by plane wave.

Derivation of the transformation law: Lossless to lossy host medium

The starting point of the derivation is the following relationship for the Green's tensor:

$$\tilde{\mathbf{G}}\left(\boldsymbol{x},\boldsymbol{x}',s;\gamma\right)=\frac{s}{(s^2+\gamma s)^{1/2}}\tilde{\mathbf{G}}\left(\boldsymbol{x},\boldsymbol{x}',(s^2+\gamma s)^{1/2};0\right)\ . \tag{2.88}$$

This relationship follows directly from the similarity between the lossless and the lossy electromagnetic field equations in the Laplace domain. The similarity may be found following a procedure analogous to the one put forth by De Hoop (1996) in his derivation of a transformation law between diffusion in a conductive medium and wave propagation in a corresponding lossless configuration.

The next step is to find a similar transformation for the scattering current $\mathbf{J}^s$. This can be achieved through the Born approximation which in the Laplace domain relates $\mathbf{J}^s$ to the plane wave incident field $\mathbf{E}^i$ according to

$$\begin{aligned}\mathbf{J}^s\left(\boldsymbol{x},s;\gamma\right)&=\left(s\Delta\varepsilon+\Delta\sigma(\gamma)\right)\ \mathbf{E}^i\left(\boldsymbol{x},s;\gamma\right)\\&=\left(s\Delta\varepsilon+\Delta\sigma(\gamma)\right)\mathrm{E}^i\left(\boldsymbol{x}_\mathrm{t},s;\gamma\right)\boldsymbol{p}_i e^{-\boldsymbol{i}k_l(s;\gamma)\boldsymbol{a}_i\boldsymbol{x}}\ ,\end{aligned} \tag{2.89}$$

where $\Delta\varepsilon=\varepsilon_\mathrm{t}-\varepsilon_l$ and $\Delta\sigma(\gamma)=-\sigma_l(\gamma)$ are the target permittivity and conductivity contrasts, $\boldsymbol{x}_\mathrm{t}$ denotes the target location, $\boldsymbol{p}_i$ and $\boldsymbol{a}_i$ are the unit vectors describing the polarization and the direction of propagation of the incident field, and

$$k_l\left(s;\gamma\right)=-\boldsymbol{i}(\mu_0\varepsilon_l)^{1/2}(s^2+\gamma s)^{1/2} \tag{2.90}$$

is the wavenumber of layer l.[11] Note that without loss of generality it has been assumed that the target is located at the origin of the coordinate system. Assuming further that $\boldsymbol{p}_i$ and $\boldsymbol{a}_i$ are independent of γ, the transformation for the scattering current is found to be

$$\mathbf{J}^s\left(\boldsymbol{x},s;\gamma\right)=\frac{s\Delta\varepsilon+\Delta\sigma(\gamma)}{(s^2+\gamma s)^{1/2}\Delta\varepsilon}\frac{\mathrm{E}^i\left(\boldsymbol{x}_\mathrm{t},s;\gamma\right)}{\mathrm{E}^i\left(\boldsymbol{x}_\mathrm{t},(s^2+\gamma s)^{1/2};0\right)}\mathbf{J}^s\left(\boldsymbol{x},(s^2+\gamma s)^{1/2};0\right)\ , \tag{2.91}$$

which is readily verified using eq. (2.89).

Substituting eqs. (2.88) and (2.91) into eq. (2.87) yields the wanted expression for the scattered field transformation:

$$\mathbf{E}^s\left(\boldsymbol{x},s;\gamma\right)=\frac{s^2+s\left(\dfrac{\Delta\sigma(\gamma)}{\Delta\varepsilon}\right)}{s^2+\gamma s}\frac{\mathrm{E}^i\left(\boldsymbol{x}_\mathrm{t},s;\gamma\right)}{\mathrm{E}^i\left(\boldsymbol{x}_\mathrm{t},(s^2+\gamma s)^{1/2};0\right)}\mathbf{E}^s\left(\boldsymbol{x},(s^2+\gamma s)^{1/2};0\right)\ . \tag{2.92}$$

An interesting way to look at this result is to introduce the vectorial transfer function

$$\mathbf{H}\left(\boldsymbol{x},s;\gamma\right)=\frac{\mathbf{E}^s\left(\boldsymbol{x},s;\gamma\right)}{\mathrm{E}^i\left(\boldsymbol{x}_\mathrm{t},s;\gamma\right)}\ , \tag{2.93}$$

---

[11] These Laplace domain expressions follow from their frequency-domain counterparts by simply substituting $\boldsymbol{i}\omega\rightarrow s$.

with which eq. (2.92) can be rewritten as

$$\mathbf{H}(\boldsymbol{x},s;\gamma)=\frac{s^2+s\left(\frac{\Delta\sigma(\gamma)}{\Delta\varepsilon}\right)}{s^2+\gamma s}\mathbf{H}\left(\boldsymbol{x},(s^2+\gamma s)^{1/2};0\right) . \tag{2.94}$$

We see that the transfer function for the lossy host medium ($\gamma>0$) is related to the transfer function for the corresponding lossless host medium ($\gamma=0$), in which the Laplace transform parameter s is replaced by $(s^2+\gamma s)^{1/2}$.

Equation (2.94) can be transformed to the time-domain using the Schouten-Van der Pol theorem in the theory of the Laplace transformation (Schouten, 1961, p. 124-126), which for a given transform pair $f(t)\leftrightarrow F(s)$ presents a general procedure for finding the time-domain counterpart of $F(\varphi(s))$, where $\varphi(s)$ is some suitable function of the Laplace transform parameter s. The resulting time-domain transformation law is

$$\mathbf{h}(\boldsymbol{x},t;\gamma)=\left(\partial_t^2+\left(\frac{\Delta\sigma(\gamma)}{\Delta\varepsilon}\right)\partial_t\right)\int_{\tau=0}^{\infty}U_{-1}(t,\tau;\gamma)\mathbf{h}(\boldsymbol{x},\tau;0)\,d\tau \tag{2.95}$$

where the kernel function U_{-1} is given by

$$U_{-1}(t,\tau;\gamma)=-\int_0^{\tau}U_0(t,\tau';\gamma)\,d\tau' \tag{2.96}$$

with

$$U_0(t,\tau;\gamma)=e^{-0.5\gamma t}I_0\left(0.5\gamma(t^2-\tau^2)^{1/2}\right)S(t-\tau) . \tag{2.97}$$

Here, I_0 denotes the modified Bessel function of the first kind and order zero and S is the Heaviside unit step function.

Equation (2.95) presents a transformation law relating the impulse response $\mathbf{h}(\boldsymbol{x},t;0)$ for the lossless host medium to the target impulse response $\mathbf{h}(\boldsymbol{x},t;\gamma)$ for the corresponding lossy host medium. In addition to being straightforward to implement on a computer, the transformation law has the following useful properties:

- It acts locally, i.e. its evaluation only requires knowledge of the impulse response $\mathbf{h}(\boldsymbol{x},t;0)$ at the particular observation point of interest.
- It is valid for all field regions (near-, intermediate-, and far-field).
- It is valid for arbitrary incidence and scattering directions.
- Its applicability is not limited to low conduction losses ($\sigma/(\varepsilon_0\omega)<1$), as is the case for the time-domain convolutional scattering model and the target impulse response models presented in section 2.1.

An example application of the transformation law is given in the following section.

2.4.2 FDTD example

To illustrate and affirm the derived transformation law, the axial backscattering response of a circular dielectric disk embedded in an unbounded homogeneous host medium was simulated by FDTD.

The simulations were carried out using the 3D FDTD modeling program developed by Mur (2001). As for the testing of the target characterization procedure in section 2.3, this required some minor modifications to Mur's total field absorbing boundary conditions (ABCs) (Mur, 1998) to allow modeling plane wave illumination of a target embedded in a lossy host medium. In this context, it is important to note that in principle Mur's ABC equations for lossless media equally apply to lossy media since they are only used to model wave propagation across the grid cells, which form the boundary of the computational domain, i.e. over a very short distance, where losses may be neglected. Consequently, as before, the modification only involved reevaluating the incident field terms in the ABCs. This, however, is where limitations as to the size of the losses are introduced since the evaluation ideally requires an analytic time-domain expression for the plane wave incident field, which only exists when the conduction losses are low. A possible work-around for this limitation is to analytically evaluate the incident field terms of the ABCs in the frequency-domain and then use the Fast Fourier Transform (FFT) to transform them to the time-domain. However, to keep things simple, for the present example the ABCs were only modified for the case of low conduction losses.

The disk was given a radius of 5 cm, a height of 4 cm, and a relative permittivity of 5.0. The host medium relative permittivity was set to 6.25 and for the lossy case a conductivity of 20 mS/m was considered. This corresponds to a γ of 0.36 ns^{-1}. For the incident plane wave, a linear polarization in the *x*-direction and a waveform equal to a Ricker wavelet (2$^{\text{nd}}$ derivative of a Gaussian pulse) with a peak amplitude frequency of 650 MHz was selected. Accordingly, only the *x*-component of the scattered field was analyzed. Note that in selecting the model parameters an attempt was made to satisfy both the phase criterion of eq. (2.5) underlying the Born approximation as well as the low conduction loss criterion. The incident fields at the disk location were obtained by simply repeating the simulations without the disk.

Figure 2.18 shows the simulated target response at a distance of 50 cm above the disk for both the lossless and the lossy host medium. Note that the losses do not just result in a decrease in amplitude but also a change in pulse shape. Since for low conduction losses the velocity and attenuation are frequency independent, the difference in pulse shape is not a result of dispersive wave propagation from the disk to the observation but can be attributed entirely to a difference in the target impulse response.

To check whether the transformation law can predict these changes in the target response, we first estimate the axial impulse response $\mathrm{h}(\boldsymbol{x},t;0)$ on the right-hand side of eq. (2.95). To do this, we make use of the fact that the target impulse response of the disk is the same in an unbounded host medium than when it is buried in the ground (see section 2.1.4), i.e. the target impulse response model of eq. (2.23) consisting of two differentiation operators is applicable. Thus, $\mathrm{h}(\boldsymbol{x},t;0)$ may be estimated by following the subset selection deconvolution procedure described in section 2.2.4 using the same parameterization as if the disk was buried in the ground, i.e. eq. (2.81). The resulting impulse response $\mathrm{h}(\boldsymbol{x},t;0)$ is shown in figure 2.19, where this time the subset selection was formulated using discrete representations for the differentiation operators, as suggested on p. 45. Hence, rather than obtaining two spikes, the estimated impulse response consists of two discrete differentiation operators, the first of which corresponds to backscatter from the top of the disk and the second to backscatter from the bottom of the disk.

Evaluation of the integral in eq. (2.95) for the estimated impulse response $\mathrm{h}(\boldsymbol{x},t;0)$ gives the time function shown in figure 2.20. The result indicates that the integration with the kernel function U_{-1} is effectively equivalent to a double integration followed by a multiplication with an exponential decay function, which agrees well with the previously derived lossy and lossless target impulse response models of eqs. (2.19) and (2.20).

Subsequent differentiation of the integration result as prescribed in eq. (2.95) yields the transformed impulse response $\mathrm{h}(\boldsymbol{x},t;\gamma)$ shown in figure 2.21.

Finally, convolving the transformed impulse response with the incident field in the lossy host medium produces the transformed target response of figure 2.22. For comparison, the simulated target response for the lossy host medium is displayed as well, showing that the transformation law accurately predicts the changes in the target response caused by the losses.

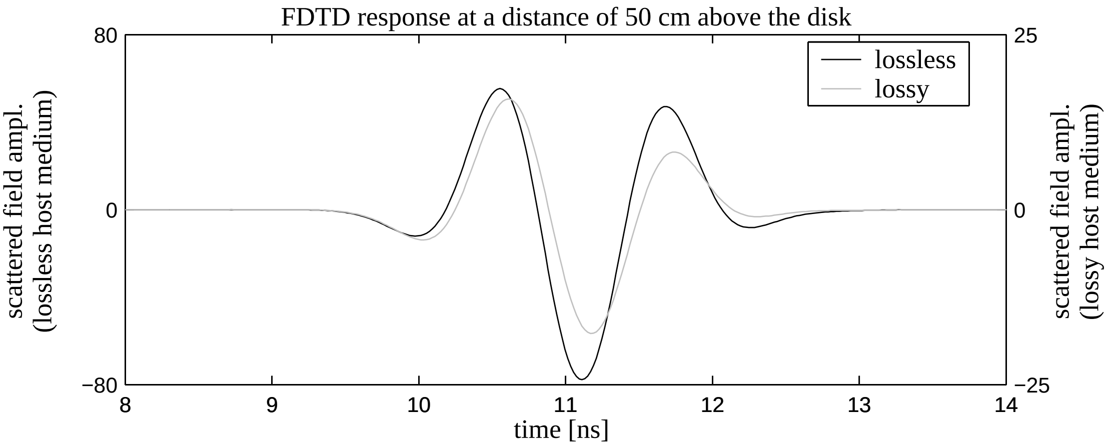

Figure 2.18: Simulated axial response of the disk in the lossless ($\varepsilon_r = 6.25$) and the lossy ($\varepsilon_r = 6.25$, $\sigma = 20$ mS/m) host medium.

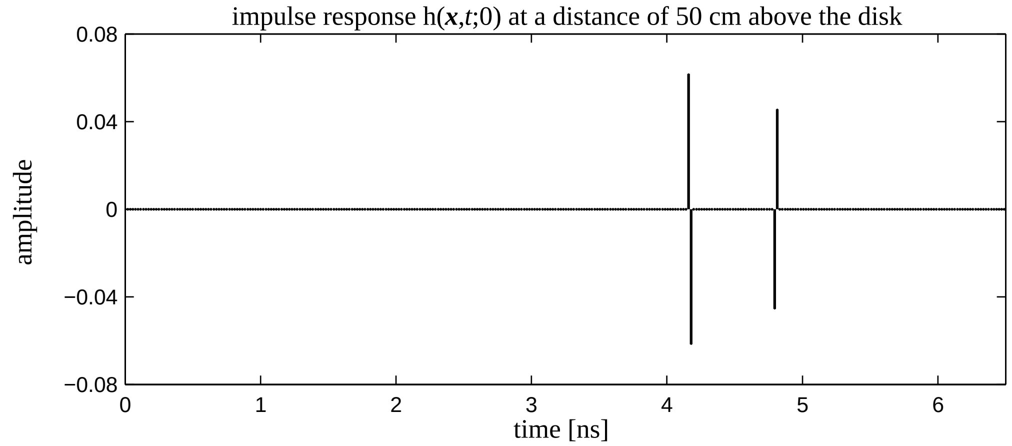

Figure 2.19: Axial impulse response $\mathrm{h}(\boldsymbol{x},t;0)$ for the lossless host medium ($\varepsilon_r = 6.25$).

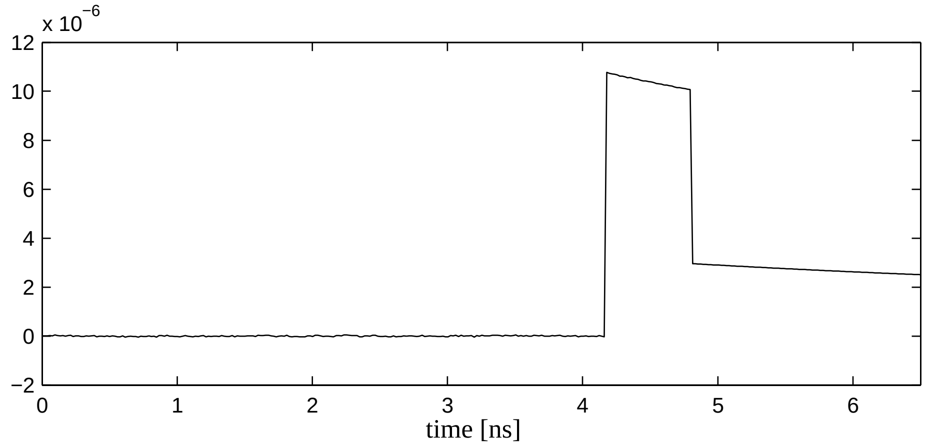

Figure 2.20: Evaluation of the integral in eq. (2.95) for the impulse response of figure 2.19.

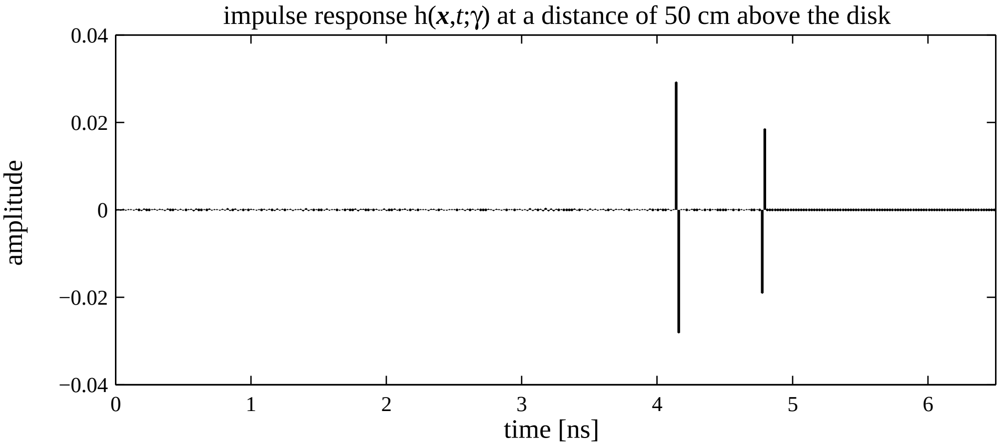

Figure 2.21: Axial impulse response $h(\boldsymbol{x},t;\gamma)$ for the lossy host medium ($\varepsilon_r = 6.25$, $\sigma = 20$ mS/m) as predicted by eq. (2.95) ($\gamma = 0.36$ ns^{-1}).

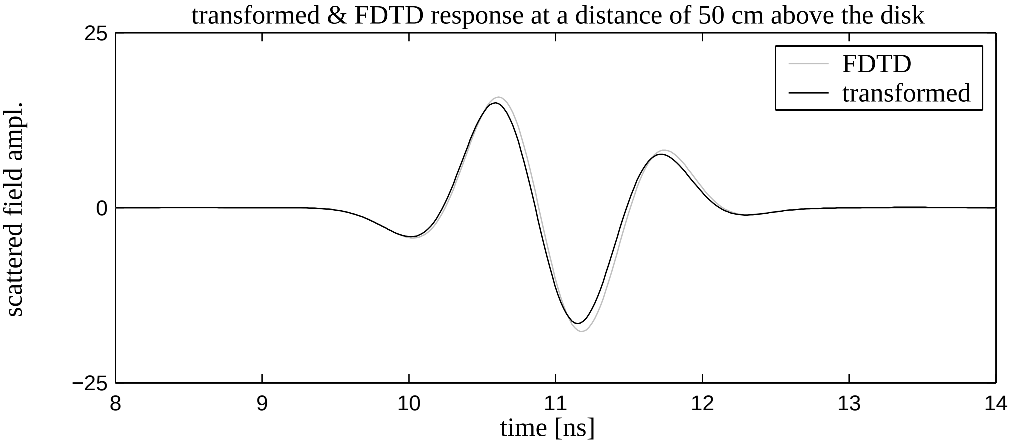

Figure 2.22: Transformed and simulated axial response of the disk in the lossy host medium ($\varepsilon_r = 6.25$, $\sigma = 20$ mS/m).

2.4.3 Some concluding remarks

Understanding the influence of soil properties on the target response of a buried landmine is very important for GPR landmine detection and identification. To this end, the presented transformation law describes how the time-domain response of a dielectric minelike target embedded in a lossless host medium is related to its time-domain response in a lossy host medium. The relationship is fairly simple and hence well suited to gain insight in how the target response changes as a result of losses. Nevertheless, the applicability of the presented transformation law is limited by a number of factors. First, the global conduction loss model is not readily applicable to a half-space host medium consisting of an air and a ground layer, since the model would also introduce some losses in air. And second, losses are to a great part associated with soil water, which also causes polarization losses and raises the real part of the permittivity, neither of which is modeled by the transformation law. Further complexity is introduced by the fact that wet soils are likely to be characterized by an inhomogeneous water distribution, which in turn results in an increased clutter level (Kovalenko and Yarovoy, 2003). These limitations underline the complexity of the landmine detection problem. Clearly, for a complete understanding of the problem, measurements of target responses for different soils remain indispensable.

2.5 Discussion

This chapter has laid the theoretical and conceptual foundation for the convolutional GPR modeling and the target identification approach described in this thesis. In this respect, three contributions of the material presented so far are instrumental. These are:

- *Convolutional models describing plane wave backscattering from a buried homogeneous minelike target*. In these models the scattering behavior of the target is described through a target transfer function/impulse response for which simple closed-form expressions in terms of target size, shape and electromagnetic contrast have been presented. Evaluation of these expressions for a circular disk lead to the interesting result that a minelike target of this shape differentiates the waveform of the incident field, i.e. its target impulse response consist of one or two differentiation operators, depending on whether the target is from metal or dielectric.
- *Subset selection deconvolution*. This time-domain algorithm constrains the deconvolution problem by assuming a sparse parameterization for the impulse response to be recovered, which is specific to the problem at hand. For the characterization of circular disk-shaped minelike targets, appropriate parameterizations follow from the derived target impulse response models. Doing so, subset selection deconvolution provides physical amplitude information and high temporal resolution, which is essential if the estimated impulse responses are to be related to target characteristics. Hence, for target characterization purposes, subset selection clearly outperforms deconvolution algorithms based on Wiener filtering or ridge regression, which were shown to produce smeared impulse responses and rely on a regularization parameter whose optimal choice is non-obvious.
- *A target characterization procedure for buried circular disk-shaped minelike targets*. The procedure uses subset selection deconvolution to estimate an impulse response, which is inverted for target characteristics on the basis of the derived

time-domain convolutional scattering model. Two types of inversions are possible: inversion for target size or, in the case of a dielectric minelike target, inversion for material properties.

The validity of the convolutional scattering models and the subset selection deconvolution based target characterization procedure has been confirmed by the FDTD simulation results. More specifically, the FDTD results demonstrated that, despite their simplicity, the convolutional scattering models adequately describe

- the target impulse response of a homogeneous circular disk-shaped minelike target and its relation to target size and contrast
- the dependency of the target response magnitude on target depth and observation height.

The FDTD results further showed that the proposed target characterization procedure is in principle able to estimate the outer dimensions of a homogeneous circular disk-shaped minelike target with millimeter accuracy ($\text{error} < 0.5\,\text{cm}$) or, given that the target is dielectric, produce very accurate estimates of its relative permittivity ($\text{error} < 11\,\%$ with respect to the permittivity contrast).

A fundamental problem, which has been encountered, is that for a dielectric minelike target the inversion of the impulse response obtained by subset selection deconvolution is inherently unresolved. As a consequence, the inversion for target size is only possible after specification of target material properties and vice versa. This raises the question whether target characterization based on no more than the vertical backscattering target response is a valid approach and whether including target responses for different incident/scattering directions in the inversion will be able to resolve target size and contrast. To find answers to these questions, imagine a *B-scan*[12] of GPR data acquired over a buried dielectric target with the antennas on the ground. In the B-scan the target will be visible as a diffraction hyperbola and it is intuitively clear that the arrival times along the hyperbola carry information on the size of the target and its depth. This fact is sometimes used to determine the radius of a buried pipeline from GPR data. Hence, in this scenario it is reasonable to assume that an inversion, which considers the entire diffraction hyperbola, will be able to resolve the size of the target and its contrast. Now let us elevate the antennas above the ground. In this case, the vertical becomes the main direction of propagation in the ground simply because at the ground surface the radiated wave is refracted towards and the scattered wave away from the vertical. As a result, the arrival times along the diffraction hyperbola become primarily a function of the depth of the target, so that target size and contrast are again practically unresolved by the GPR data. From this imaginary experiment, it becomes clear that inversion of GPR data acquired with the antennas above the ground, as is the case in landmine detection, is an ill-posed inverse problem even if target responses for different incident/scattering directions are considered. In fact, as will be demonstrated by experimental data in chapter 5, not just the arrival times but also the shape of the target response, which is measured as the antenna system is moved away from the target, carries very little additional target information. To deal with this ill-posedness, the following line of reasoning is suggested:

> Start by assuming that the detected target is an AP landmine, which tells us which material properties or target sizes to expect. Then fix one of these sets of target characteristics and invert for the other. If the inferred characteristics match those of an AP landmine, than the detected target should be treated as potentially dangerous.

---

[12] The term *B-scan* refers to a set of A-scans (see p. 6) measured along a line.

This line of reasoning will be illustrated in section 5.3, where it is used to identify Teflon disks of a prescribed size from GPR data.

In the following two chapters, the theory and concepts introduced in this chapter will be extended to account for internal mine structure (chapter 3) and the radar hardware (chapter 4), both of which are essential for application of the scattering models and the target characterization procedure to GPR data.

CHAPTER 3

SCATTERING FROM A MINELIKE TARGET WITH INTERNAL STRUCTURE

An important aspect that needs to be considered when studying scattering from plastic cased landmines is their internal structure. Each type of landmine has its own operation principle and hence internal structure varies. Nevertheless, certain common characteristics may be identified. For a pressure actuated *blast mine*[1], which is the most common type of antipersonnel mine, the internal structure may roughly be subdivided into the following four components: the casing, the explosives, the fuse, and air. Since plastics have permittivities similar to those of explosives (Von Hippel, 1954; Bruschini *et al*, 1998), from an electromagnetic point of view, the casing and the explosives may be considered as one. The explosives include the main charge, which is set off by a smaller amount of explosive called the detonator. Sometimes the firing train also contains a booster charge to amplify the ignition by the detonator. Different types of fuse mechanisms exist, such as the mechanical pressure fuse or the chemical pressure fuse. Usually the fuse is the only component of a plastic cased landmine that contains parts of metal, however its metal content may be limited to no more than a small firing pin or a striker spring (Fortuny-Guasch *et al*, 2001). Furthermore, landmines contain air gaps, e.g. below a Belleville spring. As an example of internal mine structure, figure 3.1 shows an illustration of the inside of an *M14* landmine.

As a result of the internal structure, a plastic cased landmine cannot necessarily be approximated as a homogeneous dielectric target. Especially the presence of an air gap is said to amplify the target response when the mine is buried and hence should facilitate its detection with GPR. However, to my knowledge, the effect of internal structure on the target response of a landmine has never been analyzed quantitatively or expressed by models.

This chapter presents a generalization of the scattering theory for the homogeneous dielectric minelike target, developed in the previous chapter, to account for internal structure. The generalization is achieved by introducing an inclusion, which may be either dielectric or metal, for which a generalized contrast is defined based on the Rayleigh scattering approximation. This generalized contrast is then used with a Born-type linearization of the volume integral representation of the scattered field to give a convolutional model for backscattering from a buried dielectric minelike target with internal structure, including expressions for the target transfer function/impulse response. These models are then used to extend the target characterization procedure for homogeneous disk-shaped minelike targets, described in section 2.2.4, to targets with internal structure.

The chapter is organized as follows. In section 3.1, the convolutional model for backscattering from a buried dielectric minelike target containing an inclusion is derived. As for the homogeneous target, the derivation is first carried out in the frequency-domain and the resulting convolutional model and target transfer function are then transformed to the time-domain. As a special case, we shall again look at a circular dielectric disk, which is now considered with a thin air gap or a small piece of metal. Furthermore, as a side product of the derivation, expressions for the target transfer function/impulse response of a small metal sphere are presented. In section 3.2, the target impulse response model for the circular

---

[1] *Blast mines* are designed to injure a person’s foot or leg. Typically, they are triggered by stepping on a pressure plate, thereby initiating the fuse mechanism. Other types of mines are *bounding mines*, which propel themselves into the air and are designed to injure a person’s head or chest, and *fragmentation mines*, which release metal or glass fragments during explosion. (source: http://science.howstuffworks.com)

dielectric disk with an air gap/metal piece is used to specify an impulse response parameterization suitable for subset selection deconvolution based target characterization. In particular, the possibility to determine target size is discussed. The derived scattering models and the proposed target characterization procedure are then validated using FDTD data examples in section 3.3. Finally, in section 3.4, an overview of the main results achieved and a discussion of their significance to landmine identification are given. Note that since the material presented in this chapter builds on sections 2.1, 2.2.4, and 2.3 of the previous chapter, it is strongly recommended to read these sections first. In addition, most of the notation used in this chapter has been explained in the previous chapter, and hence shall not be redefined here.

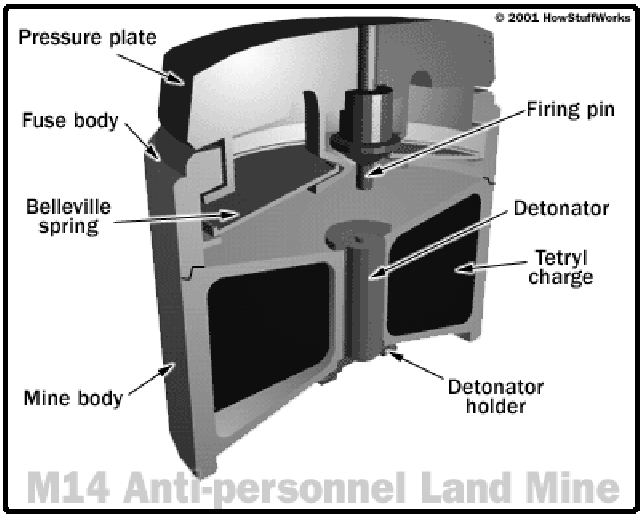

Figure 3.1: Internal structure of an *M14* landmine. (source: http://science.howstuffworks.com)

3.1 Convolutional Models for Backscattering from a Buried Dielectric Minelike Target with Internal Structure

Frequency-domain formulation

It is straightforward to generalize the previous results for the homogeneous dielectric minelike target to account for internal structure. The key to this generalization is the linear relationship between the volume scattering current $\mathbf{J}^s$ and the incident field $\mathbf{E}^i$, namely

$$\mathbf{J}^s(x) = \chi(x)\mathbf{E}^i(x) , \tag{3.1}$$

which has been assumed throughout this work, only that now the generalized contrast χ is considered spatially varying. As a result of the linear relationship expressed by eq. (3.1) and the linear form of the volume integral representation

$$\mathbf{E}^s(x) = \iiint\limits_{\text{target}} \tilde{\mathbf{G}}(x, x')\mathbf{J}^s(x')dV' , \tag{3.2}$$

the target can be thought of as being made up of non-interacting building blocks. Summation of the individual scattering responses of these building blocks gives the total target response.

To illustrate this concept, let us consider a dielectric minelike target made of a material with contrast χ_{t} having an inclusion associated with the contrast χ_{i} but otherwise homogeneous. Using eqs. (3.1) and (3.2), the total response of this target can be written as

$$\begin{aligned}\mathbf{E}^s(\boldsymbol{x}) &= \iiint\limits_{\text{target}} \tilde{\mathbf{G}}(\boldsymbol{x},\boldsymbol{x}')\chi(\boldsymbol{x}')\mathbf{E}^i(\boldsymbol{x}')dV' \\ &= \iiint\limits_{\text{target}\setminus\text{inclusion}} \tilde{\mathbf{G}}(\boldsymbol{x},\boldsymbol{x}')\chi_{\mathrm{t}}\mathbf{E}^i(\boldsymbol{x}')dV' + \iiint\limits_{\text{inclusion}} \tilde{\mathbf{G}}(\boldsymbol{x},\boldsymbol{x}')\chi_{\mathrm{i}}\mathbf{E}^i(\boldsymbol{x}')dV' \\ &= \iiint\limits_{\text{target}} \tilde{\mathbf{G}}(\boldsymbol{x},\boldsymbol{x}')\chi_{\mathrm{t}}\mathbf{E}^i(\boldsymbol{x}')dV' + \iiint\limits_{\text{inclusion}} \tilde{\mathbf{G}}(\boldsymbol{x},\boldsymbol{x}')(\chi_{\mathrm{i}}-\chi_{\mathrm{t}})\mathbf{E}^i(\boldsymbol{x}')dV' .\end{aligned} \tag{3.3}$$

The backslash operator is used to indicate omission. According to eq. (3.3) the target response is the sum of two responses: the response, which would be observed if the target had no inclusion and the response of the inclusion alone with the contrast being replaced by $(\chi_{\mathrm{i}}-\chi)$.

If the contrasts χ_{t} and χ_{i} are known, eq. (3.3) can be used to approximate the total target response. For the moment, let us assume that appropriate contrasts can be defined and apply eq. (3.3) to the case of plane wave backscattering from a buried dielectric minelike target with internal structure, as shown in figure 3.2. The configuration is identical to the one of figure 2.1 underlying the analysis of scattering from a homogeneous dielectric minelike target, except that now the target contains an inclusion of volume V_{i} at a distance l_{i} below the top surface of the target. Substituting

$$\mathbf{E}^i(\boldsymbol{x}') = \mathbf{E}^i(\boldsymbol{x}_{\mathrm{t}})e^{-\boldsymbol{i}k_1(z'-d)} \tag{3.4}$$

for the plane wave incident field $\mathbf{E}^i$ and using the far-field backscattering representation of the half-space electric Green's tensor $\tilde{\mathbf{G}}$ given by eq. (2.7), it is easy to show that eq. (3.3) leads to the familiar frequency-domain convolutional scattering model of eq. (2.10),

$$\mathbf{E}^s(\boldsymbol{x}) = \frac{T_{g\to a}\,\zeta(h,d)e^{-\boldsymbol{i}(k_0h+k_1d)}}{2\sqrt{\pi}(h+d)}\mathrm{H}_{\mathrm{t}}(\omega)\mathbf{E}^i(\boldsymbol{x}_{\mathrm{t}}) , \tag{3.5}$$

where now the target transfer function $\mathrm{H}_{\mathrm{t}}(\omega)$ is the sum of two terms:

$$\mathrm{H}_{\mathrm{t}}(\omega) = \mathrm{H}_{\mathrm{t}}^{\mathrm{hom.}}(\omega) + \mathrm{H}_{\mathrm{t}}^{\mathrm{incl.}}(\omega) \tag{3.6}$$

with

$$\mathrm{H}_{\mathrm{t}}^{\mathrm{incl.}}(\omega) = -\frac{\hat{z}_0}{2\sqrt{\pi}}(\chi_{\mathrm{i}}-\chi_{\mathrm{t}})V_{\mathrm{i}}\,e^{-\boldsymbol{i}2k_1l_{\mathrm{i}}} . \tag{3.7}$$

The term $\mathrm{H}_{\mathrm{t}}^{\mathrm{hom.}}(\omega)$ is simply the transfer function of the corresponding homogeneous dielectric minelike target, whereas the term $\mathrm{H}_{\mathrm{t}}^{\mathrm{incl.}}(\omega)$ is a transfer function accounting for the presence of the inclusion. Note that the approximations $\tilde{\mathbf{G}}(\boldsymbol{x},\boldsymbol{x}') \approx \tilde{\mathbf{G}}(\boldsymbol{x},\boldsymbol{x}_{\mathrm{i}})$ and $\mathbf{E}^i(\boldsymbol{x}') \approx \mathbf{E}^i(\boldsymbol{x}_{\mathrm{i}})$ have been made for all points $\boldsymbol{x}'$ within the inclusion, where $\boldsymbol{x}_{\mathrm{i}}$ refers to the location of the inclusion. Hence, eq. (3.7) is only valid for inclusions whose height is small compared to the wavelength λ of the incident field in the ground.

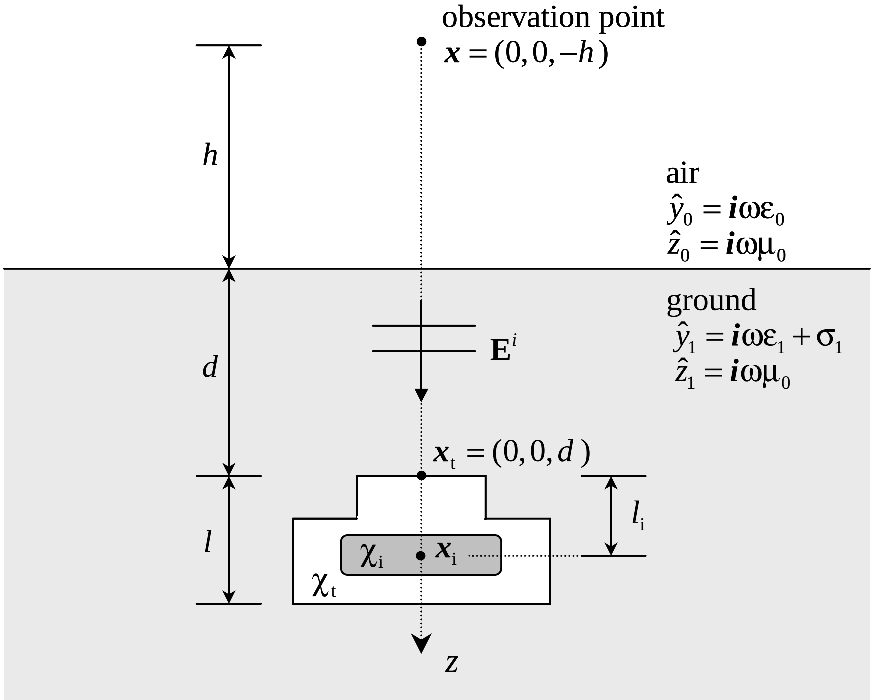

Figure 3.2: Plane wave backscattering from a buried dielectric minelike target (ε_t, μ_0) containing a dielectric (ε_i, μ_0) or metal (PEC) inclusion. The body and the inclusion of the target are associated with the generalized contrasts χ_t and χ_i, respectively.

Definition of the generalized contrasts of the target body and the inclusion

Of course now the question arises as to what are appropriate generalized contrasts for the target body and its inclusion. As demonstrated in chapter 2, the Born approximation adequately defines the generalized contrast of a homogeneous dielectric minelike target and allows for accurate estimations of its size and its permittivity. This suggests using the Born approximation to define the generalized contrast χ_t of the target body, i.e.

$$\chi_t = \Delta\hat{y}_t = \hat{y}_t - \hat{y}_1 \ . \tag{3.8}$$

Note that with this definition of χ_t, the “homogeneous” target transfer function $H_t^{\text{hom.}}(\omega)$ in eq. (3.6) is given by eq. (2.11).

The case for the generalized contrast χ_i of the inclusion, which may be either dielectric or metal, is less straightforward. The reason for this is that eq. (3.1) describes a volume current distribution and hence does not lend itself naturally to treat a metal inclusion. An exception is the case of a small metal sphere (or spherical inclusion for that matter) for which a generalized contrast can be derived using the Rayleigh scattering approximation. While strictly speaking this contrast, which hereinafter will be referred to as the Rayleigh contrast, only applies to spherical metal inclusions, it does provide a physically motivated definition of χ_i even when the inclusion is non-spherical. Another useful property of the Rayleigh contrast is that it may also be derived for a small dielectric sphere, allowing for a unified treatment of the dielectric and the metal inclusion.

The derivation of the Rayleigh contrasts proceeds as follows. Consider a small dielectric or metal sphere (PEC), respectively, with radius a embedded in an unbounded host medium with admittivity $\hat{y}_1 = \boldsymbol{i}\omega\varepsilon_1 + \sigma_1$ and impedivity $\hat{z}_1 = \boldsymbol{i}\omega\mu_0$. The sphere is illuminated by a plane wave propagating in the z-direction and polarized in the x-direction. Because the sphere is very small ($a < 0.1\,\lambda$) it behaves like a secondary point source. The x-directed incident electric field induces an x-directed electric dipole moment Il, whereas for a metal sphere the y-directed incident magnetic field induces a y-directed magnetic dipole moment Kl in addition to the x-directed electric dipole moment Il. Following Kong (1986, p. 482-485), the dipole moments can be determined by enforcing boundary conditions on the surface of the sphere. Once the dipole moments are known, the scattered field is obtained from the radiation equations for electric and magnetic dipoles. Doing so, the backscattered electric field in the far-field region of the sphere is found to be

$$\mathbf{E}^s(\boldsymbol{x}) = \frac{\Delta\hat{y}_\mathrm{s}}{\Delta\hat{y}_\mathrm{s} + 3\hat{y}_1} k_1^2 a^3 \frac{e^{-\boldsymbol{i}k_1 r_\mathrm{s}}}{r_\mathrm{s}} \mathbf{E}^i(\boldsymbol{x}_\mathrm{s}) \tag{3.9}$$

for the case of a dielectric sphere and

$$\mathbf{E}^s(\boldsymbol{x}) = \frac{3}{2} k_1^2 a^3 \frac{e^{-\boldsymbol{i}k_1 r_\mathrm{s}}}{r_\mathrm{s}} \mathbf{E}^i(\boldsymbol{x}_\mathrm{s}) \tag{3.10}$$

for the case of a metal sphere. In both equations r_s is the distance between the observation point $\boldsymbol{x}$ and the location $\boldsymbol{x}_\mathrm{s}$ of the center of the sphere. Furthermore, $\Delta\hat{y}_\mathrm{s} = \hat{y}_\mathrm{s} - \hat{y}_1$ is used to denote the admittivity contrast between the dielectric sphere and the host medium. On the other hand, by analogy to the analysis of a minelike target in an unbounded host medium discussed in section 2.1.4, from the volume integral representation of the scattered field we find that the backscattered electric field in the far-field region of a small sphere with a generalized contrast χ_s is given by

$$\mathbf{E}^s(\boldsymbol{x}) = -\hat{z}_1 \frac{e^{-\boldsymbol{i}k_1 r_\mathrm{s}}}{4\pi r_\mathrm{s}} \chi_\mathrm{s} \left(\frac{4}{3}\pi a^3 \right) \mathbf{E}^i(\boldsymbol{x}_\mathrm{s}) \; . \tag{3.11}$$

Equating eq. (3.11) with eq. (3.9), under consideration of $k_1 = (-\hat{z}_1\hat{y}_1)^{1/2}$, then yields the Rayleigh contrast of a dielectric sphere, which is

$$\chi_\mathrm{s} = \Delta\hat{y}_\mathrm{s} \frac{3\hat{y}_1}{\Delta\hat{y}_\mathrm{s} + 3\hat{y}_1} \; . \tag{3.12}$$

Likewise, by equating eq. (3.11) with eq. (3.10), the Rayleigh contrast of a metal sphere is found to be

$$\chi_\mathrm{s} = \frac{9}{2}\hat{y}_1 \; . \tag{3.13}$$

Interestingly, the Rayleigh contrast of a dielectric sphere equals the generalized contrast of the modified Born approximation given by eq. (2.4), although the latter is derived using an entirely different procedure, namely from solving the volume integral equation for the total electric field within a point scatterer (Van der Kruk, 2001, p. 87-90).

Based on the Rayleigh contrasts of eqs. (3.12) and (3.13), the generalized contrast χ_i of the inclusion may then be defined as

$$\chi_{\mathrm{i}} = \begin{cases} \Delta\hat{y}_{\mathrm{i}} \dfrac{3\hat{y}_1}{\Delta\hat{y}_{\mathrm{i}} + 3\hat{y}_1} & \text{for a dielectric inclusion} \\ \dfrac{9}{2}\hat{y}_1 & \text{for a metal inclusion .} \end{cases} \tag{3.14}$$

This completes the frequency-domain analysis of backscattering from a buried minelike target with internal structure. Before proceeding to the analysis in the time-domain, let us quickly write out the far-field backscattering target transfer function/impulse response of a small metal sphere embedded in an unbounded host medium, which shall be used in the analysis of some of the experimental data in chapter 5. The transfer function of the sphere follows immediately from substituting the Rayleigh contrast of eq. (3.13) into eq. (3.11) and comparing the resulting expression with the full-space convolutional scattering model of eq. (2.47), yielding

$$\mathbf{H}_{\mathrm{t}}(\omega) = \frac{9k_1^2}{4\sqrt{\pi}} V_{\mathrm{s}} \ , \tag{3.15}$$

where V_{s} denotes the volume of the sphere. Inverse Fourier transformation of eq. (3.15) gives the target impulse response

$$\mathbf{h}_{\mathrm{t}}(\omega) = -\frac{9}{4\sqrt{\pi} v_1^2} V_{\mathrm{s}}\, \ddot{\delta}(t) \ , \tag{3.16}$$

where $\ddot{\delta}(t)$ denotes the 2nd derivative of the delta function, i.e. it is a double differentiation operator. As usual, to make the inverse Fourier transformation tractable, the host medium has been assumed lossless. Looking at eq. (3.16), three interesting observations can be made:

- Under the Rayleigh approximation, **a small metal sphere differentiates the waveform of the incident field twice**.
- The magnitude of the metal sphere's impulse response is proportional to its volume V_{s}. Hence, a small change in radius can lead to significant increases in the magnitude of the sphere's response.
- The magnitude of the metal sphere's impulse response is inversely proportional to the square of the wave velocity v_1 in the host medium. Accordingly, the magnitude of the sphere's impulse response is smallest when the host medium is air, i.e. when $v_1 = c$. Note that this phenomena is a direct result of the Rayleigh contrast χ_{s} being proportional to the permittivity of the host medium, as indicated by eq. (3.13).

Time-domain formulation

Let us now look at backscattering from a buried minelike target with internal structure in the time-domain. All this requires is inverse Fourier transformation of eqs. (3.5)-(3.7), where the generalized contrasts χ_{t} and χ_{i} have been replaced by those of eqs. (3.8) and (3.14). For a lossless ground, this transformation is readily carried out and therefore here only the results shall be summarized:

$$\mathbf{e}^s(\boldsymbol{x},t) = \frac{T_{g\to a}\,\zeta(h,d)}{2\sqrt{\pi}(h+d)} \delta\left(t - \frac{h}{c} - \frac{d}{v_1}\right) \otimes \mathrm{h}_{\mathrm{t}}(t) \otimes \mathbf{e}^i(\boldsymbol{x}_{\mathrm{t}},t) \tag{3.17}$$

in which

$$\mathrm{h}_{\mathrm{t}}(\omega)=\mathrm{h}_{\mathrm{t}}^{\mathrm{hom.}}(\omega)+\mathrm{h}_{\mathrm{t}}^{\mathrm{incl.}}(\omega)\ , \tag{3.18}$$

where the “homogeneous” target impulse response $\mathrm{h}_{\mathrm{t}}^{\mathrm{hom.}}(\omega)$ given by eq. (2.20) and

$$\mathrm{h}_{\mathrm{t}}^{\mathrm{incl.}}(\omega)=-\frac{1}{2\sqrt{\pi}c^2}\xi V_{\mathrm{i}}\ddot{\delta}\left(t-2l_{\mathrm{i}}/v_1\right)\ . \tag{3.19}$$

with

$$\xi=\begin{cases}\Delta\varepsilon_{r,\mathrm{i}}\dfrac{3\varepsilon_{r,1}}{\Delta\varepsilon_{r,\mathrm{i}}+3\varepsilon_{r,1}}-\Delta\varepsilon_{r,\mathrm{t}} & \text{for a dielectric inclusion}\\[2ex] \dfrac{9}{2}\varepsilon_{r,1}-\Delta\varepsilon_{r,\mathrm{t}} & \text{for a metal inclusion .}\end{cases} \tag{3.20}$$

Here, $\Delta\varepsilon_{r,\mathrm{t}}=\varepsilon_{r,\mathrm{t}}-\varepsilon_{r,1}$ and $\Delta\varepsilon_{r,\mathrm{i}}=\varepsilon_{r,\mathrm{i}}-\varepsilon_{r,1}$ refer to the relative permittivity contrasts of the target and the inclusion with respect to the ground.

We see that, as a result of the inclusion, the target impulse response is simply augmented by an additional term $\mathrm{h}_{\mathrm{t}}^{\mathrm{incl.}}(\omega)$ describing the impulse response of the inclusion and consisting of one double differentiation operator. In other words, the inclusion differentiates the waveform of the incident field twice, just as a small metal sphere does. The magnitude of the impulse response of the inclusion is proportional to its volume V_{i} and a factor ξ, which is a measure of the difference in contrast between the inclusion and the target body.

Target impulse response of a circular dielectric disk containing a thin air gap or a small piece of metal

The analysis to this point is general and applies to any target shape and any type of inclusion. As an important special case, let us approximate the target impulse response of a circular dielectric disk having a constant cross-section S_{xy}, which for the homogeneous target case has been studied extensively in chapter 2 and will now be considered with a thin air gap or a small piece of metal, respectively, both of which are practically always present in landmines.

The target impulse response $\mathrm{h}_{\mathrm{t}}(t)$ follows immediately from previous results, since we may adopt eq. (2.23) for the “homogeneous” target impulse response $\mathrm{h}_{\mathrm{t}}^{\mathrm{hom.}}(\omega)$. Thus, from eqs. (3.18)-(3.20), we find

$$\mathrm{h}_{\mathrm{t}}(t)=-\frac{v_{\mathrm{t}}^{eff}}{4\sqrt{\pi}c^2}\Delta\varepsilon_{r,\mathrm{t}}S_{xy}\left(\dot{\delta}(t)-\Gamma\dot{\delta}\left(t-2l/v_{\mathrm{t}}^{eff}\right)\right)-\frac{1}{2\sqrt{\pi}c^2}\xi V_{\mathrm{i}}\ddot{\delta}\left(t-2l_{\mathrm{i}}/v_{\mathrm{t}}^{eff}\right), \tag{3.21}$$

with

$$\xi=\begin{cases}\left(1-\varepsilon_{r,1}\right)\dfrac{3\varepsilon_{r,1}}{\left(1-\varepsilon_{r,1}\right)+3\varepsilon_{r,1}}-\Delta\varepsilon_{r,\mathrm{t}} & \text{for a thin air gap}\\[2ex] \dfrac{9}{2}\varepsilon_{r,1}-\Delta\varepsilon_{r,\mathrm{t}} & \text{for a small piece of metal.}\end{cases} \tag{3.22}$$

Note that the phenomenological modifications, which had been introduced to the impulse response of a homogeneous circular dielectric disk, are also used here and have been extended to the impulse response $\mathrm{h}_{\mathrm{t}}^{\mathrm{incl.}}(\omega)$ of the air gap/metal part by replacing v_1 in eq. (3.19) by an effective target velocity v_{t}^{eff}.

An important result is that the introduction of a thin air gap or a small piece of metal did not change the overall simple form of the target impulse response. It consists of two single differentiation operators describing the backscattering from the top and the bottom of the disk, and one double differentiation operator describing the backscattering from the air gap/metal piece. Consequently, the impulse response is still suitable for use with subset selection deconvolution (recall the two applicability criteria put forth in section 2.2.3). This fact shall be used in the following section to develop a deconvolution based target characterization procedure for circular disk-shaped minelike targets with internal structure.

3.2 Deconvolution and Target Characterization

The time-domain convolutional scattering model of eq. (3.17) and the target impulse response model of eq. (3.21) can be used together with subset selection deconvolution to characterize a buried circular disk-shaped minelike target with internal structure. All this requires is a simple extension of the target characterization procedure for homogeneous minelike targets, which was put forth in section 2.2.4.

Again, the primary processing step is the use of subset selection to deconvolve the incident field $\mathrm{e}^{i}(\boldsymbol{x}_{\mathrm{t}},t)$ from the backscattered field $\mathrm{e}^{s}(\boldsymbol{x},t)$, thereby yielding an impulse response $\mathrm{h}(t)$, which satisfies the convolutional model of eq. (2.80) and may be related to target characteristics. As for the homogeneous minelike targets, the parameterization of $\mathrm{h}(t)$ for the subset selection deconvolution is found from substituting the target impulse response model into the convolutional scattering model and comparing the resulting equation with eq. (2.80). The parameterization thus obtained is

$$\mathrm{h}(t)=\mathrm{h}_1\dot{\delta}(t-\tau_1)+\mathrm{h}_2\dot{\delta}(t-\tau_2)+\mathrm{h}_3\ddot{\delta}(t-\tau_3) \tag{3.23}$$

where

$$\mathrm{h}_1=-\frac{T_{g\to a}\zeta(h,d)}{8\pi(h+d)}\frac{v_{\mathrm{t}}^{eff}}{c^2}\Delta\varepsilon_{r,\mathrm{t}}S_{xy}\ , \tag{3.24a}$$

$$\tau_1=\frac{h}{c}+\frac{d}{v_1}\ , \tag{3.24b}$$

$$\mathrm{h}_2=-\Gamma\mathrm{h}_1\ , \tag{3.24c}$$

$$\tau_2=\tau_1+\frac{2l}{v_{\mathrm{t}}^{eff}}\ , \tag{3.24d}$$

$$\mathrm{h}_3=-\frac{T_{g\to a}\zeta(h,d)}{4\pi(h+d)}\frac{1}{c^2}\xi V_{\mathrm{i}}\ , \tag{3.24e}$$

$$\tau_3 = \tau_1 + \frac{2 l_\mathrm{i}}{v_\mathrm{t}^{eff}} \; . \tag{3.24f}$$

Note that eqs. (3.24a) through (3.24d) are identical to eqs. (2.82a) through (2.82d) and have been included here for the sake of completeness and clarity.

The subset selection deconvolution for this parameterization may be implemented by considering two convolution matrices $\dot{\mathbf{X}}$ and $\ddot{\mathbf{X}}$ created from the 1st and the 2nd time derivative of the incident field $\mathrm{e}^{i}\left(\boldsymbol{x}_\mathrm{t}, t\right)$, respectively. The subset selection is then formulated as the minimization

$$\min_{i,j,k}\left(\min_{\left[\begin{smallmatrix}\mathrm{h}_1\\ \mathrm{h}_2\\ \mathrm{h}_3\end{smallmatrix}\right]} \left\| \left[\dot{\mathbf{x}}_i \; \dot{\mathbf{x}}_j \; \ddot{\mathbf{x}}_k\right] \begin{bmatrix}\mathrm{h}_1\\ \mathrm{h}_2\\ \mathrm{h}_3\end{bmatrix} - \mathbf{y}\right\|^2 \right) \qquad \begin{matrix} 1\le i<j\le N \\ i<k<j\end{matrix} \tag{3.25}$$

where $\dot{\mathbf{x}}_n$ and $\ddot{\mathbf{x}}_n$ ($n = 1,\ldots,N$) refer to the column vectors of $\dot{\mathbf{X}}$ and $\ddot{\mathbf{X}}$, and $\mathbf{y}$ is the vector representation of the scattered field $\mathrm{e}^{s}\left(\boldsymbol{x}, t\right)$. Note that since now the subset selection deconvolution involves three non-zero impulse response coefficients, in contrast to one or two for the homogeneous minelike targets, the selection by permutation has become computationally expensive and hence does no longer lend itself to real-time data processing.

Once the impulse response parameters have been estimated by subset selection deconvolution, they can be inverted for target size using eqs. (3.24a)-(3.24f). The inversion for target size proceeds in essentially the same way as for the homogeneous dielectric minelike target, in that generic material properties of the target to be characterized need to be specified, i.e. the relative permittivity $\varepsilon_{r,\mathrm{t}}$ of the target body and the effective target velocity v_t^{eff}. The specification of these properties then permits estimation of the target cross-section S_{xy}, the target height *l*, the inclusion volume V_i, and the position of the inclusion as specified by the distance l_i. Note from eqs. (3.22) and. (3.24e) that the inclusion type may be derived from the sign of the impulse response coefficient h_3, i.e. $\mathrm{h}_3 > 0$ for an air gap and $\mathrm{h}_3 < 0$ for a small piece of metal. In principle, it is also possible to invert the impulse response parameters for material properties, e.g. the relative permittivity $\varepsilon_{r,\mathrm{i}}$ of a dielectric inclusion. However since this would require specification of the inclusion volume in addition to the outer dimensions of the target, all of which cannot be specified generically, this does not seem like a sensible thing to do and hence has not been attempted in this work.

3.3 3D Finite-Difference Time-Domain (FDTD) Simulation Results and Verification

To verify the derived scattering models and to test the target characterization procedure, the FDTD simulation of *TNT Disk 1* described in section 2.3 was repeated, first with a thin circular air gap and then with a small cubical metal inclusion. The air gap (figure 3.3a) had a radius of 4 cm, a thickness of 1 cm and was included at a distance of $l_\mathrm{i} = 1.5$ cm below the top surface of the disk. The cubical metal inclusion (figure 3.3b), modeled as a PEC, had a side length of 1 cm and was considered at a distance of $l_\mathrm{i} = 0.5$ cm. The simulations were carried out under exactly the same conditions as those for the homogeneous *TNT Disk 1* (see table 2.1), except that now only a target depth of 10 cm was considered.

The target responses that resulted from these simulations are shown in figure 3.4, where the homogeneous target response of *TNT Disk 1* has been included as a reference for comparison. We see that the air gap leads to a strong increase in the magnitude of the target response and also changes its shape. In contrast, with the small metal inclusion the magnitude remains practically the same and only a very small change in the shape of the target response is observed.

It is convenient first to analyze just the effect of the inclusions. For this purpose, the responses of the air gap and the metal inclusion were isolated from the total target responses by simply subtracting the homogeneous target response. The isolated responses were then fit with the 2nd derivative of the incident Ricker wavelet, yielding independent estimates of the impulse response parameters h_3 & τ_3 without having to concurrently estimate the other four parameters of the impulse response $\mathrm{h}(t)$. The impulse response parameters so obtained are listed in table 3.1. For both types of inclusions the data fit between the predicted and the simulated response was good and is shown in figure 3.5. The good data fit confirms that an inclusion differentiates the waveform of the incident field twice, as predicted by the inclusion impulse response model of eq. (3.19). The impulse response parameters of table 3.1 were inverted for the inclusion volume V_i and the distance l_i using eqs. (3.24e) and (3.24f), the results of which are listed in table 3.2. For the inversion, the material properties of *TNT Disk 1* were specified as $\varepsilon_{r,\mathrm{t}} = 2.8$ and $v_\mathrm{t}^{eff} = 16.6\ \mathrm{cm/ns}$, which are the same as those used in chapter 2. The relatively good agreement between the estimated and the true inclusion volumes $(\mathrm{error} < 15\ \%)$ indicates that the Rayleigh contrast of eq. (3.14) is well suited to define the generalized contrast of the air gap and that of the metal inclusion. Furthermore, we observe that the locations of the inclusions have been recovered with millimeter accuracy.

Let us now consider the full target characterization procedure. The results of applying subset selection deconvolution to the total target responses are listed in table 3.3 and the corresponding data fits are shown in figure 3.6. As may be expected from the previous results, the data fit is good and demonstrates that the axial response of a buried circular disk-shaped minelike target containing an air gap or a metal inclusion is adequately modeled by an impulse response as in eq. (3.23), consisting of two single differentiation operators and one double differentiation operator. Ideally, the impulse response parameters h_1 & τ_1 and h_2 & τ_2 should equal those estimated from the homogeneous target response of *TNT Disk 1*, which are listed in table 2.2 and have been repeated in table 3.3 for easy comparison. Moreover, the parameters h_3 & τ_3 should equal those in table 3.1 estimated from the response of the air gap and the response of the metal inclusion alone. Doing the comparison, we see that the times τ_1, τ_2 and τ_3 at which the differentiation operators occur have been estimated well. The impulse response coefficients h_1, h_2 and h_3, however, deviate from their expected values, although their sizes are still of the same order of what they should be. In general, an increase in h_1 is observed, which is compensated for by commensurate changes of h_2 and h_3. This “redistribution” of energy points to the fact that introducing a third degree of freedom in the subset selection brought back some of the ill-posedness of the deconvolution problem. In other words, there are a number of solutions that all give rise to more or less the same error between the predicted and the actual target response.

Table 3.4 lists the results of inverting the impulse response parameters of table 3.3 for target size. As before, the material properties of *TNT Disk 1* were specified as $\varepsilon_{r,\mathrm{t}} = 2.8$ and $v_\mathrm{t}^{eff} = 16.6\ \mathrm{cm/ns}$. The inversion results demonstrate that in the presence of a thin air gap or a small metal inclusion, it is still possible to recover the outer dimensions of *TNT Disk 1* with reasonable accuracy $(\mathrm{error} < 1\ \mathrm{cm})$. The abovementioned deficiency of the subset selection deconvolution primarily led to a degradation of the estimation of the inclusion volume (error $<$ 35 %).

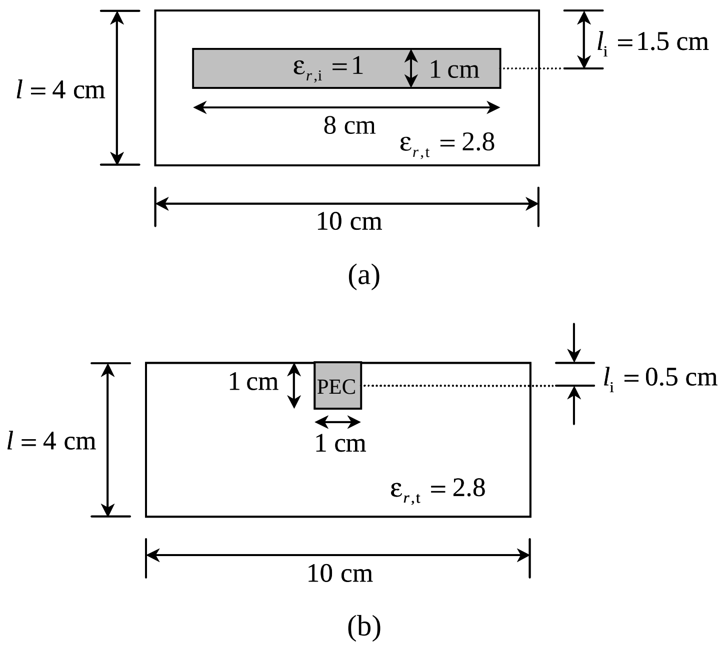

Figure 3.3: Vertical cross-section views of the targets considered in the 3D FDTD simulations:
(a) *TNT Disk 1* with a thin circular air gap
(b) *TNT Disk 1* with a small cubical metal inclusion.

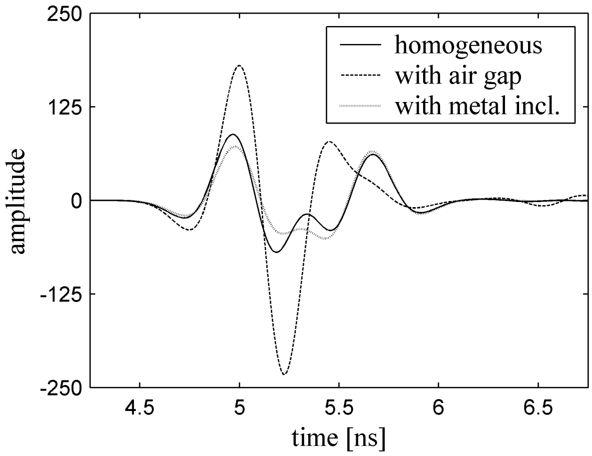

Figure 3.4: Simulated response of *TNT Disk 1* with and without internal structure ($d = 10$ cm & $h = 30$ cm).

Table 3.1: Subset selection deconvolution results for the air gap and the metal inclusion.

Impulse Response Parameters				
Target Name	h_3 $[*10^{-5}]$	τ_3		**Rel. Error**
		samples	[ns]	
air gap	20.6	192	1.849	0.13
metal inclusion	-3.7	183	1.762	0.12

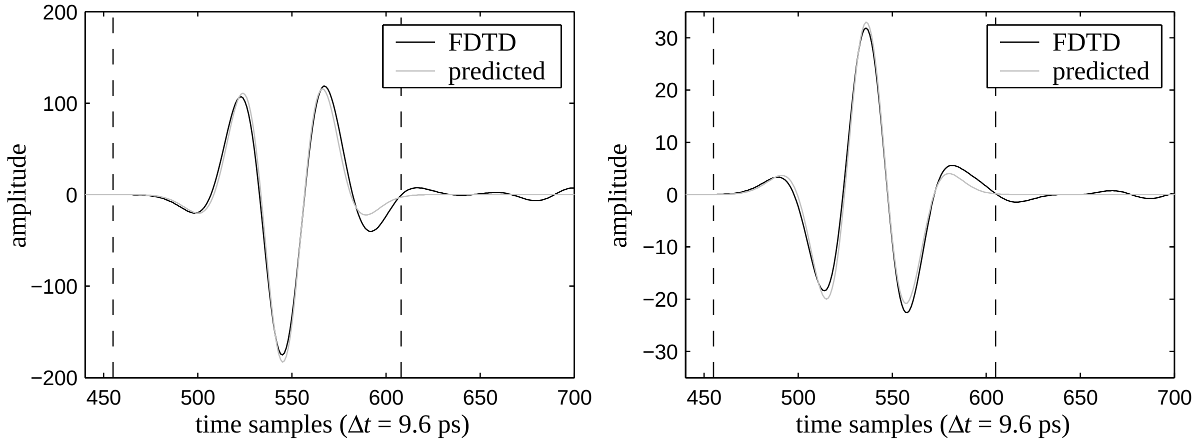

(a) (b)

Figure 3.5: Data fit between the predicted (deconvolution) and the simulated response:
(a) thin air gap
(b) small metal inclusion.
The dashed lines define the part of the response, which was fit by the deconvolution algorithm.

Table 3.2: Results of inverting the impulse response parameters of table 3.1.

Target Name	**Inversion for Target Size**[*]	
	volume V_i [cm^3]	l_i [cm]
air gap	43.6 (50.3)	1.36 (1.5)
metal inclusion	1.14 (1.0)	0.64 (0.5)

The values included in parentheses are the true values.

[*] Based on $\Delta\varepsilon_{r,t} = 2.8 - 4 = -1.2$, $v_t^{eff} = 16.6$ cm/ns, and $\tau_1 = 175$ samples (table 2.2).

Table 3.3: Subset selection deconvolution results for *TNT Disk 1* with and without internal structure ($d = 10$ cm & $h = 30$ cm).

Target Name	Impulse Response Parameters										Rel. Error
	h_1	τ_1		h_2	$\tau_2-\tau_1$		Γ	h_3	$\tau_3-\tau_1$		
	$[*10^{-4}]$	samples	[ns]	$[*10^{-4}]$	samples	[ns]		$[*10^{-5}]$	samples	[ns]	
TNT Disk 1 homogeneous [*]	14.0	175	1.685	-10.0	50	0.482	0.72	n/a	n/a	n/a	0.05
TNT Disk 1 with air gap	18.2	175	1.685	-7.0	47	0.453	0.38	16.0	17	0.164	0.02
TNT Disk 1 with metal inclusion	15.2	175	1.685	-10.2	50	0.482	0.67	-4.3	9	0.087	0.03

[*] Taken from table 2.2.

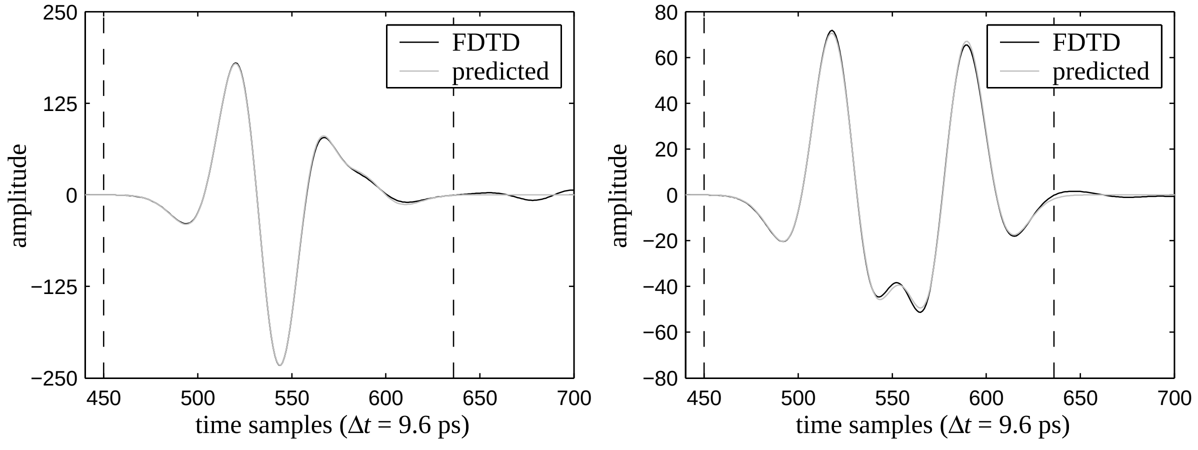

(a) (b)

Figure 3.6: Data fit between the predicted (deconvolution) and the simulated response:
(a) *TNT Disk 1* with the thin air gap ($d = 10$ cm & $h = 30$ cm)
(b) *TNT Disk 1* with the small metal inclusion ($d = 10$ cm & $h = 30$ cm).
The dashed lines define the part of the response, which was fit by the deconvolution algorithm.

Table 3.4: Results of the inversion for target size for *TNT Disk 1* with internal structure (d = 10 cm & h = 30 cm).

Target Name	Inversion for Target Size[*]			
	target radius [cm]	targt height l [cm]	volume V_i [cm^3]	l_i [cm]
TNT Disk 1 with air gap	5.9 (5.0)	3.8 (4.0)	34.0 (50.3)	1.36 (1.5)
TNT Disk 1 with metal inclusion	5.4 (5.0)	4.0 (4.0)	1.34 (1.0)	0.72 (0.5)

The values included in parentheses are the true values.

[*] Based on $\Delta\varepsilon_{r,t} = 2.8 - 4 = -1.2$ and $v_t^{eff} = 16.6$ cm/ns.

3.4 Discussion

This chapter presented a generalization of the scattering models for a homogeneous dielectric minelike target to account for the presence of an inclusion, specifically an air gap or a small piece of metal. The generalization makes use of a Born-type linearization of the volume integral representation of the scattered field in which the generalized contrast for the inclusion is defined by means of the Rayleigh scattering approximation. This approach allows for a unified treatment of dielectric and metal inclusions and leads to the fundamental result that an inclusion differentiates the waveform of the incident field twice. In particular, it is found that the impulse response of a minelike target with an inclusion is simply the sum of the impulse response, which would be observed if the target had no inclusion and an impulse response describing the effect of the inclusion, the latter consisting of no more than a double differentiation operator. This result forms the basis of the extension of the target characterization procedure for homogeneous disk-shaped minelike targets to targets with an inclusion.

Based on the FDTD simulation results, a couple of important conclusions can be drawn:

- Internal mine structure does influence the target response. Especially the presence of an air gap was found to significantly increase the magnitude of the target response and alter its shape. The presence of an air gap therefore facilitates the detection of buried plastic cased landmines with GPR. In comparison with an air gap, a small metal inclusion has a very weak effect on the target response.
- The derived target impulse response model adequately describes the contribution of a thin air gap or a small metal inclusion to the target response.
- The proposed target characterization procedure is able to determine the outer dimensions of a buried circular disk-shaped minelike target containing an inclusion with reasonable accuracy $(\text{error} < 1\ \text{cm})$.

Hence, the material presented in this chapter opens the possibility to identify minelike targets with internal structure. This possibility, however, is not without a price to be paid. First, the extended subset selection deconvolution algorithm no longer lends itself to real-time processing if the selection is carried out by permutation. And second, introducing a third degree of freedom, i.e. a third non-zero impulse response coefficient, brought back some of the ill-posedness of the deconvolution problem, resulting in a degradation of the accuracy with which the target dimensions can be estimated. Especially the estimation of the inclusion volume was found to be affected by this degradation.

These two problems will only get worse if more complicated internal structure than just a single inclusion is considered, e.g. the combination of an air gap with metallic and non-metallic parts of a fuse mechanism. This inevitably raises the question whether we are really interested in resolving the internal structure of a plastic cased landmine. For the purpose of determining the outer dimensions of a landmine, the answer to this question is more likely “No”. Hence, we should think of ways to make the effect of internal structure more manageable. A possible solution might be the use of lower frequencies, resulting in approximately coherent scattering from all parts of the landmine, i.e. its body and internal structure. Similar to the case of a small dielectric sphere under the Rayleigh scattering approximation, we may then set $\tilde{\mathbf{G}}(\boldsymbol{x},\boldsymbol{x}') \approx \tilde{\mathbf{G}}(\boldsymbol{x},\boldsymbol{x}_\mathrm{t})$ and $\mathbf{E}^i(\boldsymbol{x}') \approx \mathbf{E}^i(\boldsymbol{x}_\mathrm{t})$ for all points $\boldsymbol{x}'$ of the landmine, leading to a landmine impulse response which is directly proportional to its volume and consists of one double differentiation operator. Hence, an impulse response, which primarily carries information about the outer dimensions of the landmine is obtained. Furthermore, the subset selection deconvolution would then only have to solve for a single non-zero impulse response coefficient, which is as fast and robust as it gets.

The discussion on alternative approaches to dealing with internal structure will be picked up again in chapter 6. For now let as continue to use the scattering models as they have been derived in this chapter and the previous chapter and draw our attention to two other important aspect of GPR landmine identification, which are the radar hardware and preprocessing of the data. These aspects shall be discussed in detail in the next chapter.

CHAPTER 4

GPR LANDMINE IDENTIFICATION

In developing the theory of scattering from a minelike target, two important aspects of the GPR landmine identification problem have not yet been addressed. These are the radar hardware and the fact that a GPR system does not just measure the electric field scattered by the target, i.e. the target response, but also the direct wave between the transmitting and the receiving antenna, the ground reflected wave, as well as fields scattered from other objects/inhomogeneities below or above the ground. In EM modeling terms, these latter three components of the electric field are jointly referred to as the primary field, which is the field that would exist if the target were absent.

Thus, some further theoretical developments are necessary before the derived convolutional scattering models and the proposed target characterization procedure for circular disk-shaped minelike targets can be applied to GPR data:

- The development of hardware models describing the radiation and reception characteristics of the demining GPR and incorporation of these hardware models into the convolutional scattering models.
- The development of a calibration procedure, which determines the radiation and reception characteristics of the demining GPR.
- The development of preprocessing algorithms, which aim to remove the primary field from the GPR data, a process commonly referred to as background subtraction.

This chapter addresses these three issues, ultimately leading to a slightly modified version of the target characterization procedure, which accounts for the GPR hardware and operates on a single preprocessed A-scan.

The term “preprocessing” may be somewhat misleading, suggesting that it is merely a side issue. On the contrary, for the purpose of GPR landmine identification, careful preprocessing without loosing information on the amplitude and the shape of the target response is of fundamental importance. This requirement led to the development of a new background subtraction technique, termed weighted moving average background subtraction (WMA-BS), which first finds the anomalies in the data and then suppresses them in the estimation of the background to be subtracted. Besides background subtraction, this chapter also discusses a polarimetric preprocessing algorithm termed target frame transformation, which transforms the measured target response into the coordinate frame defined by the two main scattering axes of the target, thereby obtaining a target response that is independent of target orientation. This transformation is essential to the identification of targets having a preferential scattering axis, e.g. an elongated bombshell.

The chapter is organized as follows. In section 4.1, GPR hardware requirements are discussed in the light of the landmine identification problem and the demands imposed by the proposed target characterization procedure. Furthermore, a polarimetric video impulse GPR system developed by IRCTR is presented. In section 4.2, point source/receiver models are introduced for the transmitting antenna and the receiver chain (including the receiving antenna), which are then used to derive convolutional models for the GPR response of a surface-laid or buried minelike target. In these convolutional GPR models, the hardware characteristics are represented by a single term, called the effective radiated waveform, and a simple calibration procedure to determine this waveform will be presented. Section 4.3 is devoted to GPR data preprocessing. Here, the WMA-BS technique and the target frame transformation are introduced and their workings are illustrated using data acquired with the IRCTR video impulse GPR. In section 4.4, the convolutional GPR models are used to modify the target characterization procedure for circular disk-shaped minelike targets such that it accounts for the GPR hardware. Finally, section 4.5 gives a brief review of the material that has been presented.

4.1 GPR Hardware

4.1.1 General hardware considerations

It is difficult to set up universal rules for the hardware requirements a demining GPR has to meet as these depend on many factors such as the operation environment and the kind of data processing anticipated. With regard to the maximum allowable equipment weight, distinction needs to be made between systems designed for hand-held use and vehicle/platform mounted systems. The following discussion focuses on the requirements for applicability of the scattering models and the target characterization procedure presented in chapters 2 and 3.

Antenna system

Since all scattering models presented in this thesis are based on backscattering along the vertical direction, the antenna system should ideally be monostatic (Lambot *et al*, 2004) or configured such that the receiving antenna is positioned right below the transmitting antenna. Bistatic systems consisting of two horizontally displaced antennas should be positioned high above the ground. Note that the latter configuration is more susceptible to surface clutter and poses higher demands on dynamic range due to increased spreading losses.

The footprint of the transmitting antenna should be small to reduce the effect of unwanted clutter but big enough to give rise to a target response hyperbola, which is a robust feature for target detection and localization (Daniels, 2003; Yarovoy *et al*, 2003). Low antenna ringing is desirable as it may mask target responses and makes detection more difficult. It should be noted though that, if accurately determined and taken into account in the subset selection deconvolution, antenna ringing does not negatively affect the proposed target characterization procedure.

The receiving antenna should be designed to measure the scattered field at a local point rather than average over a surface. Hence it should have a small effective aperture. This requirement becomes more important the closer the receiving antenna is kept to the ground. In addition, in order to receive also very weak scattered fields, it is important that the receiving antenna provides high sensitivity in the frequency band covered by the radiated pulse.

A polarimetric antenna system measuring both the co-polar and cross-polar component of the scattered field provides additional information on the scattering behavior of the target under investigation. Unlike rotationally symmetric targets, for targets with a preferential scattering axis measurement of the full scattering matrix is a requisite for obtaining a target response, which is independent of target orientation. A detailed discussion on the benefit of polarimetric information for target identification and associated processing is given in section 4.3.3.

Frequency band

The frequency band of operation suitable for the proposed target characterization procedure is mainly restricted by the assumption of a linear relationship between the scattering current and the incident electric field on which the scattering models of this thesis are based. Hence, whether using a Born-type or the PO scattering approximation, as a qualitative rule the frequencies should be low enough to keep edge diffractions and mutual interaction of different parts of the target minimal. Note that the optimal frequency range, as such, depends on the expected target dimensions and contrast. For the Born approximation, a theoretical upper frequency limit, which takes the target dimensions and contrast into account, is defined by eq. (2.5). For practical purposes, however, this limit is too restrictive, as indicated by the FDTD simulation results of section 2.4. The simulations showed that both the inversion for target size and the inversion for material properties work well under the Born approximation even beyond this limit.

Additional factors determining the optimal frequency band of operation are related to the environment in which the demining GPR is to be employed. In areas where clutter due to a rough terrain or an inhomogeneous ground is a problem, low frequencies (< 1 GHz) should be used as these are less susceptible to clutter. The same is true in areas with lossy soils, since attenuation increases with frequency (Roth *et al*, 2001). In these areas low frequencies offer higher probing depths.

The frequency band should be chosen in accordance with the abovementioned theoretical and environmental considerations. As a rule of thumb, the bandwidth need not exceed 2 GHz since subset selection reduces the ill-posedness and ill-conditioning of the deconvolution problem resulting from the limited bandwidth of the radar system.

It is important to note that these guidelines are specific to the proposed target characterization procedure and its underlying scattering models. Other data processing modalities can have different requirements. This is especially true when the demining GPR is used as an imaging sensor, where the trend is to use ultra-wide bandwidths extending way beyond the frequency range of validity for the Born and the PO approximation (Zanzi *et al*, 2002; Van Dongen *et al*, 2003; Alli *et al*, 2004). Through the use of high frequencies (> 1.5 GHz) in combination with an ultra-wide bandwidth of the order of 3-4 GHz the lateral and the depth resolution of a GPR image is increased.

Linear dynamic range

Landmine detection requires a receiver chain with a high linear dynamic range, e.g. 69 dB (Yarovoy *et al*, 2002a), for receiving the weak response of plastic cased AP mines while at the same time avoiding receiver saturation by the strong direct wave. For target identification, where accurate signal shape information is crucial, linearity over the entire dynamic range becomes very critical since, depending on whether a landmine is surface-laid or buried, its response may or may not be superimposed on the direct wave.

The dynamic range of the receiver chain is usually referenced to the receiver noise level. It is important to understand that such a specification does not refer to the possibility to extract from the measured data a target response whose signal strength is approaching the dynamic range of the receiver. At most it refers to the possibility to detect such a target in a clutter free environment. Clutter can never be removed completely from the measured data and hence constitutes an additional source of noise. This additional noise limits the detection performance and, even more so, the possibility to extract “clean” target responses, which can be used for identification.

System stability

Minimal time and amplitude drift is important in two ways. First, it is the prerequisite for a good background subtraction with few residuals from the direct wave (see section 4.3.2). And second, amplitude stability is necessary if the impulse responses estimated by subset selection deconvolution are to be related to target characteristics such as size and permittivity.

Time drift can generally be corrected for by simple A-scan alignment. The case for amplitude drift is more complicated. To limit the effect of amplitude drift on system performance, any demining GPR should be calibrated regularly. A simple but accurate calibration procedure is presented in section 4.2.4.

4.1.2 Video impulse radar for landmine detection

As an example of a GPR system that is suitable for the proposed target characterization procedure, this section describes a polarimetric video impulse GPR developed at IRCTR. The radar has been used for experimental validation of the scattering models and to determine the accuracy with which target characteristics can be estimated from measured GPR data, the results of which are presented in chapter 5.

The IRCTR video impulse GPR with an effective bandwidth of 0.6-2.7 GHz (-10 dB level; see section 4.2.4) consists of the following hardware components: a 0.8 ns pulse generator, a polarimetric antenna system, a signal conditioner and a multi-channel sampling converter connected to a computer. A schematic illustration of the radar is given in figure 4.1. The signal conditioner in the receiver chain improves the signal-to-noise ratio and makes sure that the 66 dB linear dynamic range of the A-D converter is used efficiently by limiting the large amplitude of the direct wave. Detailed descriptions of the pulse generator, the signal conditioner and the sampling converter are given by Yarovoy *et al* (2000a).

A unique feature of the IRCTR video impulse GPR is its antenna design. As shown in figure 4.2, the antenna system consists of a transmitting dielectric wedge antenna (Yarovoy *et al*, 2002b) and two small receiving loops (Yarovoy *et al*, 2000b). The receiver loops are positioned 30.5 cm below the aperture of the dielectric wedge antenna using long leads, which extend downwards from the open sides of the dielectric wedge. The loops are oriented such that one measures the co-polar and the other the cross-polar component of the scattered field. Since both loops are located close (8.5 cm) to the boresight axis of the transmitting antenna, the antenna system essentially performs a local polarimetric measurement of backscattering along the vertical when the transmitting antenna is positioned right above the target. Of course, in practice, it is not always possible to tell from the data when the transmitting antenna is positioned right above the target and the measurement will never be exactly local due the horizontal offset between the loops. The implications this has on polarimetric data processing are discussed in more detail in section 4.3.3.

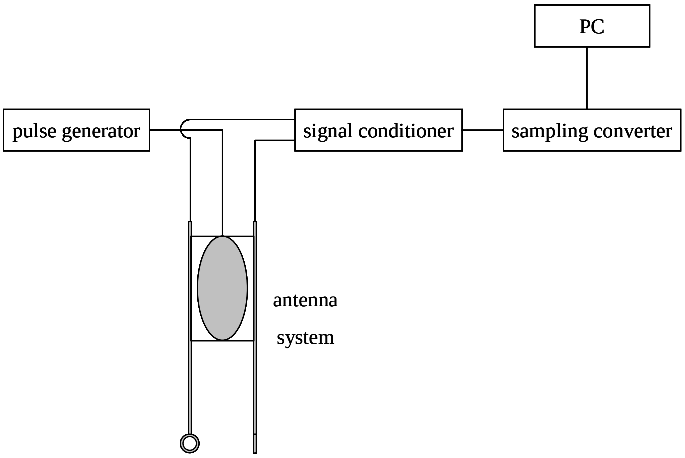

Figure 4.1: Schematic illustration of the IRCTR video impulse GPR.

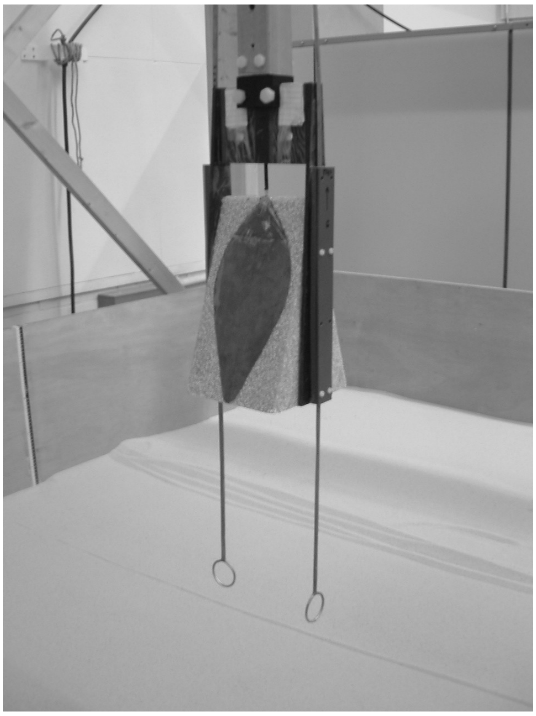

Figure 4.2: The antenna system of the IRCTR video impulse GPR.

4.2 Convolutional GPR Models

In this section, the previously presented time-domain convolutional scattering model is extended to account for the GPR hardware. For this purpose, the concept of the virtual source of the transmitting antenna (Scheers, 2001) is introduced, yielding a simple but adequate time-domain description of the antenna's far-field radiation characteristics. The receiver chain including the receiving antenna is modeled by a receiver impulse response relating the electric field at the receiving antenna to the measured A-scan. These hardware models enter as additional terms in the convolutional scattering model, resulting in expressions for the GPR response of surface-laid and buried minelike targets. Even though the hardware models have been developed with the IRCTR video impulse GPR in mind, an attempt is made to keep the treatise general and applicable to other pulsed (time-domain) GPR systems. The hardware of stepped-frequency (frequency-domain) GPR systems may be described in an analogous manner.

4.2.1 Hardware models

Transmitting antenna

The virtual source point of a time-domain antenna is a reference point from which the wavefront of the radiated far-field seems to emanate spherically with a $1/r$ amplitude decay. Accordingly, when referenced to the virtual source point, the radiated electric field $\mathbf{e}^{rad}$ at a point $\boldsymbol{x}$ in the far-field of the antenna in air can be written as

$$\mathbf{e}^{rad}\left(\boldsymbol{x},t\right)=\frac{1}{r}\delta\left(t-\frac{r}{c}\right)\otimes\mathbf{e}_0\left(\theta,\phi,t\right) , \tag{4.1}$$

where (r,θ,ϕ) are the spherical coordinates of $\boldsymbol{x}$, and $\mathbf{e}_0\left(\theta,\phi,t\right)$ is a vector with units of V (Volt) describing the polarization, amplitude and shape of the pulse radiated in the direction specified by the angles θ and ϕ.

Since in this thesis we are primarily interested in radiation along the vertical, i.e. $\theta=\phi=0$, and assume a predominant linear polarization, eq. (4.1) can be rewritten as

$$\mathbf{e}^{rad}\left(\boldsymbol{x},t\right)=\frac{1}{r}\delta\left(t-\frac{r}{c}\right)\otimes\mathrm{e}_0\left(t\right)\boldsymbol{u}_{\mathrm{TX}} . \tag{4.2}$$

Here, $\boldsymbol{u}_{\mathrm{TX}}$ is a unit vector describing the polarization of the radiated wave.

Receiver chain

Rather than modeling each component of the receiver chain separately, we take the approach of the user, who is primarily interested in the relationship between “what comes in” and “what comes out”. Assuming that all components of the receiver chain are linear devices, the entire chain can be modeled by one cumulative impulse response $\mathrm{h}_{\mathrm{RX}}\left(t\right)$. This impulse response relates the measured A-scan $\mathrm{s}\left(\boldsymbol{x}_{\mathrm{RX}},t\right)$ to the total electric field $\mathbf{e}\left(\boldsymbol{x}_{\mathrm{RX}},t\right)$ at the receiving antenna position $\boldsymbol{x}_{\mathrm{RX}}$ according to

$$\mathrm{s}\left(\boldsymbol{x}_{\mathrm{RX}},t\right)=\mathrm{h}_{\mathrm{RX}}\left(t\right)\otimes\boldsymbol{u}_{\mathrm{RX}}^{T}\mathbf{e}\left(\boldsymbol{x}_{\mathrm{RX}},t\right)+\mathrm{s}_{\mathrm{n}}\left(t\right) , \tag{4.3}$$

where the unit vector $\boldsymbol{u}_{\mathrm{RX}}$ is used to describe the polarization of the receiving antenna. The time function $\mathrm{s}_{\mathrm{n}}\left(t\right)$ has been introduced to account for random noise such as receiver noise or external electromagnetic interference EMI. The superscript T denotes transpose.

The total electric field can be split into three parts: the field scattered by the target, the direct wave between the transmitting and the receiving antenna, and unwanted reflections from the ground surface and from objects/inhomogeneities above and below the ground, i.e.

$$\mathbf{e}\left(\boldsymbol{x}_{\mathrm{RX}},t\right)=\mathbf{e}^{s}\left(\boldsymbol{x}_{\mathrm{RX}},t\right)+\mathbf{e}^{rad}\left(\boldsymbol{x}_{\mathrm{RX}},t\right)+\mathbf{e}^{c}\left(\boldsymbol{x}_{\mathrm{RX}},t\right) . \tag{4.4}$$

Here, the superscript c stands for clutter and refers to the unwanted reflections. Each part of the total electric field can be associated with its own signal part, which contributes to the measured A-scan. These are the target response signal $\mathrm{s}_{\mathrm{t}}\left(\boldsymbol{x}_{\mathrm{RX}},t\right)$, the direct wave signal $\mathrm{s}_{\mathrm{d}}\left(t\right)$ and the clutter signal $\mathrm{s}_{\mathrm{c}}\left(\boldsymbol{x}_{\mathrm{RX}},t\right)$ defined as

$$\mathrm{s}_{\mathrm{t}}\left(\boldsymbol{x}_{\mathrm{RX}},t\right)=\mathrm{h}_{\mathrm{RX}}\left(t\right)\otimes\boldsymbol{u}_{\mathrm{RX}}^{T}\mathbf{e}^{s}\left(\boldsymbol{x}_{\mathrm{RX}},t\right) , \tag{4.5}$$

$$\mathrm{s}_{\mathrm{d}}\left(t\right)=\mathrm{h}_{\mathrm{RX}}\left(t\right)\otimes\boldsymbol{u}_{\mathrm{RX}}^{T}\mathbf{e}^{rad}\left(\boldsymbol{x}_{\mathrm{RX}},t\right) , \tag{4.6}$$

$$\mathrm{s}_{\mathrm{c}}\left(\boldsymbol{x}_{\mathrm{RX}},t\right)=\mathrm{h}_{\mathrm{RX}}\left(t\right)\otimes\boldsymbol{u}_{\mathrm{RX}}^{T}\mathbf{e}^{c}\left(\boldsymbol{x}_{\mathrm{RX}},t\right) . \tag{4.7}$$

Note that the receiving antenna position vector $\boldsymbol{x}_{\mathrm{RX}}$ has been omitted on the left-hand side of the definition of the direct wave signal to acknowledge the constant offset between the transmitting antenna and the receiving antenna.

Using these definitions, eq. (4.3) can be rewritten as

$$\mathrm{s}\left(\boldsymbol{x}_{\mathrm{RX}},t\right)=\mathrm{s}_{\mathrm{t}}\left(\boldsymbol{x}_{\mathrm{RX}},t\right)+\mathrm{s}_{\mathrm{d}}\left(t\right)+\mathrm{s}_{\mathrm{c}}\left(\boldsymbol{x}_{\mathrm{RX}},t\right)+\mathrm{s}_{\mathrm{n}}\left(t\right) . \tag{4.8}$$

Equation (4.8) summarizes the information content of the measured A-scan and is the basis for GPR signal processing. For target identification, we are solely interested in the target response signal and convolutional models describing its relation to the target impulse response will be presented in sections 4.2.2 and 4.2.3. However, eq. (4.8) also underlines the necessity to estimate and remove the other signal parts from the measured A-scan before the target response signal can be analyzed. How this is done will be discussed in section 4.3.

4.2.2 GPR response of a surface-laid minelike target

Let us consider the configuration of figure 4.3 showing the antenna system of the GPR, indicated as a point source and a point receiver, right above a surface-laid minelike target. The transmitting antenna is positioned at a height h_{TX} above the ground and the receiving antenna is positioned below the transmitting antenna at a height h_{RX}. As before, the "depth" d of the target is measured from the top of the target. Note that for a surface-laid target d is negative. What we would like to have is a convolutional model for the target response signal $\mathrm{s}_{\mathrm{t}}\left(\boldsymbol{x}_{\mathrm{RX}},t\right)$ measured by the GPR. For a surface-laid target, such a model is easily derived from the time-domain convolutional model for backscattering from a minelike target in air, i.e. eq. (2.50).

Let us start by describing the incident field $\mathbf{e}^{i}$ at the target location. Using eq. (4.2), we have

$$\mathbf{e}^{i}\left(\boldsymbol{x}_{\mathrm{t}},t\right)=\frac{1}{h_{\mathrm{TX}}+d}\delta\left(t-\frac{h_{\mathrm{TX}}+d}{c}\right)\otimes\mathrm{e}_{0}\left(t\right)\boldsymbol{u}_{\mathrm{TX}} . \tag{4.9}$$

Then, from eq. (2.50), the scattered field at the receiving antenna is found to be

$$\mathbf{e}^{s}\left(\boldsymbol{x}_{\mathrm{RX}},t\right)=\frac{1}{2\sqrt{\pi}\left(h_{\mathrm{RX}}+d\right)}\delta\left(t-\frac{h_{\mathrm{RX}}+d}{c}\right)\otimes\mathrm{h}_{\mathrm{t}}\left(t\right)\otimes\frac{1}{h_{\mathrm{TX}}+d}\delta\left(t-\frac{h_{\mathrm{TX}}+d}{c}\right)\otimes\mathrm{e}_{0}\left(t\right)\boldsymbol{u}_{\mathrm{TX}} , \tag{4.10}$$

which according to eq. (4.5) produces the target response signal

$$\mathrm{s_t}\left(\boldsymbol{x}_{\mathrm{RX}},t\right)=$$
$$\mathrm{h_{RX}}\left(t\right)\otimes\frac{1}{2\sqrt{\pi}\left(h_{\mathrm{RX}}+d\right)}\delta\left(t-\frac{h_{\mathrm{RX}}+d}{c}\right)\otimes\mathrm{h_t}\left(t\right)\otimes\frac{1}{h_{\mathrm{TX}}+d}\delta\left(t-\frac{h_{\mathrm{TX}}+d}{c}\right)\otimes\mathrm{e_0}\left(t\right) \tag{4.11}$$

when a co-polar receiving antenna is used ($\boldsymbol{u}_{\mathrm{RX}}^T\boldsymbol{u}_{\mathrm{TX}}=1$) and no signal when a cross-polar receiving antenna is used ($\boldsymbol{u}_{\mathrm{RX}}^T\boldsymbol{u}_{\mathrm{TX}}=0$). Equation. (4.11) can be written in a more compact way if we introduce the effective radiated waveform $\mathrm{w}\left(t\right)$, which is defined as

$$\mathrm{w}\left(t\right)=\mathrm{h_{RX}}\left(t\right)\otimes\mathrm{e_0}\left(t\right) \tag{4.12}$$

and embodies both the characteristics of the actual radiated waveform and the receiver chain. The effective radiated waveform is sometimes also referred to as the radar impulse response (Kostylev, 1994, p. 264; Savelyev *et al*, 2003). Thus

$$\mathrm{s_t}\left(\boldsymbol{x}_{\mathrm{RX}},t\right)=\frac{1}{2\sqrt{\pi}\left(h_{\mathrm{RX}}+d\right)\left(h_{\mathrm{TX}}+d\right)}\mathrm{h_t}\left(t\right)\otimes\mathrm{w}\left(t-\frac{h_{\mathrm{RX}}+h_{\mathrm{TX}}+2d}{c}\right). \tag{4.13}$$

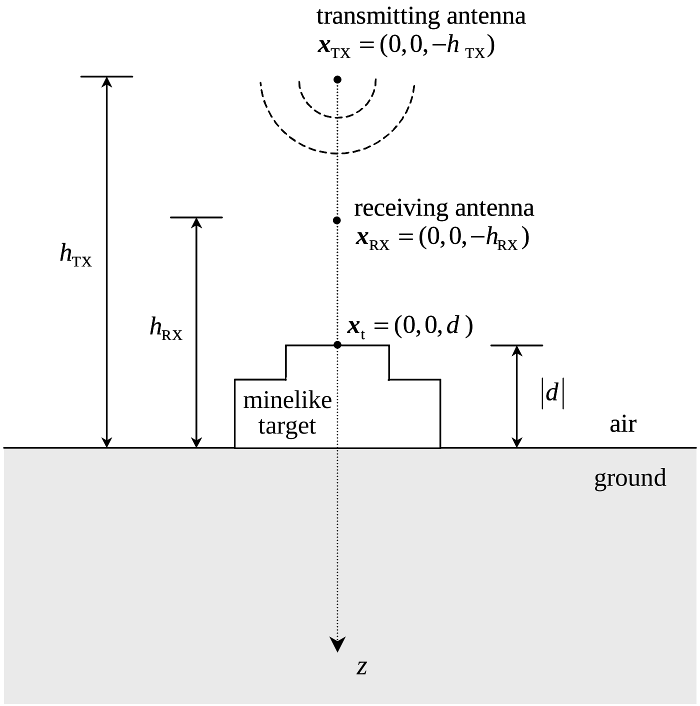

Figure 4.3: The antenna system of the GPR above a surface-laid minelike target ($d<0!$).

4.2.3 GPR response of a buried minelike target

A convolutional model for the target response signal $\mathrm{s_t}\left(\boldsymbol{x}_{\mathrm{RX}},t\right)$ of a buried minelike target can be derived in the same manner as for a surface-laid minelike target, only that now we make use of the time-domain convolutional model for backscattering from a buried minelike target, i.e. eq. (2.16). In the following, we consider the configuration of figure 4.4, which, apart from the target now being buried, is identical to the one considered for the surface-laid minelike target (see figure 4.3). As usual in the time-domain analysis of scattering from a buried minelike target, the ground is assumed to be lossless.

Let us again start by describing the incident field. Based on eq. (4.2), the incident field $\mathbf{e}^i$ at the target location can be written as

$$\mathbf{e}^i\left(\boldsymbol{x}_\mathrm{t},t\right)=\frac{T_{a\to g}}{h_\mathrm{TX}+d}\delta\left(t-\frac{h_\mathrm{TX}}{c}-\frac{d}{v_1}\right)\otimes \mathrm{e}_0\left(t\right)\boldsymbol{u}_\mathrm{TX}\ , \tag{4.14}$$

where now the normal incidence Fresnel transmission coefficient $T_{a\to g}$ for transmission into the ground, given by

$$T_{a\to g}=\frac{2}{1+\sqrt{\varepsilon_{r,1}}}\ , \tag{4.15}$$

needs to be included. It is important to note that, in writing eq. (4.14), the transmitting antenna is assumed to be elevated high above the ground ($k_0 h_\mathrm{TX}\gg 1$) and the target to be buried shallow, making the inclusion of a refraction spreading[1] term such as eq. (2.18) unnecessary.

Substituting eq. (4.14) into eq. (2.16), the scattered field at the receiving antenna is given by

$$\begin{aligned}&\mathbf{e}^s\left(\boldsymbol{x}_\mathrm{RX},t\right)=\\&\frac{T_{g\to a}\zeta\left(h_\mathrm{RX},d\right)}{2\sqrt{\pi}\left(h_\mathrm{RX}+d\right)}\delta\left(t-\frac{h_\mathrm{RX}}{c}-\frac{d}{v_1}\right)\otimes \mathrm{h}_\mathrm{t}\left(t\right)\otimes\frac{T_{a\to g}}{h_\mathrm{TX}+d}\delta\left(t-\frac{h_\mathrm{TX}}{c}-\frac{d}{v_1}\right)\otimes \mathrm{e}_0\left(t\right)\boldsymbol{u}_\mathrm{TX}\end{aligned} \tag{4.16}$$

so that, from eq. (4.5), the target response signal when using a co-polar receiving antenna ($\boldsymbol{u}_\mathrm{RX}^T\boldsymbol{u}_\mathrm{TX}=1$) is

$$\begin{aligned}&\mathrm{s}_\mathrm{t}\left(\boldsymbol{x}_\mathrm{RX},t\right)=\\&\mathrm{h}_\mathrm{RX}\left(t\right)\otimes\frac{T_{g\to a}\zeta\left(h_\mathrm{RX},d\right)}{2\sqrt{\pi}\left(h_\mathrm{RX}+d\right)}\delta\left(t-\frac{h_\mathrm{RX}}{c}-\frac{d}{v_1}\right)\otimes \mathrm{h}_\mathrm{t}\left(t\right)\otimes\frac{T_{a\to g}}{h_\mathrm{TX}+d}\delta\left(t-\frac{h_\mathrm{TX}}{c}-\frac{d}{v_1}\right)\otimes \mathrm{e}_0\left(t\right)\ .\end{aligned} \tag{4.17}$$

When using a cross-polar receiving antenna ($\boldsymbol{u}_\mathrm{RX}^T\boldsymbol{u}_\mathrm{TX}=0$), no target response signal is measured. Rearranging and making use of the definition of the effective radiated waveform, eq. (4.12), gives the more compact expression

$$\mathrm{s}_\mathrm{t}\left(\boldsymbol{x}_\mathrm{RX},t\right)=\frac{T_{g\to a}\zeta\left(h_\mathrm{RX},d\right)T_{a\to g}}{2\sqrt{\pi}\left(h_\mathrm{RX}+d\right)\left(h_\mathrm{TX}+d\right)}\mathrm{h}_\mathrm{t}\left(t\right)\otimes \mathrm{w}\left(t-\frac{h_\mathrm{RX}+h_\mathrm{TX}}{c}-\frac{2d}{v_1}\right). \tag{4.18}$$

Note the close similarity with the convolutional model for the target response signal of a surface-laid minelike target, i.e. eq. (4.13).

---

[1] To be precise, for the transmission into the ground it would be more correct to say focusing.

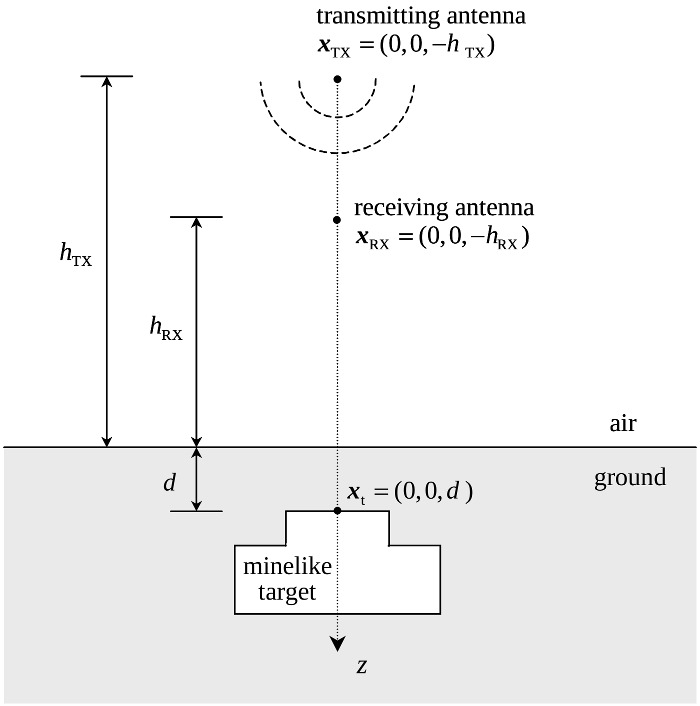

Figure 4.4: The antenna system of the GPR above a buried minelike target.

4.2.4 Calibration: Estimation of the effective radiated waveform and the direct wave signal

The effective radiated waveform and the direct wave signal can be estimated from a set of metal sheet reflection measurements with varying antenna heights. The basic idea underlying this calibration is that the reflection from the metal sheet depends on antenna height, whereas the measured direct wave signal does not. Given A-scans measured at two or more antenna heights, this difference allows us to separate the reflection signal from the direct wave signal. Since the metal sheet is a perfectly reflecting surface, i.e. its reflection coefficient is equal to minus one, the reflection signal can be related to the effective radiated waveform. In the following, the theory underlying the estimation is outlined and calibration results for the IRCTR video impulse GPR are presented.

Consider the configuration of figure 4.5 showing the antenna system of the GPR above a flat metal sheet, which is assumed to be infinite in extent. Here, the receiving antenna, positioned at a height h_{RX} above the metal sheet, is oriented such that it acts as a co-polar receiver. Given this configuration, the GPR measures an A-scan, which, neglecting noise, is the sum of two signals

$$\mathrm{s}(h_{RX},t) = \mathrm{s}_d(t) + \mathrm{s}_m(h_{RX},t), \tag{4.19}$$

namely the direct wave signal $\mathrm{s}_d(t)$ and the metal sheet reflection signal $\mathrm{s}_m(h_{RX},t)$.

An expression for the metal sheet reflection signal can be obtained by application of image theory (Balanis, 1989, p. 314-323). According to this theory, the reflected wave may be thought of as originating from an image source positioned at a distance h_{TX} below the metal sheet. In order to satisfy the boundary conditions, the strength of this image source needs to be scaled by the Fresnel reflection coefficient. Then, assuming that the receiving antenna lies in the far-field of the image source, eq. (4.2) can be used to represent the reflected wave field, which produces a metal sheet reflection signal according to the right-hand side of eq. (4.6). Thus

$$\begin{aligned} \mathrm{s_m}\left(h_{\mathrm{RX}},t\right) &= \mathrm{h_{RX}}\left(t\right)\otimes\frac{-1}{h_{\mathrm{TX}}+h_{\mathrm{RX}}}\delta\left(t-\frac{h_{\mathrm{TX}}+h_{\mathrm{RX}}}{c}\right)\otimes\mathrm{e_0}\left(t\right) \\ &= -\frac{1}{o+2h_{\mathrm{RX}}}\delta\left(t-\frac{o+2h_{\mathrm{RX}}}{c}\right)\otimes\mathrm{w}\left(t\right) \ , \end{aligned} \tag{4.20}$$

where we made use of the definition of the effective radiated waveform $\mathrm{w}\left(t\right)$, eq. (4.12), and introduced the vertical antenna offset $o=h_{\mathrm{TX}}-h_{\mathrm{RX}}$. We see that the metal sheet reflection signal is simply a scaled and shifted version of the effective radiated waveform.

The metal sheet reflection signal can be separated from the direct wave signal by considering the difference $\mathrm{s}\left(h_{\mathrm{RX},i},t\right)-\mathrm{s}\left(h_{\mathrm{RX},j},t\right)$ between two A-scans measured at two different antenna heights $h_{\mathrm{RX},i}$ and $h_{\mathrm{RX},j}$, respectively. Based on eqs. (4.19) and (4.20), this difference can be written as

$$\begin{aligned} &\mathrm{s}\left(h_{\mathrm{RX},i},t\right)-\mathrm{s}\left(h_{\mathrm{RX},j},t\right)= \\ &\left(-\frac{1}{o+2h_{\mathrm{RX},i}}\delta\left(t-\frac{o+2h_{\mathrm{RX},i}}{c}\right)+\frac{1}{o+2h_{\mathrm{RX},j}}\delta\left(t-\frac{o+2h_{\mathrm{RX},j}}{c}\right)\right)\otimes\mathrm{w}\left(t\right) \ . \end{aligned} \tag{4.21}$$

Given that the vertical antenna offset o is known, eq. (4.21) can be solved for the effective radiated wavelet $\mathrm{w}\left(t\right)$ in a least squares sense. To reduce ambiguity, it is advisable to use multiple A-scan combinations in the formulation of the least squares problem and solve for an optimal $\mathrm{w}\left(t\right)$ simultaneously. Finally, once $\mathrm{w}\left(t\right)$ has been estimated, it can be used together with eqs. (4.19) and (4.20) to estimate the direct wave signal $\mathrm{s_d}\left(t\right)$.

The virtual source point of a horn type antenna lies somewhere between its feed point and its aperture (Scheers, 2001). However, its exact position is usually unknown and therefore also the vertical antenna offset. A way to work around this is to solve eq. (4.21) for various antenna offsets and choose the solution that gives the smallest data misfit overall. Like this, an optimal combination of o and $\mathrm{w}\left(t\right)$ can be found. This approach has been tested for the IRCTR video impulse GPR and lead to the observation that the problem of estimating the vertical antenna offset is very ill-posed, even if the estimation uses multiple A-scan combinations. Hence, for the calibration of the IRCTR video impulse GPR, the antenna offset has been set with reference to the center point of the transmitting antenna's aperture, i.e. $o=30.5\ \mathrm{cm}$.

Figure 4.6 shows the effective radiated waveform and the direct wave signal of the IRCTR video impulse GPR estimated using five A-scans measured at receiving antenna heights of 12.5, 15, 17.5, 20 and 22.5 cm. The corresponding data fit is shown in figure 4.7, which demonstrates that all five A-scans can be accurately modeled from the estimated signals. Note that the calibration procedure is not only capable of determining the main pulse of the effective radiated waveform, but also the antenna ringing. This antenna ringing is a result of a wave, which bounces between the aperture and the top edge of the transmitting antenna before being radiated (Yarovoy *et al*, 2002b). From the amplitude spectrum of the effective radiated waveform, shown in figure 4.8, its peak amplitude frequency was determined as 1.8 GHz and its bandwidth as 0.6-2.7 GHz (-10 dB level).

Note that it is also possible to do the calibration using the ground as a reflecting surface as long as the ground is sufficiently flat and the reflection coefficient is known. This approach gives a better estimate of the direct wave signal but a worse estimate of the effective radiated waveform.

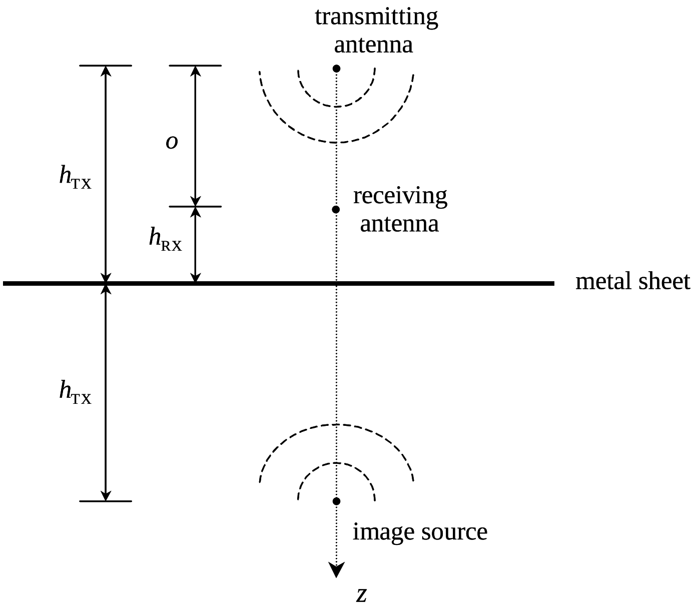

Figure 4.5: Setup for the metal sheet calibration. A-scans are measured for varying antenna heights.

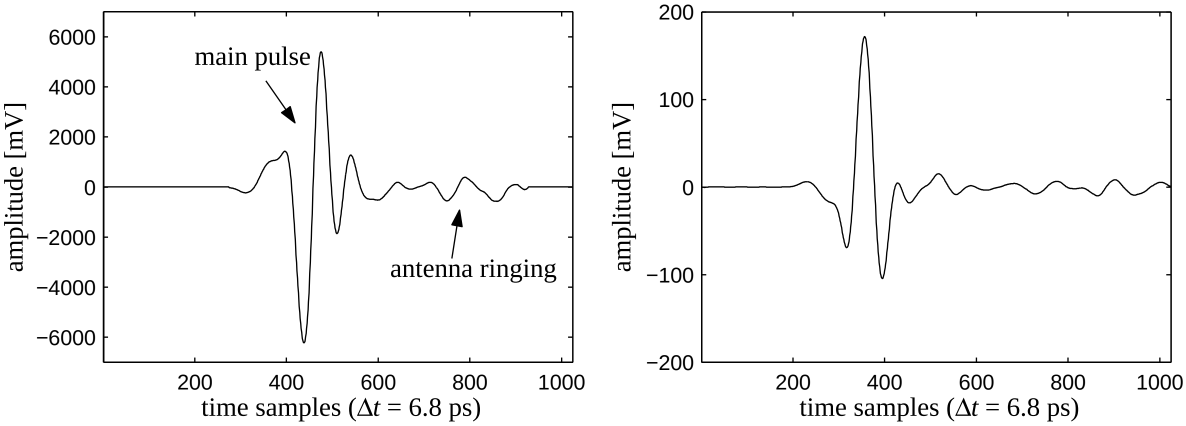

(a) (b)

Figure 4.6: Calibration results for the IRCTR video impulse GPR: (a) effective radiated waveform $\mathrm{w}(t)$, (b) direct wave signal $\mathrm{s_d}(t)$.

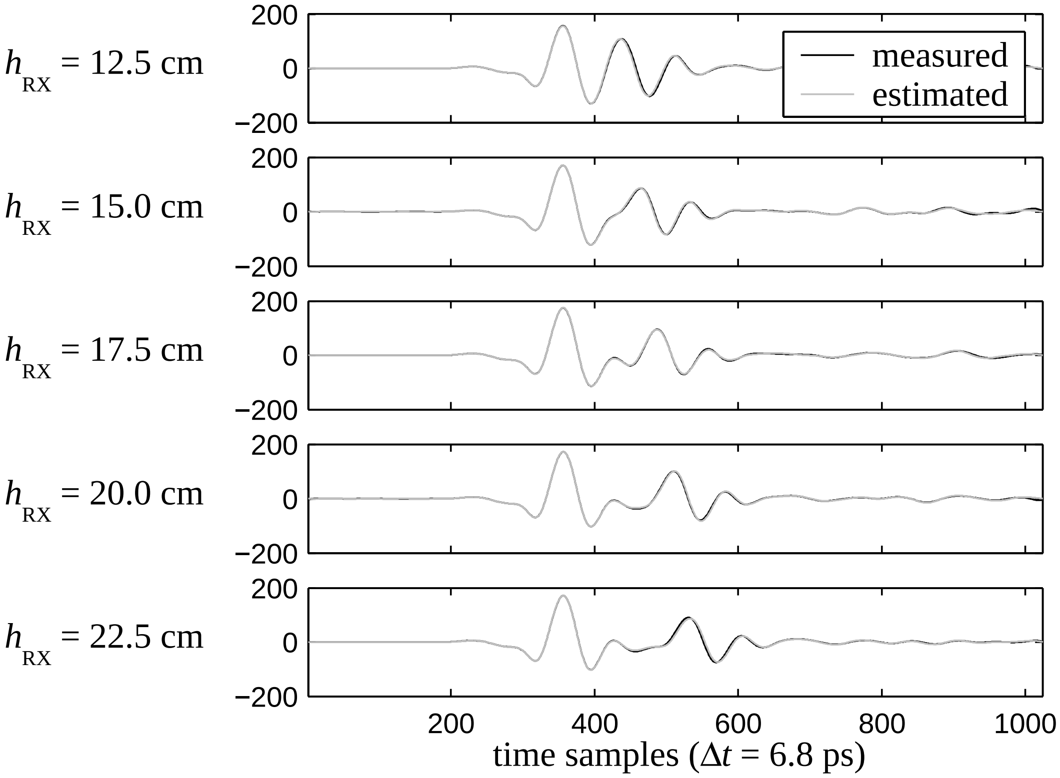

Figure 4.7: Data fit for the five A-scans used in the calibration of the IRCTR video impulse GPR (amplitudes in mV).

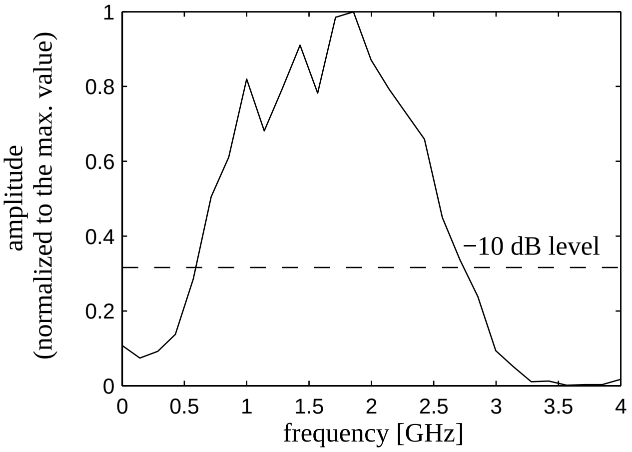

Figure 4.8: Amplitude spectrum of the effective radiated waveform of the IRCTR video impulse GPR.

4.3 Preprocessing

The main objective of preprocessing is to isolate from each measured A-scan the target response signal, which in section 4.2 has been defined as the signal produced by the field scattered from the target. The preprocessing sequence through which this is achieved consists of two stages, which in order application are:

1) DC offset and noise reduction, which are discussed in section 4.3.1.
2) Background subtraction, which aims at removing the direct wave signal and reflections from the ground surface or subsurface layering, and is covered in detail in section 4.3.2.

The target response signal of a target with a preferential scattering axis, e.g. an elongated bombshell, depends on target orientation. Therefore, in order to be able to correctly identify these types of targets, an additional preprocessing step referred to as target frame transformation is required. This transform rotates the target response into the coordinate frame defined by the main scattering axes of the target, yielding an orientation independent response. Details of how this transform works and some transform examples are presented in section 4.3.3.

The preprocessing algorithms presented in this section have been developed with target identification in mind. Hence an important requirement is that they preserve both the amplitude and the shape of the target response signal. In this sense the demands are much higher than those for target detection, where, bluntly speaking, the objective is to highlight anomalies.

4.3.1 DC offset and noise reduction

The first preprocessing step is to estimate and subtract from each A-scan its DC offset. Generally, it is sufficient to simply average the part of the A-scan before the arrival of the direct wave to obtain a usable DC offset estimate.

The next step then is to reduce the random noise, whose main contribution is usually caused by timing jitter in the sampling converter. The frequency spectrum of this noise is much wider than that of the radiated pulse. Hence most of the noise can be removed by careful low-pass filtering. In terms of the A-scan model of eq. (4.8), low-pass filtering minimizes the term $\mathrm{s}_\mathrm{n}(t)$.

4.3.2 Background subtraction

To understand background subtraction, it is useful to discuss what we mean by background and what are its differences to clutter.

A definition of clutter in the context of ground penetrating radar is given by Daniels (1996, p. 23), who states that “clutter are those signals that are unrelated to the target scattering characteristics but occur in the same sample-time window and have similar spectral characteristics to the target wavelet”. Accordingly, for a demining GPR the following primary clutter signals can be identified:

1) The direct wave.

2) The ground reflection and reflections from subsurface layering (if present).
3) Natural clutter such as scattering from soil inhomogeneities, rocks, tree roots, surface vegetation, etc.
4) Anthropogenic[2] clutter above or below the ground such as metal shrapnel, waste, pipelines, walls, etc.

Despite the fact that all these clutter signals have in common that they might mask (part of) the target response signal, a distinction can be made between the direct wave signal, which is independent of antenna position, and the remaining clutter signals, which generally are not. This difference has led us to treat them separately in the A-scan model of eq. (4.8), by introducing $\mathrm{s_d}(t)$ for the direct wave signal and $\mathrm{s_c}(\boldsymbol{x}_{\mathrm{RX}},t)$ for all unwanted reflection signals.

Background, as the name suggests, can be defined as all those signal components, which are laterally invariant or only slightly varying, i.e. everything that is not an anomaly. Defined as such, the background forms a subset of clutter. Of the above clutter signals only the direct wave, the ground reflection and reflections from subsurface layering make part of the background, and this only if the ground surface and the layering are sufficiently flat. Thus background subtraction only removes part of the clutter. What remains are anomalous signals, which should be treated as potentially dangerous targets and require identification.

Background subtraction techniques make use of the lateral invariance property of background. In addition, it is customary to assume that the targets are isolated scatterers. By far the most applied background subtraction technique is *average background subtraction* (A-BS) (Daniels, 1996, p. 150). This technique estimates the background by averaging all A-scans in an area of interest and then subtracts this estimate from each A-scan. A variant of this technique is *moving average background subtraction* (MA-BS) (Roth *et al*, 2003; Groenenboom and Yarovoy, 2002), which averages all A-scans within a data window to obtain a background estimate for the A-scan at the center of the window. The window is then moved over the data to find a background estimate for each A-scan. By doing so, the moving average background subtraction tries to account for local variations in the background and consequently results in less residuals of the ground reflection signal. Another background subtraction technique is *polynomial background subtraction* (P-BS) (Roth *et al*, 2003). This technique estimates the background by fitting a low degree polynomial in a least squares sense to each time slice[3] of the data. A similar technique is sometimes used in gravity data processing to estimate and remove the regional gravity field, leaving over local gravity anomalies, which are associated with masses close to the earth's surface (Telford *et al*, 1990, p. 26-27). Note that polynomial background subtraction using a zero degree polynomial, i.e. a straight line, is equivalent to average background subtraction, since least squares has the tendency to average. All these background subtraction techniques can be implemented in 1 D (along the scanning line) or, if data has been acquired over a grid, in 2D (over the horizontal plane).

The quality of the background subtraction generally depends on the choice of the width of the averaging window or the degree of the polynomial, respectively. However, even when a careful choice has been made, these techniques have fundamental drawbacks, which make them unsuitable for target identification. In the following, these drawbacks will be illustrated

---

[2] Originating in human activity.

[3] A time slice is an ensemble of data samples associated with the same arrival time.

using MA-BS as an example. Experience has shown that P-BS suffers from similar limitations.

Moving average background subtraction is essentially a “catch-22”[4]:

- Using a large averaging window, containing both background and target information, usually leads to ground reflection residuals, which mask part of or the entire target response signal. Even if the ground surface were perfectly flat, problems arise due to horizontal smearing of the target response. To get a better estimate of the local variations of the ground surface and to avoid smearing, there is a common tendency to work with a smaller averaging window.
- When using a small averaging window, containing mostly or only target information, less smearing and ground reflection residuals occur but now the target response signal is likely to become weaker and its shape is changed considerably. For small averaging windows, the horizontal smearing takes the form of two weak “ghost” hyperbolae, one above and the other below the actual target response hyperbola. These “ghost” hyperbolae are processing artifacts but might be mistaken as being part of the target response.

Figure 4.9 shows four synthetic B-scans illustrating some of these problems. The included A-scans are taken from the centers of the B-scans. The first B-scan (figure 4.9a) shows a diffraction hyperbola representative for the type of target response hyperbola observed in GPR data. The second B-scan (figure 4.9b) shows the same diffraction hyperbola but now superimposed with a horizontal event, simulating a perfectly flat ground reflection. The result of applying MA-BS with a large averaging window (extending over most of the B-scan) is shown in figure 4.9c. We see that the target response signal, while quite well recovered at the apex of the diffraction hyperbola, is smeared out to neighboring A-scans. The result of using a small averaging window (extending over a small fraction of the B-scan) is shown in figure 4.9d. In this case, we see from the A-scan that the target response signal at the apex of the hyperbola is not well recovered at all: both its amplitude and its shape differ considerably from those of the actual target response signal, i.e. the A-scan in figure 4.9a. Furthermore, two weak “ghost” hyperbolae have become visible. In conclusion, no matter how the width of the averaging window is chosen, moving average background subtraction will never be able to accurately recover the amplitude and the shape of the target response signal along the entire diffraction hyperbola.

---

[4] A dilemma or circumstance from which there is no escape because of two mutually incompatible conditions, both of which are necessary. The phrase comes from the title of a novel by Joseph Heller, set in the US air force in the Second World War: the hero, an American bombardier, wishes to avoid combat duty, to do which he has to be adjudged insane; but since anyone wishing to avoid combat duty is sane, he must therefore be fit for duty. (source: *The Oxford Encyclopedic English Dictionary*)

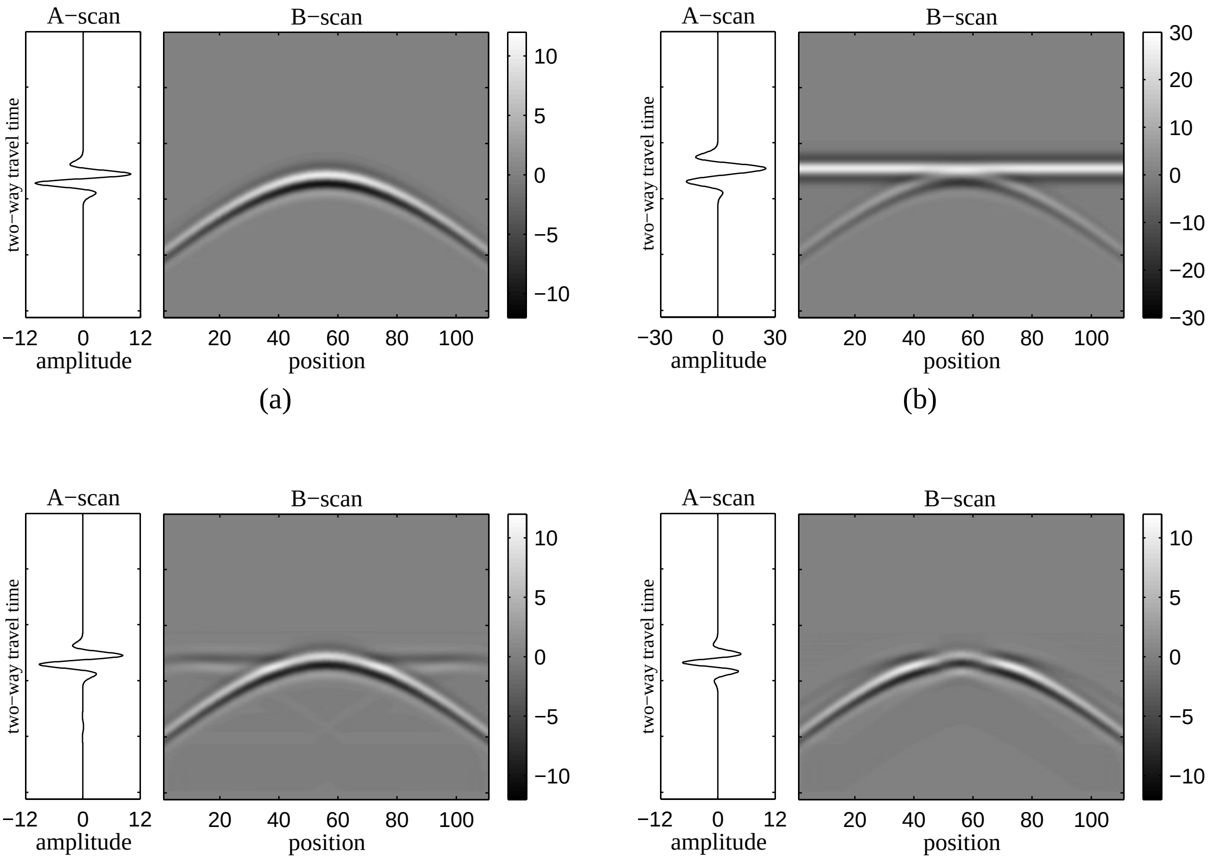

(a) (b)

(c) (d)

Figure 4.9: Illustration of the effect of window width on MA-BS: (a) Original diffraction hyperbola, (b) superposition of the hyperbola of (a) and a horizontal reflection event, (c) MA-BS result using a large averaging window, (d) MA-BS result using a small averaging window. The displayed A-scans are from the centers of the B-scans. A large window causes horizontal smearing of the target response, whereas a small window alters the amplitude and the shape of the target response.

These drawbacks led to the development of a new variant of MA-BS termed *weighted moving average background subtraction* (WMA-BS). As its name suggests, this technique uses weighted averaging[5] in the estimation of the background, thereby emphasizing A-scan samples that are part of the background while suppressing those that contain target information. Rather than being a one-step processing routine, this technique works in two stages: a preliminary background subtraction, which is used to find the anomalies and forms the basis for computing appropriate weights, and the weighted background subtraction. Besides, some auxiliary processing steps are necessary. The complete processing sequence goes as follows:

Step 1: *Subtraction of the direct wave signal* $\mathrm{s_d}(t)$ *determined from the metal sheet calibration from each A-scan of the data.*

---

[5] The weighted average of a set of numbers $\mathrm{x}_n \; (n = 1,\ldots,N)$ given the weights $\mathrm{W}_n \; (n = 1,\ldots,N)$ is defined as

$$\sum_{n=1}^{N} (\mathrm{W}_n \mathrm{x}_n) \Big/ \sum_{n=1}^{N} \mathrm{W}_n \,.$$

If all weights are set equal, the weighted average reduces to the mean.

Step 2: *Alignment of the ground reflection signal to compensate for the effect of varying antenna height above the ground surface (either due to topography or antenna movement by hand).* As a reference for the alignment a zero-crossing of the ground reflection signal is used. Depending on the expected depth of the target, a bias may have to be added to each A-scan to ensure that the reference zero-crossing occurs before the arrival of the target response signal. After the alignment, this bias is subtracted again.

Step 3: *Application of conventional moving average background subtraction (MA-BS) on the output data of step 2 using a small averaging window to locate targets and other anomalies*. The window width should be chosen such that little horizontal smearing occurs.

Step 4: *Computation of the envelope of each A-scan of the output data of step 3 using the Hilbert transform*. The envelope represents the instantaneous amplitude and essentially measures the reflectivity strength, which is proportional to the square root of the total energy of the signal at an instant in time (Yilmaz, 1987, p. 484).

Step 5: *Repetition of the moving average background subtraction on the output data of step 2 but this time using a large averaging window and weighted averaging, the weights for which are estimated from the output data of step 4.* The weight $W_n(t_i)$ applied to the i^{th} data sample of the n^{th} A-scan is computed as the ratio of the total instantaneous amplitude within the averaging window over the instantaneous amplitude associated with the data sample, i.e.

$$W_n(t_i) = \frac{\sum\limits_{k \in \text{window}} A_k(t_i)}{A_n(t_i)} \qquad (n \in \text{window}), \tag{4.22}$$

where $A_k(t_i)$ (k = A-scan number) denotes instantaneous amplitude. Equation (4.22) assigns large weights to data samples with a small contribution to the total instantaneous amplitude within the averaging window, i.e. they are treated as background. In contrast, smaller weights are assigned to data samples that have a significant contribution to the total instantaneous amplitude within the averaging window, i.e. they are treated as an anomaly. As a result of the weights less smearing occurs during the background subtraction and the amplitude and the shape of the target response signal is retained.

This procedure can also be implemented as an iterative procedure in which the background subtraction result of the previous iteration is used to compute the weights for the current iteration.

Let us return to the previous synthetic example to demonstrate the improvement achieved by using weights in the averaging process. Using the small window result of figure 4.9d to compute the weights for the weighted background subtraction yields the B-scan shown in figure 4.10. Comparison with the original diffraction hyperbola of figure 4.9a demonstrates that the WMA-BS managed to recover both the amplitude and the shape of the target response signal in all A-scans.

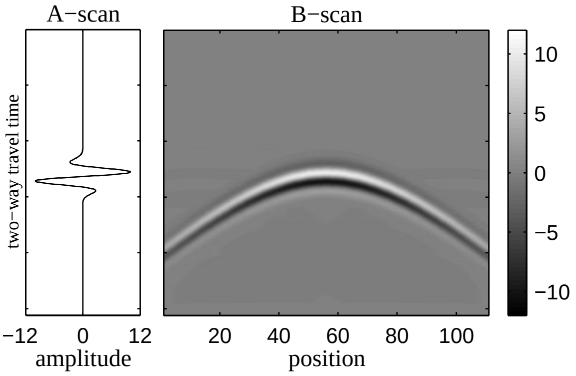

Figure 4.10: WMA-BS applied to the B-scan of figure 4.9b. The displayed A-scan is from the center of the B-scan. Comparison with figure 4.9a shows that the amplitude and shape of the target response signal are accurately recovered in all A-scans of the diffraction hyperbola.

Another example of WMA-BS is given in figure 4.11 detailing the various processing steps, from the initial B-scan to the final background subtraction result. The data, showing the co-polar response of a circular EPS (Expandable Polystyrene) disk buried 5 cm deep in dry sand, has been acquired with the IRCTR video impulse GPR. Note that the direct wave signal dominates over the ground reflection signal, which in turn dominates over the target response signal. More precisely, the peak-to-peak amplitude of the target response signal at the apex of the hyperbola is as low as –24 dB with respect to the direct wave signal, which gives an idea of the importance and challenge of a good background subtraction.

For comparison, figure 4.12 shows the much inferior background subtraction result obtained by a conventional MA-BS. For consistency, the latter used the same window width as the weighted background subtraction of the WMA-BS. While the conventional approach gives rise to residuals of both the direct wave signal and the ground reflection signal, as well as smears out the target response signal into neighboring A-scans, the WMA-BS is able to reduce these effects considerably.

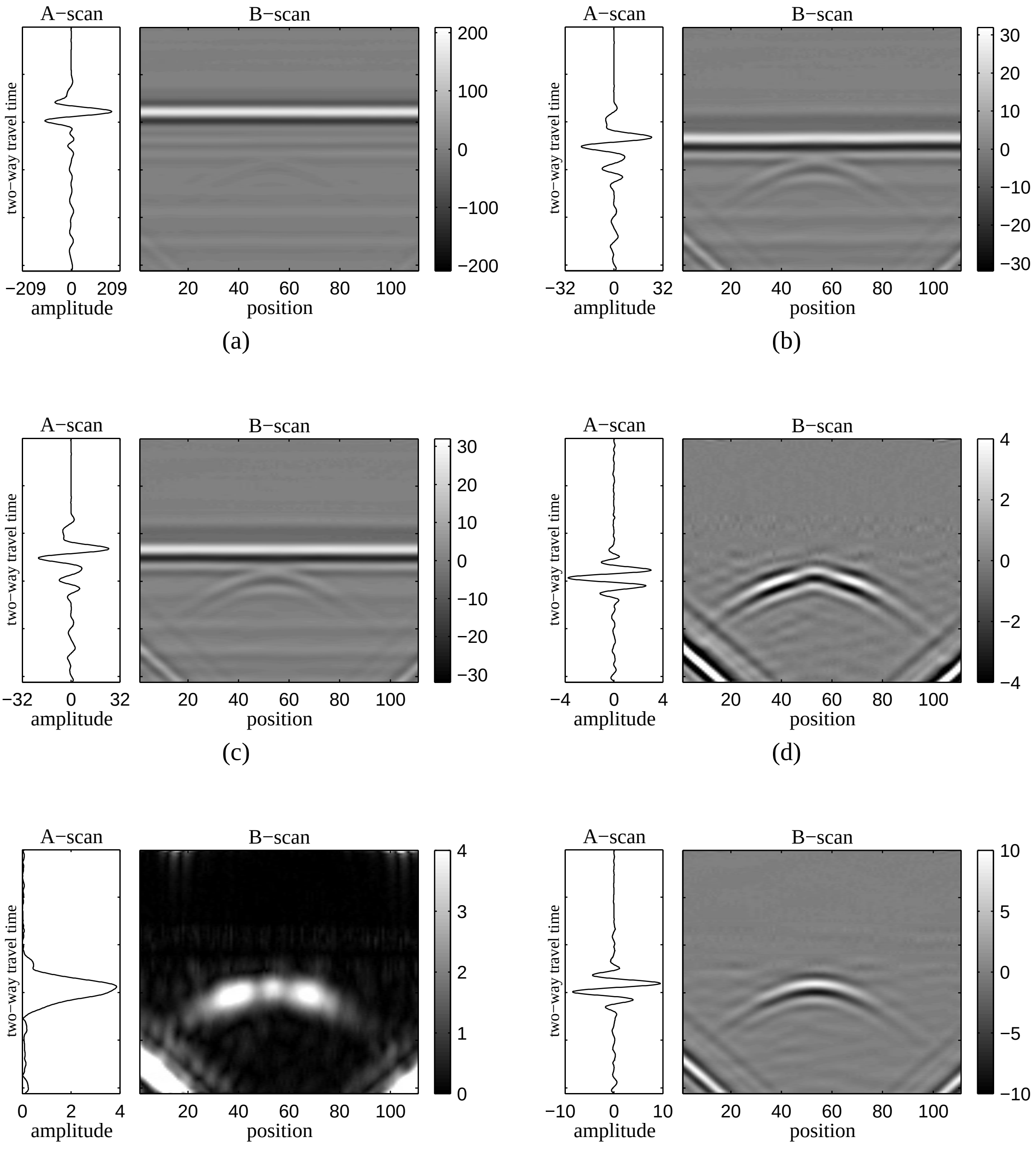

(a) (b) (c) (d) (e) (f)

Figure 4.11: Illustration of the various processing steps of WMA-BS using data acquired over a buried EPS disk: (a) Data after DC offset and noise reduction, (b) after the subtraction of the direct wave signal, (c) after the alignment of the ground reflection signal, (d) after MA-BS with a small averaging window, (e) after Hilbert transformation, (f) after the weighted background subtraction. The displayed A-scans are those at the apex of the target response hyperbola. The sloping reflection events at the lower corners of the B-scans are caused by the sidewalls of the sandbox in which the data were acquired.

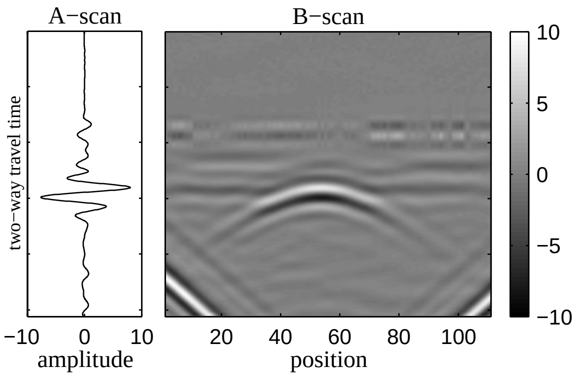

Figure 4.12: The inferior background subtraction result obtained by applying conventional MA-BS to the B-scan of figure 4.11a. The MA-BS used the same window width as the weighted background subtraction, which yielded the B-scan of figure 4.11f.

4.3.3 Target frame transformation

The target frame transformation algorithm is closely related to the physics of backscattering from an elongated target and hence this will be our starting point for explaining what the algorithm does and how it works. Since the target frame transformation involves coordinate transformations that are carried out in the frequency-domain, the backscattering is best described using the target transfer function.

In contrast to the target transfer function of a rotationally symmetric target, which may be represented as a scalar function such as eq. (2.12) or eq. (2.28), the target transfer function of an elongated target is a matrix

$$\mathbf{H}_{\mathrm{t}}(\omega)=\begin{bmatrix} \mathrm{H}_{\mathrm{t},xx}(\omega) & \mathrm{H}_{\mathrm{t},xy}(\omega) \\ \mathrm{H}_{\mathrm{t},yx}(\omega) & \mathrm{H}_{\mathrm{t},yy}(\omega) \end{bmatrix} \tag{4.23}$$

(Astanin and Kostylev, 1997, p.111), whose off-diagonal elements account for depolarization, i.e. cross-polar components in the backscattered field. In analogy to the scalar target transfer function, the target transfer function matrix relates the electric field $\mathbf{E}^i$ that is incident on the target to the backscattered field $\mathbf{E}^s$ according to the frequency-domain convolutional scattering model of eq. (2.10). Note that $\mathrm{H}_{\mathrm{t},xy}(\omega)=\mathrm{H}_{\mathrm{t},yx}(\omega)$ as a result of reciprocity (Ulaby and Elachi, 1990), i.e. the target transfer function matrix is symmetric.

An important property of the target transfer function matrix is that its elements depend on the reference frame in which the scattering is analyzed. In polarimetric GPR measurements, this reference frame is naturally defined by the two orthogonal linear polarizations, which are radiated and received. In the following, this reference frame will be called the antenna frame. When the antenna system of the GPR rotates with respect to the target, the antenna frame rotates with it and different matrix elements apply. Thus, the measured target response becomes a function of the orientation of the antenna system with respect to the target. Clearly, for target identification an orientation dependent target response is not very useful. In this case, it is necessary to analyze the scattering not in the antenna frame, but in a reference frame that is intrinsic to the target. This reference frame, called the target frame, is defined by the two natural polarization of the target, which are orthogonal to each other, though both may be elliptical. In the case of an elongated target, the natural polarizations are approximately linear and coincide with the long and short axis of the target. When the incident and backscattered fields are expressed in terms of the two natural target polarizations, the target transfer function matrix is diagonal, i.e.

$$\mathbf{H}_{\mathrm{t}}^{\mathrm{TF}}(\omega)=\begin{bmatrix}\lambda_1(\omega) & 0\\ 0 & \lambda_2(\omega)\end{bmatrix}, \tag{4.24}$$

where the superscript TF is used to specify the target frame and $|\lambda_1(\omega)|\geq|\lambda_2(\omega)|$ is assumed. Accordingly, if the incident field is polarized parallel to one of the natural target polarizations, no cross-polar field will be scattered. This is precisely what makes the target frame so special. The natural polarization that is associated with $\lambda_1(\omega)$ corresponds to the preferred natural polarization, which defines the preferential (long) scattering axis of the target. The target transfer function matrix in the target frame is related to the target transfer function matrix in the antenna frame through the target frame transformation, which is

$$\mathbf{H}_{\mathrm{t}}^{\mathrm{TF}}(\omega)=\mathbf{V}^{T}\mathbf{H}_{\mathrm{t}}(\omega)\mathbf{V}\ , \tag{4.25}$$

where the columns of $\mathbf{V}$ are simply the polarization vectors $\mathbf{v}_1$ and $\mathbf{v}_2$ describing the two natural polarizations of the target. Note that $\mathbf{V}^{-1}=\mathbf{V}^{T}$ as a result of the two natural polarizations being orthogonal to each other, i.e. **V** is a complex orthogonal matrix.

Now that the target frame transformation is defined, let us take a look at how we can apply it to scattering matrices measured with a polarimetric deming GPR system. For this purpose, we first need to define hardware models for a polarimetric transmitter and a polarimetric receiver. Such models may be obtained from simple generalizations of the point source/receiver models given by eqs. (4.2) and (4.3), namely from replacing the polarization vectors $\boldsymbol{u}_{\mathrm{TX}}$ and $\boldsymbol{u}_{\mathrm{RX}}$ of the transmitting and receiving antennas by a polarization matrix as follows:

$$\boldsymbol{u}_{\mathrm{TX}}=\boldsymbol{u}_{\mathrm{RX}}=\begin{bmatrix}1 & 0\\ 0 & 1\end{bmatrix}. \tag{4.26}$$

Note that the hardware models thus obtained represent an idealized polarimetric GPR system since the two transmitting channels are assumed to exhibit identical radiation characteristics and the two receiving channels identical reception characteristics. In practice, any differences in these characteristics need to be carefully compensated for, as will be discussed in more detail later on in the text.

Based on these polarimetric transmitter/receiver models and the frequency-domain convolutional scattering model of eq. (2.10), the measured polarimetric backscattering response of a buried elongated target may be written as

$$\mathbf{S}_{\mathrm{t}}(\boldsymbol{x}_{\mathrm{RX}},\omega)=\frac{T_{g\to a}\zeta(h_{\mathrm{RX}},d)T_{a\to g}}{2\sqrt{\pi}(h_{\mathrm{RX}}+d)(h_{\mathrm{TX}}+d)}\mathbf{H}_{\mathrm{t}}(\omega)\mathrm{W}(\omega)e^{-i(k_0h_{\mathrm{RX}}+k_0h_{\mathrm{TX}}+2k_1d)}\ , \tag{4.27}$$

where $\mathbf{S}_{\mathrm{t}}(\boldsymbol{x}_{\mathrm{RX}},\omega)$ is the scattering matrix whose elements are the target response signals measured for the four possible transmitting-receiving polarization combinations, i.e.

$$\mathbf{S}_{\mathrm{t}}(\boldsymbol{x}_{\mathrm{RX}},\omega)=\begin{bmatrix}\mathrm{S}_{\mathrm{t},xx}(\boldsymbol{x}_{\mathrm{RX}},\omega) & \mathrm{S}_{\mathrm{t},xy}(\boldsymbol{x}_{\mathrm{RX}},\omega)\\ \mathrm{S}_{\mathrm{t},yx}(\boldsymbol{x}_{\mathrm{RX}},\omega) & \mathrm{S}_{\mathrm{t},yy}(\boldsymbol{x}_{\mathrm{RX}},\omega)\end{bmatrix} \tag{4.28}$$

and $\mathrm{W}(\omega)$ refers to the effective radiated waveform in the frequency-domain. Note that since the target transfer function matrix $\mathbf{H}_\mathrm{t}(\omega)$ is symmetric, the same holds for the measured scattering matrix $\mathbf{S}_\mathrm{t}(\boldsymbol{x}_\mathrm{RX},\omega)$.

If we now apply the target frame transformation directly to the measured scattering matrix $\mathbf{S}_\mathrm{t}(\boldsymbol{x}_\mathrm{RX},\omega)$, we obtain

$$\begin{aligned}\mathbf{S}_\mathrm{t}^\mathrm{TF}(\boldsymbol{x}_\mathrm{RX},\omega) &= \mathbf{V}^T\mathbf{S}_\mathrm{t}(\boldsymbol{x}_\mathrm{RX},\omega)\mathbf{V}\\ &= \frac{T_{g\to a}\zeta(h_\mathrm{RX},d)T_{a\to g}}{2\sqrt{\pi}(h_\mathrm{RX}+d)(h_\mathrm{TX}+d)}\begin{bmatrix}\lambda_1(\omega) & 0\\ 0 & \lambda_2(\omega)\end{bmatrix}\mathrm{W}(\omega)e^{-\boldsymbol{i}(k_0h_\mathrm{RX}+k_0h_\mathrm{TX}+2k_1d)}\\ &\equiv \begin{bmatrix}\mathrm{K}_1(\omega) & 0\\ 0 & \mathrm{K}_2(\omega)\end{bmatrix}\end{aligned} \qquad (4.29)$$

which is the diagonal scattering matrix that would have been measured if the GPR had radiated and received the two natural polarizations of the target, i.e.

$$\boldsymbol{u}_\mathrm{TX} = \boldsymbol{u}_\mathrm{RX} = [\mathbf{v}_1 \quad \mathbf{v}_2] = \mathbf{V}\,. \qquad (4.30)$$

Accordingly, the scattering matrix in the target frame $\mathbf{S}_\mathrm{t}^\mathrm{TF}(\boldsymbol{x}_\mathrm{RX},\omega)$ is independent of the orientation of the target with respect to the antenna frame and hence well suited for target identification.

The question that remains to be answered is how can we find the polarization vectors $\mathbf{v}_1$ and $\mathbf{v}_2$ describing the two natural polarizations of the target. The answer follows from rewriting eq. (4.29) as

$$\mathbf{V}\begin{bmatrix}\mathrm{K}_1(\omega) & 0\\ 0 & \mathrm{K}_2(\omega)\end{bmatrix} = \mathbf{S}_\mathrm{t}(\boldsymbol{x}_\mathrm{RX},\omega)\mathbf{V}\ , \qquad (4.31)$$

demonstrating that $\mathbf{v}_1$ and $\mathbf{v}_2$ are in fact the complex eigenvectors of the measured scattering matrix $\mathbf{S}_\mathrm{t}(\boldsymbol{x}_\mathrm{RX},\omega)$, and $\mathrm{K}_1(\omega)$ and $\mathrm{K}_2(\omega)$ are its complex eigenvalues.

For a pulsed (time-domain) polarimetric GPR system the complete processing sequence to obtain an orientation independent target response goes as follows:

1) Combine the target response signals $\mathrm{s}_{\mathrm{t},xx}(\boldsymbol{x}_\mathrm{RX},t)$, $\mathrm{s}_{\mathrm{t},xy}(\boldsymbol{x}_\mathrm{RX},t)$, $\mathrm{s}_{\mathrm{t},yx}(\boldsymbol{x}_\mathrm{RX},t)$ and $\mathrm{s}_{\mathrm{t},yy}(\boldsymbol{x}_\mathrm{RX},t)$ measured for the four different transmitting-receiving polarization combinations into the time-domain scattering matrix in the antenna frame $\mathbf{s}_\mathrm{t}(\boldsymbol{x}_\mathrm{RX},t)$.
2) Transform $\mathbf{s}_\mathrm{t}(\boldsymbol{x}_\mathrm{RX},t)$ to the frequency-domain to obtain the frequency-domain scattering matrix in the antenna frame $\mathbf{S}_\mathrm{t}(\boldsymbol{x}_\mathrm{RX},\omega)$.
3) Diagonalize $\mathbf{S}_\mathrm{t}(\boldsymbol{x}_\mathrm{RX},\omega)$, i.e. find its two eigenvalues $\mathrm{K}_1(\omega)$ and $\mathrm{K}_2(\omega)$.
4) Transform $\mathrm{K}_1(\omega)$ and $\mathrm{K}_2(\omega)$ back to the time-domain to obtain the time-domain scattering matrix in the target frame $\mathbf{s}_\mathrm{t}^\mathrm{TF}(\boldsymbol{x}_\mathrm{RX},t)$.

It is important to understand that the target frame transformation in principle only applies to backscattering, i.e. a monostatic configuration, since the symmetry property of the backscattering matrix $\mathbf{S}_{\mathrm{t}}(\boldsymbol{x}_{\mathrm{RX}},\omega)$ is necessary to ensure that its eigenvectors are orthogonal and hence specify the natural polarizations of the target. A non-symmetric scattering matrix obtained from a bistatic configuration may be diagonalizable, however its eigenvectors will not be orthogonal and hence are not related to the target frame.

To give an example of target frame transformation, in the following results from analyzing polarimetric data of a buried metal tube acquired with the IRCTR video impulse GPR are presented. The metal tube, shown in figure 4.13, has a length of 11 cm, a diameter of 2 cm and was buried 10 cm deep in dry sand. Full polarimetric information was obtained by acquiring data for two orientations of the antenna system, one rotated 90 degrees from the other, yielding a total of four B-scans (two co-polar and two cross-polar ones). This was done for two different orientations of the metal tube. The first orientation, specified as *0 degrees*, corresponds to the situation where the long axis of the tube lies parallel to the y axis of the antenna frame, and the second orientation, specified as *45 degrees*, corresponds to the situation where the long axis of the tube lies at 45 degrees between the x and y axis of the antenna frame.

The polarimetric data for each orientation of the tube was then processed as follows. After initial DC offset correction and noise filtering, the background in each B-scan was removed using a two-iteration WMA-BS. Next, the target response signals $\mathrm{s}_{\mathrm{t},xx}(t)$, $\mathrm{s}_{\mathrm{t},xy}(t)$, $\mathrm{s}_{\mathrm{t},yx}(t)$, $\mathrm{s}_{\mathrm{t},yy}(t)$ for transmitting antenna positions right above the middle of the metal tube were combined into the scattering matrix $\mathbf{s}_{\mathrm{t}}(t)$, as illustrated in figure 4.14. The scattering matrices thus obtained for the two different orientations of the metal tube are compared in figure 4.15. As expected,

- the two scattering matrices are different (demonstrating the need for target frame transformation)
- the scattering matrices are symmetric
- the cross-polar elements $\mathrm{s}_{\mathrm{t},xy}(t)$ and $\mathrm{s}_{\mathrm{t},yx}(t)$ vanish for the tube orientation of *0 degrees*.

The latter observation indicates that for the tube orientation of *0 degrees* the antenna frame coincides with the target frame. Hence, target frame transformation of the scattering matrix for the tube orientation of *45 degrees* should produce the scattering matrix for the tube orientation of *0 degrees*. That this is actually the case is shown in figure 4.16, demonstrating that target frame transformation is capable of providing an orientation independent target response.

These are very good results, yet they do not give the complete picture. In practice, it is highly likely that when working with a “quasi-monostatic” antenna configuration such as that of the IRCTR video impulse GPR, there will be problems due to time offsets between the four target response signals that are combined into the scattering matrix. These time offsets are caused by small differences in, e.g., length of the connecting cables, but also by differences in length of the propagation paths to and from the target. The first source of error can be corrected for by calibration of the receiving channels and in fact, the target frame transformation example shown in figure 4.16 is the result of such a calibration, i.e. the timing in the cross-polar receiving channel was adjusted until the best transformation result was obtained. From the calibration, it was learned that time offsets as small as 50 ps degrade the transformation result noticeably. This is what makes the second source of error a serious limitation, because we have no good handle on it. To ensure that the propagation paths have equal length in the experiment with the metal tube, it was decided to combine the target response signals measured with the transmitting antenna right above the middle of the tube. This was possible because the data were acquired in a controlled indoor laboratory environment (described in more detail in chapter 5), where accurate knowledge of both the location of the metal tube and the position of the antenna system was available. In a real measurement scenario this will not be possible because obviously the exact location of the target is unknown and antenna positioning may be less accurate. Even if data is acquired on a very dense grid to determine the exact location of the target, it is unlikely that the target frame transformation result will be of the same quality as the one presented.

A workaround to this timing problem is to only apply the target frame transformation to the amplitude spectrum of the measured scattering matrix, i.e. to neglect the phase information, which is useful if the analysis of the target response continues in the frequency-domain. This concept was demonstrated with success by Farinelli and Roth (2003) who used the eigenvalues and the eigenvectors of the amplitude spectrum of the scattering matrix to determine the linearity and the orientation of targets.

Figure 4.13: The metal tube used in the target frame transformation example.

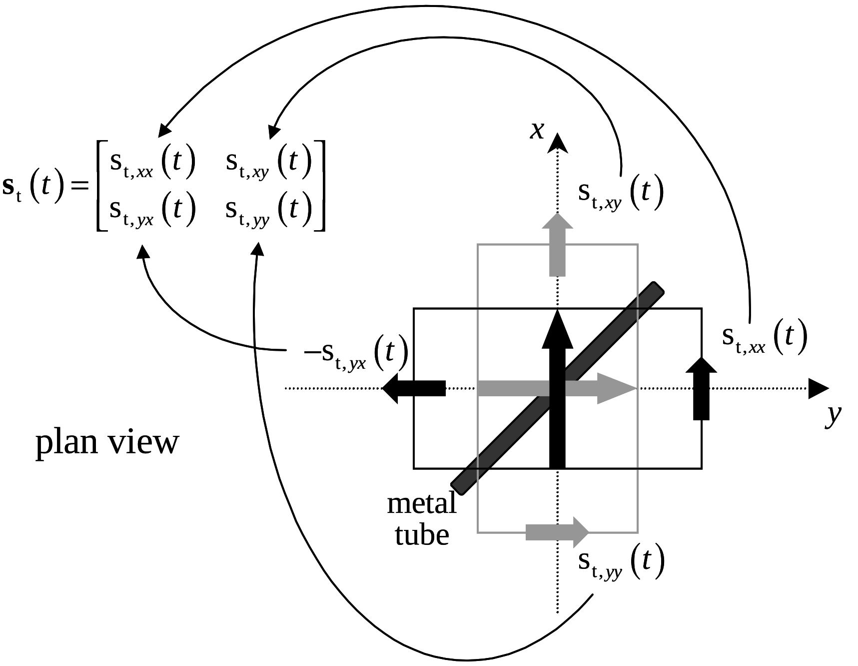

Figure 4.14: Illustration of how the target response signals measured by the IRCTR video impulse GPR are combined into the time-domain scattering matrix $\mathbf{s}_t(t)$. Each rectangle represents the antenna system, consisting of a transmitting antenna and two receiving loops (see figure 4.2), for one of the two antenna orientations for which data were acquired. The long arrow indicates the position and the polarization of the transmitting antenna and the small arrows indicate the positions and the polarizations of the receiving loops. The displayed *x* and *y* coordinate axes are those of the antenna frame.

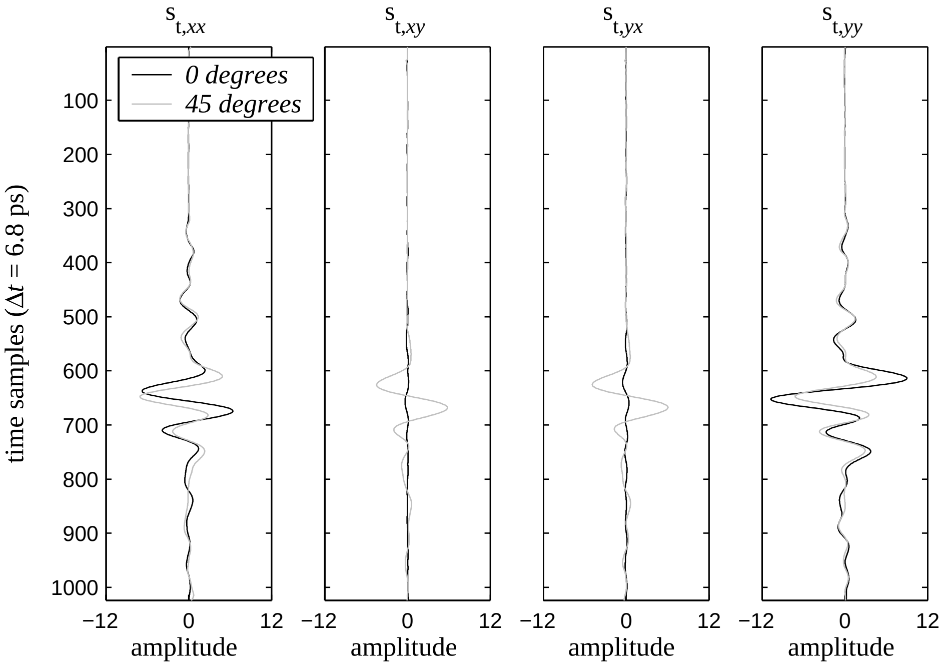

Figure 4.15: Comparison of the time-domain scattering matrices $\mathbf{s}_t(t)$ obtained for the two orientations of the metal tube (depth of burial: 10 cm).

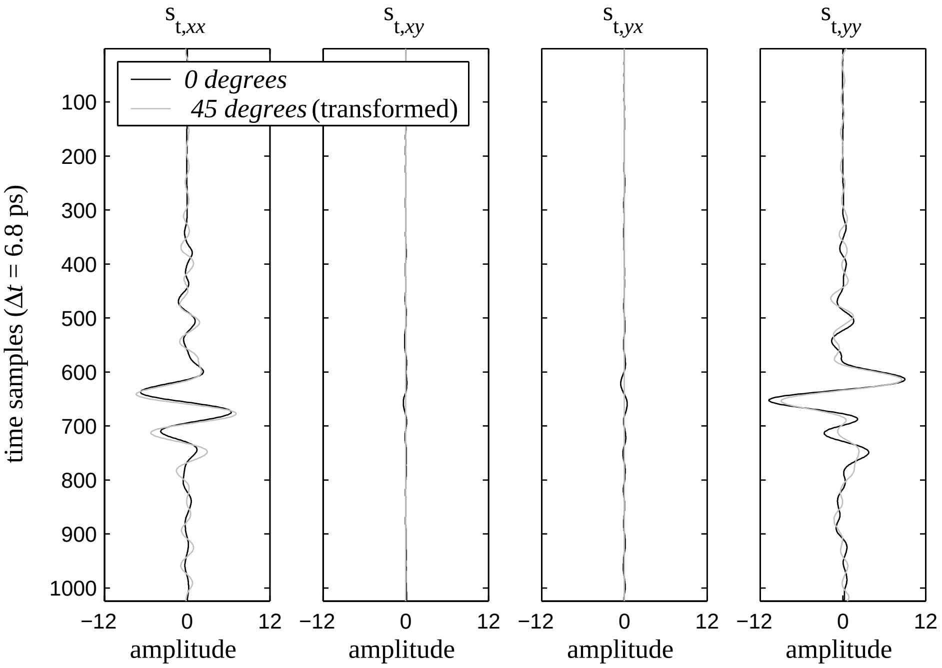

Figure 4.16: Results of transforming $\mathbf{s}_t(t)$ for the tube orientation of *45 degrees* into the target frame.

4.4 Deconvolution and Target Characterization

4.4.1 General

After preprocessing, the target response signal $s_t(\boldsymbol{x}_{RX}, t)$ at the apex of the target response hyperbola can be further processed to determine target characteristics, which in turn provide information on the likely identity of the target. Examples of such characteristics are the outer dimensions of the target, the target permittivity and the target depth. This section explains how the target characterization procedure for plane wave backscattering (sections 2.2.4 and 3.2) can be used with some modifications to estimate target characteristics from the extracted target response signal.

The first step is to fit the target response signal with an impulse response model approximating the scattering behavior of the target to be identified. The fitting is achieved through subset selection deconvolution of the effective radiated waveform, determined from the metal sheet calibration, from the target response signal, thereby yielding an impulse response $h(t)$, which satisfies

$$s_t(\boldsymbol{x}_{RX}, t) = h(t) \otimes w(t) \ . \tag{4.32}$$

The impulse response $h(t)$ consists of a fixed number of differentiation operators, the exact number of which is determined by the particular type of minelike target that is being assumed. A list of possible parameterizations for $h(t)$ and their relation to target characteristics is given in section 4.4.2.

Once the impulse response $h(t)$ has been estimated by subset selection deconvolution, its parameterization is used to invert for target size, e.g. the target cross-section, or for target material properties (dielectric minelike targets only), e.g. the relative permittivity of the target. As in the target characterization procedure for plane wave backscattering, for a dielectric minelike target the inversion is subject to ambiguity since the size and the material properties of the target are inherently unresolved. Accordingly, it is only possible to infer possible combinations of target characteristics. As before, this is achieved by specifying generic target material properties in the inversion for target size and vice versa.

As an alternative to inversion, the parameters of the estimated impulse response $\mathrm{h}(t)$ may be used as features in a classification scheme. As shown in chapters 2 and 3, differences in target size have a proportional effect on the impulse response parameters (see, e.g., figure 2.16), making it possible, in principle, to distinguish between targets. Note, however, that since the impulse response parameters also depend on antenna height, target depth and contrast (or soil properties for that matter), it is important that the classification rules take these dependencies into account or use feature combinations that are invariant to these factors, e.g. the length of the impulse response. Due to these reasons, feature based target classification is difficult to implement and has not been attempted in this thesis.

For either target identification approach (inversion or feature based classification), knowledge of antenna height[6] as well as target depth is required. The antenna height follows directly from the arrival time of the ground reflection signal and the target depth can be computed from the difference between the arrival time of the ground reflection signal and that of the target response signal. Whereas the arrival time of the target response signal is estimated as part of the impulse response estimation, the arrival time of the ground reflection signal needs to be estimated from a separate subset selection deconvolution of the effective radiated waveform from the background signal (excluding the direct wave signal). Alternatively, the arrival time of the ground reflection signal may be found from simple cross-correlation of these two signals. Subset selection deconvolution has the advantage of providing additional information on reflection strength, which may be related to the permittivity of the ground.

If the GPR is part of a multi-sensor system, the target depth information obtained like this may also be used to evaluate the information provided by the other sensors. As an example, let us consider the combination with an infrared camera. The depth range of operation of an infrared camera is limited to surface-laid targets and targets that are buried flush with the ground (Cremer, 2003). Hence the GPR depth estimate can be used to determine whether the target should or should not also be visible in the infrared images. This additional information is extremely useful to reinforce agreeing GPR and infrared detections and to correctly interpret GPR-only detections. For example, a surface-laid GPR-only detection is likely to be a false alarm. A deep GPR-only detection however should not be discredited unless other target information allows us to do so.

4.4.2 Impulse response models and their relation to target characteristics

As before, the subset selection deconvolution requires a priori information on the specific form of the impulse response $\mathrm{h}(t)$ to be estimated. Which form to choose depends on the type of minelike target that is considered to represent the scattering behavior of the target to be characterized. In chapters 2 and 3 a number of minelike targets have been introduced and

---

[6] Since the vertical offset between the transmitting antenna and the receiving antenna is constant, the heights of both antennas are fully determined by that of the receiving antenna, i.e. h_{RX} . Hence, **in this thesis antenna height always refers to** h_{RX} .

models for their target impulse responses have been derived. The general procedure for finding appropriate parameterizations for $\mathrm{h}(t)$ is to substitute these target impulse response models into the convolutional GPR models for surface-laid and buried minelike targets, eqs. (4.13) and (4.18), and compare the resulting equations with eq. (4.32). The parameterizations that follow are specified below. Note that these parameterizations are very similar to the ones presented in chapters 2 and 3 for the case of plane wave backscattering, where no GPR hardware is considered.

The circular metal disk

The target impulse response $\mathrm{h_t}(t)$ of a circular metal disk is given by eq. (2.31). Accordingly, an appropriate parameterization for the impulse response $\mathrm{h}(t)$ is one that consists of one differentiation operator, i.e.

$$\mathrm{h}(t)=\mathrm{h}_1\dot{\delta}(t-\tau_1) \ . \tag{4.33}$$

For a surface-laid metal disk, the coefficient h_1 and the time shift parameter τ_1 are

$$\mathrm{h}_1=-\frac{1}{2\pi(h_{\mathrm{RX}}+d)(h_{\mathrm{TX}}+d)}\frac{S_{xy}}{c} \ , \tag{4.34a}$$

$$\tau_1=\frac{h_{\mathrm{RX}}+h_{\mathrm{TX}}+2d}{c} \ , \tag{4.34b}$$

whereas for a buried metal disk,

$$\mathrm{h}_1=-\frac{T_{g\to a}\zeta(h_{\mathrm{RX}},d)T_{a\to g}}{2\pi(h_{\mathrm{RX}}+d)(h_{\mathrm{TX}}+d)}\frac{S_{xy}}{v_1} \ , \tag{4.35a}$$

$$\tau_1=\frac{h_{\mathrm{RX}}+h_{\mathrm{TX}}}{c}+\frac{2d}{v_1} \ . \tag{4.35b}$$

Remember that the depth *d* of a surface-laid target is negative by convention.

The homogeneous circular dielectric disk

The target impulse response $\mathrm{h_t}(t)$ of a homogeneous circular dielectric disk is given by eq. (2.23), suggesting the parameterization

$$\mathrm{h}(t)=\mathrm{h}_1\dot{\delta}(t-\tau_1)+\mathrm{h}_2\dot{\delta}(t-\tau_2) . \tag{4.36}$$

Note that this parameterization is only applicable when the disk is buried since eq. (2.23) has been derived from the Born approximation, which is strongly violated when the host medium is air, despite the phenomenological modifications that have been introduced. The impulse response parameters are

$$\mathrm{h}_1=-\frac{T_{g\to a}\zeta(h_{\mathrm{RX}},d)T_{a\to g}}{8\pi(h_{\mathrm{RX}}+d)(h_{\mathrm{TX}}+d)}\frac{v_{\mathrm{t}}^{eff}}{c^2}\Delta\varepsilon_r S_{xy} \ , \tag{4.37a}$$

$$\tau_1=\frac{h_{\mathrm{RX}}+h_{\mathrm{TX}}}{c}+\frac{2d}{v_1} \ , \tag{4.37b}$$

$$\mathrm{h}_2 = -\Gamma \mathrm{h}_1 \ , \tag{4.37c}$$

$$\tau_2 = \tau_1 + \frac{2l}{v_{\mathrm{t}}^{eff}} \ . \tag{4.37d}$$

The circular dielectric disk containing a thin air gap or a small piece of metal

When the circular dielectric disk contains an air gap or a small piece of metal, its target impulse response is given by eqs. (3.21)-(3.22). Accordingly, the parameterization for $\mathrm{h}(t)$ consists of two single and one double differentiation operator, i.e.

$$\mathrm{h}(t) = \mathrm{h}_1 \dot{\delta}(t-\tau_1) + \mathrm{h}_2 \dot{\delta}(t-\tau_2) + \mathrm{h}_3 \ddot{\delta}(t-\tau_3) \ . \tag{4.38}$$

Here, the impulse response parameters h_1 & τ_1 and h_2 & τ_2 relate to scattering from the disk body and are again given by eq. (4.37). The parameters h_3 & τ_3, describing the scattering from the air gap/metal piece, are

$$\mathrm{h}_3 = -\frac{T_{g\to a} \zeta(h_{\mathrm{RX}}, d) T_{a\to g}}{4\pi(h_{\mathrm{RX}}+d)(h_{\mathrm{TX}}+d)} \frac{1}{c^2} \xi V_{\mathrm{i}} \ , \tag{4.39a}$$

$$\tau_3 = \tau_1 + \frac{2l_{\mathrm{i}}}{v_{\mathrm{t}}^{eff}} \ . \tag{4.39b}$$

As for the homogeneous circular dielectric disk, this parameterization is only valid when the disk is buried.

The small metal sphere

The target impulse response $\mathrm{h}_{\mathrm{t}}(t)$ of a small metal sphere is given by eq. (3.16). The parameterization for $\mathrm{h}(t)$ that follows consists of a one double differentiation operator, i.e.

$$\mathrm{h}(t) = \mathrm{h}_1 \ddot{\delta}(t-\tau_1) \tag{4.40}$$

For a surface-laid sphere, the coefficient h_1 and the time shift parameter τ_1 are

$$\mathrm{h}_1 = -\frac{9}{8\pi(h_{\mathrm{RX}}+d)(h_{\mathrm{TX}}+d)} \frac{V_{\mathrm{s}}}{c^2} \ , \tag{4.41a}$$

$$\tau_1 = \frac{h_{\mathrm{RX}} + h_{\mathrm{TX}} + 2d}{c} \ , \tag{4.41b}$$

whereas for a buried sphere,

$$\mathrm{h}_1 = -\frac{9 T_{g\to a} \zeta(h_{\mathrm{RX}}, d) T_{a\to g}}{8\pi(h_{\mathrm{RX}}+d)(h_{\mathrm{TX}}+d)} \frac{V_{\mathrm{s}}}{v_1^2} \ , \tag{4.42a}$$

$$\tau_1 = \frac{h_{\mathrm{RX}} + h_{\mathrm{TX}}}{c} + \frac{2d}{v_1} \ . \tag{4.42b}$$

4.5 Discussion

This chapter introduced point source/receiver models and preprocessing algorithms that make the convolutional scattering models and the target characterization procedure presented in chapters 2 and 3 applicable to GPR data, thus opening the possibility to characterize a disk-shaped minelike target based on a single A-scan.

The presented point source/receiver models were easily incorporated into the time-domain convolutional scattering model derived in chapter 2. The resulting convolutional models for the GPR response of a surface-laid or buried minelike target constitute one of the main contributions of this thesis, since they represent the first convolutional GPR models, which give closed-form expressions for all components of the GPR chain, i.e. the hardware, the propagation to and from the target, and the target impulse response.[7] A useful property of these convolutional GPR models is that the radiation characteristics of the transmitting antenna and the reception characteristics of the receiver chain are conveniently expressed through a single term, namely the effective radiated waveform, which can be estimated accurately and fast using the presented metal sheet calibration procedure.

The point receiver model also allowed us to formulate an A-scan model, which represents the various signal components that contribute to a measured A-scan. These are the target response signal, which for backscattering along the vertical is described by the derived convolutional GPR models, the direct wave signal, the clutter signal, and noise. Prior to target characterization, all signal components other than the target response signal should be removed from the GPR data. It was shown that this is a very challenging preprocessing task, especially removing the direct wave signal and the ground reflection signal. Since these two signals dominate over the target response signal, it is important that they are removed well, albeit without changing the amplitude and shape of the target response signal, as this would render any target characterization attempt useless. In this respect, the weighted moving average background subtraction (WMA-BS) technique proved superior performance over other commonly used background subtraction techniques. The WMA-BS technique does not require straight-line data acquisition or a constant spatial sampling between A-scans and hence may well be used with handheld demining GPR systems. Since background subtraction is also required in many other GPR applications, e.g. locating buried utilities, the WMA-BS technique can be considered a very useful contribution to GPR data processing in general. Note, however, that when the GPR data are acquired with the antennas close to or on the ground, the first step of the algorithm, i.e. subtraction of the direct wave signal, needs to be omitted because then the coupling between the transmitting and the receiving antenna depends on the ground properties.

The target characterization procedure itself operates only on the A-scan at the apex of the target response hyperbola, an approach that is potentially very attractive for use with handheld demining GPR systems, where accurate antenna position information is unavailable. The procedure works in the same manner as the target characterization procedure for plane wave backscattering introduced in chapters 2 and 3, i.e. subset selection deconvolution followed by an inversion of the estimated impulse response.

The discussion on the target frame transformation may be considered a little side step, as this thesis is mostly concerned with rotationally symmetric targets. Still, it becomes an important issue when dealing with targets having a preferential scattering axis since their target response

---

[7] This is somewhat ironic, considering the basic form of these convolutional GPR models.

varies with orientation. Hence, measuring the full scattering matrix and transforming it into the target frame is essential to the correct identification of such targets. The target frame transformation examples of the buried metal tube demonstrated that an orientation independent target response can be obtained from polarimetric data acquired with the IRCTR video impulse GPR. Nevertheless, despite its seeming straightforwardness, routine application of target frame transformation is a non-trivial task simply because the co- and cross-polar components of the scattered field are measured at two distinct receiver positions. Hence, even after careful calibration of the receiving channels, small offsets in time remain a problem when combining target response signals measured by the different receiving loops into a scattering matrix. This problem can be avoided by applying target frame transformation only to the amplitude spectrum of the scattering matrix in which case timing becomes irrelevant.

This chapter completes the theoretical part of this thesis and we now have a set of tools consisting of

- a metal sheet calibration procedure (section 4.2.4)
- data preprocessing algorithms (section 4.3)
- a target characterization procedure (section 4.4)

which together can be used to determine the size or the material properties of a circular disk-shaped minelike target from GPR data and estimate its depth of burial. The following chapter describes laboratory measurements with the IRCTR video impulse GPR that were carried out to further validate these tools and determine the accuracy with which target characteristics and depth can be estimated.

CHAPTER 5

EXPERIMENTAL RESULTS AND VALIDATION

This chapter presents the results of a series of GPR experiments, which was designed to evaluate the performance of the target characterization procedure presented in the previous chapter (section 4.4) and validate the convolutional GPR models on which it is founded. These experiments are complementary to the FDTD results presented in chapters 2 and 3, which already demonstrated that in principle it is possible to characterize a buried minelike target very accurately from its backscattering response. The test conditions for the experimental validation, however, are much more challenging since the performance of the target characterization procedure does not only relate to the soundness of the procedure itself but also depends on the quality of the radar calibration and that of the GPR data after preprocessing, i.e. the level of clutter and noise that could not be removed. In addition, the characterization procedure now relies on antenna height and target depth estimates, which are determined from the arrival times of the ground reflection and the target response.

The experiments were carried out with the IRCTR video impulse GPR at an indoor experimental facility, where data were acquired over a set of surface-laid and buried minelike test targets. The test targets included a circular metal disk, two small metal spheres, a set of four differently-sized circular EPS (Expandable Polystyrene) disks, and a set of three circular Teflon disks with and without internal structure. The reason for working with these targets rather than mine simulants used in other mine detection research (Fortuny-Guasch *et al*, 2001) was that they were readily available and with precisely known size and material properties. Knowledge of these properties is important in two ways. First, to have a reference against which the output of the target characterization procedure can be compared, and second, to be able to specify the generic material properties, which are required in the inversion for target size.

The chapter is divided into three sections. Section 5.1 describes the data acquisition including information about the experimental facility, a detailed description of the test targets and an overview of the data acquisition parameters. The acquired data were analyzed using the preprocessing algorithms and the target characterization procedure described in sections 4.3 and 4.4, respectively, the results of which are presented in section 5.2. The presented results include examples of target responses after preprocessing, subset selection deconvolution results and inversion results. The overall performance of the target characterization procedure is summarized in section 5.3.

For convenience, the wording of this chapter will not distinguish between the *target response*, i.e. the scattered field, and the *target response signal*, i.e. the signal produced by the scattered field, since this chapter deals exclusively with GPR data.

5.1 Data Acquisition

5.1.1 Description of the experimental facility

The data were acquired at the indoor experimental facility shown in figure 5.1 consisting of a 2.5 m by 2.5 m sandbox made of plywood and a computer controlled *x*-*y*-*z* scanner for sub-millimeter accurate antenna positioning.

The sandbox is filled with fine dry sand. Its relative dielectric permittivity ε_r in the frequency range of 0.5-3.0 GHz was estimated from laboratory coaxial waveguide measurements (Gorriti, 2004), the results of which are shown in figure 5.2. As expected for dry sand, ε_r is fairly constant over the measured frequency band with losses close to zero. The small permittivity "jumps" are likely a result of sample inhomogeneities in the form of air gaps. Averaging over frequency yields a permittivity estimate of $\varepsilon_r \approx 2.58 - \boldsymbol{i}\,0.045$. Based on this estimate, it is reasonable to treat the sand as a lossless host medium. For comparison, the sand permittivity was also estimated from the magnitude of the ground reflection signal in the GPR data, which, neglecting losses, gave $\varepsilon_r \approx 2.6$. All inversion results presented in this chapter have been obtained with this real value for the sand permittivity.

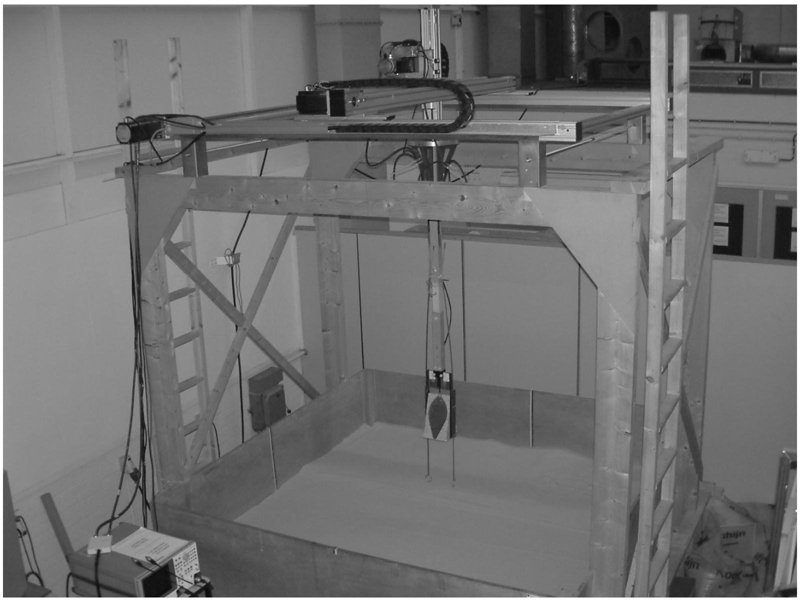

Figure 5.1: The indoor experimental facility.

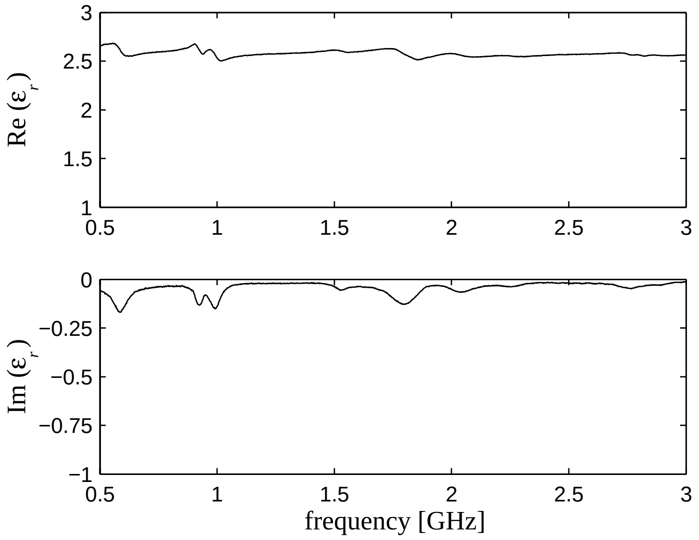

Figure 5.2: Laboratory estimates of the real (energy storage) and the imaginary (energy dissipation) part of the relative dielectric permittivity of the sand at the experimental facility.

5.1.2 Description of the test targets and burial conditions

Based on their material composition, the test targets form three groups:

- Metal targets
- Expandable Polystyrene (EPS) disks
- Teflon disks.

The metal targets (figure 5.3) include a circular metal disk and two small metal spheres. The metal disk has the same dimensions as *Metal Disk 1* whose response has been simulated by FDTD (see section 2.3), and accordingly is referred to by that same label. The small metal spheres – hereinafter referred to as *Metal Sphere 1* and *Metal Sphere 2* – have a radius of 0.8 and 0.95 cm, respectively.

The EPS disks (figure 5.4) - hereinafter referred to as *EPS Disk 1* through *4* - have a radius between 4 and 6.25 cm, and a height of either 3.8 or 4.8 cm. The disks have been cut out of sheets of Expandable Polystyrene having a relative dielectric permittivity of $\varepsilon_{r,\mathrm{t}} \approx 1$ and negligible losses as indicated by its low loss tangent, $\tan\delta < 5*10^{-5}$ (BASF, 2001). Consequently, the EPS disks can be treated as homogeneous dielectric disks with no losses.

The three Teflon disks (figure 5.5) – hereinafter referred to as *Teflon Disk 1* through *3* - were used to study the effect of internal target structure on the target response. All three disks have a radius of 5 cm and a height of 4 cm but differ internally: *Teflon Disk 1* is solid, *Teflon Disk 2* contains a thin circular air gap ($V_\mathrm{i} = 50.3\ \mathrm{cm}^2 \times 1\ \mathrm{cm}$, $l_\mathrm{i} = 1.5\ \mathrm{cm}$), and *Teflon Disk 3* has a small cylindrical metal insert ($V_\mathrm{i} = 2.7\ \mathrm{cm}^3$, $l_\mathrm{i} = 0.75\ \mathrm{cm}$). Teflon has very well-defined electrical properties and is known for its almost frequency independent relative dielectric permittivity of $\varepsilon_{r,\mathrm{t}} \approx 2.1$ and its small loss tangent, $\tan\delta < 2*10^{-4}$ (Von Hippel, 1954, p.332).

The material compositions, shapes and sizes of all test targets are summarized in table 5.1.

Data were acquired for several different target depths. In general, each test target was considered both surface-laid and when buried 5 cm deep with the exception of the EPS disks, which were only considered buried. For *EPS Disk 1* additional data were acquired for a burial depth of 10 cm for which the ground reflection and the target response are separated in time. For the buried *Metal Disk 1*, measurements were only done for target depths of 10 and 15 cm in order to avoid its target response being “polluted” by strong multiple reflections between the target and the sand surface.

To avoid ambiguities due to unknown burial conditions, great care was taken when burying the targets. First, a bucket without bottom was pushed into the sand to provide side support while digging a hole. The target was then placed into the hole and a level was used to ensure that it is not tilted. Next, the target was covered by sand and the bucket removed slowly. After burial, the sand was flattened by sweeping the edge of a large metal plate across the sand surface. The actual target depth was measured by sticking a ruler into the sand until it touched the target. The depth was measured after GPR data had been acquired to avoid additional disturbance of the sand. In all cases the actual target depths differed only by a few millimeters from the anticipated target depths.

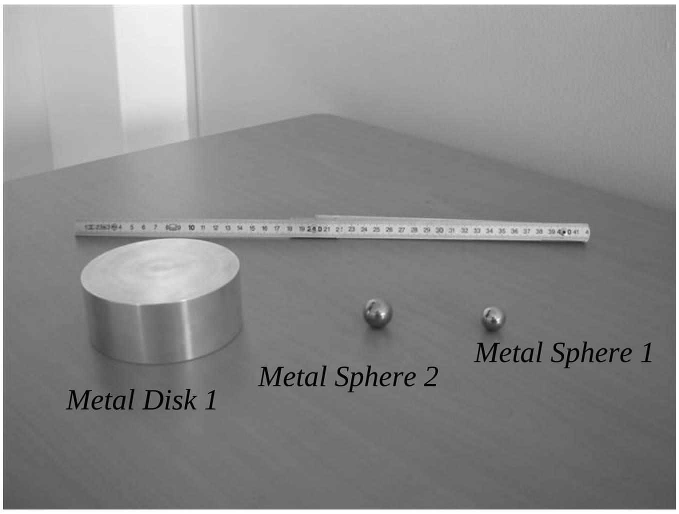

Figure 5.3: The metal targets.

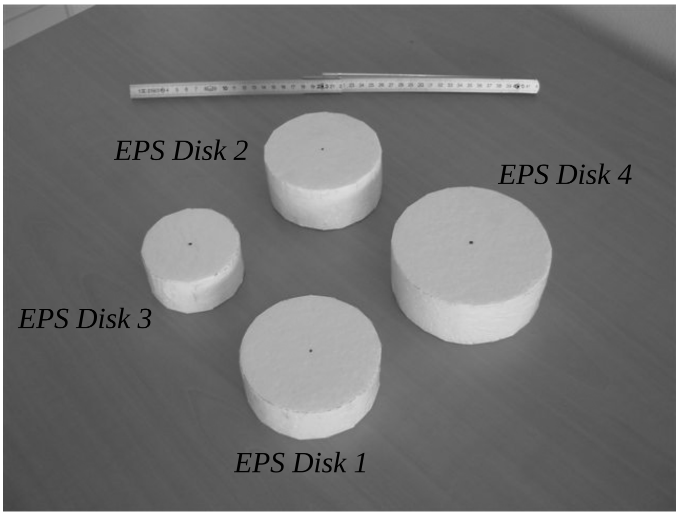

Figure 5.4: The Expandable Polystyrene disks.

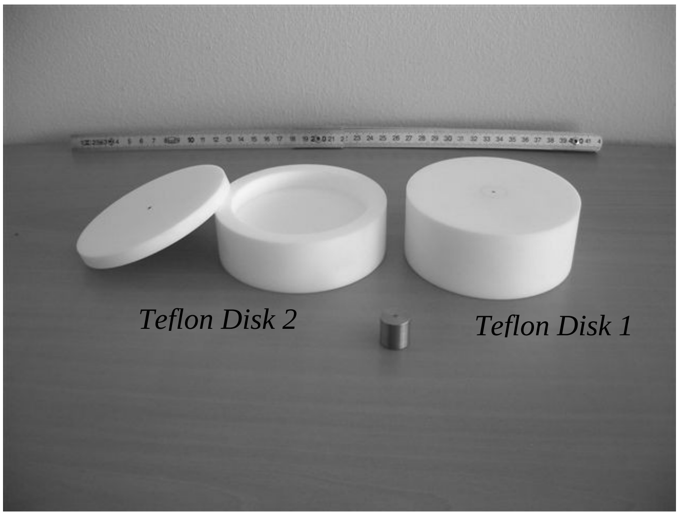

Figure 5.5: The Teflon disks. The small metal cylinder can be inserted into *Teflon Disk 1*, which is then referred to as *Teflon Disk 3*.

Table 5.1: Description of the test targets.

Target Name	**Material Composition**	**Shape**	**Outer Dimensions**		
			radius [cm]	height *l* [cm]	aspect ratio*
Metal Disk 1	metal	circular disk	5.0	4.0	1.25
Meta Sphere 1	metal	sphere	0.8	n/a	n/a
Metal Sphere 2	metal	sphere	0.95	n/a	n/a
EPS Disk 1	Expandable Polystyrene	circular disk	5.0	3.8	1.32
EPS Disk 2	Expandable Polystyrene	circular disk	5.0	4.8	1.04
EPS Disk 3	Expandable Polystyrene	circular disk	4.0	3.8	1.05
EPS Disk 4	Expandable Polystyrene	circular disk	6.25	4.8	1.30
Teflon Disk 1	Teflon	circular disk	5.0	4.0	1.25
Teflon Disk 2	Teflon with thin air gap	circular disk	5.0	4.0	1.25
Teflon Disk 3	Teflon with small metal insert	circular disk	5.0	4.0	1.25

* Ratio of the radius over the height.

5.1.3 Data acquisition procedure and parameters

The data were acquired with the IRCTR video impulse GPR presented in section 4.1.2 using the procedure illustrated in figure 5.6.

For each target, a 1.1 m long B-scan traversing the center of the target was taken in step mode along the *x*-direction of the scanner with a spatial sampling interval Δx of 1 cm between A-scans. The A-scans were acquired using a 7 ns time window of 1024 time samples corresponding to a time sampling interval Δt of approximately 6.8 ps. Stacking of 128 was applied to each A-scan sample to reduce random noise. For buried targets, B-scans were taken at two antenna heights, namely 15 cm and 20 cm; for surface-laid targets, an antenna height of 25 cm was chosen. Since all test targets are rotationally symmetric, only one orientation of the antenna system was considered, namely the one in which the transmitting antenna radiates a *y*-polarized wave. All examples and results presented in this chapter refer to the data acquired with the co-polar receiving loop of the antenna system.

The experiments were carried out over several days. Hence, to avoid degradation of performance due to system instabilities, the IRCTR video impulse GPR was calibrated on every measurement day using the procedure described in section 4.2.4.

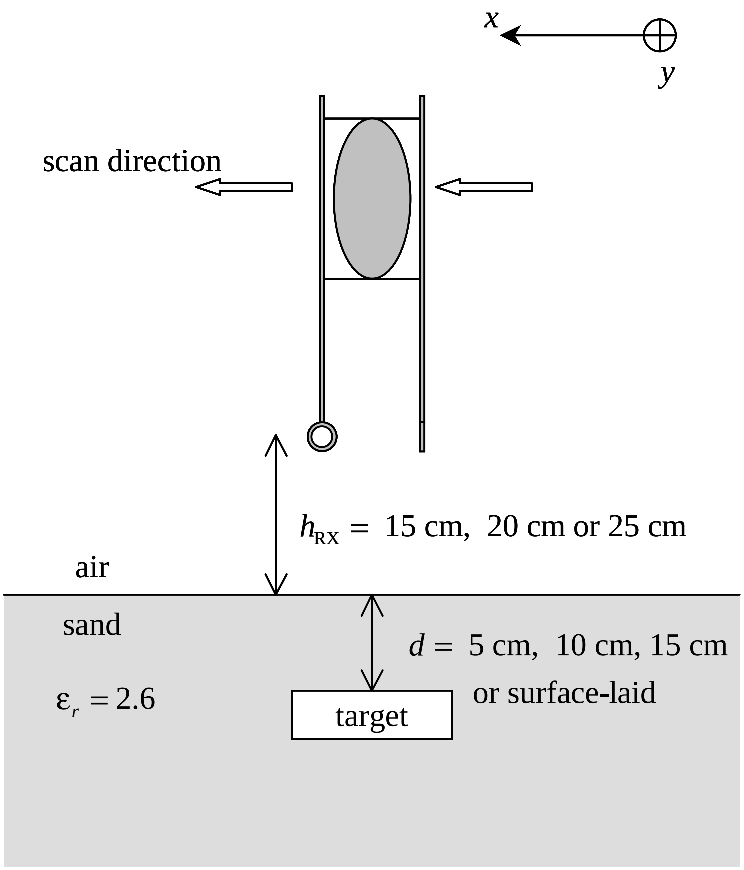

Figure 5.6: Illustration of the measurement procedure.

5.2 Data Analysis

5.2.1 General

The acquired data were processed using the algorithms presented in sections 4.3 and 4.4. This included DC offset correction, noise reduction, background subtraction, subset selection deconvolution, antenna height and target depth estimation, and inversion for target size and material properties (EPS disks only).

In the following sections, the results of the analysis are presented and illustrated by selected data examples. The results are presented by target type, since this was found most suitable for elucidating target specific scattering behavior. But before going over to the results, some general remarks concerning all targets are discussed below.

Since the scattering models underlying the target characterization procedure apply to backscattering along the vertical, only the target response at the apex of the target response hyperbola was analyzed. To give an idea of how the target response changes away from the apex, figure 5.7 shows the response of *Metal Disk 1*, in this case buried 10 cm deep, for increasing distances (0 to 15 cm) from the apex of the target response hyperbola measured using an antenna height of 15 cm. For the purpose of comparison, the responses have been aligned (figure 5.7a) and normalized with respect to the peak-to-peak amplitude (figure 5.7b).

We see that the shape of the target response is hardly changed as the distance from the apex increases, while its magnitude experiences a rapid decay down to less than half of its value at the apex. This is to be expected, since at the air-sand interface the radiated wave is refracted towards and the scattered wave away from the vertical, thus making the wave propagation along vertical the dominant propagation in the ground. Another factor, which contributes to this observation, is that any receiving antenna has a tendency to average the scattered field over its aperture. In conclusion, the example indicates that the target response away from the apex carries little additional target information. The extraction of this additional target information is complicated by the fact that any observed change in the target response is also in part due to the non-isotropic radiation characteristics of the transmitting antenna. Hence, in view of target identification, the vertical backscattering response is by far the most important target response.

Depending on whether a buried or a surface-laid test target was analyzed, different background subtraction techniques were used. A two-iteration WMA-BS (section 4.3.2) with an initial window of 21 A-scans and a window of 101 A-scans for the weighted subtraction was applied to the data acquired over the buried test targets. In contrast, when the test targets were surface-laid, the background was measured by taking a B-scan without the target being present and then subtracted from the B-scan measured in the presence of the target. Doing so, a near-to-perfect isolation of the target response can be achieved. Needless to say, this background subtraction technique can only be applied in the laboratory.

Despite the careful burial of the targets, some disturbance of the sand could not be avoided and resulted in clutter, which the WMA-BS was unable to remove. The clutter manifested itself as additional amplitude peaks before the arrival of the actual target response, an example of which is given in figure 5.8a showing the response of *EPS Disk 1* when buried 5 cm deep for an antenna height of 15 cm. Besides the additional amplitude peaks, the sand disturbance is also likely to cause some distortion of the first part of the target response. Consequently, it was decided to let the subset selection deconvolution algorithm only fit the part of the target response following its first peak, as illustrated in figure 5.8b. Experience showed that the omission resulted in a less well-posed subset selection deconvolution but nevertheless gave better impulse response estimates, especially with regard to the impulse response length. The omission of the first amplitude peak was not necessary for *Metal Disk 1* exhibiting a very strong target response for which the distortion becomes negligible.

The inversion of the impulse response obtained by subset selection deconvolution for target characteristics and target depth requires knowledge of the antenna height above the ground. For all inversions, the antenna height was estimated from the GPR data itself. This was achieved by estimating the arrival time of the ground reflection with a separate subset selection deconvolution of the effective radiated waveform from the ground reflection signal, an example of which is given in figure 5.9. To model the ground reflection signal, the subset selection deconvolution assumes an impulse response model consisting of a single spike, i.e. the impulse response is assumed to have one non-zero coefficient. The ground reflection signal to which the deconvolution is applied is determined as part of the background subtraction. Note that apart from its use to estimate antenna height, the arrival time of the ground reflection can be used together with the arrival time of the target response to determine whether a target is surface-laid or buried, allowing to choose the appropriate impulse response parameterization for the inversion. Of course this was not an objective of the analysis presented here, but would be so for field operation of the GPR, where no information on whether the target is surface-laid or buried is available.

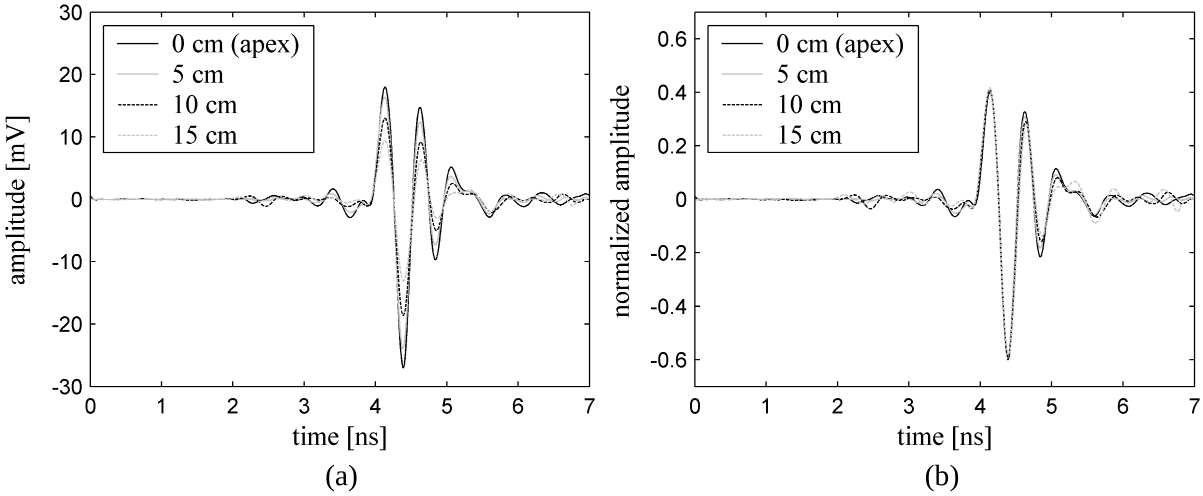

Figure 5.7: Response of *Metal Disk 1* ($d \approx 10$ cm & $h_{RX} \approx 15$ cm) at various distances (0, 5, 10 & 15 cm) from the apex of the target response hyperbola:
(a) aligned
(b) aligned and normalized with respect to the peak-to-peak amplitude.

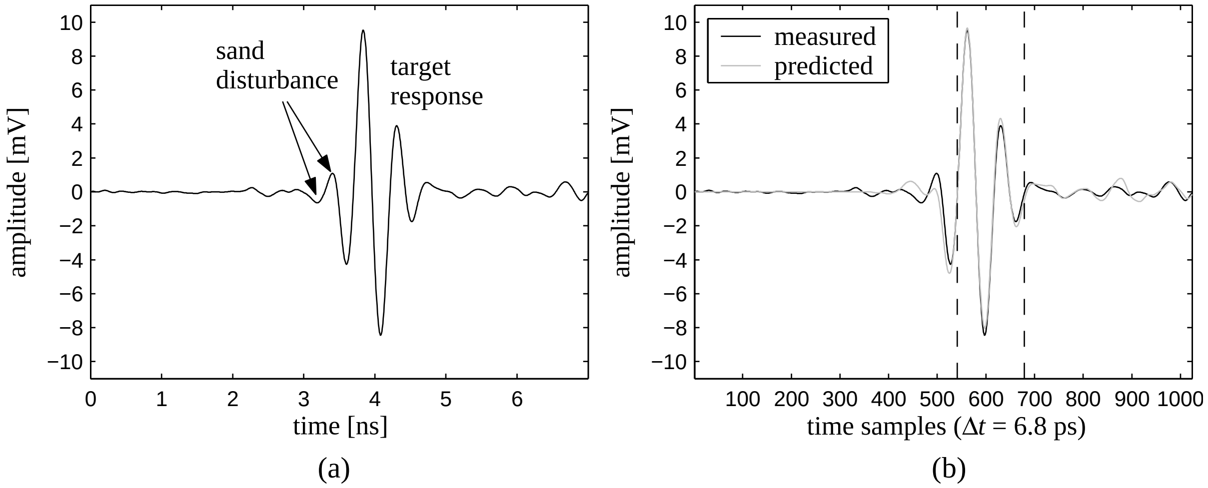

Figure 5.8: Response of *EPS Disk 1* ($d \approx 5$ cm & $h_{RX} \approx 15$ cm):
(a) The sand disturbance causes additional amplitude peaks before the arrival of the actual target response.
(b) Data fit between the predicted (deconvolution) and the measured target response. Only the part of the response between the dashed lines was fit by the subset selection deconvolution algorithm.

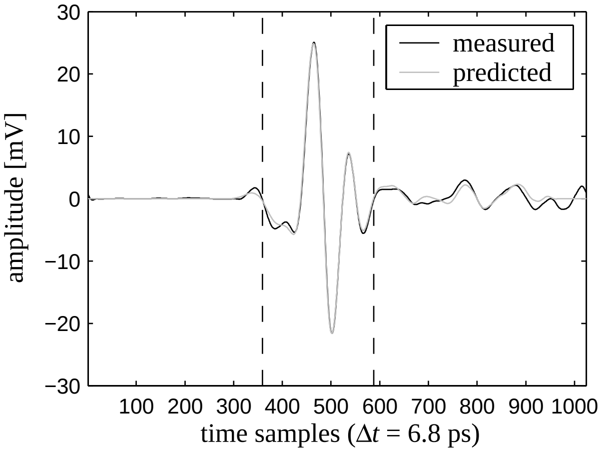

Figure 5.9: Example of deconvolving the effective radiated waveform from the measured ground reflection signal (determined as part of the background subtraction). The figure shows the data fit between the predicted (deconvolution) and the measured ground reflection signal. The dashed lines define the part of the signal, which was fit by the subset selection deconvolution algorithm. Note that the predicted ground reflection also well describes the reflected antenna ringing (between time samples 750 and 900). The time shift obtained from this type of deconvolution was used to estimate the antenna height h_{RX}.

5.2.2 Metal targets

Circular metal disk

Figure 5.10 gives an example of the response of *Metal Disk 1*, in this case buried 10 cm deep and measured with an antenna height of 15 cm. According to the convolutional GPR model for buried targets, eq. (4.18), the shape of the target response is independent of the burial depth and the antenna height. Measurements for other depths and/or antenna heights demonstrated that the shape of the response is indeed consistent if the depth is large enough for the response to be unaffected by multiple reflections between the target and the sand surface. The shape consistency is illustrated in figure 5.11 showing the response of *Metal Disk 1* for various depths and antenna heights. For easy comparison, the responses have been aligned and normalized with respect to the peak-to-peak amplitude.

The results of applying subset selection deconvolution to the responses of *Metal Disk 1* are listed in table 5.2. The differences in the impulse response coefficient h_1 can solely be attributed to the different target depths and antenna heights and in principle should obey the spreading term in eq. (4.18), which is

$$\frac{\zeta(h_{\mathrm{RX}},d)}{2\sqrt{\pi}\,(h_{\mathrm{RX}}+d)(h_{\mathrm{TX}}+d)}. \tag{5.1}$$

To analyze the ability of the spreading term to predict the changes in h_1, the coefficients h_1 from table 5.2 were plotted against eq. (5.1), the result of which is shown in figure 5.12. To make a comparison possible, the coefficients h_1 and the spreading term were normalized with respect to $d = 10\ \mathrm{cm}$ & $h_{\mathrm{RX}} = 15\ \mathrm{cm}$. From the figure, we see that the spreading term well predicts the differences in h_1 that result from changes in target depth and antenna height.

The response of *Metal Disk 1* is well modeled by an impulse response consisting of one differentiation operator, as indicated by figure 5.13 showing the deconvolution data fit for the target response of figure 5.10. This confirms again that specular scattering by a circular metal disk differentiates the waveform of the incident field.

The deconvolution results of table 5.2 were inverted for target depth and target size (disk radius) using the impulse response parameterizations of eqs (4.34)-(4.35) and antenna height estimates obtained from the arrival time of the ground reflection. The inversion results thus obtained are listed in table 5.3 and demonstrate a good agreement between the inferred and the true[1] values (shown in parentheses). Overall, the inversion results demonstrate that

1) it is possible to infer antenna height, target depth and disk radius with millimeter accuracy
2) there is a tendency to slightly overestimate the disk radius, especially when *Metal Disk 1* is surface-laid.

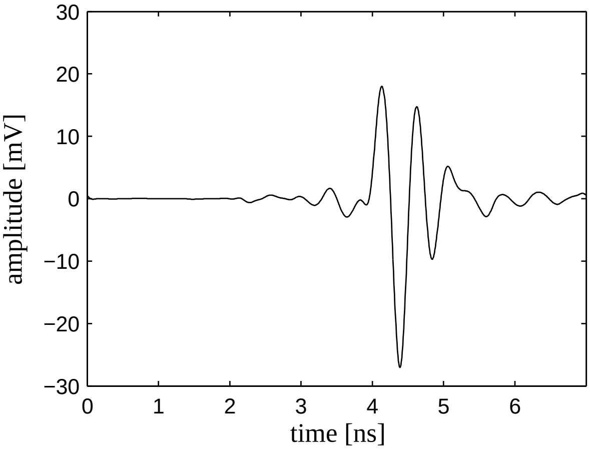

Figure 5.10: Response of *Metal Disk 1* ($d \approx 10$ cm & $h_{\mathrm{RX}} \approx 15$ cm).

---

[1] The “true” target depths and antenna heights were measured with a ruler and hence are not entirely free of measurement error.

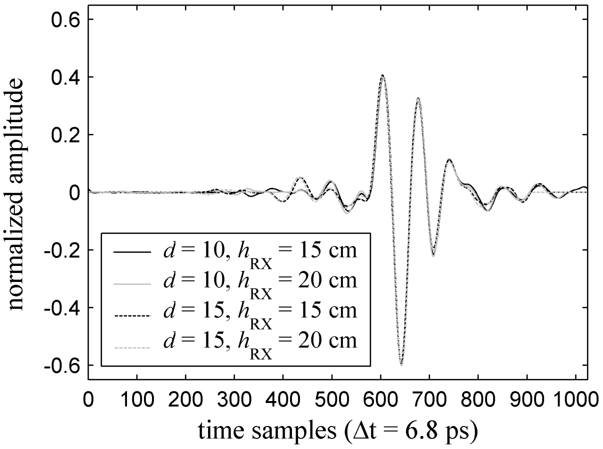

Figure 5.11: Comparison of the responses of *Metal Disk 1* for various depths and antenna heights. The responses have been aligned and normalized with respect to the peak-to-peak amplitude.

Table 5.2: Subset selection deconvolution results for *Metal Disk 1*.
Assumed impulse response model: eq. (4.33).

Target Depth	**Antenna Height**	**Impulse Response Parameters**			**Rel. Error**
d [cm]	h_{RX} [cm]	h_1 [$*10^{-5}$]	τ_1 samples	τ_1 [ns]	
-4.0[*]	25.0	-50.0	362	2.470	0.12
10.1	14.9	-36.3	460	3.141	0.11
10.1	19.9	-27.0	508	3.469	0.12
15.0	15.0	-31.2	536	3.661	0.14
15.0	20.0	-23.9	583	3.982	0.14

[*] Surface-laid.

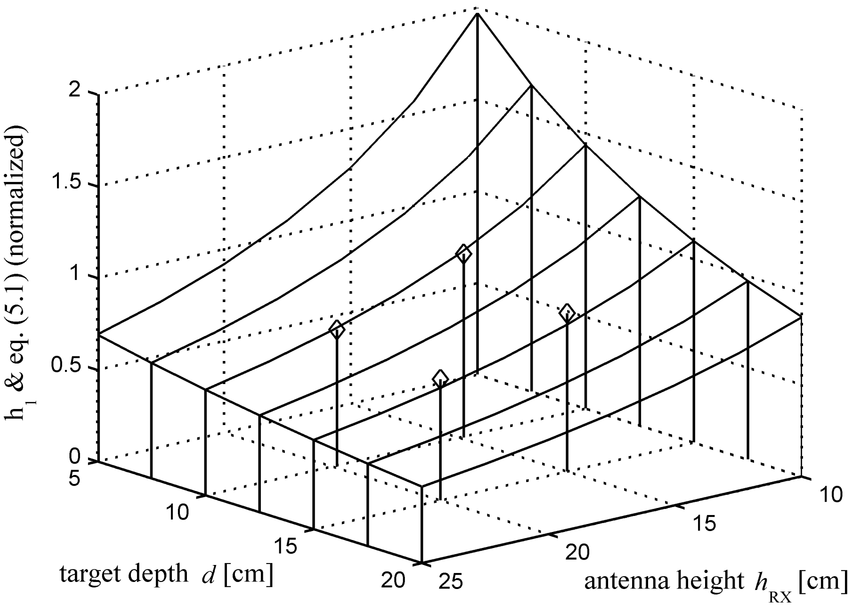

Figure 5.12: Estimates of h$_1$ from table 5.2 (diamonds) versus the spreading term of eq. (5.1) displayed as a function of target depth and antenna height. For the purpose of comparison, both were normalized with respect to $d = 10$ cm & $h_{RX} = 15$ cm.

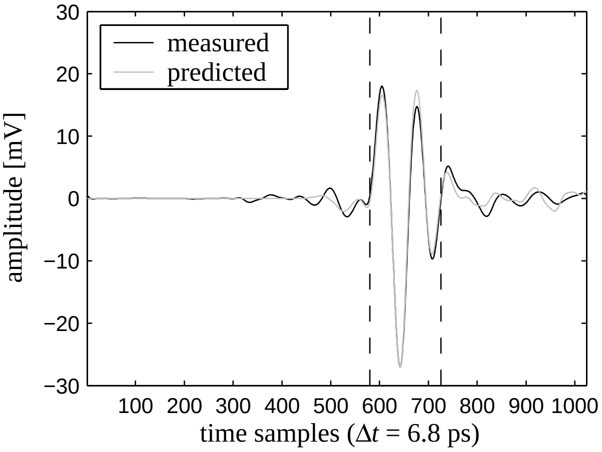

Figure 5.13: Data fit between the predicted (deconvolution) and the measured response of *Metal Disk 1* ($d \approx 10$ cm & $h_{RX} \approx 15$ cm). The dashed lines define the part of the response, which was fit by the deconvolution algorithm. Note that the predicted response also reasonably describes parts of the target response outside these limits.

Table 5.3: Results of the inversion for target size for *Metal Disk 1*.
Based on eqs. (4.34)-(4.35).

Target Depth Estimation *d* [cm]	**Antenna Height Estimation** h_{RX} [cm]	**Inversion for Target Size** target radius [cm]
-3.3 (-4.0)	24.8 (25.0)	5.8 (5.0)
10.1 (10.1)	15.2 (14.9)	5.3 (5.0)
10.2 (10.1)	20.1 (19.9)	5.2 (5.0)
14.9 (15.0)	15.1 (15.0)	5.4 (5.0)
15.0 (15.0)	19.8 (20.0)	5.4 (5.0)

The values included in parentheses are the true values.

Small metal spheres

Probably the most interesting result of the analysis of the data acquired over the metal spheres is that their response is stronger when buried than when surface-laid. This is illustrated in figure 5.14 showing two examples of the very weak response of *Metal Sphere 2*. The first was measured with the sphere surface-laid and an antenna height of 25 cm, whereas the second was measured with the sphere buried 5 cm deep and an antenna height of 20 cm. Note that in both cases the total distance between the target and the sphere is the same. The surface-laid response is of course much cleaner than the buried response, which contains clutter; nevertheless, there is a clear indication of the buried response being stronger. This fact is also reflected in the subset selection deconvolution results summarized in table 5.4, which show that the buried *Metal Sphere 2* exhibits a larger impulse response coefficient h_1.

The explanation of this rather unintuitive result is given by eq. (3.13) for the Rayleigh contrast of a small metal sphere, which states that the contrast is proportional to the permittivity of the host medium. Ergo, the contrast of the buried metal sphere is 2.6 times larger than that of the surface-laid sphere. The larger contrast compensates for the losses that incur as a result of the transmission at the air-sand interface and the refraction induced divergence, resulting in an overall stronger response of the buried sphere.

The response of the spheres is well modeled by an impulse response consisting of one double differentiation operator, as indicated by figure 5.15a showing the deconvolution data fit for the surface-laid response of *Metal Sphere 2*. This confirms that a small sphere differentiates the waveform of the incident field twice. When buried, the data fit is much worse due to clutter, as shown in figure 5.15b.

Despite the extremely weak response of the spheres and the rather “loose” data fit obtained for the buried spheres, the radii of the spheres can be estimated with sub-millimeter accuracy using the impulse response parameterizations of eqs. (4.41)-(4.42), as demonstrated by the results of the inversion for target size listed in table 5.5. The possibility to determine the radius with such high accuracy stems from the fact that the impulse response coefficient h_1 is proportional to the volume of the sphere. Consequently, a small change in radius is associated with a much greater change in h_1, allowing for a robust estimation of the radius.

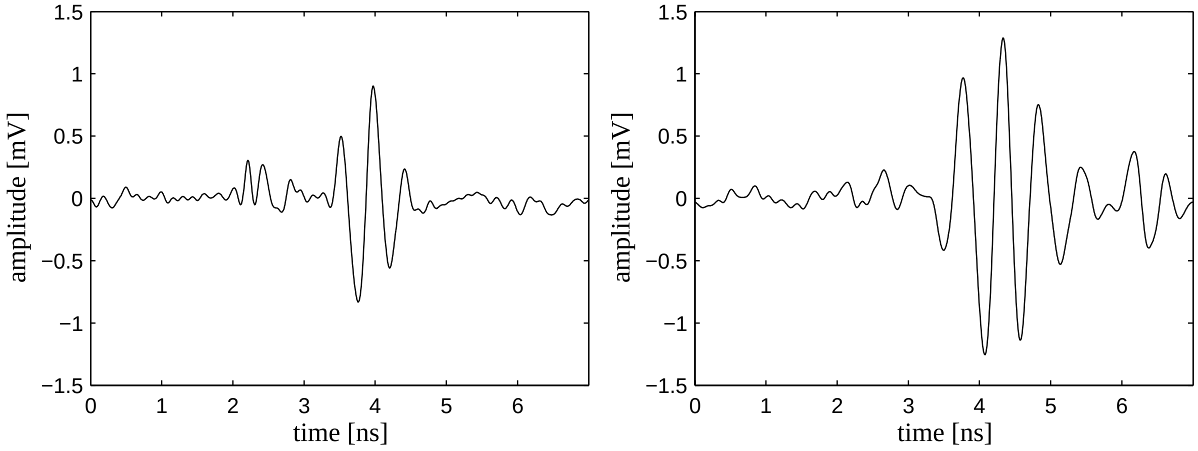

(a) (b)

Figure 5.14: Response of *Metal Sphere 2*:
(a) surface-laid & $h_{\mathrm{RX}} \approx 25$ cm
(b) $d \approx 5$ cm & $h_{\mathrm{RX}} \approx 20$ cm .

Table 5.4: Subset selection deconvolution results for the small metal spheres. Assumed impulse response model: eq. (4.40).

Target Name	**Target Depth** d [cm]	**Antenna Height** h_{RX} [cm]	**Impulse Response Parameters** h_1 [$*10^{-7}$]	τ_1 samples	 [ns]	**Rel. Error**
Metal Sphere 1	0.0[*]	25.0	-5.8	388	2.648	0.14
Metal Sphere 2	0.0[*]	25.0	-10.0	389	2.655	0.10
	5.0	15.0	-23.7	387	2.641	0.60
	5.0	20.0	-16.6	433	2.956	0.43

[*] Surface-laid.

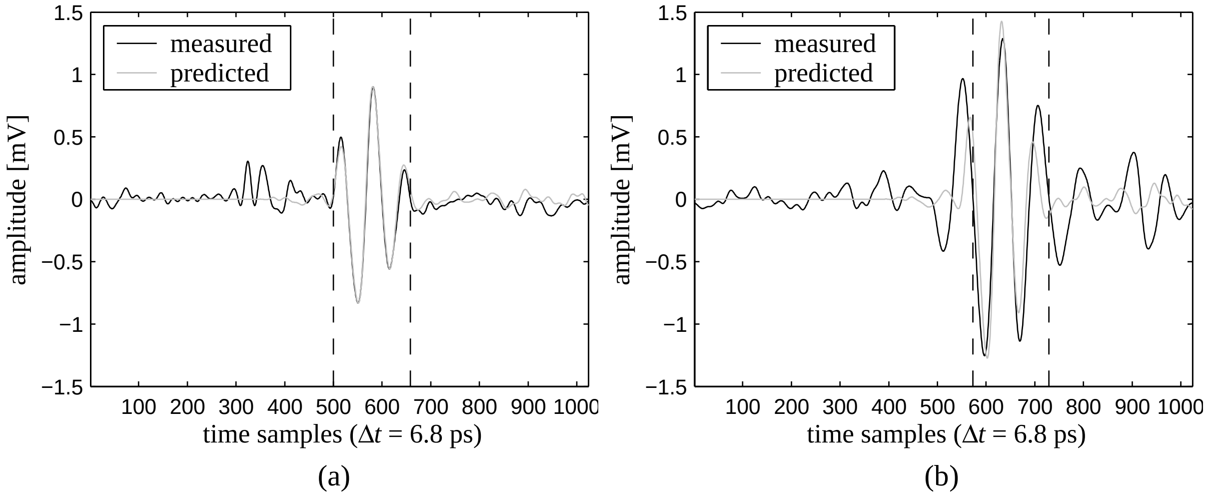

(a) (b)

Figure 5.15: Data fit between the predicted (deconvolution) and the measured response of *Metal Sphere 2*:
(a) surface-laid & $h_{RX} \approx 25$ cm
(b) $d \approx 5$ cm & $h_{RX} \approx 20$ cm .
The dashed lines define the part of the response, which was fit by the deconvolution algorithm.

Table 5.5: Results of the inversion for target size for the small metal spheres.
Based on eqs. (4.41)-(4.42).

Target Name	**Target Depth Estimation** d [cm]	**Antenna Height Estimation** h_{RX} [cm]	**Inversion for Target Size** target radius [cm]
Metal Sphere 1	-0.4 (0.0)	24.6 (25.0)	0.77 (0.80)
Metal Sphere 2	-0.3 (0.0)	24.6 (25.0)	0.93 (0.95)
	5.4 (5.0)	15.3 (15.0)	0.96 (0.95)
	5.5 (5.0)	20.0 (20.0)	0.95 (0.95)

The values included in parentheses are the true values.

5.2.3 EPS disks

Figure 5.16 gives an example of the type of target response that was measured for the EPS disks, in this case the response of *EPS Disk 2* buried 5 cm deep for an antenna height of 20 cm. Fitting the measured target responses with an impulse response model consisting of two differentiation operators yielded the subset selection deconvolution results listed in table 5.6. The generally good deconvolution data fit, such as that shown in figure 5.17, demonstrates the suitability of the impulse response model for explaining the measured responses.

The impulse response parameters obtained by subset selection deconvolution reflect the different sizes of the EPS disks. To illustrate this, figure 5.18 shows three plots of their relation to target size:

- In the first plot (figure 5.18a), the impulse response coefficients h_1 are plotted against the disk cross-sections S_{xy}. Since h_1 depends on both the target depth and the antenna height, only the coefficients obtained for a depth of 5 cm are plotted and the antenna heights of 15 cm and 20 cm are considered separately. The plot clearly shows that h_1 is proportional to S_{xy}, as predicted by eq. (4.37a).
- The second plot (figure 5.18b) displays the impulse response length $\tau_2 - \tau_1$ versus the disk height *l*. The plot shows that larger disks heights are associated with longer impulse responses, though the displayed relationship is not entirely linear, as predicted by eq. (4.37d). This deviation from linearity may be attributed to the high effective target velocity v_{t}^{eff} of the EPS disks, which makes their impulse responses very short and therefore the time shift parameter τ_2 very difficult to estimate accurately. By fitting a straight line to the data points in a least squares sense, as shown in the figure, we find $v_{\mathrm{t}}^{eff} \approx 28.9\ \mathrm{cm/ns}$, which is slightly lower than the intrinsic target velocity $v_{\mathrm{t}} = c$. This is in good agreement with the effective target velocity of *Air Disk 1* (same permittivity as EPS), which from FDTD simulations with a ground relative permittivity of 2.5 was found to be $v_{\mathrm{t}}^{eff} \approx 28.6\ \mathrm{cm/ns}$ (see table 2.4).
- In the third plot (figure 5.18c), the attenuation factors Γ are plotted against the target aspect ratios. The plot demonstrates that Γ, which can be considered an indicator of the extent to which the Born approximation is valid, decreases with the target aspect ratio, thereby confirming the result obtained from the FDTD analysis of the TNT disks (see section 2.3). In other words, the validity of the Born approximation deteriorates as the aspect ratio of the target decreases. As mentioned before in section 2.1, this may be explained by the contribution of the edge-diffracted wave to the field inside the target during the time it takes for the incident wave to pass through the target. This contribution becomes more significant as the target aspect ratio decreases, making the Born assumption break down. Note that the scatter of the data points belonging to the same disk can again be attributed to the high effective target velocity of the EPS disks, which makes it difficult to accurately estimate the second impulse coefficient h_2.

The impulse response parameters of table 5.6 were inverted for target depth, target size (disk radius and disk height) and target material properties (target relative permittivity and effective target velocity) using eq. (4.37) and antenna height estimates obtained from the arrival time of the ground reflection. In the inversion for target size, the target material properties were specified as $\varepsilon_{r,\mathrm{t}} = 1.0$, i.e. the true target relative permittivity, and $v_{\mathrm{t}}^{eff} = 28.5\ \mathrm{cm/ns}$. The choice of v_{t}^{eff} was based on the effective target velocity of *Air Disk 1*, which had been estimated from FDTD simulations (see above). In the inversion for material properties, the true disk dimensions were used to specify target size. The inversion results thus obtained together with the true target characteristics (shown in parentheses) are listed in table 5.7. Here, a few observations:

1) It is possible to infer target depth and antenna height with millimeter accuracy (as was the case for the metal targets).
2) The inversion for target size yielded disk radii and heights that are in close agreement with the true values ($\mathrm{error} < 0.6\ \mathrm{cm}$), with a tendency to slightly overestimate the disk radius (as was the case for *Metal Disk 1*).
3) The inversion for material properties yielded estimates of the target relative permittivity that were close to 1, though the accuracy of the estimation was not

> consistently of the same order, with errors ranging between 2 and 28 % with respect to the permittivity contrast. In general, there was a tendency to slightly underestimate the target permittivity, i.e. overestimating the contrast. The large permittivity errors, e.g. for *EPS Disk 3,* were accompanied by an underestimation of the effective target velocity, an observation that was already made when analyzing the FDTD data (see section 2.3).

In conclusion, the inversion for material properties was found to be less robust than the inversion for target size, which in all cases provided millimeter accurate disk dimensions, and that despite the fact that the Born approximation was always violated ($\Gamma < 0.55$). Hence in view of landmine identification, inversion for target size is more promising. This conclusion is reinforced by the fact that AP landmines exist in all different sizes, making the assumption of a generic target size impossible. On the other hand, it seems plausible to assume a generic set of material properties, which is valid for a class of AP landmines, and invert for target size.

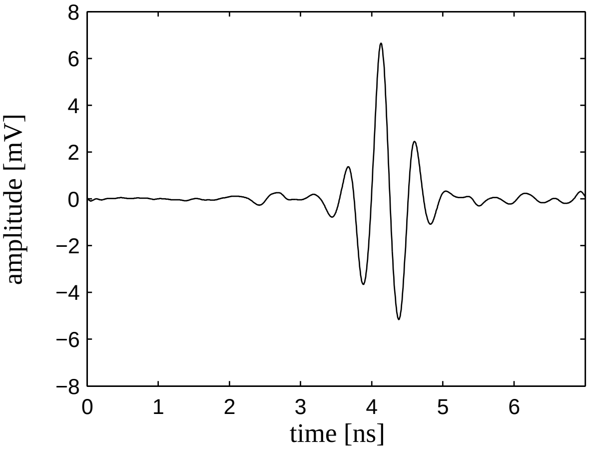

Figure 5.16: Response of *EPS Disk 2* ($d \approx 5$ cm & $h_{\mathrm{RX}} \approx 20$ cm).

Table 5.6: Subset selection deconvolution results for the EPS disks.
Assumed impulse response model: eq. (4.36).

Target Name	**Target Depth**	**Antenna Height**	**Impulse Response Parameters**						**Γ**	**Rel. Error**
	d [cm]	h_{RX} [cm]	h_1 [$*10^{-5}$]	τ_1 samples	τ_1 [ns]	h_2 [$*10^{-5}$]	$\tau_2-\tau_1$ samples	$\tau_2-\tau_1$ [ns]	Γ	
EPS Disk 1	4.9	15.1	10.2	379	2.587	-4.2	39	0.267	0.42	0.06
	4.9	20.1	6.9	426	2.908	-3.7	38	0.260	0.53	0.05
	10.0	15.0	9.2	455	3.107	-4.4	40	0.274	0.48	0.03
	10.0	20.0	7.3	502	3.428	-3.2	40	0.274	0.44	0.03
EPS Disk 2	4.9	15.1	11.1	378	2.580	-2.7	47	0.322	0.25	0.07
	4.9	20.1	7.6	425	2.901	-2.4	44	0.301	0.31	0.04
EPS Disk 3	5.3	14.7	7.2	384	2.621	-1.2	43	0.294	0.16	0.13
	5.3	19.7	5.1	430	2.935	-1.1	43	0.294	0.22	0.12
EPS Disk 4	5.4	14.6	16.8	386	2.634	-6.6	46	0.315	0.39	0.04
	5.4	19.6	12.2	431	2.942	-5.6	47	0.322	0.46	0.02

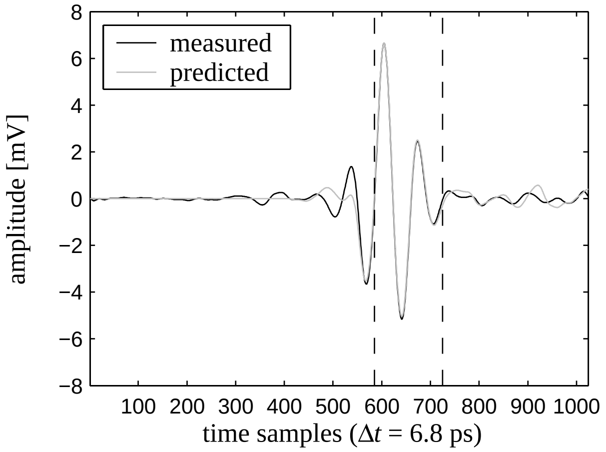

Figure 5.17: Data fit between the predicted (deconvolution) and the measured response of *EPS Disk 2* ($d \approx 5$ cm & $h_{RX} \approx 20$ cm). The dashed lines define the part of the response, which was fit by the deconvolution algorithm.

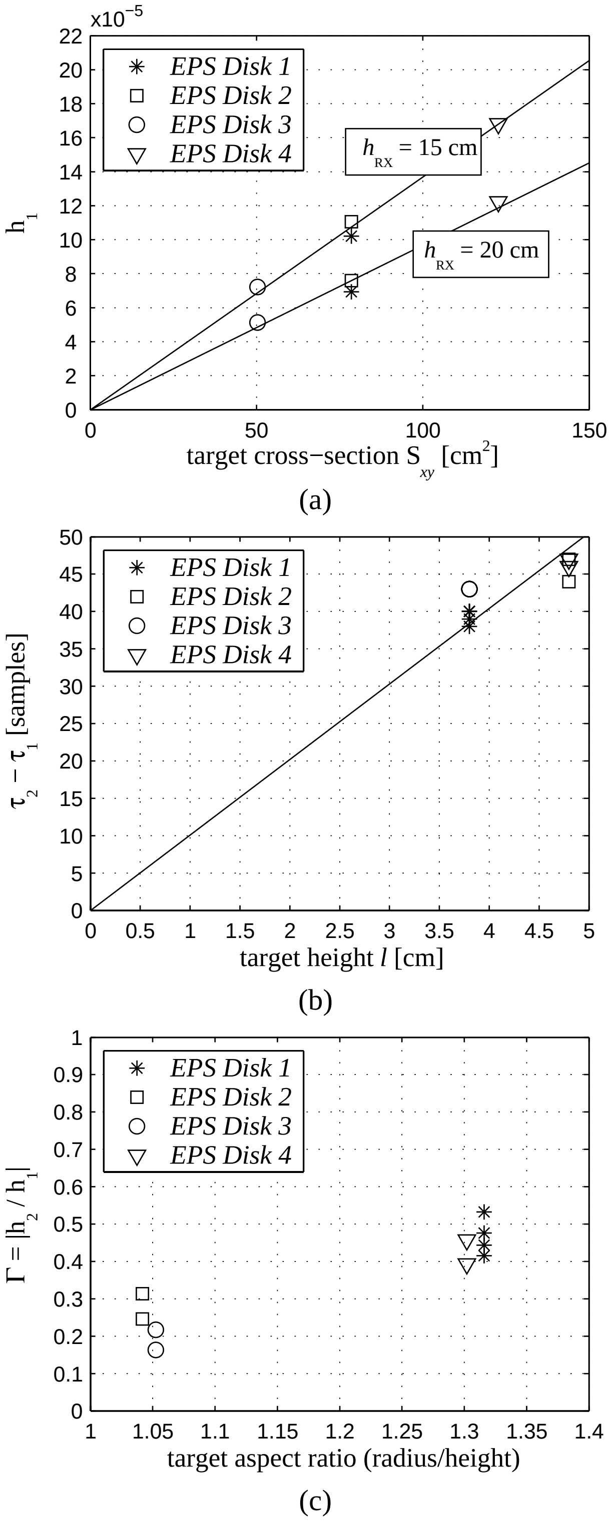

Figure 5.18: Relation between the impulse response parameters obtained by subset selection deconvolution and target size:

(a) h_1 vs. S_{xy} ($d \approx 5$ cm only)

(b) $\tau_2 - \tau_1$ vs. l

(c) Γ vs. target aspect ratio.

The straight lines represent least squares fits to the data points.

Table 5.7: Results of the inversions for target size & material properties for the EPS disks. Based on eq. (4.37).

Target Name	**Target Depth Estimation**	**Antenna Height Estimation**	**Inversion for Target Size**[*]		**Inversion for Material Properties**[§]	
	d [cm]	h_{RX} [cm]	target radius [cm]	target height l [cm]	$\varepsilon_{r,\mathrm{t}}$	v_{t}^{eff}
EPS Disk 1	5.0 (4.9)	15.2 (15.1)	5.0 (5.0)	3.8 (3.8)	0.97 (1.0)	28.5
	5.0 (4.9)	20.1 (20.1)	4.9 (5.0)	3.7 (3.8)	1.10 (1.0)	29.2
	9.7 (10.0)	15.3 (15.0)	5.4 (5.0)	3.9 (3.8)	0.67 (1.0)	27.8
	9.8 (10.0)	20.1 (20.0)	5.6 (5.0)	3.9 (3.8)	0.56 (1.0)	27.8
EPS Disk 2	5.0 (4.9)	15.0 (15.1)	5.2 (5.0)	4.6 (4.8)	0.94 (1.0)	29.9
	5.0 (4.9)	19.9 (20.1)	5.1 (5.0)	4.3 (4.8)	1.02 (1.0)	> 29.97
EPS Disk 3	5.2 (5.3)	15.3 (14.7)	4.3 (4.0)	4.2 (3.8)	0.57 (1.0)	25.8
	5.2 (5.3)	20.1 (19.7)	4.2 (4.0)	4.2 (3.8)	0.62 (1.0)	25.8
EPS Disk 4	5.5 (5.4)	15.0 (14.6)	6.5 (6.25)	4.5 (4.8)	0.94 (1.0)	> 29.97
	5.5 (5.4)	19.7 (19.6)	6.5 (6.25)	4.6 (4.8)	0.95 (1.0)	29.9

The values included in parentheses are the true values.

[*] Specified material properties: $\Delta\varepsilon_r = 1.0 - 2.6 = -1.6$ and $v_{\mathrm{t}}^{eff} = 28.5$ cm/ns (from FDTD simulations).

[§] Specified target size: true disk dimensions.

5.2.4 Teflon disks

The data acquired over the Teflon disks show that the target response is noticeably influenced by the presence of the air gap and to a much lesser extent by the small metal insert. This follows from comparison of their surface-laid responses shown in figure 5.19 and comparison of their buried responses shown in figure 5.20. In both figures, the response of *Teflon Disk 1* (homogeneous) serves as a reference for comparison. When surface-laid, the presence of the air gap weakens the target response. In contrast, when buried, the air gap leads to a much stronger target response in addition to significantly changing its shape, which confirms the observations of the FDTD analysis in section 3.3.

The target responses of the buried Teflon disks were further analyzed by subset selection deconvolution, the results of which were inverted for target depth and target size (disk radius, disk height, inclusion volume and inclusion position) using eqs. (4.37) & (4.39) and antenna height estimates obtained from the arrival time of the ground reflection. In the inversion for target size, the target material properties were specified as $\varepsilon_{r,\mathrm{t}} = 2.1$, i.e. the true target relative permittivity, and $v_{\mathrm{t}}^{eff} = 19.3$ cm/ns. The latter is the effective target velocity estimate of *Teflon Disk 1* obtained from FDTD simulations with a ground relative permittivity of 2.5 (see table 2.4). The deconvolution and inversion results are summarized in tables 5.8 and 5.9.

In principle, the impulse response coefficients h_1 & h_2 and the impulse response length $\tau_2 - \tau_1$, which describe the scattering from the disk body, should be identical for the three disks. However, looking at table 5.8, we see that these parameters are varying, especially h_1 and $\tau_2 - \tau_1$. Two reasons for this can be identified. The first reason is the very weak target response of *Teflon Disk 1* whose magnitude is of the same order as the clutter caused by the disturbance of the sand, as a result of which its impulse response parameters are likely to be inaccurate. This problem also manifests itself in the rather “loose” deconvolution data fit for *Teflon Disk 1* shown in figure 5.21a. The second reason is that the subset selection deconvolution for *Teflon Disk 3* failed, as indicated by the attenuation factor Γ of only 0.05 and the fact that the time shift parameters τ_2 and τ_3 are practically equal. This shows that the deconvolution algorithm was looking for the weak response of the metal insert but due to clutter confused it with the backscattering from the bottom of the disk. This did not happen with the air gap in *Teflon Disk 2* because it is a dominant feature. It can be concluded that using an impulse response model consisting of three differentiation operators in the subset selection deconvolution is only appropriate when there are three distinct responses to fit; otherwise the deconcolution becomes ill-posed and is likely to return the wrong answer.

Despite these problems with the subset selection deconvolution, the inversion for target size gave reasonable estimates of the outer disk dimensions, with excellent, millimeter accurate inversion performance achieved for *Teflon Disk 2*. Even the volume of the air gap could be determined with an error of only 9 % (as opposed to 35 % in the FDTD analysis of *TNT Disk 1*; see table 3.4). This demonstrates that the impulse response parameters for *Teflon Disk 2* are very accurate, which also shows in the good deconvolution data fit that was obtained for it (figure 5.21b). The radius of *Teflon Disk 1* (homogeneous) was estimated with an error of 2 cm due to clutter, yet its height could still be recovered exactly.

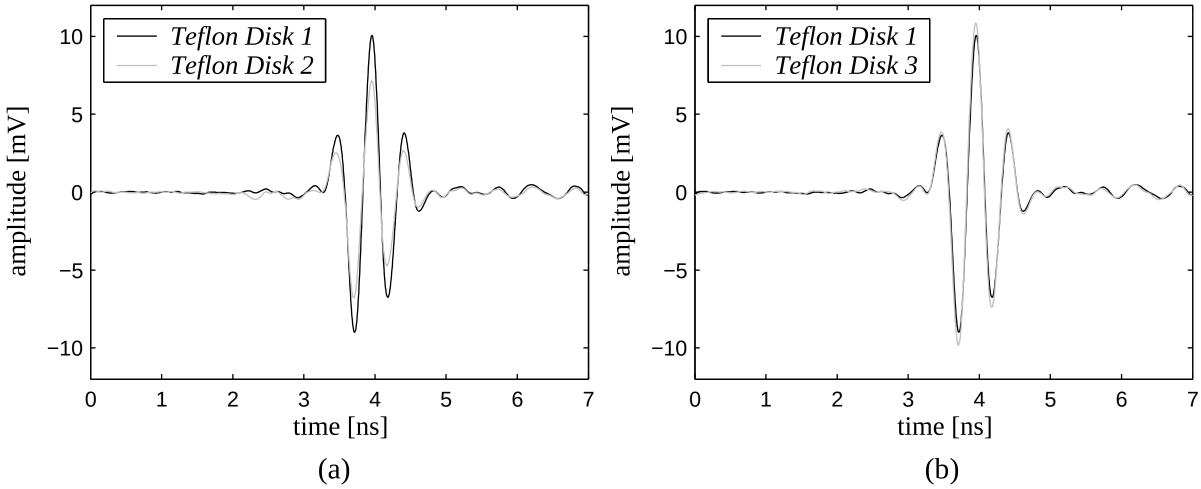

(a) (b)

Figure 5.19: Comparison of the responses of the surface-laid Teflon disks ($h_{\mathrm{RX}} \approx 25$ cm):
(a) *Teflon Disk 2* (with air gap) and *Teflon Disk 1* (homogeneous)
(b) *Teflon Disk 3* (with metal insert) and *Teflon Disk 1* (homogeneous).

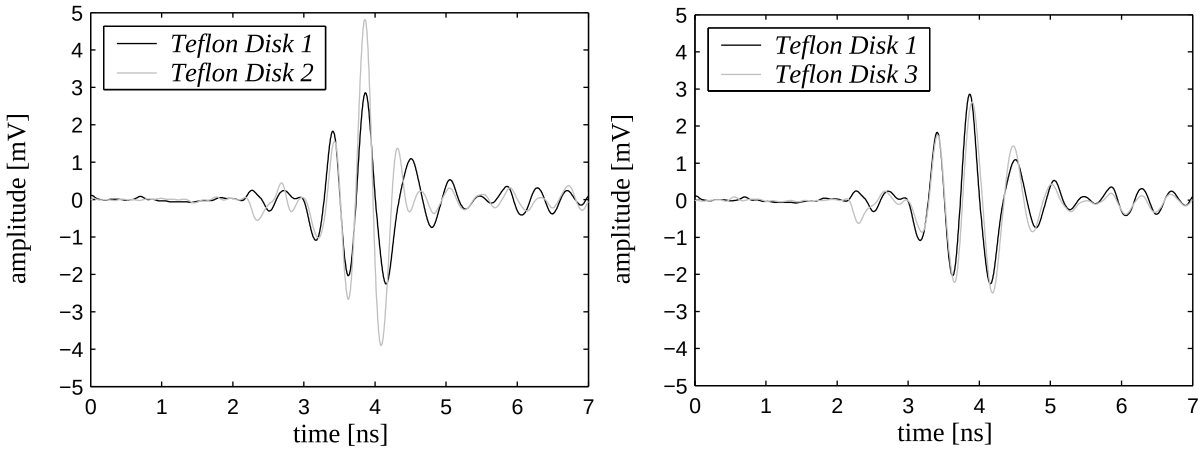

(a) (b)

Figure 5.20: Comparison of the responses of the buried Teflon disks ($d \approx 5$ cm & $h_{\mathrm{RX}} \approx 15$ cm):
(a) *Teflon Disk 2* (with air gap) and *Teflon Disk 1* (homogeneous)
(b) *Teflon Disk 3* (with metal insert) and *Teflon Disk 1* (homogeneous).
Note that the first two amplitude peaks of all three responses are a result of sand disturbance.

Table 5.8: Subset selection deconvolution results for the buried Teflon disks ($d \approx 5$ cm & $h_{\mathrm{RX}} \approx 15$ cm).
Assumed impulse response models: eq. (4.36) and eq. (4.38).

Target Name	**Impulse Response Parameters**										**Rel. Error**
	h_1 $[*10^{-5}]$	τ_1 samples	τ_1 [ns]	h_2 $[*10^{-5}]$	$\tau_2 - \tau_1$ samples	$\tau_2 - \tau_1$ [ns]	Γ	h_3 $[*10^{-6}]$	$\tau_3 - \tau_1$ samples	$\tau_3 - \tau_1$ [ns]	
Teflon Disk 1 homogeneous	4.0	383	2.616	-2.3	60	0.411	0.58	n/a	n/a	n/a	0.30
Teflon Disk 2 with air gap	2.4	381	2.600	-2.1	54	0.370	0.87	3.8	11	0.075	0.08
Teflon Disk 3 with metal insert	3.9	393	2.682	-1.8	73	0.500	0.05	-2.0	72	0.493	0.18

Table 5.9: Results of the inversion for target size for the buried Teflon disks.
Based on eqs. (4.37) and (4.39).

Target Name	**Target Depth Estimation**	**Antenna Height Estimation**	**Inversion for Target Size**[*]			
	d [cm]	h_{RX} [cm]	target radius [cm]	targt height l [cm]	volume V_{i} [cm^3]	l_{i} [cm]
Teflon Disk 1 homogeneous	5.2 (4.8)	15.2 (15.2)	6.9 (5.0)	4.0 (4.0)	n/a	n/a
Teflon Disk 2 with air gap	5.0 (4.5)	15.3 (15.5)	5.4 (5.0)	3.6 (4.0)	45.9 (50.3)	0.7 (1.5)
Teflon Disk 3 with metal insert	5.8 (5.0)	15.3 (15.0)	7.0 (5.0)	4.8 (4.0)	3.1 (2.7)	4.8 (0.75)

The values included in parentheses are the true values.

[*] Specified material properties $\Delta\varepsilon_{r,\mathrm{t}} = 2.1 - 2.6 = -0.5$ and $v_{\mathrm{t}}^{eff} = 19.3$ cm/ns (from FDTD simulations).

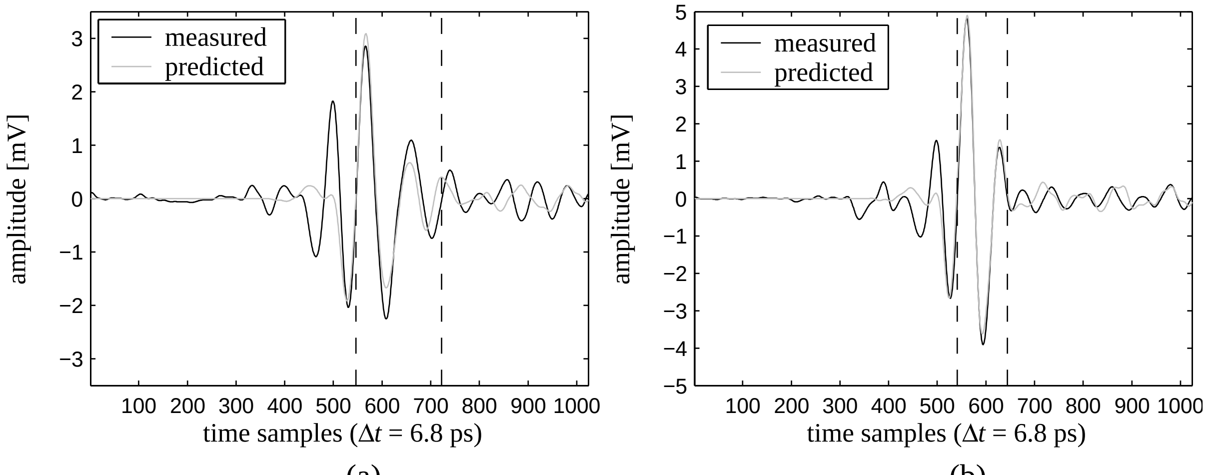

(a) (b)

Figure 5.21: Data fit between the predicted (deconvolution) and the measured target response:
(a) *Teflon Disk 1* (homogeneous) ($d \approx 5$ cm & $h_{\mathrm{RX}} \approx 15$ cm)
(b) *Teflon Disk 2* (with air gap) ($d \approx 5$ cm & $h_{\mathrm{RX}} \approx 15$ cm).
The dashed lines define the part of the response, which was fit by the deconvolution algorithm.

5.3 Discussion

The experimental results presented in this chapter confirm the validity of the convolutional GPR models for surface-laid and buried minelike targets presented in chapter 4. Overall, these models were shown to adequately describe

- the target impulse response of a disk-shaped minelike target and its relation to target size and target material properties, thus affirming the results of the FDTD analysis in chapters 2 and 3
- the dependency of the target response magnitude on target depth and the height of the antenna system
- the radiation and reception characteristics of the IRCTR video impulse GPR.

This makes the convolutional GPR models well suited for use with subset selection deconvolution to characterize a minelike target from its vertical backscattering response, which in terms of signal shape was found to be representative for the entire target response hyperbola (see figure 5.7).

In general, the inversion for target size estimated the outer disk dimensions (radius and height) with millimeter accuracy $(\text{error} < 0.5\ \text{cm})$. A particularly encouraging result is that such precision was also achieved for *Teflon Disk 2* containing an air gap. Even the volume of the air gap could be estimated very accurately $(\text{error} \approx 9\ \%)$, which is better than the results obtained in the FDTD analysis presented in chapter 3. Problems were encountered with those targets whose target response magnitude was of the same order as the clutter resulting from the disturbance of the sand, i.e. *Teflon Disk 1* and *Teflon Disk 3*. The estimation errors caused by the clutter were most noticeable in the disk radius $(\text{error} \approx 2\ \text{cm})$. Yet, these inversion results are still reasonable and demonstrate the robustness of the inversion for target size. That a weak target response does not rule out estimation of target size per se is demonstrated by the sub-millimeter (!) accurate recovery of the radii of the two small metal spheres.

The accuracy with which the inversion for material properties estimated the target relative permittivity varied from very good $(\text{error} \approx 2\ \%)$ to reasonable $(\text{error} \approx 28\ \%)$. Here both errors are specified with respect to the permittivity contrast. The results indicate that the large errors occurred when the estimated effective target velocity was too low. This sensitivity of the estimated target permittivity to errors in the estimated effective target velocity makes the inversion for material properties less robust than the inversion for target size. Note that in the latter, the estimations of disk radius and disk height are decoupled.

All presented inversion results were achieved using antenna height and target depth estimates obtained from the arrival times of the ground reflection and the target response, i.e. τ_1. In general, the antenna height and the target depth were estimated with millimeter accuracy $(\text{error} < 0.5\ \text{cm})$, which is a direct result of the excellent temporal resolution provided by the subset selection deconvolution.

It should be noted that the generally good inversion results also speak for the good performance of the metal sheet calibration procedure and of the WMA-BS technique, which was used to extract the responses of the buried targets from the GPR data.

Before closing this chapter, let us get an idea of what happens when the wrong target material properties are specified in the inversion for target size. More specifically, let us assume that we are looking for Teflon disks with radii between 3 and 7.5 cm and heights between 3.5 and 6 cm, which is representative for AP landmines in terms of both dielectric permittivity and size. From table 5.9, we see that based on their estimated outer dimensions, all three Teflon disks would have been identified as such. If we now redid the inversion for target size for the data of the EPS disks but this time assuming the material properties that are generic for Teflon disks, i.e. $\varepsilon_{r,\mathrm{t}} = 2.1$ and $v_{\mathrm{t}}^{eff} = 19.3\ \mathrm{cm/ns}$, we would find that none of the EPS disks is identified as a Teflon disk of the prescribed dimensions. In fact, the smallest disk radius obtained would be 9.2 cm (*EPS Disk 3*) and the greatest disk height would be 3.1 cm (*EPS Disk 2* and *EPS Disk 3*). This example demonstrates that even though the inversion for target size is inherently unresolved, i.e. it requires the specification of material properties, it is still possible to identify targets as belonging to a certain target class based on estimates of their outer dimensions.

CHAPTER 6

OVERVIEW OF THE RESEARCH RESULTS AND RECOMMENDATIONS

The research results of this thesis demonstrate the possibility of using deconvolution to identify AP landmines from GPR data within a very short computation time. A number of new developments in the theory of electromagnetic scattering from landmines and in GPR data processing were necessary to perform this type of target identification, specifically the derivation of convolutional models describing the GPR response of a plastic or metal cased AP landmine, the design of preprocessing algorithms that extract the target response signal from the measured data, and the development of a deconvolution based target characterization procedure. The target characterization procedure and the underlying convolutional models have been validated with success based on 3D finite-difference time-domain (FDTD) simulations and experimental data acquired with the IRCTR video impulse GPR. This chapter summarizes the most important research results that have been achieved and formulates some conclusions. At the end of the chapter, the application of the research results to identify landmines in real minefields is discussed and some recommendations for future research are given.

Convolutional models & target transfer function/impulse response models

One of the main scientific contributions of this thesis is the derivation of convolutional models describing the response of a minelike target as measured by GPR. The derivation proceeded in two stages, which are reviewed below.

In the first stage of the derivation, frequency- and time-domain convolutional models for plane wave backscattering were derived. These convolutional scattering models describe the scattering behavior of the target through a target transfer function/impulse response and the propagation of the scattered field from the target to the observation point, i.e. the position of the receiving antenna, through a phase/time shift in combination with a scaling factor. The convolutional scattering models are based on source-type integral representations of the scattered field in which a linear relationship between the scattering current and the incident field is invoked by making use of either the Born and Rayleigh approximations or the Physical Optics (PO) approximation, depending on the material composition of the target considered. Furthermore, the half-space electric Green’s tensor is approximated by a new far-field backscattering representation. Hence, the convolutional representation of the scattered field is derived from physical principles and is not imposed, as is usually the case in convolutional GPR modeling. The new far-field backscattering approximation of the half-space electric Green’s tensor was obtained from a reordering of Baños series expansion of the electric field due to a horizontal point electric dipole in the ground. An important term in the Green’s tensor approximation is the coefficient ζ describing the spreading loss caused by the refraction at the ground surface, which acts in addition to the spherical spreading loss. The coefficient ζ is indispensable for accurate modeling of the dependency of the scattered field amplitude on both the depth of the target and the height of the observation point, which in turn is a requisite for determining target size or target contrast.

In the second stage of the derivation, point source and receiver models were introduced to account for the radar hardware and the propagation of the radiated field from the transmitting antenna to the target. These hardware models enter as additional terms in the time-domain convolutional scattering model, thereby yielding a convolutional GPR model, which for the first time gives analytical expressions for all components of the GPR chain, i.e. the hardware, the propagation to and from the target and the target impulse response. In this model, the radiation characteristics of the transmitting antenna and the reception characteristics of the receiver chain (including the receiving antenna) are conveniently expressed through a single term, namely the effective radiated waveform, which can be estimated accurately and fast from a simple metal sheet reflection calibration measurement. Wide applicability of the convolutional GPR model is provided for by its formulation for both surface-laid and buried minelike targets.

A useful property of the integral representation approach to convolutional GPR modeling is that it directly yields simple closed-form expressions for the target transfer function/impulse response of a minelike target. The expressions thus obtained demonstrate that the target transfer function/impulse response of a homogeneous minelike target (dielectric or metal) is closely related to the target's cross-section profile and hence its size and shape. Furthermore, it was found that the magnitude of the target transfer function/impulse response is determined by both the contrast and the maximum cross-section of the target. For the dielectric minelike target, the target contrast is mainly determined by the difference in relative permittivity between the target and the host medium, i.e. the ground, whereas for the metal target, the target contrast is inversely proportional to the wave velocity in the host medium. In the presence of a dielectric or metal inclusion (e.g. an air gap or a small piece of metal), the target transfer function/impulse response of the homogeneous dielectric minelike target is simply augmented by an additional term describing the transfer function/impulse response of the inclusion. The transfer function/impulse response of the inclusion differentiates the waveform of the incident field twice, and its magnitude is proportional to the inclusion volume and the difference in contrast between the inclusion and the target body, for which explicit expressions have been presented. Note that, since the target impulse response model for a dielectric minelike target derived in this thesis is able to describe scattering from the bottom of the target and from internal mine structure, it is a better approximation to the target impulse response of a plastic cased AP landmine than the only earlier existing target impulse response model published by Nag and Peters (2001).

Much of the research presented in this thesis focuses on circular disk-shaped minelike targets, which are representative for a large class of AP landmines. Interestingly, it was found that a minelike target of this shape differentiates the waveform of the incident field rather than just reflecting it. Accordingly, the target impulse response of a circular metal disk consists of one differentiation operator, which describes specular scattering from the top of the target. The target impulse response of a circular dielectric disk consists of two differentiation operators, of which the first, again, describes scattering from the top of the target and the second describes scattering from the bottom of the target. When a thin air gap or a small piece of metal is present inside the dielectric disk, its target impulse response also includes a double differentiation operator, i.e. in this case its target impulse response consists of a total of three differentiation operators.

The derived frequency-domain convolutional scattering model and target transfer functions apply to minelike targets buried in any type of ground (as long as it is non-magnetic), whereas the validity of their presented time-domain counterparts is limited to a lossless ground. The reason for this is that losses lead to frequency dependence, which does not lend itself to analytical transformation to the time-domain. An exception is the case where the polarization losses are negligible and the conduction losses are either low or can be described through a global conduction loss model. In the latter case, similarity analysis in the Laplace domain can be used to derive a host medium transformation law, which relates the time-domain response of a dielectric minelike target buried in a lossless ground to its time-domain response in a lossy ground, as described in section 2.4. The relationship is fairly simple and its validity has been affirmed based on a FDTD data example. As a result of its simplicity, the transformation law is well suited to gain insight in how the time-domain target response changes as a result of losses, however its applicability to real GPR data is strongly limited by the global nature of the loss model that it assumes. Considering the difficulties in describing scattering from a target buried in a lossy ground in the time-domain, it may be concluded that under conditions where losses prevail, GPR data processing such as deconvolution should be carried out in the frequency-domain and not in the time-domain. More specifically, it should be possible to design a frequency-domain analog to the time-domain target characterization procedure presented in this thesis, which makes use of the derived frequency-domain convolutional scattering model and target transfer functions to estimate target characteristics such as size and material properties. Exploiting the possibility to account for losses in the frequency-domain, however, is by no means trivial since it requires knowledge of the complex permittivity of the ground as a function of frequency (Gorriti, 2004). Clearly, to properly address all these issues, more research is necessary, including a series of GPR experiments with targets buried in well-characterized lossy soils.

It is important to emphasize that all convolutional models and target transfer function/impulse response models presented in this thesis have been derived for backscattering along the vertical, i.e. the transmitting and the receiving antenna are both positioned right above the target. The reason for this is twofold. First, the backscattering condition tremendously simplifies the half-space electric Green’s tensor such that a non-numerical treatment of the scattering problem becomes feasible. And second, as confirmed by the experimental data, the shape of the measured target response signal hardly changes as the antenna system is moved over the target. Hence, it can be concluded that the target response signal measured at a horizontal offset from the target carries very little additional target information. These observations can be explained by the fact that at the ground surface the radiated wave is refracted towards and the scattered wave away from the vertical, making the wave propagation along the vertical the dominant propagation in the ground.

Preprocessing

The data preprocessing algorithms developed in this thesis minimize unwanted signal components that carry no target information, and compute a target response signal that is independent of the orientation of the target with respect to the antenna system. The first is achieved through low-pass noise filtering and weighted moving average background subtraction (WMA-BS), and the latter is achieved through the target frame target transformation. These algorithms are designed carefully to keep the loss of amplitude and shape information of the target response signal at a minimum, which is of utmost importance for target identification.

The newly developed WMA-BS technique is designed to remove the direct wave signal and the ground reflection signal from each measured A-scan. It works in an iterative manner by first finding the anomalies in the GPR data and then suppressing them in the estimation of the background to be subtracted. As a result, WMA-BS does not smear out the target response signal to neighboring A-scans or change its amplitude and shape, both of which are problems usually encountered with other background subtraction techniques, e.g. standard moving average background subtraction. The WMA-BS was used in the preprocessing of the experimental data acquired with the IRCTR video impulse GPR, yielding target response signals that were well suited for target characterization.

The target frame transformation is essential to the identification of a target having a preferential scattering axis since the measured response of such a target varies with target orientation. The transformation requires measurement of the co- and cross-polar components of the target response for two orthogonal transmit polarizations, which are combined into a scattering matrix. Under the backscattering condition, the so-obtained scattering matrix is symmetric and matrix diagonalization can be applied to transform the target response into the coordinate frame defined by the two natural polarizations of the target, called the target frame. In the target frame the cross-polar components vanish and the target response becomes independent of target orientation. The target frame transformation, i.e. the matrix diagonalization, is carried out in the frequency-domain and time-domain results are obtained by inverse Fourier transformation.

The concept of the target frame transformation has been tested using polarimetric data acquired over a buried metal tube and demonstrated the capability to accurately recover the target response signals, which would have been measured if the tube had been oriented with its preferential scattering axis aligned with the antenna system. Unfortunately, routine application of the target frame transformation to data acquired with the IRCTR video impulse GPR is subject to some practical complications. First, since the target response is measured with two physically distinct receiving loops, careful calibration for amplitude and timing is crucial. Even after calibration, timing can still be a problem simply due to the fact that the two receiving loops measure at different positions in space. Hence, it is important that the length of the propagation path to and from the target is exactly the same for both loops, which is difficult to achieve in a real measurement scenario. A workaround is to diagonalize only the amplitude spectrum of the scattering matrix, i.e. to neglect the phase information, which is possible if the analysis of the target response proceeds in the frequency domain (Farinelli and Roth, 2003).

Deconvolution & target characterization

A target characterization procedure has been developed, which makes use of the new subset selection deconvolution algorithm and the derived convolutional models to determine target characteristics, e.g. the outer dimensions, which in turn provide information on the likely identity of a detected target. The target characterization procedure lends itself to real-time implementation and operates on a single A-scan, viz. the preprocessed A-scan at the apex of the target response hyperbola. This makes the characterization procedure very attractive for potential use with handheld demining GPR systems.

The novelty of the subset selection deconvolution algorithm is that it uses the target impulse response models derived for circular disk-shaped minelike targets as a priori information on the specific form of the impulse response to be recovered. In other words, the algorithm assumes that the scattering behavior of the target to be characterized is well approximated by an impulse response consisting of one, two or three differentiation operators, depending on whether a circular metal disk or a circular dielectric disk with or without inclusion is assumed for the data fitting. By doing so, subset selection deconvolution provides physical amplitude information and excellent temporal resolution, both of which is crucial if the estimated impulse response is to be related to target characteristics. In addition, subset selection deconvolution reduces the ill-conditioning of the radar signal deconvolution problem, making it a robust tool for the estimation of sparse impulse responses. Hence, for target characterization purposes, subset selection clearly outperforms deconvolution algorithms based on Wiener filtering or ridge regression, which were shown to produce smeared out impulse responses and rely on a regularization parameter whose optimal choice is non-obvious. A disadvantage of subset selection deconvolution based on the impulse response model of circular dielectric disk with an inclusion is that it becomes computationally intensive, and hence is less suited for real-time processing. It is therefore advisable to limit the support[1] of the sought impulse response based on an initial guess of the arrival time of the target response.

The impulse responses obtained by subset selection deconvolution can be inverted for target size or, in the case of a dielectric minelike target, for target material properties. For a dielectric minelike target, target size parameters that can be estimated are the target cross-section, the target height, the inclusion volume and the inclusion position, whereas for a metal minelike target the target size inversion is limited to the estimation of the target cross-section. Target material properties that can be estimated are the relative permittivity of the target (body) and the effective target velocity. Since for the dielectric minelike target the inversion is inherently unresolved, it is only possible to invert for possible combinations of target characteristics. Accordingly, the inversion for target size requires specification of generic target material properties and vice versa. Since plastic cased AP landmines come in all different sizes, yet they have similar material properties, clearly the inversion for target size has more practical use than the inversion for target material properties.

The inversion of the impulse responses requires knowledge of the antenna height above the ground and target depth, with negative depths indicating that the target is surface-laid. These can be estimated from the GPR data itself, namely from the arrival time of the ground reflection and that of the target response. Here, the high temporal resolution provided by the subset selection deconvolution algorithm is very beneficial, ensuring accurate estimates of both arrival times.

Validation

The validation of the proposed target characterization procedure and its underlying convolutional models consisted of two parts: validation based on 3D FDTD simulations and experimental validation based on GPR data acquired with the IRCTR video impulse GPR at an indoor experimental facility. The FDTD simulations were done for exactly the same configuration as the one for which the convolutional scattering models were derived, i.e. plane wave backscattering. This offered the possibility to focus the analysis on the scattering from the target alone and to neglect the radar hardware and other factors that come into play when dealing with real GPR data, e.g. clutter. Furthermore, the simulations eliminated the need for preprocessing and the estimation of antenna height and target depth. As such, the FDTD validation should be understood as an analysis under ideal conditions. In contrast, the experimental validation was carried out to test the full processing chain consisting of the radar calibration, data preprocessing and target characterization. Both types of validations yielded good target characterization results and lead to similar observations. Hence, in the following the main results of the two types of validations will be presented together with differences pointed out as necessary.

In general, a very good deconvolution data fit was obtained. The deconvolution data fit for the measured target responses was almost as good as for the simulated target responses, with the exception of those targets whose response when buried had a magnitude of the same order as the clutter resulting from the disturbance of the sand. This was the case for, e.g., *Teflon Disk 1*. The generally good data fit demonstrates that very simple impulse response models

---

[1] The time window in which the impulse response is allowed to take on non-zero values.

consisting of one, two or three differentiation operators are fully sufficient to explain the axial backscattering response of a circular disk-shaped minelike target.

The results of the inversions for target size demonstrate that in most cases the outer dimensions of a homogeneous circular disk (metal or dielectric) can be estimated with millimeter accuracy ($\text{error} < 0.5\ \text{cm}$). Given internal structure, i.e. a thin air gap or a small metal inclusion, the accuracy with which the outer dimensions of a circular dielectric disk can be estimated is lower but still reasonable ($\text{error} < 1\ \text{cm}$). The estimation of the volume of the air gap or the metal inclusion inside the disk generally works less well ($\text{error} < 35\ \%$), with the best volume estimate obtained for the air gap inside *Teflon Disk 2* ($\text{error} \approx 9\ \%$). For targets whose response is very weak, i.e. *Teflon Disk 1* and *Teflon Disk 3*, clutter can seriously degrade the quality of the inversion for target size, most noticeable in the estimation of disk radius ($\text{error} \approx 2\ \text{cm}$); however this is not necessarily so, as demonstrated by the sub-millimeter accurate (!) recovery of the radii of the two small metal spheres.

The results of the inversions for material properties obtained for the simulated dielectric disks demonstrate that in principle it is possible to estimate the relative permittivity of a homogeneous circular dielectric disk very accurately ($\text{error} < 11\ \%$ with respect to the permittivity contrast). However, such excellent inversion accuracy was not always attained with the measured data, where in some cases relative permittivity errors of up to 28 % were observed (again with respect to the permittivity contrast). These errors were a result of the estimated effective target velocity being too low. The sensitivity of the estimated target permittivity to errors in the estimated effective target velocity reinforces the conclusion made earlier that the inversion for target size is more robust and has more practical use than the inversion for target material properties.

The experimental validation further demonstrated the possibility to determine antenna height and target depth with millimeter accuracy ($\text{error} < 0.5\ \text{cm}$). This confirms the capability of subset selection deconvolution to provide excellent temporal resolution. Since the estimation worked well for all targets, both surface-laid and buried, it may be concluded that determining antenna height and target depth is very robust.

Both the FDTD and the experimental data showed that internal target structure does influence the target response. Especially the presence of an air gap was found to significantly increase the target response magnitude of a buried dielectric minelike target. The presence of an air gap therefore facilitates the detection of buried plastic cased landmines with GPR. In contrast, a small metal inclusion has a very weak effect on the target response.

Application of the research results to landmine identification in real minefields & recommendations for future research

Based on the validation results, it can be concluded that out of all possible target characteristics that can be estimated with the proposed target characterization procedure, the outer target dimensions, i.e. cross-section and height, and target depth are the best candidates for AP landmine identification. This choice is based on the fact that their estimation never failed and in many cases gave millimeter accurate estimates. Furthermore, the outer target dimensions and the target depth are both very useful information for deciding whether a target is likely to be an AP landmine or not. If the GPR is part of a multi-sensor system, these target characteristics can be easily combined with target information obtained from other sensors, e.g. the presence of metal as indicated by a metal detector. In addition, target depth estimates may have practical use for assigning confidence values to detections by sensors whose performance is strongly depth dependent, e.g. an infrared camera.

Application of the research results in real minefields is not without reservation, mainly because the conditions in a minefield are far more complex than those for which the experimental validation was carried out. Hence, further research including experiments with real landmines under real minefield conditions remains indispensable. The following problems should be addressed in particular:

- Identification of a tilted AP landmine.
- Identification of an AP landmine buried under a rough ground surface.
- Identification given more complicated internal structure than just a single inclusion, e.g. the combination of an air gap with metallic and non-metallic parts of a fuse mechanism.
- Identification of an AP landmine based on a cluttered target response signal.

The following discussion takes a closer look at these problems and gives some ideas on how they could be approached from the material presented in this thesis.

To begin with, it should be noted that the general target transfer function/impulse response expression derived for a homogeneous dielectric minelike target can also be evaluated for a tilted dielectric disk. Considering the cross-section profile of a tilted disk, it is intuitively clear that the tilt will smear out the two differentiation operators of the target impulse response, the amount of smearing being determined by the amount of tilt. Hence, it needs to be analyzed up to which amount of tilt it is still reasonable to fit the target response signal with “non-smeared” differentiation operators, as subset selection deconvolution does. Clearly the easiest way to do such an analysis would be to use 3D FDTD modeling to simulate the response of a circular dielectric disk for increasing tilt angle.

When the ground surface is rough, the transmission through the ground surface becomes a random and frequency dependent process, which may only be described through statistical measures. Assuming that the target has the tendency to spatially average the incident field over its cross-section and that the receiving antenna does the same over its aperture, a rough ground surface may likely be incorporated into the derived convolutional models by simply replacing the flat surface transmission coefficients, $T_{a\to g}$ and $T_{g\to a}$, by frequency dependent rough surface transmission coefficients , $T^{\mathrm{r}}_{a\to g}$ and $T^{\mathrm{r}}_{g\to a}$, which describe the spatially averaged transmission through the rough ground surface. Such rough surface transmission coefficients may be derived using the *phase screen approximation*, which, for normal incidence and assuming a Gaussian surface height distribution, yields

$$T^{\mathrm{r}}_{a\to g} = \mathrm{T}^{\mathrm{r}}\, T_{a\to g} \qquad \& \qquad T^{\mathrm{r}}_{g\to a} = \mathrm{T}^{\mathrm{r}}\, T_{g\to a} \tag{6.1a}$$

with

$$\mathrm{T}^{\mathrm{r}} = e^{-0.5(k_1-k_0)^2\overline{\Delta^2}} \tag{6.1b}$$

(Kyle *et al*, 1996; Casey, 2001; Johnson and Burkholder, 2004), where $\overline{\Delta^2}$ is the variance of the ground surface height Δ. The effect of the surface roughness is accounted for by the multiplicative factor T^{r}, which becomes equal to one for a smooth ground surface and approaches a value of zero for increasing frequencies. A useful property of these rough surface transmission coefficients is that, given a lossless ground, T^{r} may be transformed to the time-domain:

$$\mathrm{t}^{\mathrm{r}}(t)=\frac{1}{\sqrt{2\pi\overline{\Delta^2}}\left(v_1^{-1}-c^{-1}\right)}e^{-\frac{t^2}{2\left(v_1^{-1}-c^{-1}\right)^2\overline{\Delta^2}}} \tag{6.2}$$

(Campbell and Foster, 1948, p. 85). It is important to note here that these rough surface transmission coefficients only provide an approximation for the coherent components of the transmitted field, i.e. those components that contribute in the vertical direction, and they do not account for the incoherent components of the transmitted field, i.e. those components that contribute in all directions. For a very rough ground surface, the incoherent components can make a significant contribution to the transmitted field in which case they cannot be neglected.

More advanced convolutional modeling of internal structure is less straightforward. Hence, rather than trying to develop more complex generic target impulse response models that would result in a very ill-posed deconvolution problem, one is most likely better off deconvolving landmine type specific target signatures from the measured target response signal. In terms of the target impulse response and the effective radiated waveform, the target signature of a specific landmine type may be defined as

$$\text{target signature} \equiv \mathrm{h}_{\mathrm{t}}(t)\otimes\mathrm{w}(t)\ . \tag{6.3}$$

The deconvolution of the target signature from the target response signal can be achieved through subset selection with a single non-zero impulse response coefficient. Now there are two indicators whether the detected target is a landmine of the type associated with the target signature. The first indicator is the deconvolution data fit and the second indicator is the scaling factor in the convolutional GPR model, i.e.

$$\frac{T_{g\to a}\zeta\left(h_{\mathrm{RX}},d\right)T_{a\to g}}{2\sqrt{\pi}\left(h_{\mathrm{RX}}+d\right)\left(h_{\mathrm{TX}}+d\right)} \tag{6.4}$$

for a buried target and accordingly for a surface-laid target. If the impulse response coefficient obtained from the subset selection deconvolution is close or equal to the scaling factor, than the detected target is potentially a landmine of the type associated with the target signature. On the other hand, if there is a big discrepancy between the two, than this is likely not the case. As before, the antenna height and the target depth to evaluate the spreading term can be estimated from the arrival time of the ground reflection and that of the target response. This advanced “template matching” procedure has a couple of useful features. First, there is no ambiguity as to the number of non-zero impulse response coefficients, which the subset selection needs to solve for: it is always just one. And second, since the subset selection deconvolution only has to solve for one non-zero impulse response coefficient, it is extremely fast and more robust with regard to clutter than subset selection deconvolution based on the impulse response model of a circular dielectric disk with an inclusion, which involves three non-zero coefficients. The disadvantage of this identification procedure is that more than 350 types of landmines exist. Hence, it is necessary to build up an extensive database of reference target signatures. Knowledge of which types of landmines were deployed in a certain region is very important. Since the target signature of a buried landmine depends also on the properties of the soil, it is important that the reference target signatures are measured in an environment similar to the one where the demining GPR is used. Note that identification of surface-laid landmines requires its own specific database of reference signatures.

Alternatively, as indicated before in section 3.4, one may approach the problem of complicated internal structure by arguing that it is unnecessary, if not undesirable, to resolve internal structure if all one is after are the outer dimensions of the detected target. Accordingly, for the estimation of the outer dimensions of a target, it may be sufficient to work at lower radar frequencies than the IRCTR video impulse GPR, close to the upper limit of the Rayleigh scattering regime. I would suggest a GPR operating with a peak amplitude frequency which satisfies $0.1 < a/\lambda < 0.15$, where a is the radius of the landmine and λ is the wavelength at the peak amplitude frequency. For example, given typical landmine radii (3-5 cm) and a ground with a relative dielectric permittivity of 4.0, a suitable peak amplitude frequency would be 500 MHz. At those frequencies, constant values may be assumed for the Green's tensor and the electric field at points within the landmine. As a result, the impulse response of the landmine consists of just one double differentiation operator and has a magnitude that is directly proportional to the product of its volume and its average generalized contrast (taken over the volume of the landmine), regardless of its internal structure, shape and tilt. Assuming that a generic average contrast exists, which is representative for a number of AP landmines, target volume can be estimated from the impulse response obtained by subset selection deconvolution based on an impulse response model consisting of one double differentiation operator. Again, this would be extremely fast and more robust with regard to clutter than subset selection deconvolution based on impulse response models consisting of multiple differentiation operators. Other benefits would be lower propagation losses and reduced sensitivity to roughness of the ground surface. A disadvantage of working at lower frequencies is that the height of the receiving antenna would have to be increased such that the far-field backscattering approximation of the half-space Green's tensor remains valid.

As a final remark, I believe that clutter will always limit the target identification capabilities of GPR (even if some of the ideas suggested above turn out to be good ones). Clutter represents the most important physical limitation of GPR target identification and this limitation cannot be removed by data processing. Hence, an important topic of future research should be the experimental estimation of the minimum allowable signal-to-clutter ratio for which the target characterization procedure presented in this thesis will still produce useful results.

REFERENCES

Alli, G., Bonopera, C., Sarri, A., Pinelli, G., and De Pasquale, G., 2004, Data processing for mine-detection polarimetric ground penetrating radar array, in *Proc. of the 10th International Conference on Ground Penetrating Radar,* Delft The Netherlands, vol. 2, 669-672.

Astanin, L. Y., and Kostylev, A. A., 1997, *Ultrawideband radar measurements*: Institution of Electrical Engineers (IEE).

Balanis, C. A., 1989, *Advanced engineering electromagnetics*: John Wiley & Sons.

Baños, A., 1966, *Dipole radiation in the presence of a conducting half-space*: Pergamon Press.

BASF, 2001, Packaging with Styropor: Product Publication. http://www.basf.de/basf/html/plastics/englisch/pages/pdfs/schaumpdf.htm

Baum, C. E., 1998, The SEM representation of scattering from perfectly conducting targets in simple lossy media, in C. E. Baum, ed., *Detection and identification of visually obscured targets*: Taylor & Francis, 47-79.

Born, M., 1933, *Optik*: Springer-Verlag.

Bruschini, C., Gros, B., Guerne, F., Pièce, P.-Y., and Carmona, O., 1998, Ground penetrating radar and imaging metal detector for antipersonnel mine detection: *Journal of Applied Geophysics*, vol. 40, no. 1-3, 59-71.

Campbell, G. A., and Foster, R. M., 1948, *Fourier integrals for practical applications*: Van Nostrand.

Carin, L., Geng, N., McClure, M., Sichina, J., and Nguyen, L., 1999, Ultra-wide-band synthetic-aperture radar for mine-field detection: *IEEE Antennas Propagat. Magazine,* vol. 41, no. 1, 18-33.

Casey, K. F., 2001, Rough-surface effects on subsurface target detection, in *Conf. Proc. SPIE,* vol. 4394, Detection and Remediation Technologies for Mines and Minelike Targets VI, Orlando, FL, USA, 754-763.

Chan, L. C., Moffat, D. L., and Peters Jr., L., 1979, A characterization of subsurface radar targets: *Proc. IEEE*, vol. 67, no. 7, 991-1000.

_____1981, Subsurface radar target imaging estimates: *IEEE Trans. Antennas Propagat.*, vol.29, no. 2, 413-417.

Chen, C.-C., and Peters Jr., L., 1997, Buried unexploded ordnance identification via complex natural resonances: *IEEE Trans. Antennas Propagat.*, vol.45, no. 11, 1645-1654.

Chew, W. C., 1990, *Waves and fields in inhomogeneous media*: Van Nostrand Reinhold.

Cremer, F., 2003, *Polarimetric infrared and sensor fusion for the detection of landmines*: Ph.D. thesis, Delft University of Technology, The Netherlands.

Damarla, R., Sullivan, A., Kappra, K., Sichina, J., and Wong, D., 2000, Detection of unexploded ordnance (UXO) using physical optics (PO) simulated images as templates, in *Conf. Proc. SPIE*, vol. 4033, Radar Sensor Technology V, 80-89.

Daniels, D. J., 1996, *Surface-penetrating radar*: Institution of Electrical Engineers (IEE).

Daniels, D. J., Gunton, D. J., and Scott, H. F., 1988, Introduction to subsurface radar: *IEE Proc.*, vol. 135, pt. F, no. 4, 278-321.

Daniels, D. J., and Curtis, P., 2003, Minetect, in *Proc. of the 2nd Int. Workshop on Advanced Ground Penetrating Radar*, Delft, The Netherlands, 110-114.

Dasgupta, N., Geng, N., Dogaru, T., and Carin, L., 1999, On the extended-Born technique for scattering from buried dielectric targets: *IEEE Trans. Antennas Propagat.*, vol.47, no. 11, 1739-1742.

De Hoop, A. T., 1996, A general correspondence principle for time-domain electromagnetic wave and diffusion fields: *Geophys. J. Int.*, vol. 127, no.3, 757-761.

Farinelli, P., and Roth, F., 2003, Frequency domain analysis of the polarimetric ground penetrating radar response of landmines and minelike targets, in *Conf. Proc. SPIE*, vol. 5089, Detection and Remediation Technologies for Mines and Minelike Targets VIII, Orlando, FL, USA, 437-447.

Fortuny-Guasch, J., Hosgood, B. D., Kokonozi, A., Lewis, A. M., and Sieber, A. J., 2001, Study of generic mine-like objects for R&D in systems for humanitarian demining, J. T. Dean, ed., *Project MIMEVA – Final report*: Institute for Systems, Informatics and Safety, European Commission Joint Research Centre, Italy.

Geng, N., and Carin, L., 1999, Wide-band electromagnetic scattering from a dielectric BOR buried in a layered lossy dispersive medium: *IEEE Trans. Antennas Propagat.*, vol.47, no. 4, 610-619.

Gershenson, M., 1997, Simple interpretation of time-domain electromagnetic sounding using similarities between wave and diffusion propagation: *Geophysics*, vol. 62, no. 3, 763-774.

Golub, G. H., and Van Loan, C. F., 1983, *Matrix computations*: The Johns Hopkins University Press.

Gorriti, A. G., 2004, *Electric characterization of sands with heterogeneous saturation distribution*: Ph.D. thesis, Delft University of Technology, The Netherlands.

Groenenboom, J., and Yarovoy, A., 2002, Data processing and imaging in GPR system dedicated for landmine detection: *Subsurface Sensing Technologies and Applications*, vol. 3, no. 4, 387-402.

Habashy, T. M., Groom, R. W., and Spies, B. R., 1993, Beyond the Born and Rytov approximations: A nonlinear approach to electromagnetic scattering: *J. of Geophys. Res.*, vol. 98, no. B2, 1759-1775.

Huynen, I., Steisel, J., Van den Bosch, I., and Stockbroecks, B., 2003, Detection of natural frequencies as signatures of buried cylindrical targets, in *Proc. EUDEM2-SCOT-2003*, International Conference on Requirements and Technologies for the Detection, Removal and Neutralization of Landmines and UXO, Brussels, Belgium, 270-275.

Johnson, J. T., and Burkholder, R. J., 2004, A study of scattering from an object below a rough surface: *IEEE Trans. Geosci. Remote Sensing*, vol. 42, no. 1, 59-66.

JRC Landmine Signature Database: The Institute for the Protection and Security of the Citizen, European Commission Joint Research Centre, Italy. Available: http://apl-database.jrc.it

Keller, G. V., 1987, Electromagnetic rock and mineral properties, in M. N. Nabighian, ed., *Electromagnetic methods in applied geophysics, Vol. I, Theor*y: Society of Exploration Geophysicists (SEG), 13-51.

Kennaugh, E. M., and Moffatt, D. L., 1965,Transient and impulse response approximations: *Proc. IEEE*, vol. 53, no. 8, 893-901.

King, R. W. P., and Shen, L. C., 1979, Radiation into the air above a horizontal dipole in the earth: *Radio Science*, vol. 14, no. 6, 1049-1056.

Kong, J. A., 1986, *Electromagnetic wave theory*: John Wiley & Sons.

Kovalenko, V., and Yarovoy, A., 2003, Analysis of target responses and clutter based on measurements at the test facility for landmine detection systems located at TNO-FEL, in *Proc. of the 2nd Int. Workshop on Advanced Ground Penetrating Radar*, Delft, The Netherlands, 82-88.

Kostylev, A. A., 1994, Methods of signal processing in measurement of UWB radar response, in *Radar target characteristics: Measurements and applications*: CRC Press, 237-276.

Kyle W. H., Holland, M. R., Miller, J. G., Nagy, P. B., and Rose, J. H., 1996, Effective ultrasonic transmission coefficients for randomly rough surfaces: *J. Acoust. Soc. Am.*, vol. 100, no. 2, pt. 1, 832-839.

Lambot, S., Slob, E.C., Van den Bosch, I., Antoine, M., Gregoire, M., Vanclooster, M., 2004, Modeling of GPR signal and inversion for identifying the subsurface dielectric properties, in *Proc. of the 10th International Conference on Ground Penetrating Radar*, Delft The Netherlands, vol. 1, 79-82.

MacDonald, J. A., Lockwood, J. R., and McFee, J., 2003, Research plan for a multi-sensor landmine detector, in *Proc. EUDEM2-SCOT-2003*, International Conference on Requirements and Technologies for the Detection, Removal and Neutralization of Landmines and UXO, Brussels, Belgium, 625-632.

Mur, G., 1998, Total-Field Absorbing boundary conditions for the time-domain electromagnetic field equations: *IEEE Trans. Electromagn. Compat.*, vol. 40, no. 2, 100-102.

Mur, G., 2001, *FDTD3D: The C++ finite-difference code for electromagnetic fields in three dimensions and time*: Delft University of Technology, The Netherlands.

Nag, S., and Peters Jr., L., 2001, Radar images of penetrable targets generated from ramp profile functions: *IEEE Trans. Antennas Propagat.*, vol.49, no. 1, 32-40.

Olhoeft, G. R., 1998, Electrical, magnetic, and geometric properties that determine ground penetrating radar performance, in *Proc. GPR'98*, 7th International Conference on Ground Penetrating Radar, Lawrence, KS, USA, 177-182.

Powers, M. H., 1995, *Dispersive ground penetrating radar modeling in 2D*: Ph.D. thesis, Colorado School of Mines, CO, USA.

Press, W. H., Teukolsky, S.A., Vetterling, W. T., and Flannery, B. P., 1992, *Numerical Recipes in C (2nd Edition)*: Cambridge University Press.

Raiche, A. P., 1974, An integral equation approach to three-dimensional modeling: *Geophys. J. Roy. Astr. Soc.*, vol. 36, 363-376.

Roth, F., Van Genderen, P., and Verhaegen, M., 2001, Analysis of the influence of mine and soil properties on features extracted from GPR data, in *Conf. Proc. SPIE*, vol. 4394, Detection and Remediation Technologies for Mines and Minelike Targets VI, Orlando, FL, USA, 428-439.

_____2002, Radar response approximations for buried plastic landmines, in *Conf. Proc. SPIE*, vol. 4758, 9th International Conference on Ground Penetrating Radar, Santa Barbara, CA, USA, 234-239.

_____2003, Processing and analysis of polarimetric ground penetrating radar landmine signatures, in *Proc. of the 2nd Int. Workshop on Advanced Ground Penetrating Radar*, Delft, The Netherlands, 70-75.

Savelyev, T. G., Van Kempen, L., and Sahli, H., 2003, GPR anti-personnel mine detection: improved deconvolution and time-frequency feature extraction", in *Conf. Proc. SPIE*, vol. 5046, NDE and Health Monitoring of Aerospace Materials and Composites II, San Diego, CA, USA, 232-241.

Scheers, B., 2001, *Ultra-wideband ground penetrating radar with application to the detection of anti personnel landmines*: Ph.D. thesis, Université Catholique de Louvain, Belgium.

Scheers, B., Archeroy, M., and Vander Vorst, A., 2000, Time domain modelling of UWB GPR and its application on landmine detection, in *Conf. Proc. SPIE*, vol. 4038, Detection and Remediation Technologies for Mines and Minelike Targets V, Orlando, FL, USA, 1452-1460.

Scheers, B., Archeroy, M., and Vander Vorst, A., 2001, Migration technique based on the time-domain model of the ground penetrating radar, in *Conf. Proc. SPIE*, vol. 4491, Subsurface and Surface Sensing Technologies and Applications III, San Diego, CA, USA, 111-119.Turner, G., 1994, Subsurface radar propagation deconvolution: *Geophysics*, vol. 59, no. 2, 215-223.

Schouten, J. P., 1961, *Operatorenrechnung – Mit Anwendung auf technische Probleme*: Springer-Verlag.

Stern, W., 1930, Über Grundlagen, Methodik und bisherige Ergebnisse elektrodynamischer Dickenmessung von Gletscherei: *Zeitschrift für Gletscherkunde, für Eiszeitforschung und Geschichte des Klimas*, vol. 15, 24-42.

Strifors, H. C., Gaunaurd, G. C., and Sullivan, A., 2002, Influence of soil properties on time-frequency signatures of conducting and dielectric targets buried underground, in *Conf. Proc. SPIE*, vol. 4726, Automatic Target Recognition XII, Orlando, FL, USA, 15-25.

Sullivan, A., Geng, N., Carin, L., Nguyen, L., and Sichina, J., 1999, Performance analysis for radar detection of buried anti-tank and anti-personnel land mines, in *Conf. Proc. SPIE*, vol. 3710, Detection and Remediation Technologies for Mines and Minelike Targets IV, Orlando, FL, USA, 1043-1050.

Telford, W. M., Geldart, L. P., and Sheriff, R.E., 1990, *Applied Geophysics*: Cambridge University Press.

Ulaby, F. T., and Elachi, C., 1990, *Radar polarimetry for geoscience applications*: Artech House.

Van der Kruk, J., 2001, *Three-dimensional imaging of multi-component ground penetrating radar data*: Ph.D. thesis, Delft University of Technology, The Netherlands.

Van der Lijn, F., Roth, F., and Verhaegen, M., 2003, Estimating the impulse response of buried objects from ground penetrating radar signals, in *Conf. Proc. SPIE*, vol. 5089, Detection and Remediation Technologies for Mines and Minelike Targets VIII, Orlando, FL, USA, 387-394.

Van Dongen, K. W. A., Van den Berg, P. M., and Nicolaescu, I., 2003, Subsurface imaging using measured antenna footprints, in *Proc. of the 2nd Int. Workshop on Advanced Ground Penetrating Radar*, Delft, The Netherlands, 195-200.

Verweij, M. D., 2001, Combining fractional time derivative loss models and the similarity transformation technique to turn lossless configurations into lossy ones, in *Conf. Proc. SPIE*, vol. 4491, Subsurface and Surface Sensing Technologies and Applications III, 183-192.

Von Hippel, A. R., 1954, Dielectric materials and applications: John Wiley & Sons.

Ward, S. H., and Hohmann, G.W., 1987, Electromagnetic theory for geophysical applications, in M. N. Nabighian, ed., *Electromagnetic methods in applied geophysics, Vol. I, Theor*y: Society of Exploration Geophysicists (SEG), 130-311.

Xiong, Z., and Tripp, A. C., 1997, 3-D electromagnetic modeling for near-surface targets using integral equations: *Geophysics*, vol. 62, no. 4, 1097-1106.

Yarovoy, A. G., Van Genderen, P., and Ligthart, L. P., 2000a, Ground penetrating impulse radar for landmine detection, in *Conf. Proc. SPIE*, vol. 4084, 8th International Conference on Ground Penetrating Radar, Gold Coast, Australia, 856-860.

Yarovoy, A., De Jongh, R., and Ligthart, L., 2000b, Ultra-wideband sensor for electromagnetic field measurements in time domain: *Electronics Letters*, vol. 36, no. 20, 1679-1680.

Yarovoy, A. G., Ligthart, L. P., Schukin, A., and Kaploun, I., 2002a, Polarimetric video impulse radar for landmine detection: *Subsurface Sensing Technologies and Applications*, vol. 3, no. 4, 271-293.

Yarovoy, A. G., Schukin, A. D., Kaploun, I. V., and Ligthart, L. P., 2002b, The dielectric wedge antenna: *IEEE Trans. Antennas Propagat.*, vol.50, no. 10, 1460-1472.

Yarovoy, A., Kovalenko, V., and Fogar, A., Impact of ground clutter on buried object detection by ground penetrating radar, 2003, in *Proc. IGARSS 2003*, IEEE International Geoscience and Remote Sensing Symposium, Toulouse, France, vol. 2, 755-757.

Yilmaz, Ö., 1987, *Seismic data processing*: Society of Exploration Geophysicists (SEG).

Zanzi, L., Lualdi, M., Braun, H. M., Borisch, W., and Triltzsch, G., 2002, An ultra high frequency radar sensor for humanitarian demining tested on different scenarios in 3D imaging mode, in *Conf. Proc. SPIE*, vol. 4758, 9th International Conference on Ground Penetrating Radar, Santa Barbara, CA, USA, 240-245.

SUMMARY

Future landmine detection systems are likely to use combinations of different types of sensors to increase the detection and reduce the false alarm rate. Ground penetrating radar (GPR) has great potential for use in such a multi-sensor system due to its ability to detect, localize and identify both plastic and metal cased landmines, whether surface-laid or buried.

This thesis presents new developments in the area of target identification with GPR, which open the possibility to identify plastic and metal cased antipersonnel (AP) landmines from a single measured GPR return signal, called A-scan, within a very short computation time. The underlying basis of these developments is to formulate the target identification as a convolution-deconvolution problem. This entails representing the measured target response through a convolutional model, which describes the sequence of radiation, propagation, target scattering and receiving, and using deconvolution to estimate an impulse response from which target characteristics (its outer dimensions or material properties) and target depth may be inferred. These characteristics in turn provide information on the likely identity of the detected target.

The three main contributions of this thesis are:

- The systematic derivation of a convolutional GPR model including closed-form expressions for the target transfer function/impulse response of an AP landmine in terms of its size, shape, electromagnetic contrast and internal structure.
- The development of a deconvolution based target characterization procedure for circular disk-shaped minelike targets, which are representative for a large class of AP landmines. The target characterization procedure operates on the target response at the apex of the target diffraction hyperbola.
- The design of preprocessing algorithms that extract a target response suitable for target characterization from the measured GPR data.

The derivation of the convolutional GPR model is based on source-type integral representations of the scattered field in which a linear relationship between the scattering current and the incident field is invoked by making use of either the Born and Rayleigh approximations or the Physical Optics (PO) approximation, depending on the material composition of the landmine, i.e. plastic cased or metal cased. Furthermore, the half-space electric Green’s tensor is approximated by a new far-field backscattering representation. The GPR hardware is modeled by introducing point source/receiver models. Doing so, the radiation characteristics of the transmitting antenna and the reception characteristics of the receiver chain, which includes the receiving antenna, are conveniently expressed through a single term, namely the effective radiated waveform. This waveform can be estimated from a simple metal sheet reflection calibration measurement. An important result of this derivation is that a homogeneous circular disk-shaped minelike target buried in a lossless ground differentiates the waveform of the incident field rather than just reflecting it. A similar scattering behavior was found for internal mine components, specifically an air gap or a small piece of metal, both of which differentiate the waveform of the incident field twice. Accordingly, the target impulse response of a circular disk-shaped minelike target is sparse, consisting of only a few differentiation operators.

The target characterization procedure builds on a new time-domain least squares deconvolution algorithm, termed subset selection deconvolution, which is used to deconvolve the effective radiated waveform from the measured target response. The novelty of the subset selection deconvolution algorithm lies in the fact that it uses the sparse target impulse response models that have been derived for circular disk-shaped minelike targets as a priori information on the form of impulse response to be estimated. As a result, subset selection deconvolution provides physical amplitude information and excellent temporal resolution, which are essential for inferring target characteristics and depth from the estimated impulse response. This approach also reduces the ill-posedness and noise sensitivity inherent to the deconvolution of band-limited signals. Based on the derived convolutional GPR model, two types of impulse response inversions are formulated: the inversion for target size and the inversion for target material properties. The inversion for target size estimates the outer dimensions of the target and, given a dielectric minelike target, the volume of its internal components. The inversion for material properties estimates the relative permittivity of the body of a dielectric minelike target.

Preprocessing is an important aspect of GPR target identification. The thesis introduces two new preprocessing algorithms, which are the weighted moving average background subtraction (WMA-BS) and the target frame transformation, and illustrates their workings using experimental data acquired with an ultra-wideband polarimetric video impulse GPR developed at the International Research Centre for Telecommunications-Transmission and Radar (IRCTR). The WMA-BS algorithm is designed to remove the direct wave signal and the ground reflection signal from each measured A-scan. The algorithm works in an iterative manner by first finding the anomalies in the GPR data and then suppressing them in the estimation of the background to be subtracted. As a result, WMA-BS does not smear out the target response to neighboring A-scans or change its amplitude and shape, both of which are problems usually encountered with conventional moving average background subtraction. The target frame transformation rotates the polarimetric target response, i.e. the scattering matrix, into the coordinate frame defined by the two natural polarization of the target. Like this a target response that is independent of target orientation is obtained, which is essential to the identification of targets with a preferential scattering axis, e.g. an elongated bombshell.

The target characterization procedure and its underlying convolutional GPR model are validated for a number of circular disk-shaped minelike targets, with and without internal structure, using data from 3D finite-difference time-domain (FDTD) simulations and indoor experiments with the IRCTR video impulse GPR. The FDTD and experimental results demonstrate that the inversion for target size can estimate the outer dimensions of a homogeneous minelike target (metal or dielectric) with millimeter accuracy $(\text{error} < 0.5\text{ cm})$. In the presence of internal structure, the accuracy with which the outer dimensions of a dielectric minelike target can be estimated is lower but still reasonable $(\text{error} < 1\text{ cm})$. The estimation of the volume of an air gap or a small piece of metal inside a dielectric minelike target generally works less well $(\text{error} < 35\,\%)$. The results of the inversions for material properties obtained with the FDTD data demonstrate that in principle it is possible to estimate the relative permittivity of a homogeneous dielectric minelike target very accurately $(\text{error} < 11\,\%$ with respect to the permittivity contrast). However, such excellent inversion accuracy was not always attained with the experimental data $(\text{error} < 28\,\%$ with respect to the permittivity contrast). The experimental validation further demonstrated the possibility to determine target depth with millimeter accuracy $(\text{error} < 0.5\text{ cm})$.

In conclusion, the inversion performance achieved for the experimental data demonstrates that the proposed target characterization procedure has a lot of potential for AP landmine identification. To this end, estimates of the outer dimensions of the target and depth are considered particularly useful. Not only do these characteristics provide information for deciding whether a detected target is likely to be an AP landmine or not, but their estimation also never fails in the data examples considered and in many cases gives millimeter accurate estimates. If the GPR is part of a multi-sensor system, these target characteristics can be easily combined with target information obtained from other sensors, e.g. the presence of metal as indicated by a metal detector. In addition, target depth estimates may have practical use for assigning confidence values to detections by sensors whose performance is strongly depth dependent, e.g. an infrared camera.

Unquestionably, the research results presented in this thesis are not fully representative for the target characterization performance that can be attained in a real minefield simply because the conditions in a minefield are far more complex than those for which the experimental validation was carried out. Hence, further research including experiments with real landmines under real minefield conditions remains indispensable. Since clutter represents the most important physical limitation to GPR target identification, one of the primary topics of future research should be the experimental estimation of the minimum allowable signal-to-clutter ratio for which the target characterization procedure presented in this thesis will still produce useful results.

Despite these limiting factors, it is important to note that the systematic approach in the development of the convolutional GPR model and of the target characterization procedure allows for their adaptation to more complex GPR scenarios than the ones considered in this thesis. Some conceivable adaptations are the introduction of rough surface transmission coefficients to account for a rough ground surface and the use of the derived frequency-domain convolutional scattering model to characterize targets buried in a lossy ground. Another interesting adaptation would be the use of the convolutional GPR model to develop a target identification scheme that is based on the deconvolution of landmine type specific target signatures.

Friedrich Roth

SAMENVATTING

Convolutiemodellen voor de identificatie van landmijnen met behulp van grondradar

Toekomstige landmijndetectiesystemen zullen waarschijnlijk verschillende typen sensoren combineren om zo de detectie te verbeteren en het aantal valse alarm meldingen te verminderen. Grondradar (GPR) biedt goede mogelijkheden voor integratie in een dergelijk multisensor-systeem vanwege zijn mogelijkheid om zowel kunststof- als metaalbehuisde landmijnen te detecteren, lokaliseren en identificeren, of het nu gaat om op de oppervlakte geplaatste mijnen of begraven mijnen.

Dit proefschrift toont nieuwe ontwikkelingen op het gebied van GPR doelidentificatie toegepast op de identificatie van kunststof- en metaalbehuisde antipersoneels (AP) landmijnen. De identificatie maakt gebruik van één enkel gemeten GPR reflectiesignaal, A-scan genaamd, en heeft een zeer korte berekentijd. De basis van deze ontwikkelingen is de formulering van het doelidentificatieprobleem als een convolutie/deconvolutie-probleem. Dit houdt in dat de gemeten doelresponsie door een convolutiemodel wordt gerepresenteerd die de achtereenvolgende stappen van uitstraling, voortplanting, doelverstrooiing en ontvangst beschrijft en dat deconvolutie gebruikt wordt om een schatting te verkrijgen van de impulsresponsie. Hieruit kunnen vervolgens doeleigenschappen (uitwendige afmetingen en materiaaleigenschappen) en doeldiepte worden afgeleid. Deze eigenschappen leveren tenslotte informatie over de waarschijnlijke identiteit van het gedetecteerde doel.

De drie hoofdbijdragen van dit proefschrift zijn:

- De systematische afleiding van een GPR convolutiemodel inclusief analytische uitdrukkingen voor de doeloverdrachtsfunctie/impulsresponsie van een AP landmijn als functie van zijn afmetingen, vorm, electromagnetische contrast en interne structuur.
- De ontwikkeling van een op deconvolutie gebaseerde doelkarakteriseringsprocedure voor mijnachtige doelen in de vorm van een ronde schijf, welke representatief zijn voor een grote klasse van AP landmijnen. De procedure maakt gebruik van de doelresponsie op het hoogste punt van de doeldefractiehyperbool.
- De ontwikkeling van voorbewerkingsalgoritmen die de GPR meetgegevens dusdanig voorbewerken dat ze geschikt worden voor doelkarakterisering.

De afleiding van het GPR convolutiemodel is gebaseerd op bron-type integraalrepresentaties van het verstrooide veld waarbij een lineair verband tussen de verstrooistroom en het invallende veld wordt verondersteld. Hierbij worden hetzij de Born- en Rayleigh-benaderingen gebruikt, hetzij de fysisch optische (*Physical Optics*, PO) benadering, afhankelijk van de materiële samenstelling van de landmijn, dat wil zeggen kunststofbehuisd of metaalbehuisd. Bovendien wordt de elektrische Green's tensor voor halfruimten benaderd door een nieuwe verre-veld terugverstrooiingsrepresentatie (*backscattering representation*). Het GPR systeem wordt gemodelleerd door puntbron/puntontvanger modellen. Op deze manier worden de zendeigenschappen van de zendantenne en de ontvangsteigenschappen van de ontvangstketen met inbegrip van de ontvangstantenne, eenvoudig uitgedrukt door één enkele term, namelijk de effectief uitgestraalde golfvorm. Deze golfvorm kan simpelweg geschat worden aan de hand van een calibratiemeeting waarbij de reflectie door een metalen plaat wordt gemeten. Een belangrijk resultaat van deze afleiding is dat een schijfvormig

mijnachtig doel begraven in een verliesvrije ondergrond resulteert in een golfvorm die de afgeleide is van de golfvorm van het invallende veld. Een overeenkomstig verstrooiingsgedrag wordt gevonden voor interne onderdelen van mijnen, met name voor een luchtgevulde holte of voor een klein metalen onderdeel. Beide resulteren in golfvormen die overeenkomen met de tweede afgeleide van de golfvorm van het invallende veld. Zodoende is de doelimpulsresponsie van een schijfvormig mijnachtig doel ijl (*sparse*) en bestaat deze uit slechts enkele differentiaal operatoren.

De doelkarakteriseringsprocedure borduurt voort op een nieuw tijdsdomein kleinste-kwadraten deconvolutie-algoritme genaamd *subset selection deconvolution* die gebruikt wordt om de effectief uitgestraalde golfvorm van de gemeten doelresponsie te deconvolueren. Het nieuwe van de *subset selection deconvolution* is gelegen in het feit dat dit algoritme gebruik maakt van de ijle doelimpulsresponsie-modellen die zijn afgeleid voor schijfvormige mijnachtige doelen. Deze modellen worden gebruikt als a priori informatie voor de vorm van de te schatten impulsresponsie. Op deze manier levert *subset selection deconvolution* fysische amplitude-informatie en voortreffelijke temporele resolutie, welke essentiëel zijn bij het afleiden van doeleigenschappen en doeldiepte uit de geschatte impulsresponsie. Deze benadering vermindert ook de slecht gesteldheid en de ruisgevoeligheid inherent aan de deconvolutie van bandbegrensde signalen. Op basis van het afgeleide GPR convolutiemodel worden twee typen inversies van de impulsresponsie geformuleerd: de inversie voor doelafmetingen en de inversie voor doelmateriaaleigenschappen. De inversie voor doelafmetingen leidt tot een schatting van de uitwendige afmetingen van het doel en, gegeven dat het een diëlektrisch mijnachtig object betreft, het volume van haar interne onderdelen. De inversie voor materiaaleigenschappen leidt tot een schatting van de relatieve permittiviteit van het lichaam van een diëlektrisch mijnachtig doel.

Voorbewerking van de data is een belangrijk aspect van GPR doelidentificatie. In het proefschrift worden twee nieuwe voorbewerkingsalgoritmen geïntroduceerd te weten de *weighted moving average background subtraction* (WMA-BS) en de *target frame transformation*. Ook wordt geïllustreerd hoe deze werken gebruikmakend van experimentele data verkregen met een ultra-breedband polarimetrische video impuls GPR die ontwikkeld is bij het International Research Centre for Telecommunications-Transmission and Radar (IRCTR). Het WMA-BS algoritme is ontwikkeld om het direkte golfsignaal en het grondreflectiesignaal uit elke gemeten A-scan te verwijderen. Het algoritme werkt op een iteratieve manier door eerst de anomalien in de GPR data te lokaliseren en deze vervolgens te onderdrukken bij het schatten van de achtergrond die van de data dient te worden afgetrokken. Zodoende smeert het WMA-BS algoritme de doelresponsie niet uit naar naburige A-scans noch verandert het haar amplitude en vorm. Beide problemen treft men vaak aan bij het conventionele *moving average background subtraction* algoritme. De *target frame transformation* roteert de polarimetrische doelresponsie, dat wil zeggen de verstrooiingsmatrix, naar het coördinatenstelsel gedefiniëerd door de twee natuurlijke polarisaties van het doel. Hiermee wordt een doelresponsie verkregen die onafhankelijk is van de doeloriëntatie, wat essentiëel is voor de identificatie van doelen met een voorkeursverstrooiingsas zoals een langwerpige granaathuls.

De doelidentificatieprocedure en het ten grondslag liggende GPR convolutiemodel zijn gevalideerd voor een aantal schijfvormige mijnachtige doelen, met en zonder interne structuur, aan de hand van 3D eindige-differentie tijdsdomein (FDTD) simulaties en laboratoriumexperimenten met de IRCTR video impuls GPR. De FDTD en experimentele resultaten tonen aan dat de inversie voor doelafmetingen waarden voor de uitwendige afmetingen van homogene mijnachtige doelen (metaal of diëlektrisch) oplevert met hoge nauwkeurigheid (fout < 0.5 cm). In het geval dat de doelen interne structuur bevatten, vermindert deze nauwkeurigheid maar blijft zij nog steeds heel redelijk (fout < 1 cm). De schatting van het volume van een luchtholte of een klein metalen deel in een diëlektische mijnachtig doel lukt over het algemeen minder goed (fout < 35 %). De resultaten van de inversies voor materiaaleigenschappen, verkregen op basis van FDTD data, tonen aan dat het in principe mogelijk is de relatieve permittiviteit van een homogeen diëlektrisch mijnachtig doel zeer nauwkeurig te schatten (fout < 11 % t.o.v. het permittiviteitscontrast). Echter met experimentele data werd deze nauwkeurigheid niet gehaald (fout < 28 % t.o.v. het permittiviteitscontrast met de achtergrond). De experimentele validatie toonde verder aan dat de doeldiepte met hoge nauwkeurigheid kan worden bepaald (fout < 0.5 cm).

De inversieprestaties bereikt met experimentele data tonen aan dat de voorgestelde doelkarakteriseringprocedure goede mogelijkheden biedt voor AP landmijnidentificatie. Vooral de schattingen van de uitwendige afmetingen en de doeldiepte worden als bijzonder waardevol gezien. Ze geven niet alleen nuttige informatie om te beslissen of een gedetecteerd doel een AP landmijn is of niet, maar ze waren ook nooit volledig verkeerd en gaven in veel gevallen waarden met een nauwkeurigheid in de orde van millimeters. Bovendien kunnen deze schattingen eenvoudig gecombineerd worden met doelinformatie verkregen met behulp van andere landmijndetectiesensoren, bijvoorbeeld informatie over de aanwezigheid van metaal verkregen door een metaaldetector. Een andere mogelijke toepassing is het gebruik van de doeldiepte om vertrouwenswaarden te verbinden aan detecties door sensoren waarvan de prestatie diepteafhankelijk is. Een voorbeeld van zo een sensor is een infrarood camera.

Er moet echter wel worden opgemerkt dat de aangetoonde prestatie van de doelkarakteriseringsprocedure niet helemaal representatief is voor hetgeen in een echt mijnenveld kan worden bereikt. De reden hiervoor is simpelweg het feit dat de omstandigheden in een mijnenveld veel complexer zijn dan die in een laboratorium. Verder wetenschappelijk onderzoek inclusief GPR experimenten met echte landmijnen onder omstandigheden van een echt mijnenveld blijft daarom ongetwijfeld noodzakelijk. Aangezien *clutter* de primaire fysische begrenzing aan doelidentificatie met behulp van GPR is, is het vooral belangrijk om de minimale signaal-*clutter* verhouding te bepalen waarvoor de voorgestelde doelkarakteriseringsprocedure nog steeds bruikbare schattingen oplevert.

Ondanks deze beperkingen maakt de systematische aanpak in de ontwikkeling van het GPR convolutiemodel en van de doelkarakteriseringsprocedure de aanpassing mogelijk aan complexere GPR omstandigheden dan degene die in dit proefschrift zijn behandeld. Denkbare aanpassingen zijn de invoering van transmissiecoëfficiënten voor ruwe oppervlakten en het gebruik van het afgeleide frequentiedomein verstrooiings-convolutiemodel voor de karakterisering van doelen begraven in een verliesgevende ondergrond. Een verdere mogelijke aanpassing is het gebruik van het GPR convolutiemodel om een doelidentificatieschema te ontwikkelen dat gebaseerd is op de deconvolutie van doelsignaturen van specifieke landmijntypen.

Friedrich Roth

ACKNOWLEDGEMENTS

Doing a PhD is immense undertaking which involves many activities: the exploration and exchange of ideas, the discipline to work out details, the documentation of research results in a clear and interesting fashion, just to name a few. No doubt, such an undertaking can only take place in a creative and supportive environment. Looking back at the last four and a half years that I spent in Delft, I can say that I was once again lucky to have met and worked with people that made it possible.

Special thanks go to my supervisors Piet van Genderen and Michel Verhaegen for helping me to define the track of my research and to stay on it. Piet van Genderen for the endless interest he has shown in my research and for requiring clear explanation of every single research result obtained, which always helped me in finding the next step to take. Michel Verhaegen for sharing his vast experience in deconvolution algorithms and least squares problems without which the use of subset selection deconvolution would never have crossed my mind. Further, I wish to thank the thesis committee members for their thorough review of the thesis manuscript and their constructive suggestions for improvement.

The International Research Centre for Telecommunications-Transmission and Radar (IRCTR) provided an excellent environment for doing both theoretical and experimental GPR research, which to a great part may be attributed to the expertise and enthusiasm of Alex Yarovoy. The principle of IRCTR that every theory developed has to be validated by experiment would be meaningless without the support of the technical staff. In this respect, I particularly enjoyed the help of Joost van Heijenoort with setting up my experiments and the support of Paul Hakkaart in getting the Teflon disks made.

I am also greatly indebted to Ainhoa Gorriti from the department of Geotechnology for measuring the dielectric permittivity of the sand at the experimental facility where I did my GPR experiments, and of many other soil samples that I needed to have analyzed. The afternoons spent in her lab were always great fun and full of interesting conversations.

I also would like to thank the outstanding students that I had the opportunity to work with. Fedde van der Lijn did the first formulation of the subset selection deconvolution algorithm and tested it on FDTD data, Paola Farinelli produced the first successful experimental results of the target frame transformation, and Eveline Ligthart gave me the possibility to be involved in GPR image processing, a topic that deserves a PhD thesis in its own right. Working with them was by far the most fun and gratifying part of my PhD.

For the translation of the summary and the propositions I relied on the support of Richard Bloemenkamp, Jacco de Wit and Xander Campman. Thank you all for the fast and spontaneous help when the printing deadline was approaching.

Outside of work, many friends in Delft provided for the relaxation and enjoyment that was necessary for “recharging my battery”. Here special thanks go to Berni, Cristina, Chris, Rute, Bruno and Hélène. At this point, I would also like to thank my housemates at the *Cameretten* for giving me the feeling of coming “home” whenever I got back from working long evening hours on campus.

Finally, I would like to thank my parents, my brother and my sister for supporting and encouraging me in all my pursuits. They are my unlimited source of strength for tackling every challenge life offers.

Friedrich Roth

ABOUT THE AUTHOR

Friedrich Roth was born in Munich, Germany, on the 24th of December 1972. During his childhood his family relocated to Antwerp, Belgium. He received the European Baccalaureate degree from the European School Mol (near Antwerp) in 1991. After two years of various pursuits - one semester of French language at the Université Toulouse Le Mirail, France, his social service at a protestant cultural center in Hamburg, Germany, and a four-month backpacking trip through China - he felt that his interest in natural science and travel abroad called for a career in the Geosciences and enrolled in the Geophysics program at the University of Hamburg in 1993. There, he enjoyed the possibility to participate in various geophysical surveys, among which a seismic risk analysis on Cyprus and a marine heat flow study at the East Pacific Rise. Focusing on ground penetrating radar (GPR), he transferred to the Colorado School of Mines, USA, in 1996, where he was awarded a MSc in Geophysics in 1999. While at Mines, he studied the possible use of inertial navigation for real-time antenna position and orientation estimation for ground penetrating radar surveys. In 2000, he moved to The Netherlands and joined the International Research Centre for Telecommunications-Transmission and Radar (IRCTR) at the Delft University of Technology as a PhD student. His research on landmine identification with GPR, for which he was awarded the Young Scientist Best Paper Award at 10th International Conference on Ground Penetrating Radar in 2004, led to the present PhD thesis. Currently, he is a Marie Curie Research Fellow at the Schlumberger Riboud Product Center in Clamart, France, where he works on finite element modeling of resistivity imaging tools, which are used to map the geology of oil reservoirs near boreholes.

PUBLICATIONS BY THE AUTHOR

Roth, F., Van Genderen, P., and Verhaegen, M., Convolutional Models for buried target characterization with ground penetrating radar, submitted for publication to *IEEE Trans. Antennas Propagat.*

Yarovoy, A., **Roth**, F., Kovalenko, V., and Ligthart, L., Application of UWB near-field polarimetry to classification of GPR targets, accepted for publication in *Ultra-wideband, short-pulse electromagnetics 7*: Kluwer Academic/Plenum Publishers, 8p.

Roth, F., Van Genderen, P., and Verhaegen, M., 2004, Radar scattering models for the identification of buried low-metal content landmines, in *Proc. of the 10th International Conference on Ground Penetrating Radar*, Delft The Netherlands, vol. 2, 689-692.

Roth, F., Van Genderen, P., and Verhaegen, M., 2003, Host medium transformation of the early-time radar response of a buried dielectric target, in *Proc. IGARSS 2003*, IEEE International Geoscience and Remote Sensing Symposium, Toulouse, France, vol. 2, 1356-1358.

Roth, F., Van Genderen, P., and Verhaegen, M., 2003, Processing and analysis of polarimetric ground penetrating radar landmine signatures, in *Proc. of the 2nd Int. Workshop on Advanced Ground Penetrating Radar,* Delft, The Netherlands, 70-75.

Farinelli, P., and **Roth**, F., 2003, Frequency domain analysis of the polarimetric ground penetrating radar response of landmines and minelike targets, in *Conf. Proc. SPIE*, vol. 5089, Detection and Remediation Technologies for Mines and Minelike Targets VIII, Orlando, FL, USA, 437-447.

Van der Lijn, F., **Roth**, F., and Verhaegen, M., 2003, Estimating the impulse response of buried objects from ground penetrating radar signals, in *Conf. Proc. SPIE*, vol. 5089, Detection and Remediation Technologies for Mines and Minelike Targets VIII, Orlando, FL, USA, 387-394.

Roth, F., Van Genderen, P., and Verhaegen, M., 2002, Radar response approximations for buried plastic landmines, in *Conf. Proc. SPIE*, vol. 4758, 9th International Conference on Ground Penetrating Radar, Santa Barbara, CA, USA, 234-239.

Roth, F., Van Genderen, P., and Verhaegen, M., 2001, Analysis of the influence of mine and soil properties on features extracted from GPR data, in *Conf. Proc. SPIE*, vol. 4394, Detection and Remediation Technologies for Mines and Minelike Targets VI, Orlando, FL, USA, 428-439.

Roth, F., and Olhoeft, G. R., 2000, GPR antenna position and orientation estimation using strapdown inertial navigation, in *Conf. Proc. SPIE*, vol. 4084, 8th International Conference on Ground Penetrating Radar, Gold Coast, Australia, 596-601.

Roth, F., 1999, *Strapdown inertial navigation for ground penetrating radar data acquisition: theory and experiments*: MSc thesis, Colorado School of Mines, Golden, CO, USA, 217p. + CD.